Universidad de Oviedo

Universidá d'Uviéu

University of Oviedo

Programa de Doctorado en Materiales

Estudio de la difusividad y fragilización por hidrógeno del acero 42CrMo4 templado y revenido

Study on hydrogen diffusivity and embrittlement of quenched and tempered 42CrMo4 steel

---

TESIS DOCTORAL

Alfredo Zafra García

Junio 2021

Universidad de Oviedo

Universidá d'Uviéu

University of Oviedo

Programa de Doctorado en Materiales

Estudio de la difusividad y fragilización por hidrógeno del acero 42CrMo4 templado y revenido

Study on hydrogen diffusivity and embrittlement of quenched and tempered 42CrMo4 steel

---

TESIS DOCTORAL

Directores de tesis

Dr. D. Francisco Javier Belzunce Varela

Dra. Dña. María Cristina Rodríguez González

Universidad de Oviedo
Universidá d'Uviéu
University of Oviedo

RESUMEN DEL CONTENIDO DE TESIS DOCTORAL

1.- Título de la Tesis	
Español: Estudio de la difusividad y la fragilización por hidrógeno en el acero 42CrMo4 templado y revenido	Inglés: Study on hydrogen diffusivity and embrittlement of quenched and tempered 42CrMo4 steel.

2.- Autor	
Nombre: Alfredo Manuel Zafra García	DNI:
Programa de Doctorado: Materiales	
Órgano responsable: Comisión Académica Programa de Doctorado en Materiales	

RESUMEN (en español)

El hidrógeno se considera actualmente como una de las alternativas más prometedoras a los combustibles fósiles tradicionales. De hecho, la fabricación de vehículos propulsados por hidrógeno, así como la construcción de infraestructuras para su repostaje se están impulsando enormemente en las economías modernas. En este tipo de instalaciones, componentes metálicos como recipientes a presión, válvulas o tuberías, están expuestos directamente a la acción de hidrógeno gaseoso a elevada presión. La utilización de aceros poco aleados de media y alta resistencia permitiría fabricar productos más ligeros y reducir los costes de fabricación. Sin embargo, estos aceros son susceptibles de padecer el fenómeno de fragilización por hidrógeno, viéndose sus propiedades mecánicas notablemente afectadas.

Por lo tanto, el objetivo de esta tesis es estudiar los efectos del hidrógeno en el comportamiento a tracción, tenacidad a la fractura y fatiga del acero 42CrMo4 templado y revenidos a diferentes temperaturas, así como en la zona afectada térmicamente de grano grueso de las soldaduras realizadas con este acero. Las probetas utilizadas en los ensayos mecánicos se precargaron con hidrógeno gaseoso en un reactor a presión a 19.5MPa y 450ºC durante 21h. También se precargaron probetas cilíndricas para determinar la capacidad de absorción de hidrógeno y la cinética de desorción de los grados estudiados. Mediante desorción térmica (analizador de hidrógeno Leco DH603) se midió la concentración de hidrógeno presente en todos los aceros y la energía de activación del hidrógeno en sus trampas microestructurales. Se llevaron a cabo simulación mediante elementos finitos para evaluar la difusividad de todos los aceros. Además, se realizaron ensayos de permeación electroquímica de hidrógeno para evaluar la interacción entre los átomos de hidrógeno y las trampas microestructurales. Empleando la metodología de sucesivos transitorios crecientes ha sido posible determinar el coeficiente de difusión aparente y de la red, así como la densidad de trampas de hidrógeno.

En función de los resultados obtenidos, la solubilidad de hidrogeno disminuye al hacerlo el tamaño de grano austenítico y al aumentar la temperatura de revenido, mientras que el coeficiente de difusión (el aparente y el de la red) aumentan. Consecuentemente, los aceros más duros y con microestructuras más groseras mostraron una mayor densidad de trampas de hidrógeno. Esto se debe a su mayor densidad de dislocaciones, que constituyen la principal trampa de hidrógeno en estos aceros, con una energía de atrapamiento asociada de 27 kJ/mol. Por tanto, la susceptibilidad al fenómeno de fragilización por hidrógeno fue mucho mayor en aquellos aceros revenidos a menor temperatura (mayor límite elástico) y en las microestructuras más groseras. Se ha demostrado que los índices de fragilización aumentaron al disminuir la velocidad de aplicación de la carga o la frecuencia y que únicamente el hidrógeno difusible es responsable del daño por hidrógeno. Finalmente, se realizó un exhaustivo análisis fractográfico empleando microscopía electrónica de barrido. Mientras que la coalescencia de microhuecos (CMH) fue el modo de fallo dúctil típico en los aceros ensayados sin hidrógeno interno, en las probetas precargadas con hidrógeno tuvieron lugar micromecanismos de fractura frágiles como la descohesión entre la matriz y las intercaras de los carburos (DMC) o de las lajas martensíticas (DLM). Detectándose incluso fractura

intergranular (IG) en los aceros más duros y las microestructuras más groseras, al ser ensayadas a la menor velocidad de desplazamiento o frecuencia, debido a una mayor acumulación de hidrógeno en la zona de proceso cercana al frente de grieta. Este análisis fractográfico reveló la acción sinérgica del mecanismo de plasticidad localizada debida al hidrógeno (HELP) y de descohesión favorecida por hidrógeno (HEDE). De hecho, en primer lugar, el mecanismo HELP favorece el movimiento de las dislocaciones y por lo tanto el transporte y consiguiente acumulación de hidrógeno en la zona de proceso, y posteriormente el mecanismo HEDE ocasiona la descohesión entre intercaras microestructurales específicas.

RESUMEN (en Inglés)

Hydrogen is nowadays considered one of the most promising alternatives to traditional fossil fuels. In fact, commercial fuel cell vehicles and hydrogen refuelling stations are currently under construction in most industrialised countries. In these hydrogen infrastructures, different metallic components such as hydrogen pressure vessels, pipes or valves are directly exposed to high-pressure hydrogen gas. The application of medium and high-strength low-alloyed steels for the construction of these components enables lighter products as well as manufacturing cost reductions. However, these steels may undergo hydrogen embrittlement during their service life under high hydrogen pressure, being their mechanical properties considerably affected.

Therefore, the aim of this thesis is to study the effects of hydrogen on the tensile, fracture toughness and fatigue behaviour of 42CrMo4 steel quenched and tempered at different temperatures and in the coarse grain heat affected zone welds produced with this steel. The specimens used in all the mechanical tests were pre-charged with hydrogen gas in a reactor at 19.5 MPa and 450ºC for 21 hours. Cylindrical specimens were alike pre-charged to determine hydrogen uptake and desorption behaviour. Thermal desorption analysis (using a Leco DH603) was employed to measure the hydrogen concentration in each steel and to determine the activation energy for desorption of hydrogen atoms from the microstructural trapping sites. Finite element simulations were also performed to study the hydrogen diffusivity of the different steel grades. Furthermore, electrochemical hydrogen permeation tests were carried out in order to evaluate the interaction between hydrogen atoms and the microstructure of the studied grades. Employing successive build-up transients methodology, it was possible to accurately determine the apparent and lattice diffusion coefficients, as well as the density of trapping sites.

According to the obtained results, hydrogen solubility was seen to decrease with increasing tempering temperature, and decreasing prior austenitic grain size, following the hydrogen diffusion coefficients (both apparent and lattice) the opposite trend. In this line, the harder and coarser microstructures displayed a greater density of hydrogen trapping sites. This is explained in virtue of their greater dislocation density, being these the main trapping sites in these steels, with binding energies of around 27 kJ/mol. It was also observed that hydrogen embrittlement was much greater in the steel grades tempered at the lowest temperatures (with highest yield strengths) and the coarsest microstructures. It was demonstrated that hydrogen embrittlement indexes always increased when applying lower displacement rates/testing frequencies and that only diffusible hydrogen is responsible for hydrogen embrittlement. Finally, a comprehensive fractographic analysis was performed using scanning electron microscopy and the main operative failure micromechanisms due to the presence of internal hydrogen were determined. While microvoids coalescence (MVC) was found to be the typical ductile failure micromechanism in the absence of hydrogen in all the studied steel grades, brittle decohesion mechanisms (carbide-matrix interface decohesion, CMD, and martensitic lath interface decohesion, MLD) were observed under internal hydrogen in all the studied grades. Intergranular fracture (IG) was also found in the case hardest and in the coarse grain steels when tested under the lowest displacement rates or frequencies, in which hydrogen accumulation in the process zone ahead of the notch tip is maximal. This fractographic analysis revealed the action of hydrogen-enhanced localized plasticity (HELP) mediated hydrogen-enhanced decohesion (HEDE) micromechanism, in which HELP took place first, providing enough hydrogen in the process zone to modify the local resistance, and eventually weakening the cohesion of internal interfaces (HEDE).

SR. PRESIDENTE DE LA COMISIÓN ACADÉMICA DEL PROGRAMA DE DOCTORADO EN MATERIALES

A single grain of rice can tip the scale.

Acknowledgements

The completion of this doctoral thesis represents a milestone, both in my life and in my scientific career. That is why I would like to take this opportunity to thank all the people that have made it possible.

First of all, my special thanks go to Javier and Cristina, supervisors of this work, who guided and supported me through these five years of research and gave me the chance to work in their research group. This PhD work would not have been possible without you both. Thanks also to all my thesis colleagues of the Materials and Construction departments, especially Borja and Guille, with whom I shared both successful and frustrating moments in the lab. I also wish to acknowledge the Spanish Ministry of Science, Innovation and Universities for the financial support received to carry out the research projects MAT2014-58738-C3 (SAFEHIDROSTEEL) and RTI2018-096070-B-C31 (H2steelweld), and also to the Board of Education and Culture of the Principality of Asturias for the Severo Ochoa grant, PA-18-PF-BP17-038.

I really appreciate the selfless help of Juan and Nacho, who helped me to overcome different technical issues that I encountered at the lab. I would also like to acknowledge Victor Vega for his time and technical support regarding scanning electron microscopy which constitute, without any doubt, a key element of this work. Thanks to all the professors at the Materials department, especially Inés, Vicky, Florina and Arantza, with whom I have had the pleasure of collaborating in practical lessons. Thanks also to Prof. Chiara Colombo, for her fruitful collaboration and helpfulness in Milano during difficult times. I would also like to show my gratitude to Prof. Emilio Martinez-Pañeda, both for the interesting discussions about hydrogen embrittlement and for opening new doors in my research career.

I would also like to thank my project colleagues from Burgos, Andrés, Iván and Jesús, for the interesting conversations and ideas during those long project meetings. Of course, I could not forget the GEFazos, those gala dinners were unforgettable.

Furthermore, I also want to thank all the undergraduate and master students that have performed their final projects on hydrogen embrittlement with me, your effort in the lab was both inspiring and motivating. Also, thanks to all the foreign visitors, as I have learnt particular things from all of you too.

And last but not least, I would like to express my deepest gratitude to my family and closest friends, who have always been there along these years of hard work. You are the reason of this thesis.

Alfredo

June 2021

Abstract

Hydrogen is nowadays considered one of the most promising alternatives to traditional fossil fuels. In fact, commercial fuel cell vehicles and hydrogen refuelling stations are currently under construction in most industrialised countries. In these hydrogen infrastructures, different metallic components such as hydrogen pressure vessels, pipes or valves are directly exposed to high-pressure hydrogen gas environments. The application of medium and high-strength low-alloyed steels for the construction of these components enables lighter products as well as manufacturing cost reductions. However, these steels may undergo hydrogen embrittlement (HE) during their service life under high hydrogen pressure, being their mechanical properties considerably affected.

Therefore, the aim of this thesis is to study the effects of hydrogen on the tensile, fracture toughness and fatigue crack growth behaviour of 42CrMo4 steel quenched and tempered at different temperatures. In addition, hydrogen effects on the mechanical properties of the coarse grain heat affected zone (CGHAZ) of welds produced with this steel were also studied. To do so, the CGHAZ was simulated by means of a laboratory heat treatment consisting in austenitizing at a higher temperature. The specimens used in all the mechanical tests were pre-charged with hydrogen gas in a reactor at 19.5 MPa and 450ºC for 21 hours.

Cylindrical specimens were also pre-charged in the aforementioned conditions to determine hydrogen uptake and hydrogen desorption behaviour. The hydrogen concentration in each steel was measured by means of thermal desorption analysis (TDA), in a Leco DH603 hydrogen analyser. In addition, TDA also allowed us to determine the activation energy for desorption of hydrogen atoms from the microstructural trapping sites present in all these steels. Finite element simulations (FEM) were also employed to study the hydrogen diffusivity of the different steel grades. Furthermore, electrochemical hydrogen permeation tests were performed in order to evaluate the interaction between hydrogen atoms and the microstructure of the studied grades. Employing successive build-up transients methodology, it was possible to accurately determine the apparent and lattice diffusion coefficients, as well as the density of trapping sites.

According to the obtained results, hydrogen solubility and hydrogen strongly trapped in the steel microstructure were seen to decrease with increasing tempering temperature, and decreasing prior austenitic grain size, following the hydrogen diffusion coefficients (both apparent and lattice) the opposite trend. In this line, the harder and coarser microstructures displayed a greater density of hydrogen trapping sites. This is explained in virtue of their greater dislocation density, being these the main trapping sites in martensitic CrMo steels, with binding energies of around 27 kJ/mol.

It was also observed that hydrogen embrittlement was much greater in the steel grades tempered at the lowest temperatures (with highest yield strengths) and the coarsest microstructures. In addition, hydrogen embrittlement indexes always increased when applying lower displacement rates and lower testing frequencies in the mechanical tests. It was also demonstrated that only diffusible hydrogen, hydrogen atoms able to move at room temperature, are responsible for hydrogen embrittlement.

Finally, a comprehensive fractographic analysis was performed using scanning electron microscopy (SEM) and the main operative failure micromechanisms due to the presence of internal hydrogen were determined. While microvoids coalescence (MVC) was found to be the typical ductile failure micromechanism in the absence of hydrogen in all the studied steel grades, brittle decohesion

mechanisms (carbide-matrix interface decohesion, CMD, and martensitic lath interface decohesion, MLD) were observed under internal hydrogen in all the studied grades. Intergranular fracture (IG) was also found to be operative in the case of the hardest steels and in the coarse grain steels when tested under the more severe conditions (lowest displacement rates or frequencies) in which hydrogen accumulation in the process zone ahead of the notch tip is maximal. This fractographic analysis revealed the action of hydrogen-enhanced localized plasticity (HELP) mediated hydrogen-enhanced decohesion (HEDE) micromechanism, in which HELP took place first, providing enough hydrogen in the process zone to modify the local resistance, and eventually weakening the cohesion of internal interfaces.

Resumen

El hidrógeno se considera actualmente como una de las alternativas más prometedoras a los combustibles fósiles tradicionales. De hecho, la fabricación de vehículos propulsados por hidrógeno, así como la construcción de infraestructuras para su repostaje se están impulsando enormemente en la mayoría de los países industrializados. En este tipo de instalaciones, componentes metálicos como recipientes a presión, válvulas o tuberías, están expuestos directamente a la acción de hidrógeno gaseoso a elevada presión. La utilización de aceros poco aleados de media y alta resistencia permitiría fabricar productos más ligeros, así como reducir los costes de fabricación. Sin embargo, este tipo de aceros son susceptibles de padecer el fenómeno de fragilización por hidrógeno, viéndose sus propiedades mecánicas notablemente afectadas.

Por lo tanto, el objetivo de esta tesis es estudiar los efectos del hidrógeno en el comportamiento a tracción, tenacidad a la fractura y crecimiento de grieta por fatiga del acero 42CrMo4 templado y revenidos a diferentes temperaturas. Además, también se han estudiado los efectos del hidrógeno en las propiedades mecánicas de la zona afectada térmicamente de grano grueso (ZAT-GG) de las soldaduras realizadas con este acero. Para ello se ha producido una microestructura similar a la existente en esta zona mediante un tratamiento térmico controlado, austenizando a elevadas temperaturas. Todas las probetas utilizadas en los ensayos mecánicos se precargaron con hidrógeno gaseoso en un reactor a presión a 19.5MPa y 450ºC durante 21h.

También se precargaron probetas cilíndricas en las mismas condiciones para determinar la capacidad de absorción de hidrógeno y la cinética de desorción de cada uno de los grados de acero estudiados. La concentración de hidrógeno se midió mediante desorción térmica utilizando un analizador de hidrógeno Leco DH603. Además, también se utilizó la desorción térmica para determinar la energía de activación del hidrógeno en las trampas microestructurales existentes en estos aceros. Se hizo uso también de la simulación mediante elementos finitos para estudiar la difusividad de todos estos aceros. Además, se realizaron ensayos de permeación electroquímica de hidrógeno para evaluar la interacción entre los átomos de hidrógeno y las trampas microestructurales, y empleando la metodología de sucesivos transitorios crecientes ha sido posible determinar el coeficiente de difusión aparente y de la red, así como la densidad de trampas de hidrógeno.

En función de los resultados obtenidos, tanto la solubilidad como la cantidad de hidrógeno fuertemente retenido en la microestructura del acero disminuyen al hacerlo el tamaño de grano austenítico y al aumentar la temperatura de revenido, mientras que el coeficiente de difusión (tanto el aparente como el de la red) por el contrario aumenta. Consecuentemente, los aceros más duros y con microestructuras más groseras mostraron una mayor densidad de trampas de hidrógeno. Esto se explica en virtud de su

mayor densidad de dislocaciones, que en este tipo de aceros martensíticos CrMo constituyen la principal trampa de hidrógeno, con una energía de atrapamiento asociada de 27 kJ/mol.

De este modo, la susceptibilidad al fenómeno de fragilización por hidrógeno fue mucho mayor en aquellos aceros revenidos a menor temperatura (mayor límite elástico) y en las microestructuras más groseras. Además, los índices de fragilización siempre aumentaron al disminuir la velocidad de aplicación de la carga o la frecuencia y se demostró también que únicamente el hidrógeno difusible, capaz de difundir en la microestructura del acero a temperatura ambiente, es responsable del daño.

Finalmente, se realizó un amplio y detallado análisis fractográfico empleando microscopía electrónica de barrido (SEM), identificándose los principales micromecanismos de fractura provocados por la presencia de hidrógeno interno. Mientras que la coalescencia de microhuecos (CMH) fue el modo de fallo dúctil típico en los aceros ensayados sin hidrógeno interno, en las probetas precargadas con hidrógeno tuvieron lugar micromecanismos de fractura frágiles como la descohesión entre la matriz y las intercaras de los carburos (DMC) y la descohesión entre lajas martensíticas (DLM). También se detectó fractura intergranular (IG) en los aceros más duros, así como en las microestructuras más groseras, al ser ensayadas en las condiciones más desfavorables (menor velocidad de desplazamiento o menor frecuencia). Esto se debe a una mayor acumulación de hidrógeno en la zona de proceso cercana al frente de grieta. Este análisis de las superficies de fractura reveló la acción conjunta y sinérgica del mecanismo de plasticidad localizada debida al hidrógeno (conocido como HELP por sus siglas en inglés) y de descohesión favorecida por hidrógeno (conocido como HEDE también por sus siglas en inglés). De hecho, en primer lugar, tiene lugar el mecanismo HELP, favoreciendo el movimiento de las dislocaciones y por lo tanto el transporte y consiguiente acumulación de hidrógeno en la zona de proceso, y finalmente el mecanismo HEDE es el responsable del daño final, ocasionando la descohesión entre intercaras microestructurales específicas.

Table of Contents

Nomenclature

BCC	Body-centered cubic
CG	Coarse grain
CGHAZ	coarse-grain heat affected zone
C_H	Hydrogen concentration
C_{Hdiff}	Diffusible hydrogen concentration
C_{H0}	Initial hydrogen concentration
C_{Hr}	Deep trapped or residual hydrogen concentration
C_{0app}	Apparent hydrogen sub-surface cathodic concentration
D	Diffusion coefficient
D_{app}	Apparent diffusion coefficient
Δa	Crack growth
ΔK	Stress intensity factor range
D_L	Lattice hydrogen diffusion coefficient
e	Tensile final elongation
E_a	Activation energy for desorption of hydrogen from the trap
E_b	Trap binding energy
EI	Embrittlement index
E_L	Binding energy of hydrogen in the Fe lattice
ε_{max}	Maximum deformation
EPT	Electrochemical permeation tests
ε_{peq}	Equivalent plastic strain
f	Fatigue load frequency
FCC	Face-centered cubic
FCGR	fatigue crack propagation/growth rate
FWHM	Full width at half maximum
H	Hydrogen atom
HAZ	Heat affected zone
HE	Hydrogen embrittlement
HEDE	Hydrogen-enhanced decohesion mechanism
HELP	Hydrogen-enhanced localized plasticity
IG	Intergranular fracture
J	Fracture toughness

J_c	Cathodic current density
J_p	Permeation current density
J_{ss}	Steady state permeation current density
$J_{0.2/BL}$	J value for the onset of crack growth (0.2 mm)
K_{app}	Applied stress intensity factor
K_t	Stress concentration factor
$K_{th/0.2}$	Threshold stress intensity factor
LLD	Load line displacement
MLD	Martensitic lath decohesion
MVC	Microvoid coalescence
N_t	Density of hydrogen traps
OQ	Oil quenching
PAGS	Prior austenite grain size
ϕ	Heating rate
P_{max}	Maximum load
ppm	Parts per million (weight %)
PRHIC	Plasticity related hydrogen induced cracking
PWHT	Post welding heat treatment
R	Fatigue Load ratio
RA	Reduction in area
SEM	Scanning electron microscope/microscopy
σ_h	Local hydrostatic stress
σ_{uts}	ultimate tensile strength
σ_{yy}, σ_{22}	Stress parallel to the load direction
σ_{ys}	Yield strength
TDA	Thermal desorption analysis
TDS	Thermal desorption spectrometry
θ_t	Fraction of occupied traps
WQ	Water quenching
x_H	Diffusion distance
XRD	X-ray diffraction

Chapter 1

Introduction

Study on hydrogen diffusion and embrittlement of quenched and tempered 42CrMo4 steel

PhD Thesis

1. Introduction

The global energy demand, boosted by the growth of industrialized countries, is predicted to increase in the order of 45% by 2030 and by more than 300% by the end of the century [1]. Consequently, the alarm of accelerated global warming is shifting the energy focus from fossil fuel resources to clean and renewable energies, such as hydrogen. In fact, hydrogen, and specifically green hydrogen obtained from renewable energy sources (Figure 1.1), is expected to represent between 6% and 18% of the total energy consumption by 2050 [2,3]. However, the major technical drawback of hydrogen as an energy carrier is its very low energy density per unit of volume (10 MJ/m^3) compared to other gaseous fuels such as methane (33 MJ/m^3) and propane (87 MJ/m^3). This increases the supply costs of hydrogen to up to 5 times more than those of natural gas [4]. Therefore, hydrogen storage and distribution pressures must increase considerably, from the current situation of 15-20 MPa to 80-100 MPa. However, the use of traditional low-strength ferritic steels for the manufacture of these facilities would require very thick walls, shooting up manufacturing and installation costs by more than 30% [5].

Figure 1.1. Green hydrogen (produced from renewable energies) stored in pressure vessels [6].

It is then clear that the development of medium and high-strength steel grades, suitable for the manufacture of pipes, vessels, and other components able to safely withstand very high gaseous hydrogen pressures is a decisive issue in the modern energy landscape. In this regard, quenched and tempered CrMo steels, namely 42CrMo4 steel, with enhanced mechanical strength and fracture toughness, have a longstanding tradition in storage and transport of hydrogen containing gases and fluids, for example in the petrochemical and nuclear industries [7–10]. These steels are now also considered adequate candidates for these kinds of new applications.

However, as reported for the first time in 1874 by W.H. Johnson [11], this class of steels are prone to suffer the so-called hydrogen embrittlement (HE) phenomenon, that manifests in a notorious degradation of their most important mechanical properties (tensile strength, elongation, fracture toughness and fatigue crack propagation rate) [12–15]. While other kinds of subcritical failure mechanisms such as erosion and corrosion are visible and thus can be easily detected and repaired, the damage caused by HE phenomena is normally not visible and therefore much more dangerous and could lead to catastrophic failures.

An example of these problems is the sudden collapse of a compressed hydrogen storage tank, whose consequences can be observed in Figure 1.2. This failure was caused by the fast growth of large fatigue cracks which were induced by the entry of hydrogen in the steel microstructure. The total damage paid by the insurance company in this case was approximately 50 million of US$ [16].

Figure 1.2. Catastrophic failure of compressed hydrogen storage tank [16].

Atomic hydrogen is able to penetrate, due to its small size, into the steel microstructure and diffuse through its lattice driven by stress and concentration gradients [17–19]. Eventually it is trapped in lattice imperfections, known as hydrogen traps [20,21] and also in highly stressed areas. It is known that the accumulation of quite large hydrogen concentrations in these preferential sites modifies the failure micromechanisms when the steels are submitted to mechanical loads [22,23]. The two most relevant micromechanisms in the case of steels are hydrogen-enhanced decohesion (HEDE) and hydrogen-enhanced localised plasticity (HELP) [24]. In fact, the assumption that HE phenomenon is governed by a combination of a defined local amount of hydrogen accumulated in specific regions of the steel microstructure along with critical stress levels, is nowadays widely accepted [25,26]. Typically, hydrogen promotes brittle fractures, being the fracture surfaces characterized by cleavage or intergranular fracture micromechanisms, depending on the strength level of the steel and on the concentration of internal hydrogen.

Therefore, it seems clear that the characterization of hydrogen behaviour in medium and high-strength steels is important for the understanding, prediction, and prevention of HE phenomenon, in order to assure their safe use in hydrogen storage and transport applications. However, although the study on the effects of hydrogen in the mechanical properties of quenched and tempered CrMo steels has attracted the attention of researchers and engineers during the last decades, a deeper understanding of certain aspects related to this phenomenon is still necessary. Some of these are, for example, the interaction between hydrogen atoms and the different traps present in the steel's microstructure, the effects of hydrogen in coarse microstructures, such as those present in the heat affected zone of welds, and the characteristics of the fracture micromechanisms fostered by hydrogen action.

1.1. Objectives

In this context, the general aim of this thesis is to study hydrogen embrittlement phenomena in the quenched and tempered 42CrMo4 steel in order to assess the suitability of this steel for the manufacturing of welded pipes and vessels able to safely transport and store high pressure hydrogen gas. Therefore, the specific objectives of this thesis are the following:

- Performing microstructural and mechanical characterization in absence of hydrogen on high and medium strength 42CrMo4 steel grades obtained by means of quench and tempering heat treatments.
- Determining both the apparent and lattice hydrogen diffusion coefficients in all that quenched and tempered 42CrMo4 grades and in some of their CGHAZ and exploring their relation with their microstructures.
- Identifying the main microstructural hydrogen traps on all the already mentioned grades, their density and trapping energy.
- Studying the influence of internal hydrogen on the tensile, fracture toughness and fatigue crack growth behaviour of these steels. The influence of different testing variables, such as displacement rate, frequency (in cyclic tests) and hydrogen concentration present in the tested samples will be also studied.
- Understanding the relationship among internal hydrogen concentration, hydrogen diffusion coefficient, density of trapping sites and hydrogen accumulation in specific microstructural locations with the reduction in the mechanical properties of the steels, including the effect of the steel strength/hardness.
- Performing a thorough fractographic analysis as to identify the main failure micromechanisms operative in all the aforementioned mechanical tests in order to contribute to a better understanding of the failure mechanisms associated to hydrogen embrittlement, HELP and HEDE.

Along this thesis, the influence of tempering temperature (hardness and yield strength) and the austenitization temperature (prior austenitic grain size) was evaluated and explained. The austenitization temperature modification allowed us to reproduce the microstructure present in the coarse-grain heat affected zone (CGHAZ) of welds made on this steel.

Finally, some general recommendations regarding the design and use of quenched and tempered 42CrMo4 steel for its safe service for long periods of time in contact with hydrogenated media are provided.

Chapter 2

State of knowledge

Study on hydrogen diffusion and embrittlement of quenched and tempered 42CrMo4 steel

PhD Thesis

2. State of knowledge

2.1. Introduction

This chapter provides a brief insight into hydrogen embrittlement phenomenon (HE) regarding medium and high-strength structural steels. The theoretical background, along with a concise bibliographic review on the following points are given: interaction of hydrogen with the microstructure of steels, techniques used to characterize hydrogen diffusion and trapping; main fracture mechanisms associated to HE and effects of hydrogen on the mechanical properties of steels.

2.2. What is hydrogen embrittlement?

HE is a phenomenon suffered by most metals and alloys that produces the degradation of their mechanical properties. As observed in Figure 2.1, three concurrent conditions must exist for the occurrence of this phenomenon: the presence of hydrogen in the material's lattice, which implies absorption from an external hydrogen source (i.e., a hydrogen rich environment), tensile stresses, and a susceptible microstructure.

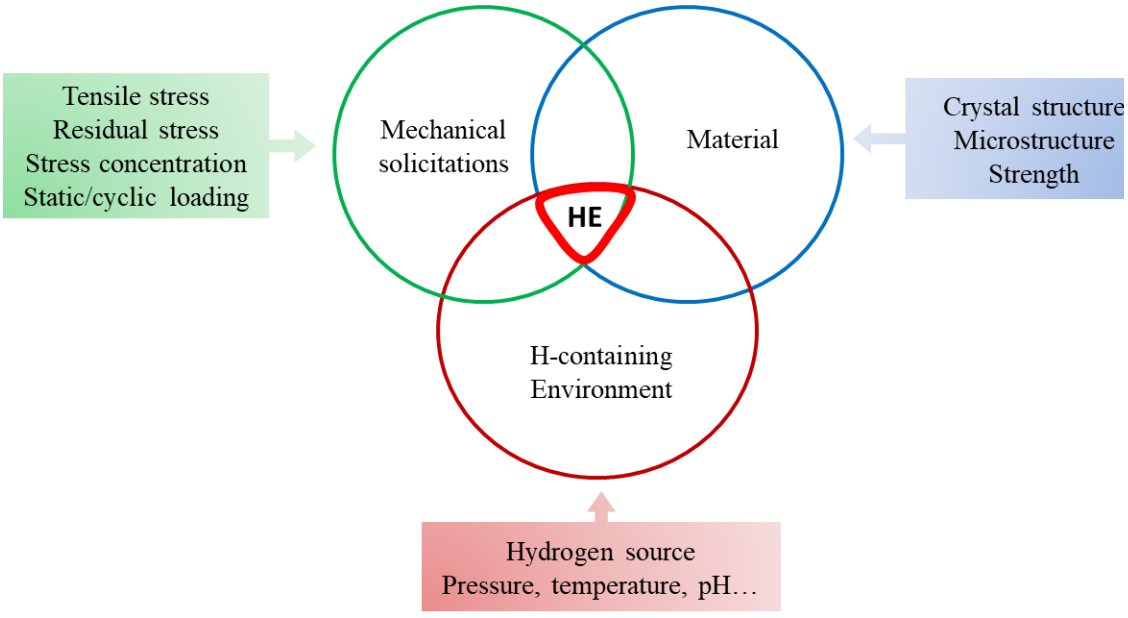

Figure 2.1. Necessary conditions for the occurrence of the HE phenomenon.

Hydrogen atoms can enter into metal components during manufacturing processes, such as casting, welding, pickling, electric discharge machining and electrolytic coating and/or they can be absorbed from an external environment during their lifespan under certain working conditions. Examples of environments/conditions from where hydrogen can be absorbed are cathodic protection, corrosion phenomena in different aqueous media and direct contact with pure hydrogen gas, or with hydrogen-containing gases, at high pressure [27–30].

Considering the latter assumption (external continuous hydrogen source), hydrogen atoms are first adsorbed by the steel surface, then they enter into the steel lattice (absorption process), diffuse and, finally, they interact with the steel microstructure to produce the embrittlement phenomenon, characterized by a drastic reduction in the steel´s most important mechanical properties (tensile strength, elongation, fracture toughness and fatigue crack propagation rate) [12–15]. HE takes place when hydrogen concentration accumulated in the process zone just ahead of a crack or a notch exceeds a certain threshold hydrogen concentration under the local external applied tensile load. Sometimes, the existence of residual stresses within the metal is enough to trigger HE.

In general, HE has greater effects on high strength metals and alloys, such as steels and aluminium and titanium alloys. In fact, regarding ferritic steels (with BCC structures), hydrogen susceptibility increases with the steel yield strength [31]. Therefore, martensitic microstructures tempered at low temperatures, with high dislocation densities, are the most sensitive to HE. On the other hand, austenitic steels (with FCC structures) are in general immune to HE, due to their extremely low hydrogen diffusion coefficient and very high hydrogen solubility. Figure 2.2 shows a list with the typical microstructures found in steels, from higher to lower HE susceptibility [32].

Microstructure	
Untempered martensite Untempered martensite and bainite Bainite Tempered martensite Ferrite and pearlite Acicular ferrite Austenite	**Decreasing susceptibility to HE** ↓

Figure 2.2. Typical microstructures found in steels from higher to lower HE susceptibility [32].

On the other hand, regarding welded joints, the presence of hydrogen in the heat affected zone, HAZ, may give rise to the well-known “cold cracking” phenomenon, that takes place at room temperature after cooling [32]. The possible absorption of hydrogen during service added to the hydrogen introduced in the weld during bead deposition leads to an extreme likelihood of hydrogen-induced cracking in these problematic microstructures. In fact, in the case of ferritic microstructures, hydrogen diffusivity at room temperature is considerably high, and hydrogen atoms are able to reach the most critical areas of the components, such as notches, cracks, etc. in relatively short times.

Historically, the HE phenomenon was described for the first time in a paper entitled “On some remarkable changes produced in iron and steel by the action of hydrogen and acids”, published by William H. Johnson in 1874 [11]. After abundant experimental research on the matter for a century, in the 1960s, authors like McNabb and Foster [20] focused their efforts in understanding hydrogen diffusion and trapping phenomena in metallic alloys. Meanwhile, Troiano [33] studied its influence on the mechanical properties of metals. In the 1970s and 1980s, the works of Pressouyre [34] and Oriani [18] were the most remarkable, extending the diffusion investigations performed in previous decades and providing the first characterization of hydrogen trapping sites in pure iron.

From the last years of the twentieth century until today, the research activity about HE phenomenon was intense, being worth to mention the contributions of authors such as Gangloff [35], Wang [36], Yamabe [37] and Murakami [38] on the influence of hydrogen on the mechanical properties of steels, and Nagao, Nibur, Dadfarnia, Dofronis, Robertson and Somerday [22,39,40] on the HE mechanisms.

Nevertheless, despite 150 years of study, there are still a lot of aspects of HE that are not fully understood, especially those related to the interaction of hydrogen with the multiple microstructural traps present in the steels. In addition, the emergence of new metallic alloys, and the necessity to develop specific alloys able to safely work in hydrogen enriched environments, explains the importance of this research topic. Furthermore, there is currently a great effort on the development of complex computational models able to predict hydrogen-induced cracking, based in cohesive elements [41,42] and phase field methods [43], that need to be fed with a great number of experimental parameters.

2.3. Interaction of hydrogen atoms with the steel microstructure

2.3.1. Hydrogen solubility in the crystal lattice

The hydrogen ability to enter in solid solution in metals is due to its small atomic size. Table 2.1 provides the atomic diameters of some elements frequently present in the steel's microstructure, being hydrogen, with 0.092 nm, the smallest.

Element	Atomic diameter, d_H [nm]
H	0.092
B	0.194
C	0.154
N	0.142
O	0.120

Table 2.1. Atomic diameter of elements typically present in the steel structure.

On the other hand, Table 2.2 shows the atomic diameter of Fe atoms in BCC and FCC crystalline structures, as well as the size of their interstitial sites (octahedral and tetrahedral). In general, as the atomic diameter of hydrogen is comparable in size to that of the Fe interstitial sites, hydrogen mobility in Fe is notorious even at room temperature. The larger octahedral interstitial sites present in FCC iron justifies the higher hydrogen solubility typical of these structures. On the other hand, the lower atomic packing factor (APF) of the BCC structures justifies their higher hydrogen diffusivity.

	d_{Fe} (nm)	APF	$d_{\text{octahedral interstitial sites}}$ (nm)	$d_{\text{tetrahedral interstitial sites}}$ (nm)
Fe-α (BCC)	0.248	0.68	0.038 (6/cell)	0.072 (12/cell)
Fe-γ (FCC)	0.252	0.74	0.104 (4/cell)	0.057 (8/cell)

Table 2.2. Atomic diameter of Fe in BCC and FCC crystalline structure and diameter of their correspondent interstitial sites. Atomic packing factor (APF).

Apart from its crystalline structure, hydrogen solubility in iron and steels also depends on the hydrogen partial pressure, or on the available hydrogen concentration in the surroundings, temperature, and also on the presence of certain microstructural features, such as dislocations, vacancies, inclusions, internal interphases, etc., all of them are known as hydrogen traps.

Sievert's law, shown in *Equation (2.1)*, is usually used to describe the relationship between hydrogen solubility, S_H, and the partial pressure of hydrogen in the surrounding atmosphere, being K an equilibrium constant.

$$S_H = K\sqrt{P_{H_2}} \qquad \textit{Equation (2.1)}$$

In addition, according to Arrhenius law (*Equation (2.2)*), hydrogen solubility in steel increases with the temperature, being S_0 a constant, ΔH the activation energy, R the universal gas constant (8.314 J/mol K) and T the temperature.

$$S_H(T) = S_0\, e^{\frac{-\Delta H}{RT}} \qquad \textit{Equation (2.2)}$$

Figure 2.3 shows the changes in solubility in pure iron as a function of temperature [32].

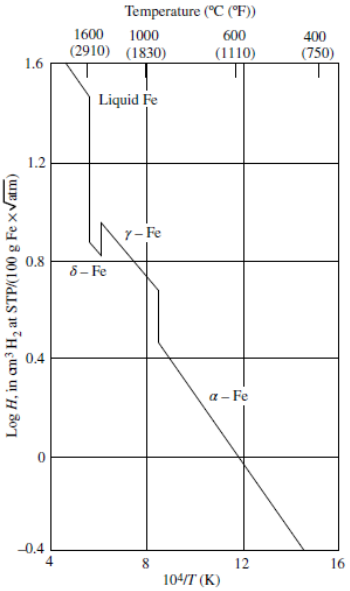

Figure 2.3. Hydrogen solubility in pure iron versus temperature [32].

It is worth noting the solubility drop that takes place in the transformation of Fe-γ to Fe-α. At low temperature (RT), hydrogen excess that cannot be hold in the lattice, but can be retained in those microstructural defects known as hydrogen traps. This way, the amount of hydrogen within the metal, iron in this case, will be greater than its lattice solubility, being the latter, in fact, only a small fraction of the total hydrogen content.

2.3.2. Hydrogen transport

The movement of hydrogen atoms in steels occurs primarily through two mechanisms: interstitial diffusion and transport by dislocations [44].

2.3.2.1. Interstitial diffusion

This is the typical way of hydrogen transport in unloaded, stress free metals. Taking advantage of its low atomic size, hydrogen atoms move easily in Fe-α crystal lattices hopping between adjacent interstitial lattice sites. The main driving force for hydrogen diffusion is provided by gradients in the chemical potential due to an uneven hydrogen concentration in the material. Therefore, hydrogen diffuses from high to low hydrogen concentration regions until equilibrium is reached. Hydrogen flux, J, depends on the hydrogen concentration gradient, $\partial C/\partial x$, through a constant called hydrogen diffusion coefficient, D. Mathematically, diffusion can be expressed according to first Fick's law as it is shown in *Equation (2.3*) [45]:

$$J = -D\frac{\partial C}{\partial x} \qquad \textit{Equation (2.3)}$$

Assuming a constant D value, when the concentration gradient changes over time, the second Fick`s law describes now the diffusion phenomenon according to *Equation (2.4*):

$$\frac{\partial C\ (x,t)}{\partial t} = D\frac{\partial^2 C(x,t)}{\partial x^2} \qquad \textit{Equation (2.4)}$$

Similarly to hydrogen solubility, diffusivity is also temperature dependent and can be expressed, according to the Arrhenius equation, as follows (*Equation (2.5*):

$$D = D_0\, e^{\frac{-\Delta H}{RT}} \qquad \textit{Equation (2.5)}$$

Figure 2.4 shows the evolution of the hydrogen diffusion coefficient with temperature, for both ferritic and austenitic steels. Notice the great diffusivity difference between both crystalline structures.

Temperature plays an important role in HE phenomenon. In general, hydrogen damage tends to decrease when the working temperature of the component is far lower or higher than room temperature. In the former case, hydrogen diffusion decreases drastically and could even be cancelled (at cryogenic temperatures for example), so hydrogen atoms are not able to accumulate on potential crack initiation sites. In the latter case, thermal agitation is very intense and able to empty the microstructural defects (thermal activation) where hydrogen accumulation would take place at room temperature, being impossible to attain the required critical hydrogen concentration for embrittlement.

On the other hand, the large variation of the hydrogen diffusion coefficient in ferritic steels at temperatures close to RT shown in Figure 2.4 is a result of microstructural differences among steels, that is, differences in the density of their microstructural traps.

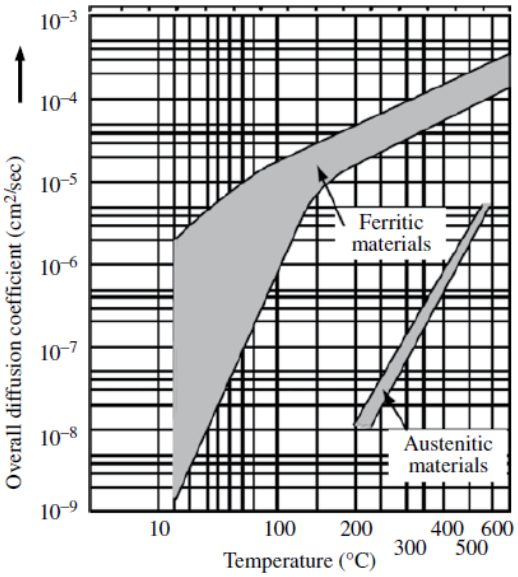

Figure 2.4. Diffusion coefficient of hydrogen in ferrite and austenite as a function of temperature [32].

2.3.2.2. Transport by dislocations

When mechanical loads are involved and plastic deformation takes place, internal hydrogen atoms may be dragged by dislocations. This transport mechanism arose in an attempt to explain the somehow fast transport (faster than lattice diffusion) of hydrogen in strained zones within the material [44]. Basically, hydrogen atoms absorbed into the steel lattice become attached to dislocations, where there are local regions with a larger free volume, moving also with them. This is graphically explained in Figure 2.5 for two different situations: external hydrogen with initially empty traps (Figure 2.5(a)) and internal hydrogen with initially saturated traps (Figure 2.5(b)).

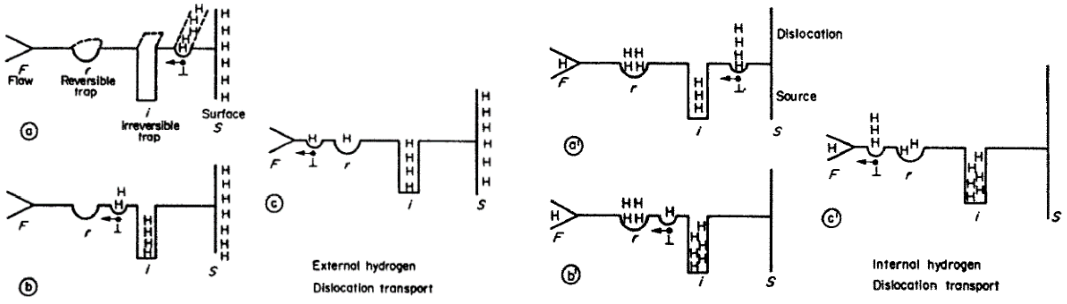

(a) *(b)*

Figure 2.5. Mechanisms of hydrogen transport by dislocations in the case of (a) external hydrogen (a→b→c) and (b) internal hydrogen (a'→b'→c') [44].

Dislocations take hydrogen atoms from the surface in Figure 2.5(a). Being hydrogen traps empty in this case, a fraction of hydrogen atoms carried by dislocations are retained in certain microstructural traps (irreversible and reversible) in their way to a flaw (F), where hydrogen is supposed to accumulate. On the other hand, all the microstructural traps are filled with hydrogen in Figure 2.5(b). Now, although dislocations will lose hydrogen when encountering strong traps, they are also able to pick up more hydrogen from weaker traps, and consequently more hydrogen is able to reach the flaw.

2.3.3. Hydrogen trapping in martensitic CrMo steels

HE of medium and high strength CrMo steels is related to the uptake, diffusion, and accumulation of hydrogen atoms in lattice imperfections always present in these steels (energetically favourable for hydrogen trapping), usually known as hydrogen traps [20,21]. These defects, that increase in number with the strength of the steel [46,47], reduce hydrogen diffusivity and increase hydrogen solubility in the steel and, in general, increase the risk of HE and thus the occurrence of premature failure.

In this context, hydrogen atoms are known to be retained in quenched and tempered CrMo steels (tempered martensite microstructures) in microstructural traps, such as prior austenitic grain boundaries, martensitic lath and packet interfaces, dislocations, interfaces between matrix and precipitated carbides (cementite in the case of the non-alloyed steels) and interfaces between matrix and inclusions (MnS, Al_2O_3, etc.) [48,49]. These lattice imperfections make hydrogen diffusion coefficient around 2 orders of magnitude lower in CrMo steels than in pure Fe (see Figure 2.4) [18,50–54].

Steel trapping characteristics can be described by the density of trapping sites, N_t, the fraction of occupied traps θ_t, and the trap binding energy, E_b. Focusing on the latter, it is generally considered that the interaction energy, or trap binding energy, E_b, between hydrogen atoms and microstructural traps typically ranges between 10 and 100 kJ/mol, in comparison with the binding energy of hydrogen in the iron lattice, E_L, which is usually reported to be 8 kJ/mol.

The definition of E_b is graphically shown in Figure 2.6, where the thermodynamic trapping model proposed by Oriani is represented [18]. The lattice binding energy, E_L, and the activation energy for desorption of hydrogen from the trap, E_a, are shown, along with diffusion and trapping phenomena.

Depending on the value of E_b, hydrogen traps are frequently classified in two groups: weak or reversible traps and very strong or irreversible traps (at room temperature, RT). This classification is also exemplified in Figure 2.6. Traps with a high binding energy (>50-60 kJ/mol) are defined as irreversible traps and hydrogen atoms trapped in them are considered non-diffusible. Reversible traps, on the other hand, are sites from which hydrogen atoms can escape due to fluctuations in their thermal energy. The diffusible hydrogen, i.e. the hydrogen able to move through the steel microstructure at room temperature, is hence the sum of interstitial and reversible hydrogen atoms, and local equilibrium is usually assumed to exist between both [17,55].

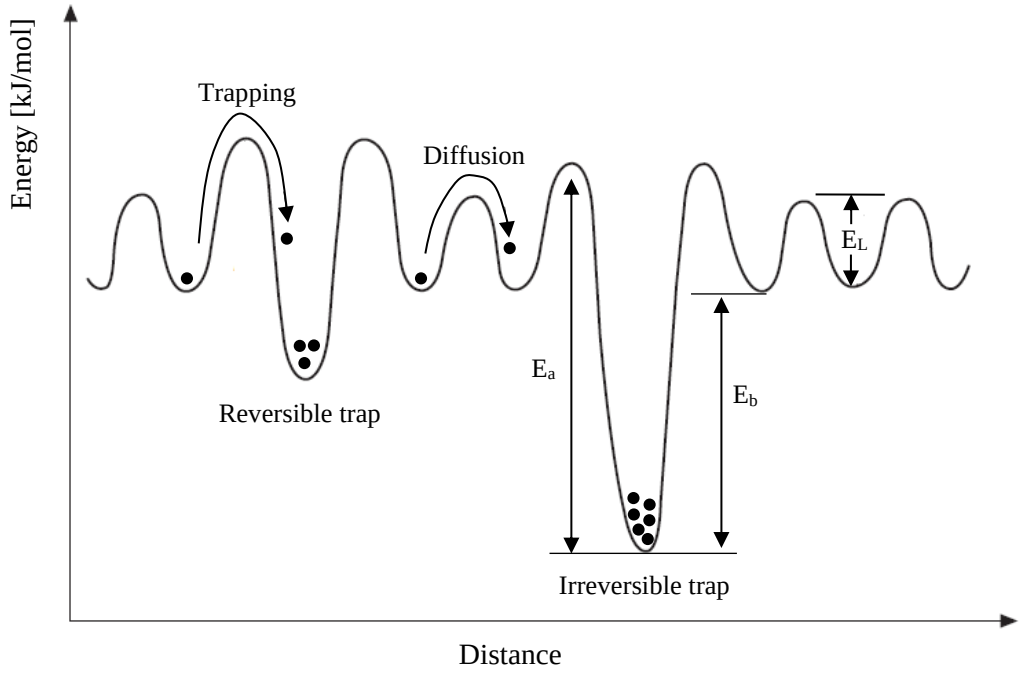

Figure 2.6 Potential energy of hydrogen in interstitial position and traps (reversible and irreversible). E_L is the lattice diffusion energy, E_b the binding energy of the trap and E_a the activation energy for desorption of hydrogen atoms from the trap. Adapted from [18].

For some decades now, different authors have determined the trap binding energies of the different microstructural traps present in CrMo quenched and tempered steels. Thermal desorption analysis, TDA, or thermal desorption spectrometry, TDS, are the main techniques employed to this end. Table 2.3 shows values extracted from the literature, with the corresponding references.

Hydrogen trapping site	E_b [kJ/mol]	Reference
α /Fe-Cr-Mo carbides interphases	11-12	[17,56]
α /Fe_3C interphases	10-18	[21,56–60]
Dislocation elastic stress field	20	[61,62]
Dislocations	20-32	[18,21,55,57,62–81]
Dislocation cores	52-61	[62–64,75,82]
General grain boundaries	17-62	[21,55–57,63,64,78,81,83,84]
Martensite lath boundaries	20-28	[49,85,86]
α/MnS interphases	72	[21,64]

Table 2.3. Binding energies, E_b, of hydrogen in some typical microstructural traps in CrMo martensitic steels.

In general, Nagao et al. [59] concluded that hydrogen is trapped in dislocations, grain boundaries and cementite precipitates in quenched and tempered (between 450 and 650ºC) 0.13-0.17%C low-alloy steels. They assumed that hydrogen trapping is negligible along MnS interphases due to the low relative number of these inclusions present in these steels, and that large cementite precipitates are non-effective hydrogen traps as they are incoherent with the matrix. Jiang et al. [87] recently studied the distribution of trapping sites, specifically ferrite/carbides interfaces, in a

quenched and tempered (650ºC/2h) 42CrMo4 steel by means of atom probe tomography. They demonstrated that hydrogen trapping in the interfaces of those Cr-Mo-Mn carbides (with a size of around 100 nm) located on grain boundaries is significant (much more than in those precipitated in the matrix). Hydrogen trap binding energies provided in [74] were determined on a 0.42%C quenched and tempered CrMoNi steel (tempered at 580-620ºC for 5 hours). These authors reported that most characteristic traps had trapping energies of 20-32 kJ/mol, which were attributed to hydrogen trapped in dislocations and in martensite lath and packet interfaces. By means of electrochemical permeation and thermal desorption tests, Frappart et al. [75] calculated trap binding energies of 26 kJ/mol and 52 kJ/mol in a 0.45%C-1.5%Mo quenched and tempered (at 675ºC for 20 min) steel, which they respectively attributed to hydrogen trapped in dislocations/semi-coherent precipitates and in the dislocation cores.

Anyway, an interesting conclusion that can be drawn from the reviewed works on this specific topic is that, in the context of a complex martensitic microstructures, it becomes difficult to isolate the hydrogen trapping effect of each individual trap, as most of them have similar binding energies [84], and the current measurement techniques are frequently not accurate enough to make distinctions among them [49]. It should also be considered that dislocations are not uniformly distributed along the microstructure of the steel, but instead, they localize on internal interfaces (prior austenite grain boundaries and lath, block, and packet martensite interfaces), where also precipitate most of carbides in the course of the tempering treatment.

2.3.4. Hydrogen permeation tests for diffusion and trapping assessment

An adequate characterization of hydrogen uptake, diffusion and trapping in steels is crucial for understanding, predicting, and preventing hydrogen embrittlement [88,89]. Reliable and useful information on all these processes can be obtained using electrochemical permeation techniques, which are nowadays considered to be the most widespread and appropriate method for measuring hydrogen diffusivity [90–92].

The evaluation of hydrogen adsorption, permeation and transport in metals using electrochemical tests was developed by Devanathan and Stachurski [93] who invented the double permeation cell, that is now known with that name. The practical use of this technique regarding the preparation of specimens, control and monitoring of environmental variables, test procedure and analyses of results are described in the ASTM G148 standard [94]. In these tests, a thin metal membrane (the working specimen) is placed for testing between two independent electrochemical cells. Hydrogen is then introduced into the membrane entry side and diffuses through the membrane until escaping through its exit side, where it is immediately electrochemically oxidised and detected as a density current.

The practical use of electrochemical permeation tests, EPT, is based on the existence of well-defined hydrogen entry conditions on the input side of the membrane (rapid establishment of a certain hydrogen concentration beneath the entry side of the tested specimen) in order to ensure that the measured hydrogen permeation flux is fully controlled by diffusion laws and that hydrogen transport is mainly due to hydrogen atoms hopping among interstitial lattice sites. However, the facts that surface processes on the entry side are usually quite slow and that

hydrogen trapping or de-trapping always takes place during hydrogen transport through the membrane may also be considered [95]. These problems especially affect structural steels, in which the mobility of hydrogen is high, and which also have microstructural traps with high trapping capacity. In this respect, the use of successive partial build-up and decay transients produced by a relatively small increase or decrease of the applied current density (surface hydrogen concentration) was demonstrated to be a good practice to reduce these problems [90].

Assuming that the kinetics of hydrogen transport is governed by diffusion through the lattice (interstitial diffusion), along with trapping and de-trapping at specific microstructural sites, permeation results are dependent on the progressive filling of both reversible and irreversible traps. Therefore, hydrogen diffusivity is sensitive to the increase in the subsurface hydrogen concentration, increasing with it until a constant value is detected. This value corresponds to the real lattice hydrogen diffusion coefficient of the steel, usually denoted as D_L, when all the microstructural traps have been completely filled [91,96,97].

Typically, single hydrogen permeation tests are performed by applying a constant cathodic current density, Jc, until the permeation current reaches a steady state value, J_{ss}. The most common values of this cathodic current density found in the scientific literature vary between 1 and 10 mA/cm^2, although sometimes smaller or larger values are reported. For example, Fallahmohammadi et al. [98] used 0.25 mA/cm^2, whereas Frappart et al. [91] applied cathodic currents within the range of 5-200 mA/cm^2. Using this type of tests, a unique value of the hydrogen diffusion coefficient, D_{app}, is usually calculated. This permeation transient is usually followed by a decay transient (hydrogen discharge phase), during which hydrogen effuses out of the specimen when the cathodic current is switched off. This procedure is often used to determine the density of reversible traps in the steel, and sometimes the lattice diffusion coefficient [99]. Nevertheless, depending on the steel microstructure (traps nature and density) and on the applied cathodic current density (amount of hydrogen generated on the hydrogen charged surface of the specimen), the single permeation transient methodology is not appropriate to fully characterize the interaction between hydrogen and microstructure, as microstructural traps are progressively filled, and the hydrogen diffusion coefficient is not constant but in fact dependent on trap filling, i.e, on the hydrogen concentration present in the steel [100].

The ASTM G148 hydrogen permeation standard [94] recommends performing at least two consecutive hydrogen permeation processes in order to measure hydrogen diffusion in the presence of empty and filled microstructural traps. In fact, Park et al. [101] performed three successive hydrogen charge/discharge cycles in order to characterize diffusivity in a structural steel submitted to different pre-deformations. Additionally, Liu et al. [69] demonstrated the need to record successive permeation transients in order to study the evolution of the hydrogen diffusion coefficient versus the applied cathodic current. Moreover, the partial charge/discharge method proposed by Zakroczymski [53] and extensively applied by [70,98,99,102] was demonstrated to be a convenient technique to measure diffusion coefficients under equilibrium conditions and thus to determine hydrogen diffusion coefficients in steels.

As previously mentioned, the transport of hydrogen in steels is affected by numerous microstructural factors. This point can be quantitatively appreciated in Table 2.4, which compiles

the hydrogen permeation results obtained by several authors on CrMo steels with different microstructures, strength levels and grain sizes.

Ref.	Steel	Heat treatment or micro (Hardness or yield strength)		D_{app} [m^2/s]	D_L [m^2/s]	C_H [ppm]	N_t [$1/m^3$]
[103]	1Cr0.2Mo	Q+T650/30min (328HV)		$6.1\cdot10^{-11}$	$3.1\cdot10^{-10}$	0.9	-
	1Cr0.8Mo	Q+T660ºC/2h (338HV)		$6.1\cdot10^{-11}$	$4.1\cdot10^{-10}$	0.7	-
	1Cr0.2MoVTi	Q+T660ºC/2h (335HV)		$2.3\cdot10^{-11}$	$2.5\cdot10^{-10}$	1.2	-
	1Cr0.8MoVTi	Q+T700ºC/2h (336HV)		$2.5\cdot10^{-11}$	$2.5\cdot10^{-10}$	0.7	-
[104]	42CrMo4	Normalized		$3.6\cdot10^{-10}$	-	0.3	-
[76]	2.25Cr1Mo	WQ (447HV)		$2.1\cdot10^{-11}$	-	2.8	$1.1\cdot10^{27}$
		WQ+T590ºC/8h (304HV)		$6.5\cdot10^{-11}$	-	3.7	$2.4\cdot10^{26}$
		WQ+T640ºC/8h (257HV)		$2.9\cdot10^{-11}$	-	10.1	$4.9\cdot10^{26}$
		WQ+T690ºC/8h (243HV)		$8.5\cdot10^{-11}$	-	19.5	$1.4\cdot10^{26}$
		WQ+T740ºC/8h (213HV)		$5.3\cdot10^{-11}$	-	3.5	$2.4\cdot10^{26}$
[105]	25CrMo4	Ferritic-perlitic		$3.6\cdot10^{-10}$	-	-	-
	42CrMo4	Bainitic		$3.3\cdot10^{-10}$	-	-	-
		FC 250/6h		$4.1\cdot10^{-10}$	-	-	-
[106]	2.25Cr1Mo	WQ (372HV)		$4.5\cdot10^{-11}$	-	3.9	-
		AC+T700/1h (214HV)		$9.8\cdot10^{-11}$	-	2.1	-
		AC+T750/1h (173HV)		$1.6\cdot10^{-10}$	-	1.1	-
[107]	2.25Cr1Mo	Bainitic σ_{ys}=580MPa		$2.3\cdot10^{-11}$	-	1.3	-
	3Cr1MoV	Bainitic σ_{ys}=660MPa		$0.9\cdot10^{-11}$	-	3.3	-
[91]	0.45C1.5Mo	Q+T martensitic steel		$4.9\cdot10^{-11}$	$7.8\cdot10^{-11}$	0.5	$1.3\cdot10^{25}$
[52]	34CrMo4	WQ+T200ºC		$3.1\cdot10^{-11}$	-	0.5	-
		WQ+T540ºC		$2.1\cdot10^{-11}$	-	0.9	-
		WQ+T680ºC		$8.6\cdot10^{-11}$	-	0.2	-
[99]	2.25Cr1Mo	Q+T (190HV)		$1.5\cdot10^{-11}$	$2.8\cdot10^{-10}$	-	$3.5\cdot10^{25}$
[98]	2.25Cr1Mo	Annealed (170HV)		$8.2\cdot10^{-11}$	$1.5\cdot10^{-9}$	-	-
		Q+T (211HV)		$1.4\cdot10^{-11}$	$6.4\cdot10^{-10}$	-	-
		WQ (478HV)		$1.0\cdot10^{-11}$	$2.0\cdot10^{-10}$	-	-
[108]	1Cr0.12Mo0.2Ni	Q+T600ºC/3h		$1.8\cdot10^{-10}$	-	0.7	$3.7\cdot10^{25}$
[109]	2.25Cr1Mo0.25V	Welding +705/8h	BM (230HV)	$5.1\cdot10^{-12}$	-	5.6	-
			WM (226 HV)	$6.5\cdot10^{-12}$	-	3.2	-
			HAZ (231 HV)	$6.2\cdot10^{-12}$	-	3.7	-
[110]	0.6Cr1Mo	As received	BM (210HV)	$1.7\cdot10^{-12}$	-	2.5	-
		1200/20min+WQ	HAZ (385HV)	$3.1\cdot10^{-12}$	-	3.5	-

Table 2.4. Hydrogen permeation results (average values) obtained by different authors with CrMo steels. The hydrogen concentration C_H was obtained from permeation tests or from thermal desorption measurements. N_t is the density of hydrogen traps.

Indeed, the effect of steel hardness (or yield strength) and microstructure on hydrogen transport and trapping has been widely studied. Parvathavarthini et al. [24] compared the hydrogen permeation behaviour of water-quenched, air-cooled and furnace-cooled 2.25Cr1Mo steel and also investigated the effect of tempering the as-quenched structure. They found that hydrogen diffusion coefficients and solubilities are respectively inversely and directly correlated with the Vickers hardness of the steel. Similar results were obtained by Moli-Sanchez et al. [52] using a 34CrMo4 steel quenched and tempered at different temperatures (between 200 and 680ºC) and also by Garet et al. [105], comparing now ferritic-pearlitic and bainitic CrMo microstructures.

The same effects of tempering were also reported by Depover et al. [86] using W alloyed quenched steels, which they associated with the reduction in dislocation density produced during tempering. These authors additionally demonstrated that large carbides precipitated in the course of tempering were not able to trap hydrogen but, nevertheless, small carbides (with sizes below 20 nm) can act as high energy hydrogen traps. Galindo-Nava et al. [111] also demonstrated that dislocations are the main factor in controlling the mobility of hydrogen in quenched and tempered martensitic steels.

In particular, plastic deformation and internal stresses can lead to significant changes in hydrogen mobility and trapping. Kumnick and Johnson [112] investigated the effect of cold plastic deformation on hydrogen diffusion in annealed Armco steel, while other authors performed similar studies in different irons and steels [55,101,113]. All these researchers observed a delay in hydrogen diffusivity when the applied plastic deformation is increased, as the greater the applied strain, the greater the dislocation density in the steel, which are known to be the most important microstructural traps in conventional steels. The binding energy generally attributed to dislocations is around 20-32 kJ/mol as can be seen in Table 2.3, and the dislocation density increase due to plastic deformation will hence increase the amount of reversible hydrogen trapped in the steel, thereby increasing HE.

On the other hand, Wang et al. [114] reports that hydrogen diffusion coefficient decreases, and hydrogen absorption increases with the increase of the austenitizing temperature, due to grain size coarsening. Similar results were obtained by other authors [110,115,116] when comparing the trapping and diffusion behaviour between the fine grain base metal and the coarse grain heat affected zone in CrMo steel pipelines welds. Indeed, Han et al. [117] showed an even more severe diffusivity drop when coarser grain sizes were produced by applying a higher heat input in welding.

Despite all the existing information on this topic related to steels, the determination of the lattice diffusion coefficient and the density of trapping sites is still a challenge. Therefore, the development of experimental methodologies able to give accurate and repetitive results is a necessity. In addition, large parametric studies, considering all those variables involved in hydrogen permeation tests may be helpful to better understand the absorption and diffusion processes in complex microstructures.

2.4. Mechanisms associated to hydrogen embrittlement

It is well known that the presence of atomic hydrogen in the crystalline lattice modifies the operative failure micromechanisms on steels submitted to mechanical loads as a consequence of hydrogen embrittlement [22,23]. In fact, the assumption that this phenomenon is governed by a combination of a defined local amount of hydrogen accumulated in specific regions of the steel microstructure and critical stress levels, is widely accepted [25,26]. However, the exact HE mechanism that takes place under certain circumstances is still a subject of intense debate [88].

Various HE mechanisms can take place in steels and other metals, such as those based on hydride-formation, hydrogen-enhanced decohesion, hydrogen-enhanced localized plasticity, adsorption-induced dislocation emission, and hydrogen-vacancy interactions. However, regarding internal hydrogen embrittlement involving diffusion and accumulation of hydrogen in the process zone located just ahead notched or cracked regions where high hydrostatic stresses develop, the two most relevant and frequently reported micromechanisms in CrMo martensitic steels, are hydrogen-enhanced decohesion (HEDE) and hydrogen-enhanced localized plasticity (HELP) [118,119].

The HEDE mechanism, also known as HID (Hydrogen-Induced Decohesion), initially described by Pfeil [120] and later studied and developed by Gerberich [121], Troiano [33] and Oriani [122], is based in the reduction of the interatomic bonding energy between adjacent crystallographic planes, grain boundaries and other internal interfaces. HEDE assumes that the cohesive strength is reduced when a critical hydrogen concentration is reached in the process zone ahead of a crack tip, where hydrogen accumulates and becomes trapped, due to the existence of high hydrostatic stresses. When the interatomic bonding strength, weakened by the presence of hydrogen, is overcome by the local tensile stress in the crack tip region, micro-cracks appear, and crack growth will occur. In practice, the HEDE mechanism in martensitic steels gives rise to a decrease of the fracture strength and is characterized by brittle fracture surfaces with limited plasticity, which manifested as intergranular, IG, fractures and quasi-cleavages. When decohesion mechanisms take place along martensitic lath interfaces, it is sometimes referred to as plasticity-related hydrogen induced cracking (PRHIC) [39,123] or martensitic lath decohesion (MLD) [40].

On the other hand, Birnbaum, Sofronis, Robertson and co-workers from 1980 onwards [124–126] proposed the HELP mechanism, based on the assumption that hydrogen accumulates in the strained region located ahead of a crack or notch attracted by the high hydrostatic stress. This theory suggests that hydrogen atoms increase dislocation mobility (by reducing the Peierls stress for dislocation movement), thus enhancing localized plasticity. Eventually, shear failure along slip planes takes place. Therefore, in contrast to the brittleness characteristic of the HEDE mechanism, HELP is characterized by a very localized plastic flow and shear deformation on highly stressed regions with great amounts of accumulated hydrogen. Consequently, in practice, this mechanism is usually associated to shallow and elongated dimples visible on the fracture surface. This highly localized plastic flow leads to a lower total elongation at failure and reduction in area under tensile loads on a macroscopic scale [47].

It is necessary to point out that despite decades of research on the mechanisms of hydrogen assisted failures, controversy still exists in terms of identifying the development of appropriate failure mechanism for HE in different materials tested under different conditions [88]. For example, Miresmaeili et al. [25] demonstrated by means of a numerical study, that the occurrence of HEDE or HELP mechanism will depend on the critical shear stress for dislocations slip, which in turn depends on the stress level developed in the steel and on the hydrogen concentration. Therefore, they attributed the development of HELP mechanisms (softening) to low hydrogen concentrations along with low-medium yield strength steels, and HEDE mechanisms (hardening) to high hydrogen concentrations in higher strength steels. These effects were experimentally demonstrated by X. Li et al. [26].

Although some authors have been able to isolate the effect of HEDE and HELP mechanisms [127], other studies claim today that under certain situations, isolated and independent HELP and HEDE micromechanisms are unable to explain hydrogen failures [128–130], but they may act in a cooperative manner, in a synergistic interplay, HELP+HEDE or HELP mediated HEDE [131]. In this regard, it is also worth mentioning that some research works have associated the combined action of HEDE and HELP mechanisms to the premature failure of martensitic CrMo steel specimens with internal hydrogen [131]. This theory is illustrated in Figure 2.7, adapted from [24]. In fact, the combined action of both mechanisms is closer to explain the experimental observations on failed surfaces, where microvoids coalescence, cleavage and intergranular fracture are usually noticed at the same time.

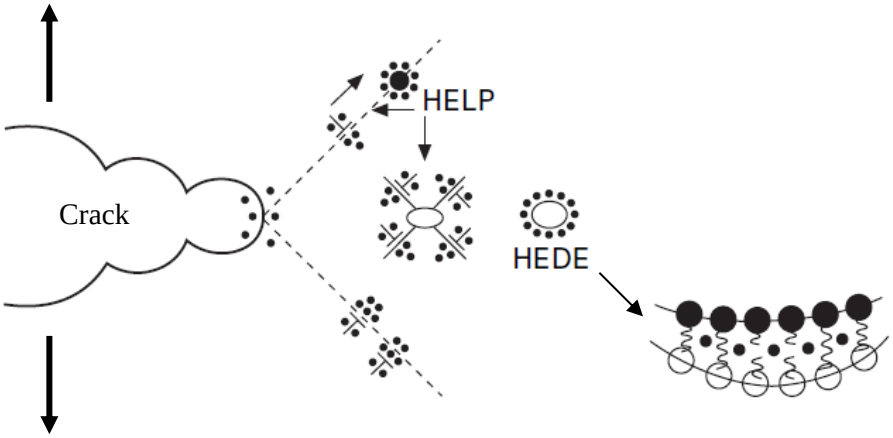

Figure 2.7. Combined action of HELP and HEDE mechanisms that usually takes place in hydrogen-assisted cracking in martensitic steels. Adapted from [24].

2.5. Effects of hydrogen on the mechanical properties of steels

The effects of hydrogen on the mechanical properties of medium and high-strength steels have already been extensively studied in recent years [47]. The presence of internal hydrogen in the microstructure of steels was reported to be detrimental for their tensile properties, decreasing ductility and strength. Fracture toughness is also reduced, and fatigue crack growth rate is accelerated. Furthermore, all these changes usually go hand in hand with relevant alterations of the fracture micromechanisms. As it was seen in the previous section, hydrogen promotes brittle fracture.

When evaluating the interaction between hydrogen atoms, the microstructure of the steels and the applied loads, there are two basic ways to analyse the effects of hydrogen on the mechanical properties of steels: testing in high pressure hydrogen gas (external hydrogen), and testing in air after pre-charging the specimens in a hydrogen-charged medium (internal hydrogen) [35]. In the case of external hydrogen provided by high hydrogen pressures, the measurement of mechanical properties requires the use of very expensive, unique facilities, as material test specimens are

exposed to high-pressure hydrogen gas while simultaneously being subjected to specific mechanical loads. A simple and convenient alternative is to pre-charge the specimens with hydrogen first and then test them in air, since it is generally accepted that the fundamental interactions between hydrogen and microstructure do not depend on the test methodology once hydrogen has been dissolved into the metal [132,133]. For this reason, several studies on the effect of hydrogen on the mechanical properties of steels have been performed using pre-charged specimens. As hydrogen diffusion depends exponentially on temperature, the use of high temperatures greatly accelerates hydrogen pre-charging in a gaseous hydrogen atmosphere providing high hydrogen contents after relatively short charging times. Only temperatures under 450ºC can be used with steels to prevent hydrogen attack (reaction of dissolved hydrogen with carbon to form methane, CH_4 [7]). A third methodology, known as cathodic charging or electrochemical charging, that consists in introducing hydrogen in the specimens from an aqueous solution by applying a cathodic current (or overpotential), is also widely used among researchers in this field as it is convenient and practical both to specimen pre-charging and for "in situ" testing.

2.5.1. Effects of hydrogen on the tensile properties

The effects of hydrogen on the tensile behaviour of medium-high strength steels depend on the dimensions and geometry of the specimens, on the stress concentration factor (if notched specimens are employed) and on certain test variables such as the displacement or strain rate, hydrogen concentration (hydrogen pressure), or test temperature [134][135].

Regarding the tensile properties of smooth specimens (without stress concentrators) tested in presence of internal hydrogen, most of authors have demonstrated that hydrogen effect is mainly reflected in a ductility reduction (elongation and reduction in area) remaining the strength related parameters, namely yield strength and ultimate tensile strength, practically unaffected [136]. This is well exemplified in Figure 2.8, obtained from Gangloff and Somerday [137], where it is observed that, as the strength of the steel increases, hydrogen embrittlement measured as the relative reduction of area of a smooth specimen in monotonic tensile testing, also increases.

However, other works claim that even small hydrogen concentrations present in smooth specimens may lead to a strong decrease of the mechanical strength, as Murakami et al. [14] showed for a high-strength quenched and tempered steel (600-700HV). In fact, Figure 2.9 extracted from Wang et al. [134] shows the stress-strain curves of a quenched and tempered 34CrMo4 steel (σ_{ys}=1320 MPa). A clear reduction of both strength and ductility when increasing the concentration of diffusible hydrogen is observed.

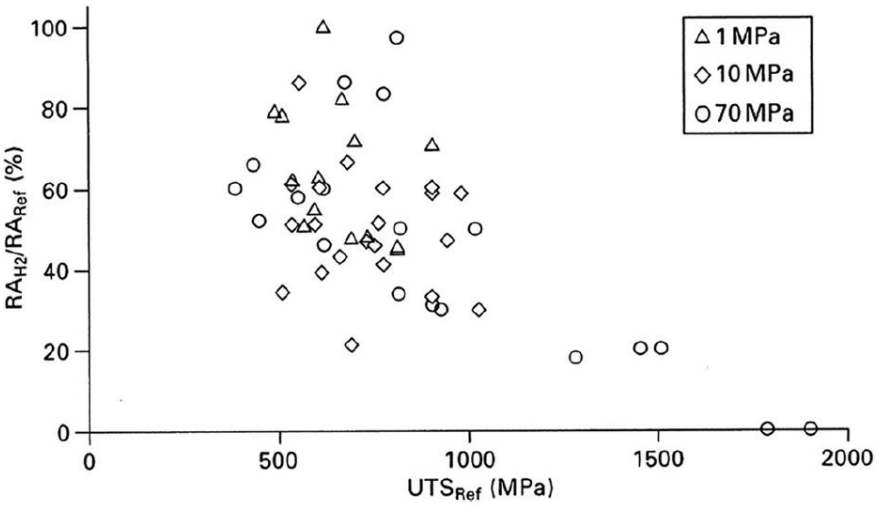

Figure 2.8. Influence of the steel strength on the relative reduction of area of smooth tensile specimens [137].

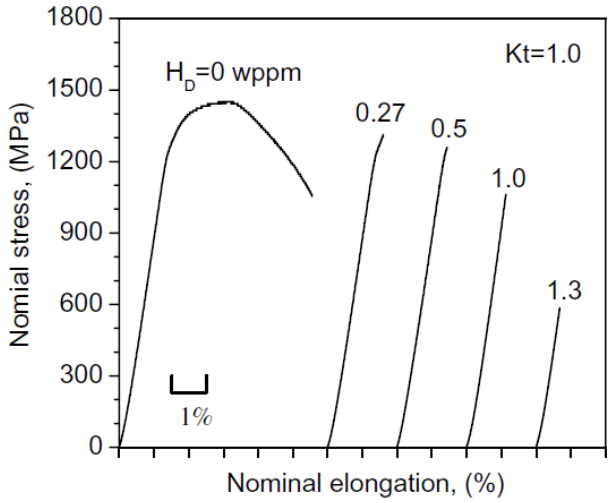

Figure 2.9. Stress-strain curves of smooth tensile specimens of a high strength 34CrMo4 with different diffusible hydrogen concentrations [134].

On the other hand, there is a strong consensus on the effects of hydrogen on notched tensile properties: when a stress concentrator is present, both ductility and strength related parameters are significantly reduced [36]. Wang et al. [138] demonstrated (Figure 2.10) how hydrogen embrittlement increases with the stress concentrator factor, K_t, under tensile loads (greater notch length or lower notch radius) tested with the same initial hydrogen concentration. They state that hydrostatic stress gradients developed in the notch region facilitates hydrogen accumulation in this area, increasing the local hydrogen content and reducing the stress needed to break the specimen. This idea also supports the experimental evidence that hydrogen embrittlement increases with the yield strength of the steel, as the magnitude of the hydrostatic stress developed in the notch tip region is proportional to this property. In addition, Figure 2.10 also shows that the deleterious effect of hydrogen is increased when lower test speeds (displacement rates) are applied. In this case, hydrogen atoms have more time to diffuse through the steel microstructure

and greater hydrogen concentrations may eventually be attained in the process zone. Several authors have studied the effect of the displacement rate on the tensile behaviour of steels in presence of internal hydrogen [139–141] and similar results were found.

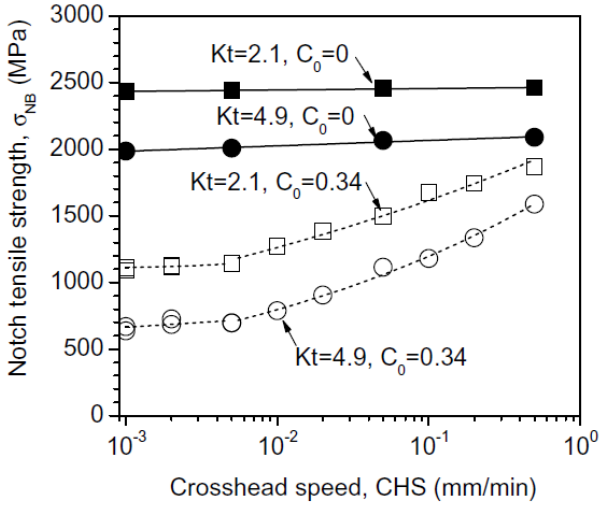

Figure 2.10. Influence of stress concentrator factor, K_t and test displacement rate in the ultimate strength of notched steel specimens(σ_{ys}=1320) [138].

2.5.1.1. Effects of hydrogen on the tensile properties of steel welds

Pipes and pressure vessels (made on CrMo steels) employed in the energy sector are generally used under severe service conditions, such as high temperature and high hydrogen partial pressures, e.g., hydro-processing, hydro-treating and hydro-cracking reactors. These components are built from hot rolled, curved, and welded plates. They generally have thick walls, of 150-350 mm, inner diameters from 3 to 5 m, and lengths of 10-30 m, and welds are the most critical elements [142]. In general, it is well known that the uneven microstructural characteristics of the HAZ and the grain coarsening and hardening usually induced by the weld thermal cycle, cause the coarse-grain heat affected zone, CGHAZ, present just beside the fusion line, to have the lowest mechanical properties [143]. This fact has pushed some researchers to study the effects of hydrogen in the tensile properties of coarse grain microstructures.

For instance, L.R.O. Costa et al. [144] compared, by means of tensile tests, the behaviour of base metal and welded joint of a normalized and tempered 2.25Cr1Mo steel. They found that hydrogenated samples obtained from the weld always behaved in a more brittle manner than those from the base metal, due to the availability in the former of more hydrogen trapping sites. The presence of internal hydrogen altered the character of the fracture, from partially brittle to fully brittle. Furthermore, under the most aggressive charging conditions, fracture always started in the region with the coarsest grains (CGHAZ), giving always rise to cleavage features. They also observed a growth of brittle area in specimens with wider HAZs (wider HAZ was produced by longer exposure to high temperatures during the thermal cycle of the welding process, enabling grain growth), establishing that the coarser the grains in the CGHAZ region, the more susceptible the weldments are to hydrogen embrittlement. On this same subject, Takasawa et al. [145] studied the influence of grain size, and also dislocation density, in the hydrogen embrittlement of several high-strength (Ni)CrMo steels with ultimate strengths between 900 and 1100 MPa. To that end,

they performed in-situ tensile tests in cylindrical smooth specimens under 45 MPa of pure hydrogen. Their findings are summarized in Figure 2.11. In general, it can be said that both grain refinement and reduction in dislocation density are effective ways of reducing the susceptibility to HE. In this kind of bainitic-martensitic steels, they justify that prior austenitic grain boundaries are locations with high dislocation density (due to slip constraint), and an increase in grain size will also increase the hydrogen content per unit boundary length.

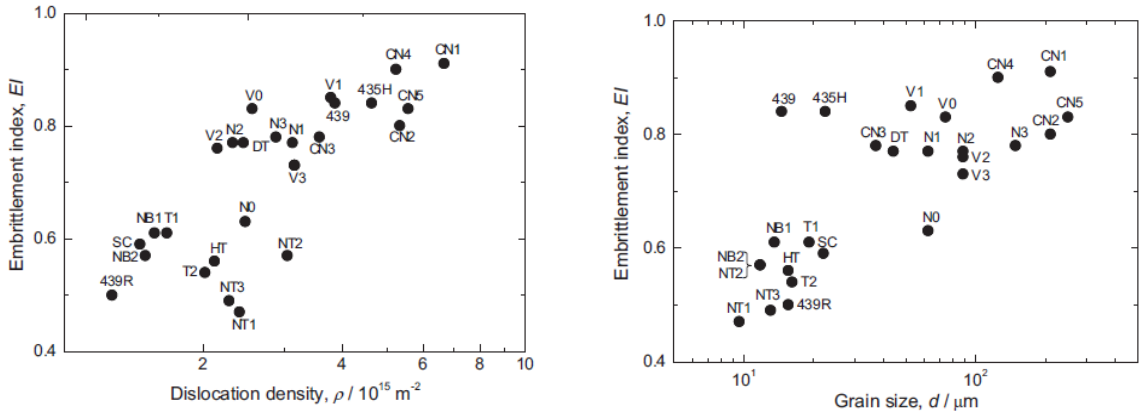

(a) *(b)*

Figure 2.11. Embrittlement index associated to reduction in area plotted against (a) dislocation density and (b) grain size [145].

There is also a relevant work from X. Li et al. [146] concerning hydrogen embrittlement of 304L austenitic steel welds that is worth to mention. They reported a great loss of ductility (both in elongation and in area reduction) in tensile specimens when the hydrogen content in the weld was increased by means of cathodic charging and this behaviour was accompanied by relevant changes in the fracture micromechanisms: typical ductile dimples in hydrogen-free samples evolving to quasi-cleavage, cleavage, a mixture of cleavage and intergranular, and only intergranular with increasing hydrogen contents. Furthermore, they also studied the effects induced by a plastic pre-deformation in the welded joint [26], reporting an exponential increase of hydrogen content (also introduced by cathodic charging), and thus on the steel HE as plastic deformation was increased, due to the multiplication of the dislocation density.

As it is usually difficult to obtain standard tensile specimens from the CGHAZ of a real weld, due to its small size, some researchers have performed laboratory heat treatments to reproduce the microstructure present in this area of the HAZ to overcome this obstacle. For example, T. Zhang et al. [147] demonstrated by means of slow strain rate tests in high-pressure hydrogen gas, all conducted on simulated HAZs specimens, the important HE produced on all the different sub-regions of a HAZ. The hydrogen embrittlement index associated to reduction in area even reached 5% in the CGHAZ and its whole fracture surface was brittle (quasi-cleavages), with secondary cracks.

2.5.2. Effects of hydrogen on the fracture toughness

Considering the detrimental effects of hydrogen on the tensile properties of medium and high-strength steels and their welds, the characterization of fracture toughness becomes crucial to

design components resistant against crack initiation and growth in presence of internal and external hydrogen.

Several authors have assessed the fracture toughness of steels under external hydrogen pressures [5,35,148–155], reporting a significant dependence of this property on the hydrogen pressure (internal hydrogen concentration), temperature, yield strength of steel and applied loading rate.

According to San Marchi and Sommerday [148], the fracture toughness of 2.25Cr1Mo steel in high pressure hydrogen gas is significantly lower than in an inert gas, increasing the sensitivity to HE as the yield strength of the steel and the external hydrogen pressure increase. Barthélémy [149] reported a 50% reduction in the fracture toughness of a plain carbon steel tested in gaseous hydrogen at only 6.9 MPa. For a higher hydrogen pressure (30 MPa), Briottet et al. [5] reported for a X80 high-strength pipeline steel (σ_{ys}≈600 MPa) a drastic decrease of almost 95% in the fracture toughness for the onset of crack initiation (J-R curve), dropping from 215 kJ/m^2 in air to only 15 kJ/m^2. Similarly, Ogawa et al. [152] performed fracture toughness tests on compact tensile (CT) specimens on a low carbon non-alloyed steel (σ_{ys}=360 MPa), in air and in hydrogen gas under pressures of 0.7 and 115 MPa, noticing a significant degradation in the fracture toughness, manifested in the load-displacement curves (Figure 2.12(a)) and also in the J-toughness-crack growth curves (Figure 2.12(b)).

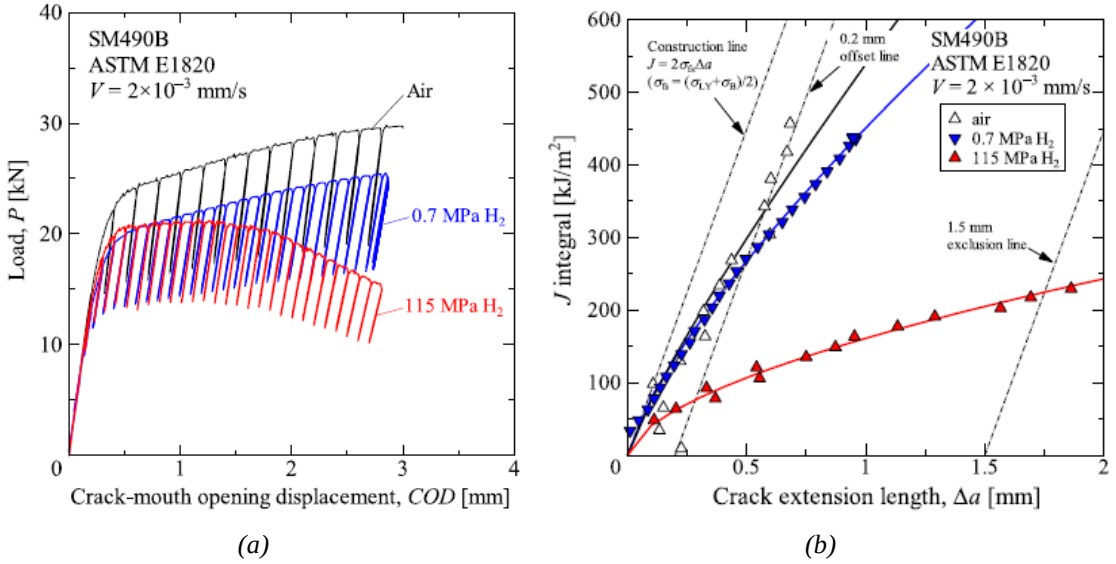

(a) *(b)*

Figure 2.12. Influence of hydrogen pressure in the fracture toughness of a carbon steel tested in 0.7 and 115 MPa hydrogen gas [152]. (a)Load-COD and (b) J- Δa curves.

Under the highest hydrogen pressure (i.e., higher hydrogen concentration in the steel), maximum embrittlement was shown (over 70%) and a fracture surface characterized by quasi-cleavage facets instead of dimples (ductile fracture) in air. Regarding 42CrMo4 steel, although results on fracture toughness are scarce, Iijima et al. [156] studied the influence of high pressure gaseous hydrogen (between 10 and 115 MPa) and displacement rate (between 0.12 and 0.0012 mm/min) in the fracture toughness of a grade with a yield strength of 700 MPa. They found that the measured values of the threshold for subcritical crack extension, K_{JIH}, decreased with either increasing gas pressure or decreasing displacement rate. In fact, they reported fracture toughness

reductions as high as 80% when the highest hydrogen pressure and the lowest displacement rate were employed.

On the other hand, Gangloff et al. [35] showed that CrMo steels with yield strengths below 750 MPa, with a lower bound fracture threshold under high hydrogen gas pressure of at least 50 MPa$\sqrt{m}$, could provide reliable performance in hydrogen services. Additionally, Nibur and Somerday [132] observed that the dependence of mechanical properties on hydrogen gas pressure is usually strongest at low pressure and becomes less sensitive at the highest pressures, establishing that often exists a pressure threshold above which mechanical properties are essentially invariant.

As already mentioned, some authors have performed fracture toughness characterization pre-charging the specimens with hydrogen first and then testing them in air. For example, Liu et al. [157] observed a continuous drop in the fracture toughness of a ferritic low-alloy steel (≈215HV) thermally precharged at 10 MPa of pure hydrogen, as the hydrogen content introduced in the steel increased (different hydrogen concentrations were achieved changing the reactor temperature between 150 and 300ºC). Being the fracture toughness drop maximum (32%) under the maximum hydrogen content. They also reported a clear change in the fracture micromechanism, from a ductile one, microvoid coalescence MVC, to a mixture fracture of dimples and cleavage facets. Similarly, Álvarez et al. [141] using ultra-low displacement rate (0.001 mm/min) tests on structural steels S355 (145 HB) and H8 (285 HB), reported embrittlement indexes associated to J_{IC} parameter as high as 67% and 91% respectively, accompanied by a similar modification of the fracture micromechanisms (from MVC in the absence of hydrogen to cleavage in the presence of internal hydrogen). Regarding the family of CrMo steels, according to Pillot and Coudreuse [7], the J crack growth initiation value, $J_{0.2BL}$, respectively decreased from 600 to 60 kJ/m^2 and from 400 to 250 kJ/m^2 in CrMo and CrMoV steels due to the presence of internal hydrogen. Again, they also noticed the impact of displacement rate in fracture toughness results, as the $J_{0.2BL}$ parameter decreased more than 80% when reducing the loading rate from 0.3 mm/min to 0.005 mm/min.

Using now electrochemical hydrogen charging, an early work published in 1975 by Townsend [158] already showed (in-situ low displacement rate tests on cantilever beam specimens cathodically charged in 3.5% wt. NaCl) that even small hydrogen concentrations (below 1 ppm) could considerably reduce the crack growth resistance of a 42CrMo4 steel. Wang [159] assessed the fracture toughness of a X70 pipeline steel (σ_{ys}=583 MPa) using slow rate tests (0.01 mm/min) in electrolytic pre-charged specimens and also in-situ cathodic charging. For the former, he only reported a critical K_{IQ} drop of 10% under very high hydrogen concentrations (7 ppm), being the only change in fracture mechanisms a reduction in the average diameter of dimples. However, under in-situ testing, the decrease of fracture toughness surpassed 40% under the same charging conditions, which also came with the observation of a distinct cleavage zone with facet features and secondary cracking at the onset of crack growth. Using also electrochemically hydrogen pre-charged specimens, Thomas et al. [160] showed, on an ultra-high-strength Aermet 100 steel (σ_{ys}=1765 MPa), a very strong decrease of the plain-strain fracture toughness from 143 MPa$\sqrt{m}$ in air to 15 MPa$\sqrt{m}$ with internal hydrogen, changing the fracture micromechanism from ductile to transgranular cleavage.

Finally, it is worth noting the work carried out by Colombo et al. [15] who, using electrochemically hydrogen pre-charged specimens on a quenched and tempered 25CrMo4 (σ_{ys}=715 MPa), reported a decrease in J_{IQ} for the onset of crack growth from 215 kJ/m^2 in air to 22 kJ/m^2 (90% drop) in the presence of internal hydrogen. The authors claimed that their results were comparable with those obtained by Loginow and Phelps [151] in a similar steel grade tested in gaseous hydrogen at very high pressure. In this line, Álvarez et al. [161] assessed the hydrogen embrittlement susceptibility of a CrMoV steel, comparing high temperature gaseous hydrogen pre-charging and electrochemical hydrogen pre-charging, obtaining embrittlement indexes of 20% and 84% respectively. These results indicate that more damage is generated when electrochemical charging methods are used, because more hydrogen is introduced into the samples (in general, very high cathodic density currents, far from real operation conditions, are used in order to facilitate embrittlement).

To sum up, literature on the influence of hydrogen on the fracture toughness of ferritic-martensitic steels is quite abundant. Nevertheless, complementary studies to attain a better comprehension of the effects that heat treatment, microstructure, strength level, hydrogen content, diffusion and density of trapping sites have on the fracture toughness of CrMo steels are still needed for the design of safe vessels, pipes, and other components for long services under high pressure hydrogen and to calibrate accurate and useful numerical models.

2.5.2.1. Hydrogen effects on the fracture toughness of steel welds

As it was already mentioned, the applied weld thermal cycle has a significant effect on the microstructure heterogeneity of the HAZ of welds [162–167] and, consequently, on their susceptibility to hydrogen embrittlement [147,168,169]. At this respect, the fracture toughness of base metals, BM, heat affected zones and weld metals, WM, in different steel welded joints in the presence of hydrogen were studied by several authors [7,109,144,170]. The coarse CGHAZ is usually the region of the weld with the lowest fracture toughness, as well as the most embrittled region due to the entrance of hydrogen [114,147]. It is usually characterized by brittle fracture modes (cleavage and even intergranular fracture), being therefore the weld location where crack initiation and subcritical propagation is most likely to occur.

Some works have illustrated the effect of hydrogen on the fracture toughness of CrMo (and other similar low alloy structural steels) steel welds [142,162,171,172]. For example, L. Duprez et al. [171] gave a brief overview on the HE susceptibility of high-strength low-alloy steels (HSLA) and their welds, reporting that when tested in gaseous hydrogen, the WM and HAZ regions show brittle fracture surfaces, both transgranular and intergranular, which they explained were due to their higher hardness and coarser microstructures. T. An et al. [162] performed elasto-plastic fracture toughness tests on CT specimens on BM and WM X80 steel (both with σ_{ys} around 550 MPa) under a hydrogen partial pressure of 0.6 MPa and a loading rate of 0.012 mm/min. The fracture toughness parameter J_{max} (calculated at the maximum load registered in the tests) decreased 8% in the BM and 40% in the WM, when tested in the hydrogen environment, being the size of microvoids reduced due to hydrogen. In this line, Pillot et al. [142,172] report a decrease in fracture toughness of 2.25Cr1Mo and 2.25Cr1MoV steel welds with increasing hydrogen contents: the higher the hydrogen content, the higher the ductile-to-brittle transition temperature. They claim that special attention should be paid to HAZ and weld metal, WM

regions, as they are prone to suffer the highest HE, even with low hydrogen contents around 1-2 ppm.

However, as already mentioned in the case of tensile tests but even more remarkable in fracture toughness tests, the HAZ is a very narrow zone that includes various microstructures, making the independent mechanical characterization of the CGHAZ very difficult. In order to obtain reliable fracture toughness results, the tip of the fatigue pre-crack should be located at the coarse-grain region of the HAZ specimen [173]. Even then, in the course of the fracture test, the crack usually grows towards adjacent softer microstructures, avoiding the harder CGHAZ. As a result, data scattering is very common in these tests, and therefore, there is a lack of consensus about the best way to characterize the fracture toughness of the HAZ. This, eventually gives rise to a great uncertainty regarding the integrity assessment of welded joints [166,169]. Nevertheless, as the fracture toughness evaluation of hydrogenated HAZs is a crucial factor for the service safety of welded industrial facilities working under hydrogen pressure, such as pressure pipes and vessels, some researchers have overcome these obstacles by means of simulating real HAZs using specific laboratory heat treatments [168–170].

For example, A. Alvaro et al. [170] quantified the HE susceptibility of a simulated HAZ of a X70 structural steel (σ_{ys}=775 MPa) by means of fracture toughness tests performed on SENT specimens inside a pressure vessel filled with hydrogen gas at different pressures. They reported embrittlement indexes associated to J_Q parameter of around 95% when tests were performed under hydrogen pressures greater than 0.6 MPa. Fracture surface observations confirmed these results, revealing a change in the fracture mode from ductile microvoid coalescence (tests in air) to brittle transgranular. They justify these results in another work [168] with the help of hydrogen permeation tests, finally getting to the point that during the cooling of the simulated weld, martensitic transformation takes place, and residual stresses and dislocation density increase; hence the number of trap sites for hydrogen increase as well. As a result, hydrogen mobility in the microstructure slows down, and hydrogen concentration capability becomes higher, increasing the risk of HE.

Based on this information, it is clear that welding processes induce local microstructural modifications, being the effect of hydrogen in the fracture toughness of the base metal different from that in the HAZ. The CGHAZ often shows the lowest fracture toughness, especially when measured under internal hydrogen. Extensive analysis of the hydrogen effects on these coarse grain microstructures is therefore essential for ensuring the safety and long-term reliability of hydrogen containing pipes and vessels made from CrMo steels. Currently, more studies are needed to understand the operative fracture micromechanisms in the presence of hydrogen in complex microstructures such as those found in the CGHAZ. Furthermore, fracture mechanics-based data (K_{IC}, J_{IC}, and $CTOD_{Ic}$) available for 42CrMo4 steel in the presence of hydrogen with controlled hydrogen contents is rather scarce, but they should be very appreciated for feeding complex numerical models able to predict whether a crack will start propagation under certain hydrogen conditions.

2.5.2.2. Importance of post-welding heat treatments in hydrogen embrittlement

As previously seen, the HAZ, and specially the CGHAZ, is considered the weakest region in pipelines and vessels manufactured with quenched and tempered steels working under hydrogen pressure. These steel welded components require post-weld heat treatments, PWHT, in order to relax and redistribute residual stresses, temper the HAZ microstructure and to satisfy both the strength and hardness requirements. Additionally, PWHT normally leads to a decrease in hydrogen solubility in martensitic steels mainly due to lowering dislocation density and residual stresses, giving rise to a reduction of hydrogen embrittlement [174].

In order to minimize hydrogen embrittlement of welded joints, CrMo and CrMoV steels may be post-weld tempered at high temperatures, where their strength and hardness significantly decline as was shown, among other works, in [175–177]. Typically, the application of tempering temperatures within the range of 650-720ºC for 2-10 hours provides the best mechanical behaviour under internal hydrogen. Tvrdy et al. [8] after demonstrating that even low-strength CrMo and CrMoV pressure vessel steels are susceptible to subcritical crack growth under stress intensity factor levels far below the critical fracture toughness value of the corresponding steel, K_{IC}, they further demonstrated that resistance to hydrogen embrittlement of their welds (hardened microstructures) considerably increases after tempering at the maximum possible temperature. In fact, Mitchell et al. [175] studied the optimisation of the PWHT in a 1.25Cr-0.5Mo pressure vessel steel to be used in a high temperature hydrogen service and suggested that tempering in the range of 670º-710ºC for 8 hours could represent the optimal solution for resistance to hydrogen embrittlement. Similarly, Dai and Lippold, proposed a PWHT of 660ºC/10h as the optimal one for reducing hydrogen-assisted cracking of the CGHAZ in 2.25Cr1Mo steels.

2.5.2.3. Influence of hydrogen on the threshold stress intensity factor determined through constant load tests

Although less common, an additional mechanical test used to assess the effects of hydrogen on the fracture toughness of steels is the constant load test, better described as constant stress intensity factor test. Typically, WOL (wedge-opening-load), CT (compact tension) or DCB (double cantilever beam) specimens, pre-charged with hydrogen or tested in a hydrogenated medium, are used. The main goal of this methodology is to evaluate if a pre-existing crack will grow due exclusively to hydrogen diffusing towards the stressed process region when a constant load is applied and maintained. Consequently, this test allows to determine the threshold stress intensity factor, K_{th}, below which cracks are not able to propagate under internal or external hydrogen.

As in the case of fracture toughness, this parameter is also dependent on the yield strength of the steel and on the hydrogen content absorbed by the steel (i.e., hydrogen pressure) [178–180]. The results reported by Moody et al. [181] on the influence of hydrogen pressure on the stress intensity factor threshold, K_{th}, measured on a 34CrMo4 steel tempered to attain different strength levels is clearly seen in Figure 2.13.

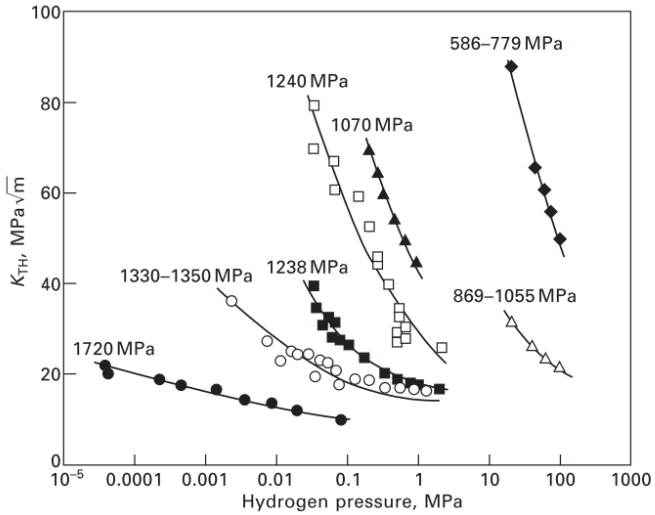

Figure 2.13. Threshold stress intensity factor, K_{th}, plotted as a function of hydrogen pressure for 34CrMo4 steel tempered to attain different strength levels [181].

Loginow and Phelps [151], also correlated the stress intensity factor for crack arrest, K_{IHa}, with the yield strength and hydrogen pressure for different intermediate-strength structural steels. On the other hand, Wang et al. [155] have developed a simple quantitative model to predict the effects of hydrogen gas on the fracture toughness of steels, based on Oriani's assumption that crack will initiate propagation at the elastic-plastic boundary ahead of the crack tip when hydrogen concentration reaches a certain critical value (critical cohesive stress) after long-term hydrogen diffusion assisted by the local hydrostatic stress [122].

However, variability in the results is sometimes reported, depending on the kind of tests performed and, on the hydrogen charging conditions. For example, T. Matsumoto et al. [178], who determined the threshold stress intensity factor for hydrogen-assisted cracking, K_{IH}, in a quenched and tempered 34CrMo4 steel with a yield strength of 772 MPa, obtained very different results when performing constant displacement tests (WOL specimens) and rising load tests (CT specimens) in high-pressure hydrogen gas at 115 MPa. The reported values corresponding to these crack initiation thresholds were respectively 65 MPa$\sqrt{m}$ and 33MPa$\sqrt{m}$.

Regarding this same issue, Somerday and Nibur [180], measuring the threshold stress-intensity factor at crack arrest, K_{THa}, in different CrMo steels exposed to 100 MPa hydrogen gas, highlighted the importance of checking the specimen's dimensional requirement for small-scale yielding and plane strain. In fact, although only those specimens of higher strength steels (σ_{ys}>900 MPa) fulfilled the plain-strain condition, they asserted that the lack of shear lips on fracture surfaces, along with finite element analysis confirmed that linear-elastic fracture mechanics could be confidently applied and the stress-intensity factor, K, could be used. They showed that K_{THa} decreases as the steel yield strength increases (although this trend becomes less pronounced for σ_{ys}>900 MPa), and also detected the activation of PRHIC micromechanism in all the steels, with increasing amounts of IG and secondary cracking in the higher-strength grades (σ_{ys} >900 MPa).

Regarding gaseous pre-charged specimens, S. Konosu et al. [182] evaluated the effects of hydrogen in the crack growth rate, da/dt, under constant load on three normalized and tempered

CrMo steels (yield strength between 460 and 500 MPa). They used CT specimens (B_n=20 mm) hydrogen pre-charged in an autoclave at 450ºC and 15 MPa for 48 h (under these conditions they measured a hydrogen concentration of 3.2 ppm). These CT specimens were submitted then to constant load tests in air for 8-10 h, leading to values of the threshold stress intensity factor K_{IH} at the onset of hydrogen assisted crack growth between 40 and 60 MPa$\sqrt{m}$. In addition, in another paper [183] the same authors followed the same testing procedure but employing now thinner CT specimens, with B_n=10 mm, demonstrating that the results (K_{IH}) were similar to those obtained with thicker samples (B_n=20 mm).

When determining K_{th}, test duration is often a subject of discussion. In this regard, Wei and Novak [184] reported the results of an interlaboratory test program, conducted by an ASTM Join Task Group that included eight laboratories. Using pre-cracked DCB specimens of heat treated 34CrMo4 steel (σ_{ys}=1240 MPa), these laboratories performed in-situ (specimens cathodically charged in 3%NaCl) constant load tests for different time intervals, being the results quite similar in all the cases (around 30-35 MPa$\sqrt{m}$).

Due to their interesting analysis of fracture surfaces produced in this case using incremental load tests on cathodically charged specimens, it is worth noting the work developed by Das et al. [185] on three different grades of tempered martensitic steels, 35CrMo4, 41Cr4 and 36NiCrMo4 (with hardnesses around 43-44 HRC). The susceptibility to HE of 36NiCrMo4 were the lowest, followed by 41Cr4 and 35CrMo4, and differences in the respective failure modes micromechanisms were detected. Those specimens tested in air always displayed a ductile failure mode, characterized by ductile-dimple morphology. However, as the cathodic potential for hydrogen charging was increased, brittle mechanisms associated to hydrogen embrittlement were detected. From less to more severity, they appreciated the following features:

I. Sheared coalescence of microvoids (slightly different from the typical ductile dimple morphology).
II. Transgranular mode of fracture, mostly along martensite lath interfaces accompanied by apparent limited ductility.
III. Mixed morphology of intergranular and transgranular fracture with ‘quasi cleavage’ features (flat facets of grains mixed with cleavage areas).
IV. Generalized brittle intergranular (IG). Three additional levels were distinguished within IG fracture:
    a. Intergranular with pockets of ductile features
    b. Very fine sheared-fibrous pattern on the flat facets of grain surfaces
    c. Completely clean grain facets

Results on constant load testing of CGHAZ microstructures in presence of internal hydrogen are scarce. Q. Wang et al. [114] studied the effect of quenching temperature (1200, 1000 and 900ºC for 20 min) in a CrMoV martensitic steel (oil quenched and tempered at 700ºC for 1h) using sulphide-stress cracking DCB (SSC) tests and related their results with hydrogen-microstructure interaction provided through hydrogen permeation tests. They showed that crack growth rate decreased, and the stress intensity factor threshold increased when decreasing the quenching temperature, due to the decrease of the dislocation density, the PAGS, and the martensitic lath and packet sizes. They also observed that the average diameter of precipitates distributed at the

aforementioned internal boundaries increased (around 35%), while their volume fraction remained practically constant. In general terms, hydrogen diffusivity increased, and hydrogen contents decreased when reducing the quenching temperature. These same authors [186], also reported (using the same steel and methodology), an increase in the stress intensity factor threshold when increasing the tempering temperature (from 650 to 700 and 720ºC), as hydrogen concentration in the microstructure was seen to decrease. Increasing the tempering temperature was correlated with a decrease in the dislocation density and an increase in the fraction of high-angle grain boundaries, giving rise to lower SSC propagation rates.

Just to end the review on this topic, it is important to quantitatively establish the effects of metallurgical and environmental variables on the environment-assisted cracking resistance of steels. In service assessment and quality control, these data should be used to establish the suitability of a particular steel for a given application under a specific stress, flaw size, and environment and, therefore, to establish a certain criterion for component inspection. In addition, as can be observed in this brief bibliographic review, most of the available K_{th} data are focused on high-strength steels (σ_{ys}>900 MPa), while reliable information relative to medium-strength steels, between 500 and 800 MPa, is still rather limited.

2.5.3. Effects of hydrogen on the fatigue crack growth rate of steels

As happened with the previous mechanical properties, when hydrogen is present in medium and high-strength steels the fatigue crack growth rate, FCGR, modifies due to: (I) test variables, such as the external hydrogen pressure, the stress intensity factor range, ΔK, the load ratio, R, and the frequency, f; (II) the steel microstructure, that will determine hydrogen diffusivity and hydrogen concentration dissolved in the steel lattice; and (III) the yield strength that will dictate the magnitude of the developed local stresses in the crack front region and therefore hydrogen accumulation.

Many authors [187–191] have observed so far that the fatigue crack growth rate of ferritic-martensitic steels increases at least one order of magnitude when specimens are loaded in gaseous hydrogen at ΔK>10 MPa$\sqrt{m}$ under low test frequencies (0.1 and 1 Hz), in comparison with tests performed at room temperature in air. In general, fatigue crack growth rate is accelerated when the external hydrogen pressure is increased [192], although some authors have shown that the effect of hydrogen pressure becomes negligible for pressures higher than a determined value [188], just as happened with the fracture toughness. For example, the results obtained by Slifka et al. [193] on a pipeline X100 steel (σ_{ys}=705 MPa) are presented in Figure 2.14, where a clear increase in da/dN is observed when increasing the hydrogen pressure from 1.7 to 7 and to 21 MPa. These results are in line with those reported in [148].

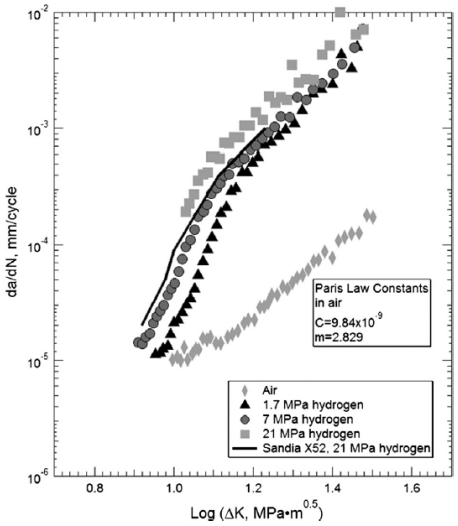

Figure 2.14. Fatigue crack growth rate (da/dN) vs. stress intensity factor range (ΔK) for X100 pipeline steel tested at R=0.5 and 1 Hz under different hydrogen pressures[193].

Hua et al. [191] measured the fatigue crack growth rate of quenched and tempered 25CrMo4 steel (σ_{ys}=750 MPa) under higher hydrogen pressures, 45, 70 and 92 MPa, at R=0.1 and f=1 Hz. CT specimens of 12.5 mm thickness were extracted from different locations of a vessel's wall (crack growth in longitudinal direction). They reported an increase of the fatigue crack growth rate with the applied hydrogen pressure. The fatigue crack growth rate under 92 MPa was approximately 30-50 times greater than in air, being this difference maximal at lower values of ΔK. They also highlight the importance of the testing frequency in fatigue crack growth rate. In this respect, Nibur et al. [194] studied the influence of load ratio and frequency in the FCGRs of the same 25CrMo4 quenched and tempered steel (now with a σ_{ys}=607 MPa) in 45 MPa hydrogen gas. They demonstrated that lower frequencies and higher R gave rise to higher FCGRs for a given value of ΔK. However, they supported the independence of these two variables, as changing the frequency from 0.1 Hz to 1 Hz reduced the crack growth rate at R=0.5 but had no effect at R=0.1. On the other hand, Cialone and Holbrook [195] showed in CT specimens of X42 pipeline steel ($\sigma_{ys}\approx$350 MPa), tested under a hydrogen pressure of 6.9 MPa and a frequency of 1 Hz, that hydrogen clearly accelerates the fatigue crack growth rate of the entire reported ΔK range at R=0.1. However, at R=0.8, fatigue crack growth rates in hydrogen and nitrogen gas were similar for low-medium values of ΔK, and they only increased in hydrogen at higher ΔK levels. In this line, other authors have reported hydrogen to induce a complex relationship among R ratio, frequency, and crack growth rate at intermediate ΔK levels [196].

As an example of applying extremely high external hydrogen pressures, Yamabe et al. [197] compared the fatigue crack growth rate of a quenched and tempered CrMo steel (σ_{uts}=861 MPa) in air and in 115 MPa gaseous hydrogen. These authors show that hydrogen pressure does not affect the fatigue crack growth rate at ΔK<10 MPa$\sqrt{m}$ (similar to the findings in [198]), although an important acceleration of crack growth rate was seen at higher ΔK values.

Regarding now the 42CrMo4 steel, J.H. Chuang et al. [199] studied the influence of hydrogen in the fatigue crack growth rate of this steel quenched and tempered at 230, 300, 370, 450 and 550ºC. CT specimens were tested in this work (between 10 and 30 MPa$\sqrt{m}$.) both in air and in gaseous

hydrogen under a loading frequency of 20 Hz, a stress ratio R=0.1 and a hydrogen pressure of 0.02 MPa. Their results showed a pronounced acceleration of crack growth rate in those steel grades tempered between 230 and 370ºC (σ_{ys} between 1533 and 1470 MPa), while the influence of hydrogen became negligible for those tempered at higher temperatures (450 and 550ºC). They also related this susceptibility to hydrogen embrittlement with changes in fracture modes: they observed IG fracture for lower tempering temperatures, while transgranular fracture and some quasi-cleavage facets were observed for higher tempering temperatures. However, when compared with the results obtained by other authors, the lack of hydrogen embrittlement in the lower-strength grades may be due to the use of a very high frequency and very low hydrogen pressure, insufficient to produce hydrogen induced cracking. Likewise, Tau et al. [200] studied the hydrogen-assisted fatigue crack propagation in a set of bainitic-martensitic microstructures of 25CrMo4 steel, reporting a great acceleration of the FCGR in all the martensitic grades, being greater as the steel yield strength increased. It is interesting to note that at ΔK values higher than 20-25 MPa$\sqrt{m}$ some of the less susceptible, tougher steel grades exhibited a plateau zone where crack growth rate (da/dN) seems to be stable. This behaviour, characteristic of an environmental assisted cracking mechanism, was also observed by other authors [201].

Thermal pre-charging was respectively employed by Macadre et al. [187] and Cheng and Chen [202]. In both works a hydrogen pressure of 100 MPa at 85ºC for 200 h was applied to pre-charge 0.33 ppm of hydrogen in a quenched and tempered NiCrMo steel (σ_{ys}=754 MPa) and 2 ppm in a quenched and tempered SAE 52100 steel (σ_{ys}=1794 MPa), respectively. The effects of internal hydrogen on the fatigue crack growth rate observed by these authors using hydrogen pre-charged specimens were similar to those already exposed related to external hydrogen: fatigue crack growth rate increases considerably due to the presence of hydrogen (strongly depending on the applied frequency) under intermediate ΔK values between 20 and 40 MPa$\sqrt{m}$.

Regarding now electrochemically hydrogen pre-charged specimens, Colombo et al. [15] performed fatigue crack growth rate tests on 12.5 mm CT specimens of 25CrMo4 steel (with diffusible hydrogen contents between 1.9 and 2.7 ppm). Figure 2.15 shows the fatigue crack growth enhancement resulting from the presence of internal hydrogen, as well as the influence of the testing frequency. Again, a plateau region, where the fatigue crack growth rate remains practically constant was noticed, in this case for ΔK>20 MPa$\sqrt{m}$. They found that the fracture mechanism of fatigue specimens tested with internal hydrogen was brittle and typical fatigue striations were not detected in the failed surfaces. In addition, in the most advanced stage of propagation, fracture became partially intergranular with many secondary cracks.

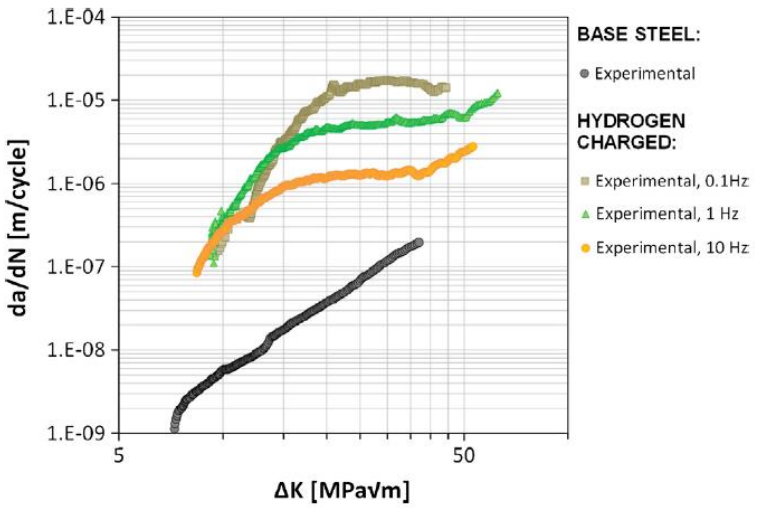

Figure 2.15. Influence of testing frequency in the fatigue crack growth rate of electrochemically hydrogen pre-charged samples of 25CrMo4 steel [15].

Finally, Vargas-Arista et al. [203] studied the fatigue crack propagation in the HAZ of 42CrMo4 weldings, reporting that even in absence of internal hydrogen, an increase in the prior austenite grain size, PAGS, induced a decrease of the HAZ fatigue resistance. This behaviour was attributed to reduced interactions between the advancing crack and grain boundaries, as a result of the larger grain size and larger microstructural units present in the HAZ. There is a general agreement [148][204] on the fact that hydrogen tends to deteriorate even more the aforementioned susceptibility to hydrogen embrittlement of the HAZ, accelerating the fatigue crack growth rate specially in the CGHAZ, and fostering brittle micromechanisms. For example, Tsay et al. [205] compared the FCGR behaviour in air and in gaseous hydrogen of BM and CGHAZ of a 2.25Cr1Mo steel weld, both in the as-welded condition and after the application of a PWHT (tempering at 700ºC for 1h). The HAZ experience the greater acceleration of FCGR due to hydrogen (quasi-cleavage facets and intergranular fracture were observed), which was somehow reduced after the application of the PWHT. Nagarajan et al. [206] also evaluated the relationship between dissolved hydrogen and grain size, and their impact on the fatigue crack growth behaviour of a 42CrMo4 steel. They found different fatigue behaviours depending on the applied stress intensity factor range but, in general, it can be said that a finer grain size produces additional crack growth resistance since the crack tip encounters a larger number of grain boundaries, reducing the crack propagation rate because crack grows along a more tortuous path.

After this brief review on the hydrogen effects on fatigue behaviour, one can realize that there are still some matters that need to be more deeply studied. Apart from the fact that fatigue crack growth rates in medium strength CrMo steels are not usually referred to the hydrogen content present in the steel nor to hydrogen trapping phenomena, the assessment of other relevant aspects, such as the combined effect of stress ratio and frequency, the influence of grain size and post-welding heat treatments, the analysis of the fracture micromechanisms, etc., would contribute to a better understanding of the interaction between hydrogen, cyclic loads, and steel microstructure.

Chapter 3

Experimental procedure

Study on hydrogen diffusion and embrittlement of quenched and tempered 42CrMo4 steel

PhD Thesis

3. Experimental procedure

3.1. Introduction

The present chapter describes all the techniques and procedures applied during the experimental part of this thesis, which can be divided in four different parts:

Part 1: the as-received 42CrMo4 steel was submitted to different quench and tempering heat treatments. Microstructural characterization was performed on the obtained steel grades. Next, the CGHAZ of a real 42CrMo4 weld was replicated by means of a laboratory heat treatment and different post welding heat treatments were applied. Finally, some of the aforementioned steel grades were cold rolled in order to produce different degrees of plastic deformation.

Part 2: electrochemical hydrogen permeation tests were performed in order to evaluate hydrogen diffusion and trapping in all the studied steel grades, including those plastically deformed.

Part 3: cylindrical pins of all the studied steel grades were thermally pre-charged in a reactor filled with high pressure hydrogen gas. Hydrogen measurements were performed in a Leco DH603 hydrogen analyser, which allowed the determination of the hydrogen desorption curves and the estimation of trap binding energies.

Part 4: the effects of internal hydrogen on the mechanical properties of all the studied steel grades were evaluated by means of tensile tests, fracture toughness tests, constant load tests (pre-cracked CT specimens) and fatigue crack growth tests, using hydrogen gas pre-charged specimens in all the cases.

3.2. Steel and heat treatments

A commercial 42CrMo4 steel (AISI 4140) was used in this work. Its chemical composition in weight % is shown in Table 3.1. The steel was supplied as normalized hot rolled plates with the following dimensions, 1000×1000×12 mm^3. Its hardness and tensile properties are shown in Table 3.2.

Steel	%C	%Cr	%Mo	%Mn	%Si	%Cu	%V	%P	%S	%N
42CrMo4	0.42	0.98	0.22	0.62	0.18	0.02	0.01	0.008	0.002	0.005

Table 3.1. Chemical composition of 42CrMo4 steel (weight %).

Steel grade	Heat treatment	HB	σ_{ys} [MPa]	σ_{uts} [MPa]	e [%]	Z [%]
42CrMo4_AR	Normalizing	185	550	667	20.9	58.2

Table 3.2. Hardness and tensile properties of 42CrMo4 steel in the as-received condition (normalized).

This is a medium-carbon, CrMo alloyed steel, frequently used in quenched and tempered (Q+T) condition, when an optimal combination of strength and fracture toughness is required

[8,142,172,175]. In fact, after the adequate Q+T heat treatment, this steel could constitute a prospective candidate for the manufacturing of pipes and vessels devoted to the distribution and storage of high-pressure gaseous hydrogen. Therefore, the influence of the tempering temperature (i.e., the strength level) on hydrogen diffusion and embrittlement was studied.

250×250×12 mm^3 steel plates were austenitized at 845ºC for 40 min, quenched in water, and tempered at 700, 650, 600, 550 and 500ºC for 2 hours, respectively, obtaining the 5 steel grades indicated in Table 3.3. The laboratory furnaces used in this task are shown in Figure 3.1.

(a) *(b)*

Figure 3.1. (a) Furnaces used to perform heat treatments and (b) austenitized 42CrMo4 steel plates.

Steel grade	Heat treatment
42CrMo4-700	845ºC/40min + water quenching + 700ºC/2h tempering
42CrMo4-650	845ºC/40min + water quenching + 650ºC/2h tempering
42CrMo4-600	845ºC/40min + water quenching + 600ºC/2h tempering
42CrMo4-550	845ºC/40min + water quenching + 550ºC/2h tempering
42CrMo4-500	845ºC/40min + water quenching + 500ºC/2h tempering

Table 3.3. Steel grades studied in this work and their correspondent heat treatments.

3.2.1. Microstructural characterization

The microstructures of all the steel grades obtained after the application of the different Q+T heat treatments, were examined using both optical microscopy, OM, and scanning electron microscopy, SEM, applying an acceleration voltage of 20 kV. The used microscopes are shown in Figure 3.2.

The samples were previously ground with SiC paper until 1200 grit, then polished on synthetic cloths with 6 and 1 µm diamond pastes and finally etched with Nital-2%. Vilella's reagent etching was used with the as-quenched microstructure to determine the average prior austenite grain size, PAGS. Vickers hardness measurements, HV30, applying a load of 30 kg for 15 s, were performed on all the steel grades. Between five and ten measurements were made on each grade to provide an average hardness value and the corresponding standard deviation.

(a) *(b)*

Figure 3.2. (a) Nikon optical microscope and (b) JEOL-JSM5600 scanning electron microscope.

Additionally, the full width at half maximum (FWHM) parameter was measured by means of X-ray diffraction in all the samples as an indirect estimation of the dislocation density [207,208], which is a key microstructural parameter related to hydrogen diffusion and trapping. In fact, the FWHM parameter measured on a certain diffraction peak is often used to assess material hardening during heat treatments [209]. Its value was experimentally determined using an X STRESSTECH 3000-G3R diffractometer equipped with a Cr-tube (with a wavelength, $\lambda = 0.229$ nm) on the crystallographic (211) plane of ferrite/martensite, which corresponds to a diffraction angle, 2θ, of 156.4º. The FWHM parameter is dependent not only on the dislocation density, but is also influenced by structural distortion, thus constituting a suitable parameter indirectly related to hydrogen diffusion and trapping.

3.2.2. Replication of the coarse grain heat affected zone of a 42CrMo4 weld

Pipes and pressure vessels are built from hot rolled, curved, and welded plates of great dimensions. Even in the absence of internal hydrogen, the uneven microstructural characteristics of the heat affected zone, HAZ, and specially the grain coarsening and hardening distinctive of the coarse-grain heat affected zone, CGHAZ, could notably reduce the local mechanical properties of the steel.

Based on such considerations, the effects of internal hydrogen on the mechanical properties of the CGHAZ of a 42CrMo4 weld were also studied in this thesis. With this aim, a heat treatment able to reproduce the microstructure developed in this particular region of the weld, allowing the manufacture of standardized specimens, was developed.

In first place, semiautomatic welding with a preheating temperature, T_p, of 200ºC was employed to deposit a weld bead using a carbon steel wire, onto a 12 mm thick 42CrMo4-700 steel plate (this was considered the base steel). The welding parameters are specified in Table 3.4, V being the voltage, I the current, v the welding speed and H the heat input applied in the welding process, calculated according to Equation (3.1).

Steel grade	Coupon size [mm]	Welding Process	T_p [ºC]	V [V]	I [A]	v [mm/min]	H [kJ/mm]
42CrMo4-700	250x125x12	Semiautomatic, GMAW (1)	200	30	200	165	1.96

Table 3.4. Parameters used to deposit a weld bead onto a 42CrMo4-700 steel plate (1)Gas Metal Arc Welding.

$$H = \frac{V \cdot I}{v} \qquad \textit{Equation (3.1)}$$

Next, the weld was microstructurally characterized. After carefully cutting the welded coupon to avoid microstructural alterations, the specimen was ground and polished on synthetic cloths and 6 and 1 µm diamond pastes and etched with Nital 2%. Additionally, Vickers microhardness measurements, HV1, were carried out in the CGHAZ, very close to the fusion line (first 200 µm), applying a load of 1000 g for 15 s. At least ten measurements were made, and the average hardness value was calculated. Finally, the microstructure of the CGHAZ was observed using OM and SEM.

Due to the relative high hardness measured in the CGHAZ region (as it will be shown in the results chapter) and in order to promote microstructural homogeneity and stress relaxation, a post welding heat treatment, PWHT, consisting in tempering at 700ºC for 2 h, was applied (being the same tempering previously applied to the base steel). Next, microstructural characterization and microhardness measurements, HV1, were performed on the tempered CGHAZ.

After a complete characterization of the CGHAZ (before and after the PWHT), it was necessary to design a heat treatment that allows the replication of the CGHAZ on a large metal volume. With this aim, the following aspects were considered.

The approximate cooling rate, ν_c, of the heat affected zone, at a temperature, T, equal to 700ºC, produced on the deposition of a weld bead under a preheat temperature, T_p, of 200ºC, was estimated according to Equation (3.2) developed by Rosenthal [210]. The thermal conductivity, λ, of the 42CrMo4 steel was taken as 31 W/mK [211].

$$v_c = 2\pi\lambda \frac{\left(T - T_p\right)^2}{H} \qquad \textit{Equation (3.2)}$$

A cooling rate at 700ºC of 25 K/s was thus obtained. It was then seen that this ν_c value could alternatively be obtained at the mid-thickness of a large 12 mm thick steel plate quenched in oil [212].

In addition, it is necessary to apply a very high austenitization temperature to reproduce the coarse austenitic grain size present in the CGHAZ. However, the time at high temperature must be limited in order to avoid oxidation and decarburization phenomena. Consequently, an austenitization at 1200ºC for 20 minutes followed by oil quenching was applied to 250×150×12 mm^3 steel plates. The obtained replicated CGHAZ, was characterized by means of HV30 hardness measurements and microstructural analysis.

As indicated in Table 3.5, two different PWHTs were applied to the replicated CGHAZ in order to improve its mechanical properties. At first, as it had been made with the CGHAZ of the real weld, a tempering treatment at 700ºC for 2 h was carried out, obtaining the coarse grain variation of the base steel grade (42CrMo4-700), that will be referred hereafter as 42CrMo-700-CG. Then an additional PWHT was also applied consisting in tempering at 725ºC for 4 h, steel grade designated as 42CrMo-725-CG. Microstructural characterization and HV30 hardness measurements were subsequently performed on both steel grades.

Steel grade	Heat treatment
42CrMo4-700-CG	1200ºC/20min + oil quenching + 700ºC/2h tempering
42CrMo4-725-CG	1200ºC/20min + oil quenching + 725ºC/4h tempering

Table 3.5. Coarse grain steel grades studied in this work and their correspondent heat treatments.

3.2.3. Cold rolling of steel plates

Different degrees of plastic deformation were applied at room temperature in the laboratory rolling mill shown in Figure 3.3.

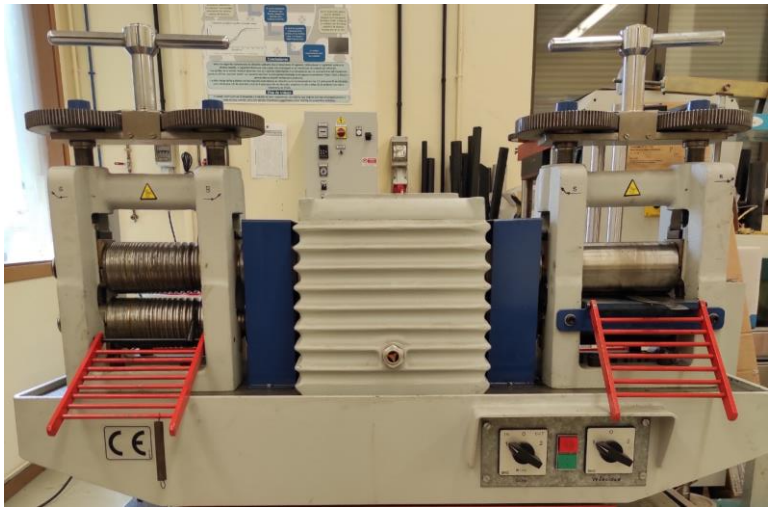

Figure 3.3. Rolling mill used to obtain plastically deformed steel plates.

This allowed to correlate the applied plastic strain, and thus the dislocation density variation, with changes in hydrogen diffusivity and trap density.

Thin sheets of 42CrMo4-700 and 42CrMo4-700-CG were cold rolled to obtain different thickness reductions, R, of 10, 20, 30, 50 and 67%. The equivalent plastic strain, ε_{peq}, can be easily obtained from R, through Equation (3.3), being t_0 and t_f the initial and final thickness, respectively.

$$\varepsilon_{peq} = Ln\left(\frac{t_f}{t_0}\right) = Ln(1 - R) \qquad \textit{Equation (3.3)}$$

Notice that, as the rolling process implies a thickness reduction, negative values are obtained. Then, the absolute value was considered.

3.3. Electrochemical hydrogen permeation tests

The hydrogen diffusion and trapping behaviour of the different 42CrMo4 steel grades was characterized by means of electrochemical permeation tests. Flat specimens measuring 20×20 mm^2 (a circular area of 1.25 cm^2 was tested), with a thickness of between 0.65 and 1 mm, depending on the steel grade, were used in this study. The harder steel grades, for example those plastically deformed, were thinner to reduce test duration. As the surface condition of the specimen is very important to obtain reliable results in these tests [213–215], both sides were ground with SiC paper until 1200 grit, then polished using 6 and 1 μm diamond pastes and cleaned with acetone prior to testing.

The permeation tests were performed in a double electrolytic cell based on the one developed by Devanathan and Stachurski [93], as is shown schematically in Figure 3.4(a). With an approximate volume of 250-300 ml, both cells satisfy the ASTM G148 [94] recommendation of a solution volume-to-surface area ratio greater than 20 ml/cm^2.

Both cells are separated by the steel specimen, which represents the working electrode, WE, in each cell. The cathodic cell, where hydrogen generation takes places (applying a cathodic current, hydrogen is cathodically generated and hydrogen atoms are adsorbed on the surface of the metal), was filled with an acid solution (pH≈1) composed of 1M H_2SO_4 and 0.25 g/l As_2O_3 to mitigate hydrogen recombination reactions [76,106,216,217]. The anodic cell, on the other side of the specimen and where hydrogen oxidation occurs, was filled with a basic solution (pH≈12.5) of 0.1M NaOH. The hydrogen reduction and oxidation reactions that take place in each cell are shown in Figure 3.4(b). Thin platinum plates with a total surface area of 1 cm^2 (similar to the specimen's permeated area) were used as counter electrodes, CE. A reference silver/silver chloride electrode (Ag/AgCl, RE) with a Luggin capillary was employed in the anodic cell and the equipment used for data acquisition was a pocketSTAT Ivium potentiostat with a current operation range of ±10 mA. All these tests were performed at room temperature.

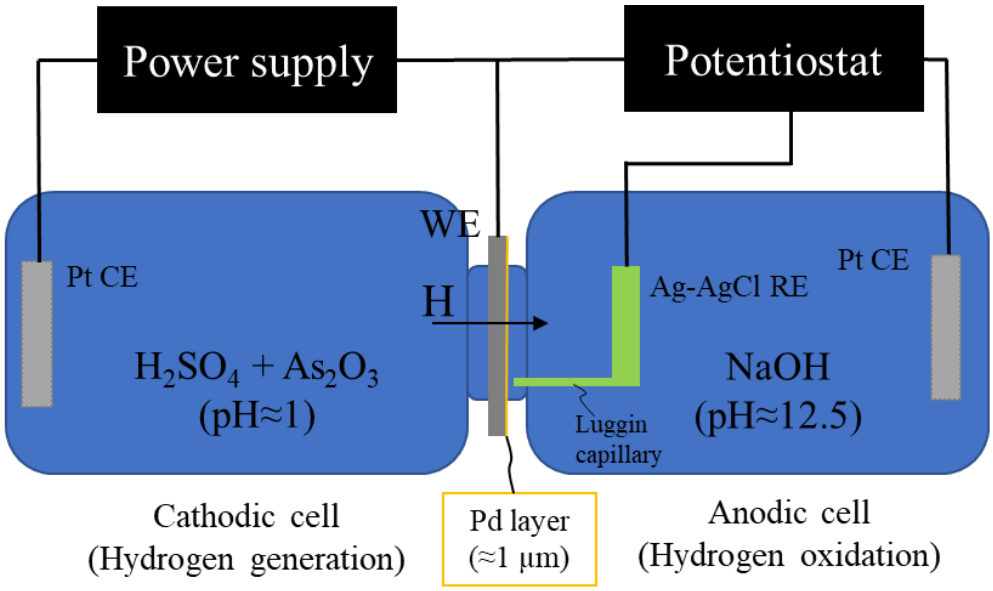

(a)

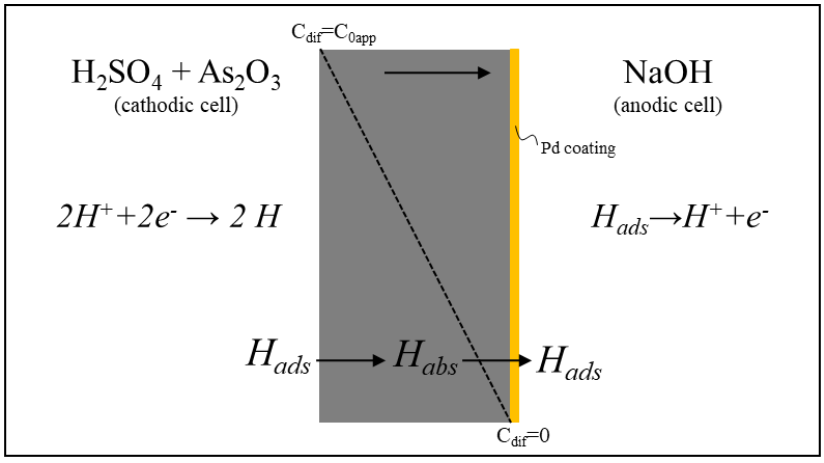

(b)

Figure 3.4. (a) Scheme of the double permeation cell employed in the hydrogen permeation experiments and (b) hydrogen reduction-oxidation reactions and diffusible hydrogen distribution in the specimen.

Before starting the tests, the background current density in the anodic cell must be reduced to a steady-state value below 0.1 µA/cm^2, which in any case was subtracted from the measured oxidation current prior to data analysis. Hydrogen oxidation was enhanced in the anodic cell, ensuring a virtually zero hydrogen concentration on the exit side of the specimen (Figure 3.4(b)) via the application of a palladium coating. This coating, with a thickness of around 1-2 µm, measured using SEM, was electrodeposited on the anodic side of the sample from a commercial palladium bath containing 2 g/l of Pd, applying a current density of 3 mA/cm^2 for 5 min.

In fact, there is general consensus as to the importance of using palladium coatings on the detection side of ferrous samples so that the permeation results may be reliably exploited in order to ensure the oxidation of hydrogen atoms on palladium-coated surfaces under most charging conditions [218]. Moreover, the possibility of having introduced hydrogen in the sample during

the process of Pd electrodeposition was discarded, as different hydrogen measurements were performed on the Pd-coated samples obtaining values below 0.1 ppm in all cases.

3.3.1. Single transient permeation experiments

Single permeation experiments, such as the one shown in Figure 3.5, were performed with the 42CrMo4-700 steel grade in order to experimentally measure the amount of hydrogen introduced in the specimens once the permeation current density, J_p, reaches a steady-state hydrogen flux, J_{ss}. Single permeation tests were performed under different cathodic current densities, J_c, (0.25, 0.5, 0.75, 1 and 2 mA/cm^2) with the aim of establishing the relationship between the cathodic current, the apparent hydrogen diffusion coefficient, D_{app}, and hydrogen concentration in the steel.

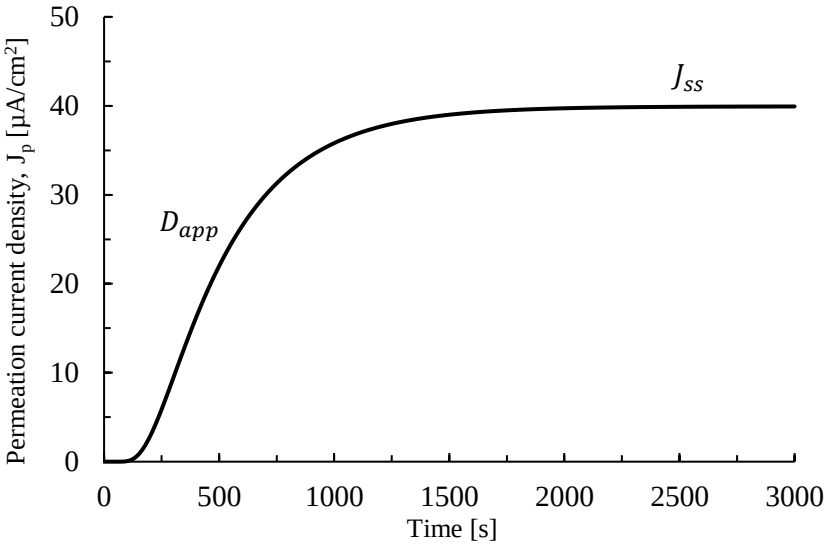

Figure 3.5. Typical record obtained in a single permeation experiment.

The hydrogen content was measured at the end of these single permeation tests in a Leco DH603 hydrogen analyser. Before starting the measurement, the H-charged sample was cleaned with acetone and carefully dried using cold air. The analysis to determine the total hydrogen concentration (diffusible + deeply trapped) consisted in keeping the sample at 1100ºC for 400 s. Hydrogen content determination is further described in section 3.5 of this same chapter.

The apparent hydrogen diffusion coefficient, D_{app}, was calculated from the permeation transient according to the time lag, t_{lag}, method, using Equation (3.4), derived from Fick's solutions under the appropriate boundary conditions [94].

$$D_{app} = \frac{L^2}{M \cdot t_{lag}} \qquad \textit{Equation (3.4)}$$

L being the specimen thickness; t_{lag}, the time needed to reach 63% of the steady-state permeation current, J_{ss}; and *M*, a constant with a value equal to 6 for J_p=63%J_{ss}.

3.3.2. Build-up permeation transients

It is now well known that the apparent hydrogen diffusion coefficient depends on the applied cathodic charging density, i.e., amount of hydrogen introduced in the steel [13,14] increasing as hydrogen progressively fills the different hydrogen traps present in the steel microstructure. The permeation methodology employed to consider this fact is shown in Figure 3.6. It consists in recording several build-up permeation transients produced by sequentially increasing the cathodic current density until a steady-state value of the hydrogen diffusion coefficient is reached. Operating in this way, it is possible to study the entrance of hydrogen in progressively H-filled microstructures in order to calculate the diffusion coefficient evolution as a function of the applied cathodic current density, until final saturation of all the microstructural traps in the last(s) transient(s). This last hydrogen diffusion coefficient is known as the lattice hydrogen diffusion coefficient of the steel, D_L, which is non-affected by the presence of microstructural traps, as they are completely filled [69,99,102,220].

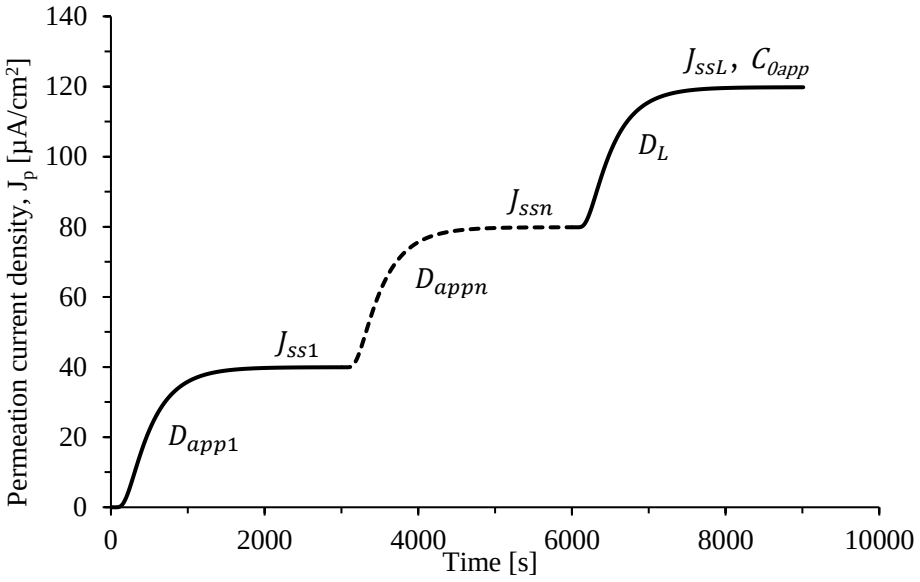

Figure 3.6. Typical record obtained in consecutive build-up permeation transients.

Depending on the hydrogen trapping capacity of each steel grade, different stepped permeation tests were performed. Usually, the cathodic current was increased in 0.5 mA/cm^2 steps for the first two transients and using 1 mA/cm^2 steps until saturation was reached, when a constant value of the diffusion coefficient was finally obtained. Anyway, a first permeation transient under a cathodic current of 0.5 mA/cm^2, D_{app1}, was always used with all the steel grades in order to assess the diffusivity under a low hydrogen trap occupancy condition.

Once all hydrogen traps are saturated, and a stable hydrogen distribution in the specimen like the one showed in Figure 3.4(b) can be assumed, it is possible to determine the apparent sub-surface hydrogen concentration on the charging side of the sample, C_{0app}, using Equation (3.5), derived from the second Fick´s law.

$$C_{0app} = \frac{J_{ssL} \cdot L}{D_L \cdot F} \qquad \textit{Equation (3.5)}$$

Where, J_{ssL} is the steady-state permeation current density of the last transient and, F, the Faraday constant (96485 C/mol). C_{0app} can be converted from mol/cm^3 to ppm wt. by multiplying by M_H/ρ_{Fe}, M_H being the molar mass of hydrogen (1 g/mol) and ρ_{Fe} the density of iron (7.87 g/cm^3). It is worth to mention here that the hydrogen subsurface concentration, C_{0app}, depends on the sample thickness when permeation tests are done using thin membranes, being on the contrary independent on thickness in the case of thick membranes [221,222].

The relationship between the hydrogen generated by cathodic polarization on the charging side of the specimen, J_c, and the permeation current density detected on the exit side, J_{ss}, obeys Equation (3.6), in which η is the efficiency of the permeation process, which mainly depends on the hydrogen recombination rate ($H_{ads}+H_{ads} \rightarrow H_2$ (gas)) at the entry surface.

$$J_{ss} = \eta \cdot J_c \qquad \textit{Equation (3.6)}$$

Stepped build-up hydrogen permeation transients are also useful to evaluate the density of hydrogen traps, N_t. The mathematical formulation that allows the calculation of N_t is based on the formalisms developed by McNabb-Foster [20] and Oriani [18], subsequently improved by Kumnick and Johnson [82,112], who proposed two different approaches for determining the value of N_t depending on the degree of trap occupancy.

When trap occupancy is low, i.e., the first permeation transient, the density of trapping sites, N_t, can be determined according to Equation (3.7).

$$N_t = N_L \left(\frac{D_L}{D_{app1}} - 1 \right) \cdot exp\left(-\frac{E_b}{R \cdot T} \right) \qquad \textit{Equation (3.7)}$$

where D_L is the value of the lattice hydrogen diffusion coefficient of the studied steel (obtained in the last transient, when all traps are filled); $D_{app1,}$ the apparent hydrogen diffusion coefficient calculated in the first permeation transient to guarantee low trap occupancy; E_b, the trap binding energy, estimated from TDA measurements in this study; R, the gas constant; and T, the absolute temperature (298 K). N_L is the density of the interstitial sites in the steel, which can be calculated as proposed by Krom and Bakker [223] by means of Equation (3.8).

$$N_L = \frac{N_A \cdot \beta \cdot \rho_{Fe}}{M_{Fe}} \qquad \textit{Equation (3.8)}$$

N_A being the Avogadro constant (6.022×10^{23} at/mol); β=6, the number of tetrahedral interstitial sites per atom in the BCC Fe crystal lattice; M_{Fe}, the molar mass of iron (55.8 g/mol); and ρ_{Fe}, the density of iron (7.87 g/cm^3). The value of N_L obtained using Equation (3.8) is 5.1×10^{29} sites/m^3.

For high trap occupancy (trap saturation), the trapping site density, N_t, is calculated by means of Equation (3.9).

$$N_t = \frac{C_{0app}}{3}\left(\frac{D_{LFe}}{D_L} - 1\right) \cdot N_A \qquad \textit{Equation (3.9)}$$

where C_{0app} is the apparent hydrogen sub-surface concentration on the charging side of the sample, calculated from Equation (3.5) in the last build-up transient; D_L is the lattice hydrogen diffusion coefficient estimated also in the same last build-up transient, where traps are fully filled; D_{LFe} is the value of the lattice hydrogen diffusion coefficient of pure iron (the value of 7.3×10^{-9} m^2/s reported by Kiuchi et al. [50] was considered in this work); and N_A is the Avogadro constant. This same approach was used by Yen and Huang [224], Dong et al. [72] and Izadi et al. [225], among others.

3.4. Gaseous hydrogen pre-charge

The specimens used in the different mechanical tests and also cylindrical pins for hydrogen measurements were pre-charged with pure gaseous hydrogen in the high-pressure reactor (with a diameter of 73 mm and a total length of 180 mm) shown in Figure 3.7.

Figure 3.7. High-pressure hydrogen reactor used to pre-charge the steel samples. It is located in Idonial Technology Centre, Asturias, Spain.

The reactor was manufactured in accordance with the ASTM G146 standard [226] and was located in the workshop of Idonial Technology Centre in Asturias, Spain. Before hydrogen charging, air was removed from the vessel using three alternate inert gas purges to reduce the oxygen level to the required minimum.

To ensure that all the specimens were saturated with hydrogen (the maximum thickness of the tested specimens was 10 mm), the following conditions were applied: 21 hours at 450ºC under a pressure of 19.5 MPa of pure hydrogen.

The high temperature hydrogen solubility of the quenched and tempered 42CrMo4 steel grades under high pressure and high temperature hydrogen gas can be approximated by the equilibrium lattice hydrogen content of BCC iron, as reported by Hirtz [80], using Equation (3.10), considering that microstructural traps are not active at this high temperature:

$$C_H = 104.47 \cdot \sqrt{f} \cdot e^{(-28600/RT)} \qquad \textit{Equation (3.10)}$$

Where, f represents the fugacity, in MPa. According to San Marchi [227], fugacity can be expressed in terms of hydrogen pressure, p, according to Equation (3.11).

$$f = p \cdot e^{(bp/RT)} \qquad \textit{Equation (3.11)}$$

Where, b is a constant with a value of 15.84 when the pressure, p, is expressed in MPa. Applying these equations to the specified hydrogen charging conditions, a hydrogen content of 4.1 ppm was thus introduced into the 42CrMo4 steel samples.

After charging the specimens for 21 hours, a cooling ramp of 1 hour until reaching a temperature of 85ºC, as shown in Figure 3.8(a), was always necessary for their extraction from the reactor. Although the hydrogen pressure of 19.5 MPa was maintained during the entire cooling phase, the decrease in temperature creates a thermodynamic driving force for hydrogen egress from the specimens, which led to a significant hydrogen loss, as will be shown later. To avoid further hydrogen losses after the cooling phase, the hydrogen pre-charged specimens were immediately removed from the reactor and introduced in a cryogenic storage dewar containing liquid nitrogen (-196ºC), Figure 3.8(b). They were then transported to the laboratory and preserved in the dewar until the moment of testing.

Once the specimen was extracted from the cryogenic storage dewar, it is necessary to allow it to warm up to room temperature before starting the mechanical test. By recording the evolution of the specimen's surface temperature with time using a thermocouple, in combination with a simple thermal analysis performed using Abaqus, a heat transfer coefficient, h, between the specimen's surface and the calm laboratory air of 22 W/m^{2}K was estimated. Therefore, considering a constant thermal conductivity, λ, of 31 W/mK for the 42CrMo4 steel [31], the time needed for the centre of the specimen to attain room temperature (approximately 20ºC), was determined to be around 15 minutes for tensile specimens and 25 min for CT specimens.

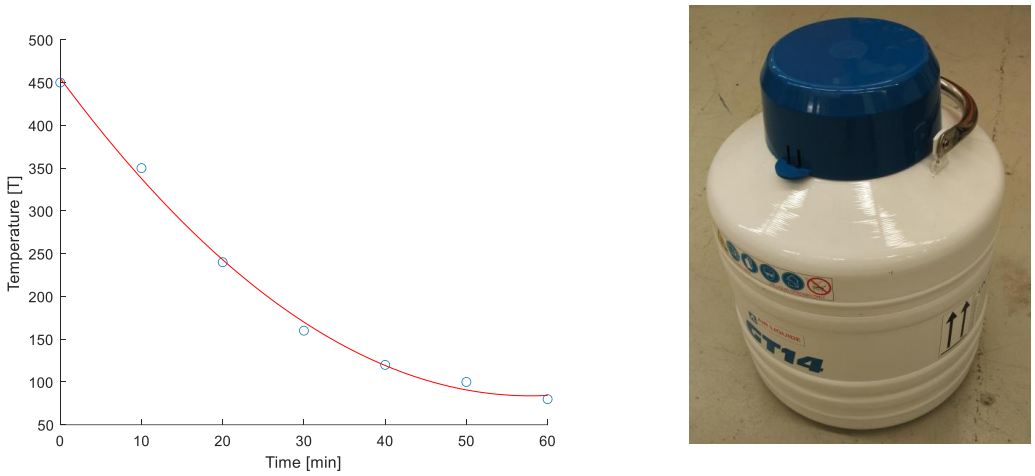

(a) *(b)*

Figure 3.8. (a) Reactor cooling ramp applied for samples extraction and (b) cryogenic storage dewar.

3.5. Hydrogen measurements

The total hydrogen content present in each steel grade was measured on hydrogen pre-charged cylindrical pins (with a diameter of 10 mm and a length of 30 mm) by means of thermal desorption analysis (TDA) in a Leco DH603 hydrogen analyser, Figure 3.9.

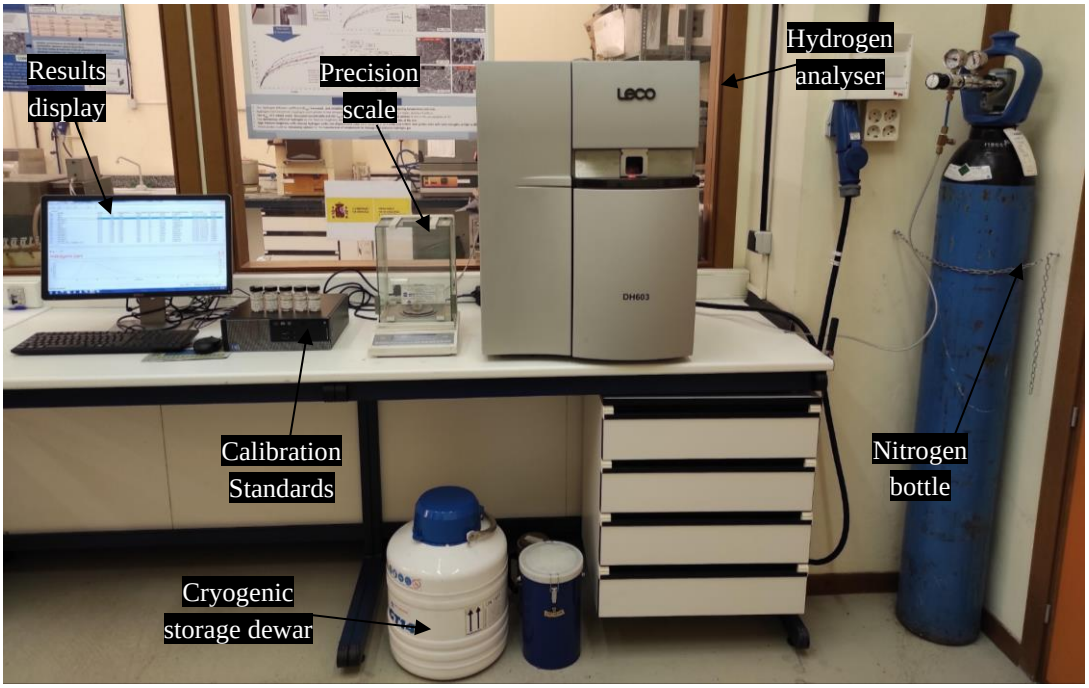

Figure 3.9. Leco DH603 hydrogen analyser with the different elements involved in the measurement.

The analysis measurement principle is based on the difference in thermal conductivity between a reference gas flow of pure nitrogen and a secondary flow composed of nitrogen and the hydrogen thermally extracted from the analysed specimen. This variation of thermal conductivity generates

a potential difference in a Wheatstone bridge circuit that converts it into an electrical intensity signal. The software of the equipment determines the variation of the signal intensity over time, providing the area beneath the curve. This integrated area is related to the amount of hydrogen extracted from the sample (in micrograms, μg) by means of a previously calibration equation. The concentration of hydrogen, in weight part per million (ppm), is finally obtained dividing the micrograms of hydrogen by the mass of the sample.

For the calibration of the equipment, calibrated standards of 0.7, 2.0±0.6, 2.8±0.6, 5.1±0.7, 6.17±0.49 and 7.24±0.34 ppm, supplied by Leco Co., were employed. Figure 3.10 shows the calibration curve and the corresponding equation, being x the integrated area and y the hydrogen content, in μg.

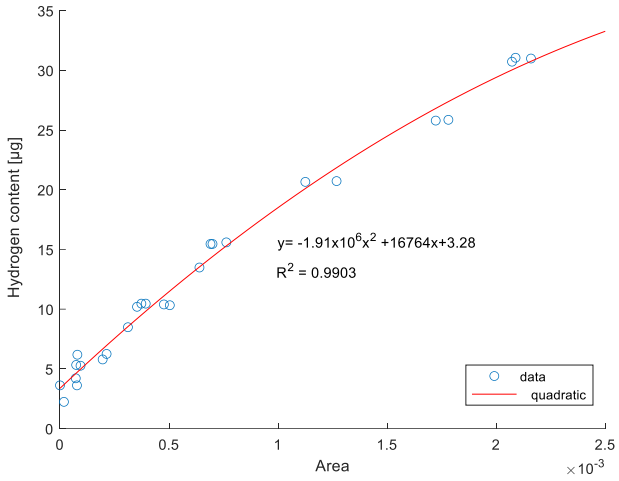

Figure 3.10. Calibration curve of Leco DH603 used in hydrogen measurements.

Before starting the measurement, each pin was cleaned in an ultrasonic bath with acetone for 3 minutes and carefully dried using cold air (clean nitrile gloves were always used to handle the samples). Next, the mass of the specimen (around 20±1 g in all cases) was measured using a precision scale. Finally, the thermal desorption analysis applied to determine the total hydrogen concentration consisted in keeping the sample at 1100ºC for 400 s.

3.6. Desorption curves and hydrogen diffusion coefficient estimation

As one of the purposes of this study was to correlate the loss of mechanical properties with the amount of hydrogen present in the steel during the tests, the hydrogen desorption curves of the different steel grades were determined at room temperature, RT. These curves represent the hydrogen content versus time elapsed at room temperature (ppm vs time). The procedure to obtain the desorption curves was the following: all the hydrogen pre-charged cylindrical pins were removed from the liquid nitrogen at the same time and left in air at RT; then, the total hydrogen concentration of the different samples was measured at different time intervals, until approximately one month.

In addition, numerical fitting of the experimentally measured hydrogen desorption data was used to estimate the apparent hydrogen diffusion coefficient, D_{app}, of the studied steel grades. An axisymmetric bi-dimensional diffusion analysis of the aforementioned cylindrical samples was performed using a commercial FEM software (Abaqus CAE), employing 4-node linear axisymmetric quadrilateral elements, with a size of 1 mm.

However, due to the hydrogen loss that takes place during the reactor cooling phase, it is not possible to determine D_{app} directly from the experimental desorption curve. The hydrogen concentration in the specimens at the end of the gaseous pre-charge is supposed to be homogeneous (hydrogen saturation), however, after the cooling phase (at the beginning of the RT desorption), the hydrogen distribution in the cylindrical pin is not homogeneous, having higher hydrogen concentration in the bulk than in the surface.

Consequently, in first place, it is necessary to determine the hydrogen distribution in the specimen at the end of the cooling phase. This was achieved by performing a diffusion analysis from a homogeneous distribution in all the specimen equal to 4.1 ppm to an average hydrogen content equal to the initial value measured at RT in the hydrogen analyser, C_0. The desorption kinetics of this step is not relevant, so a random diffusion coefficient, D_{rdm}, was used.

Once the hydrogen distribution in the specimen at the beginning of the RT desorption was known (first point of the experimental desorption curve), it was used as the initial boundary condition of the second step of the diffusion analysis. The residual or final hydrogen content, C_r, after a long stay at room temperature (deep trapped hydrogen concentration), likewise experimentally determined using Leco analyser, was taken as our final boundary condition (homogeneous in all the sample).

Fick´s diffusion law, described by Equation (3.12), was applied to a cylinder with a radius, R, of 5 mm. J being the hydrogen flux, D_{app} the apparent diffusion coefficient, and C_H the hydrogen concentration in the specimen. Although hydrogen transport is known to be concentration dependent and also depends on the density and energy of traps [36], a constant diffusion coefficient was used is this simplified analysis:

$$J = -D_{app} \nabla C_H \qquad \textit{Equation (3.12)}$$

The evolution of hydrogen over time at room temperature (both radial and longitudinal diffusion were considered) was determined by varying D_{app}. The diffusion coefficient which best fitted the experimental data was taken as the apparent diffusion coefficient of the steel. Figure 3.11 explains our operative procedure.

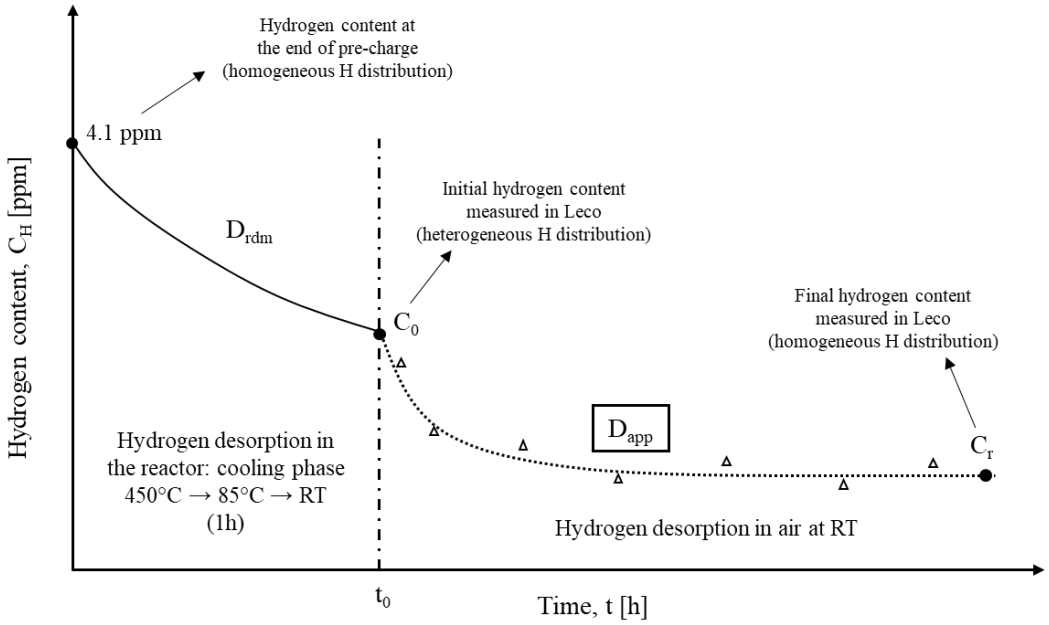

Figure 3.11. Scheme used to estimate D_{app} from hydrogen desorption at room temperature on hydrogen pre-charged samples (radius R=5 mm and length L=30mm).

3.7. Estimation of trap binding energies

Thermal desorption analysis (TDA) was also used to describe the traps present in these steel grades. Hydrogen pre-charged samples were heated under a defined temperature profile, so the stored hydrogen atoms effuse differently depending on the kind of trapping site and its associated activation energy. The trap activation energy, E_a, was thus determined by detecting the released hydrogen as a function of the heating rate [31,228]. The trap binding energy, E_b, was then calculated, assuming $E_a=E_b+E_L$ (E_L being the activation energy of hydrogen diffusion in an iron lattice, which has an approximate value of 8 kJ/mol [66]).

Assuming that the egress of hydrogen from a trap site is a thermally activated process, the hydrogen evolution rate from trapping sites can be written according to the following expression Equation (3.13).

$$\frac{dX_H}{dt} = A(1 - X_H) \cdot e^{\left(-E_a/RT\right)} \qquad \textit{Equation (3.13)}$$

Where, X_H is the fraction of hydrogen evolved from a trapping site characterized by an activation energy, E_a, A being a constant. Hence, when a hydrogen-charged specimen is heated at a uniform rate, $\phi(dT/dt)$, a hydrogen peak related to the trap activation energy is detected at a certain temperature, T_p. Using the model developed by Lee and Lee [21], derived from Fick's second law, the trap activation energy, E_a, can be calculated from the slope of the linear regression obtained when plotting $\ln(\phi/T_p^2)$ versus $1/T_p$, according to Equation (3.14). This equation is valid for low trap occupancy in the case of low lattice hydrogen contents [31,229].

$$\frac{\partial\left[ln\left(\phi/T_p^2\right)\right]}{\partial\left(1/T_p\right)} = -\frac{E_a}{R} \qquad \textit{Equation (3.14)}$$

These tests were also performed on the aforementioned Leco DH603 hydrogen analyser using the following heating rates: 4800, 3600, 2400, 1800, 1200, 800 and 400ºC/h.

3.8. Mechanical tests

The mechanical behaviour of all the 42CrMo4 steel grades was characterized using both uncharged and hydrogen pre-charged specimens. Tensile tests on smooth and notched specimens, fracture toughness tests, constant load tests on pre-cracked samples and fatigue crack growth tests were performed in air at room temperature.

3.8.1. Tensile tests

Tensile tests on both smooth and circumferentially-notched round-bar specimens, whose dimensions and geometries are shown in Figure 3.12, were performed in air at room temperature on an Instron 5582 tensile testing machine, following the indications given by the ISO 6892-1:2017 standard [230].

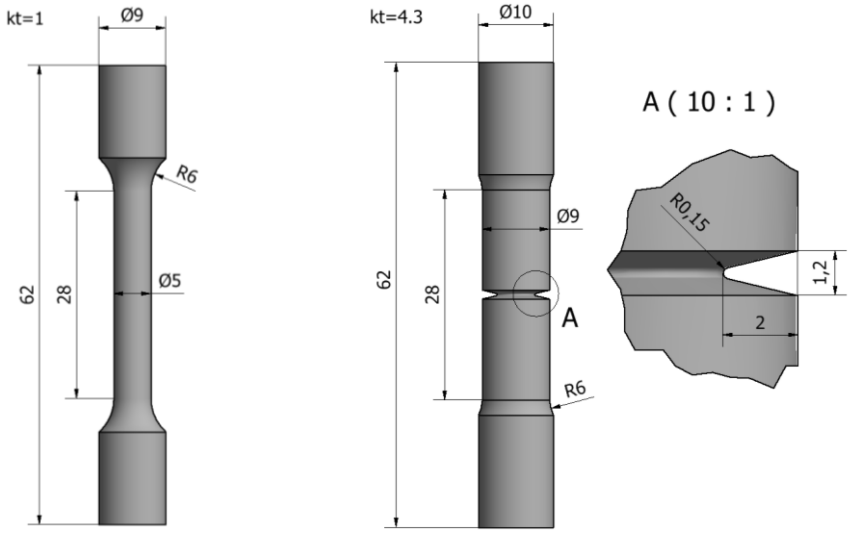

Figure 3.12. Geometry and dimensions (mm) of (a) smooth and (b) notched specimens used in the tensile tests.

Longitudinal deformation of the specimens during the tests was measured by means of an Instron 2630-100 extensometer with a calibrated length of 25 mm. A tensile specimen in the course of the tensile test can be seen in Figure 3.13.

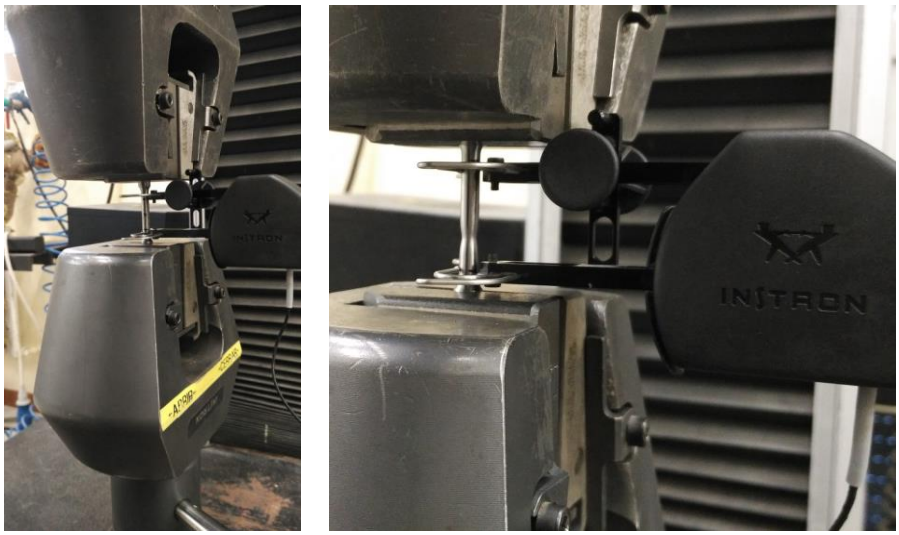

Figure 3.13. Tensile test performed in an Instron 5582 machine and detail of the Instron strain gauge.

The notched tensile specimens had a notch root depth and radius, ρ, of 2 and 0.15 mm respectively, and a notch cross-section radius, r, of 2.5 mm. Being its corresponding stress concentration factor, $k_t = 4.3$, according to Equation (3.15), proposed by Neuber [231]. This value is in line with those calculated by other authors for similar specimen geometries [134,232].

$$K_t = \frac{{}^{r}/_{\rho}\left({}^{r}/_{\rho}+1\right)^{1/2} + 0.8\,{}^{r}/_{\rho} + 1.3\left[\left({}^{r}/_{\rho}+1\right)^{1/2}+1\right]}{{}^{r}/_{\rho} + 0.6\left({}^{r}/_{\rho}+1\right)^{1/2} + 2} \qquad \textit{Equation (3.15)}$$

The behaviour of uncharged and hydrogen pre-charged specimens was compared in these tests. All the uncharged tests were performed under a displacement rate of 0.4 mm/min. However, different displacement rates, 0.4, 0.04, 0.004 and even 0.002 mm/min, were applied in the case of the hydrogen pre-charged specimens with the aim of studying the influence of this parameter on hydrogen embrittlement (HE).

Additionally, with the aim of evaluating the ability of the steel to recover its properties as hydrogen progressively egress from the specimens, hydrogen pre-charged tensile notched specimens of the steel grade tempered at 500ºC were degassed in air at room temperature for different times and then tested at the same displacement rate of 0.04 mm/min.

In the course of these tests, the applied load vs specimen elongation was continuously recorded, and the stress-strain (σ-ε) curve was determined. The yield strength, σ_{ys} (only in smooth specimens), ultimate strength, σ_{uts}, final elongation, e, and reduction in area, RA, were determined. In the case of the notched specimens, the ultimate strength was defined as the maximum tensile load divided by the initial cross-sectional area of the notch region.

The extent of hydrogen embrittlement was assessed by means of the embrittlement index (EI), defined in Equation (3.16). EI varies from 0 (no embrittlement at all) to 100% (maximum possible hydrogen embrittlement).

$$EI\ [\%] = \frac{X - X_H}{X} \cdot 100 \qquad \textit{Equation (3.16)}$$

Where, X and X_H are the measured steel property respectively evaluated without and with hydrogen.

3.8.1.1. Stress distribution in notched specimens

In order to fully characterize the behaviour of the notched tensile specimens and discuss the obtained experimental results, the distribution of the local normal stress perpendicular to the notch plane, σ_{22}, the hydrostatic stress, σ_h, and the Von Mises stress, σ_{VM}, were obtained at the moment of fracture of the tensile notched specimens. σ_h and σ_{VM} were respectively calculated according to Equation (3.17) and Equation (3.18), being σ_{11}, σ_{22} and σ_{33} the principal stresses.

$$\sigma_h = \frac{\sigma_{11} + \sigma_{22} + \sigma_{33}}{3} \qquad \textit{Equation (3.17)}$$

$$\sigma_{VM} = \sqrt{\frac{(\sigma_{11} - \sigma_{22})^2 + (\sigma_{22} - \sigma_{33})^2 + (\sigma_{33} - \sigma_{11})^2}{2}} \qquad \textit{Equation (3.18)}$$

A 2D axisymmetric elastic-plastic finite element model defined with a Hollomon hardening law ($\sigma_v = {\varepsilon_{plv}}^n$) obtained from the tensile tests performed on smooth specimens in the absence of hydrogen, was developed. The geometry of the specimen was unevenly meshed; this mesh being finer in the vicinity of the notch root. 8-node biquadratic axisymmetric quadrilateral elements with reduced integration (CAX8R) were used with a minimum size of around 40 μm.

3.8.2. Fracture toughness tests

Fracture toughness tests were performed on compact tensile, CT, specimens with a width, W, of 48 mm, a thickness, B, of 12 mm, and an initial notch, a_n, of 20 mm. Specimen's geometry and dimensions are shown in Figure 3.14. First of all, the specimens were fatigue pre-cracked under a load ratio, R, of 0.1 and a frequency, f, of 10 Hz, until reaching a crack length versus width ratio, a/W, equal to 0.5 (a_0=25 mm), as indicated in the ASTM E1820 standard [233]. Next, lateral notches were machined on both sides of the specimen to obtain a net thickness, B_n, of 10 mm, as to assure a plane strain state.

Fracture tests were carried out in a servohydraulic universal MTS testing machine provided with a load cell of 100 kN, Figure 3.15. The crack growth throughout the test was determined by means of the compliance method using a COD gauge (also shown in Figure 3.15) and performing partial discharges (25%).

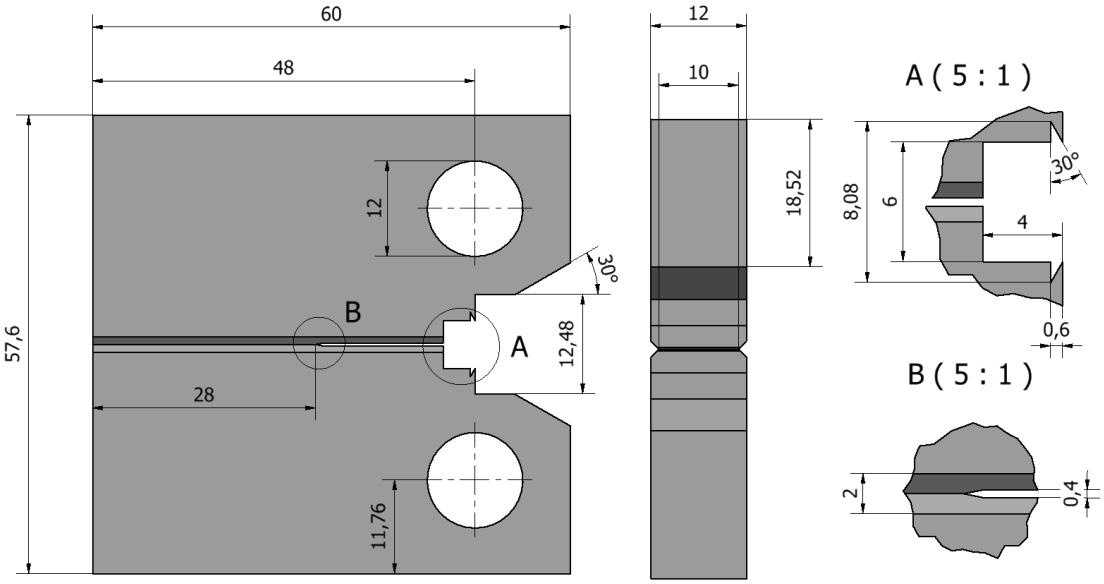

Figure 3.14. Geometry and dimensions (mm) of the CT specimens used in the fracture toughness tests.

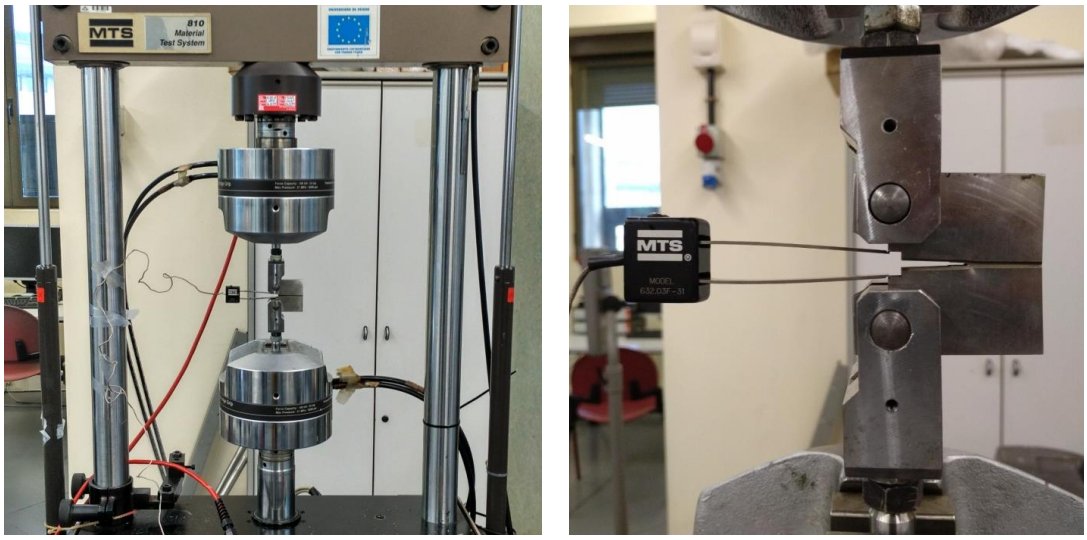

Figure 3.15. Fracture toughness test performed in a dynamic MTS testing machine with a load cell of 100 kN and detail of the COD gauge.

The value of J obtained in each discharge was determined as the sum of its elastic and plastic component, as shown in Equation (3.19).

$$J = J_{el} + J_{pl} \qquad \textit{Equation (3.19)}$$

The elastic component, J_{el}, was calculated from the stress intensity factor, K, through Equation (3.20), considering a Poisson's ratio, ν, equal to 0.3 and an elastic modulus, E, of 210GPa.

$$J_{el} = \frac{K^2(1-\nu^2)}{E} \qquad \textit{Equation (3.20)}$$

The plastic component was obtained by integrating the area below the load-LLD (load line displacement) plot, as shown in Equation (3.21) and following the procedure described in [233].

$$J_{pl_{(i)}} = \left[J_{pl_{(i-1)}} + \frac{\eta_{(i-1)} \left(A_{pl_{(i)}} - A_{pl_{(i-1)}} \right)}{B_n (W-a)_{(i-1)}} \right] \cdot \left[1 - \gamma_{(i-1)} \cdot \frac{a_{(i)} - a_{(i-1)}}{(W-a)_{(i-1)}} \right] \qquad \textit{Equation (3.21)}$$

Where A_{pl} represents the area below the Load-LLD curve for each deload and ai is the crack length. For a CT specimen the values of η and γ are calculated according to Equation (3.22) and Equation *(3.23)*, respectively.

$$\eta = 2 + \frac{0.522\ (W-a)_{i-1}}{W} \qquad \textit{Equation (3.22)}$$

$$\gamma = 1 + \frac{0.76\ (W-a)_{i-1}}{W} \qquad \textit{Equation (3.23)}$$

After the test, the initial, a_0, and final, a_f, crack lengths were corrected by measuring them on the fracture surface of the broken specimens. Consequently, the resistance curves, J-Δa, were obtained and the fracture toughness parameter, $J_{0.2/BL}$ (in kJ/m^2), was determined. This parameter corresponds to the value of J after an effective crack growth of 0.2 mm regarding the blunting of the crack tip and was employed to assess the fracture toughness for the onset of crack growth. The slope of the blunting line was determined using Equation (3.24), where σ_{ys} and σ_{ut} are the yield and ultimate strength, respectively.

$$\frac{J}{\Delta a} = 2 \left(\frac{\sigma_{ys} + \sigma_{uts}}{2} \right) \qquad \textit{Equation (3.24)}$$

It should be noted that, due to the high brittleness of the hardest steel grades (grades tempered at 550 and 500ºC) when tested with internal hydrogen under low displacement rates, it was not possible to determine the value of $J_{0.2/BL}$. Therefore, in these cases, the value of P_Q was calculated from the load-COD curve applying the 95% secant line methodology as specified in [233]. From this value, K_Q at instability and derived J_Q (Equation (3.20)) parameters were estimated following the indications of the aforementioned standard.

The fracture toughness tests of the uncharged specimens were carried out under a nominal displacement rate of 1 mm/min, except for the hardest steel grades (550 and 500ºC), where a test displacement rate of 0.1 mm/min was applied. Hydrogen pre-charged specimens were tested under displacement rates of 1, 0.1, 0.01, and also 0.001mm/min in the case of the hardest grades, in order to study the influence of this parameter on HE.

With the aim of evaluating the ability of the steel to recover its mechanical properties as hydrogen progressively egress from the specimens, hydrogen pre-charged CT specimens of the steel grade tempered at 500ºC were degassed in air at room temperature for different times and then tested at the same displacement rate of 0.01 mm/min to determine the fracture toughness.

As in the tensile tests, the drop of fracture toughness due to the presence of hydrogen in the microstructure of the steel was assessed by means of the embrittlement index EI ($J_{0.2/BL}$), defined in Equation (3.16).

3.8.3. Constant K tests

Hydrogen-assisted cracking was also assessed (in 42CrMo4-700, 42CrMo4-650, 42CrMo4-700-CG and 42CrMo4-725-CG) using constant load tests performed on pre-cracked CT specimens with geometry and dimensions similar to those already shown in Figure 3.14. They were fatigue pre-cracked in the same conditions as the specimens used in the fracture toughness tests (a/W=0.5) and lateral notches were machined on both sides of the specimen as well until reaching a net thickness B_n of 10 mm. These tests were also performed in the servohydraulic universal MTS testing machine shown in Figure 3.15.

The aim of these tests was to determine if the initial crack (a_0=25 mm) was able to grow under a certain constant applied load, P (constant stress intensity factor, K) due exclusively to the accumulation of hydrogen in the stressed region produced ahead of the crack tip (ASTM E1681 standard [234]). Additionally, representing the applied intensity factor, K_{app}, versus crack growth, Δa, these tests allow us to determine the threshold stress intensity factor value, $K_{th/0.2}$, for crack growing under internal hydrogen. A crack propagation of 0.2 mm was established as crack growth criterion (as in the definition of the fracture toughness parameter $J_{0.2/BL}$).

Consequently, hydrogen pre-charged CT specimens of each steel grade were subjected to constant loads of different magnitudes during a fixed time interval of 24 hours (longer times were dismissed to avoid hydrogen losses). The applied stress intensity factor, K_{app}, were calculated according to Equation (3.25).

$$K = \left[\frac{P}{\sqrt{BB_nW}}\right] f\left(\frac{a_0}{W}\right) \qquad \textit{Equation (3.25)}$$

with:

$$f\left(\frac{a_0}{W}\right) = \frac{\left[\left(2 + {a_0}/{W}\right)\left(0.886 + 4.64\left({a_0}/{W}\right) - 13.32\left({a_0}/{W}\right)^2 + 14.72\left({a_0}/{W}\right)^3 - 5.6\left({a_0}/{W}\right)^4\right)\right]}{\left(1 - {a_0}/{W}\right)^{3/2}}$$

After the completion of these tests, the specimens were fatigued until fracture and the initial and final crack lengths were measured on the fracture surface of the broken specimens. The applied stress intensity factor was thus corrected with the actual value of a_0 and ten measurements were performed along the specimen thickness to determine the value of a_f, needed to obtain an accurate crack growth Δa measurement.

3.8.4. Fatigue crack growth tests

Fatigue crack growth, FCG, tests were performed using standard compact tensile, CT, specimens with a width of 48 mm and a thickness of 10 mm (see Figure 3.16). Before hydrogen pre-charging, the specimens were fatigue pre-cracked at R=0.1 and 10 Hz following the ASTM E647 standard

[22] up to achieving an initial crack length, a_0=7 mm (equivalent to a/W=0.15). In this case, the servohydraulic universal MTS testing machine equipped with a load cell of 250 kN, shown in Figure 3.17, was used.

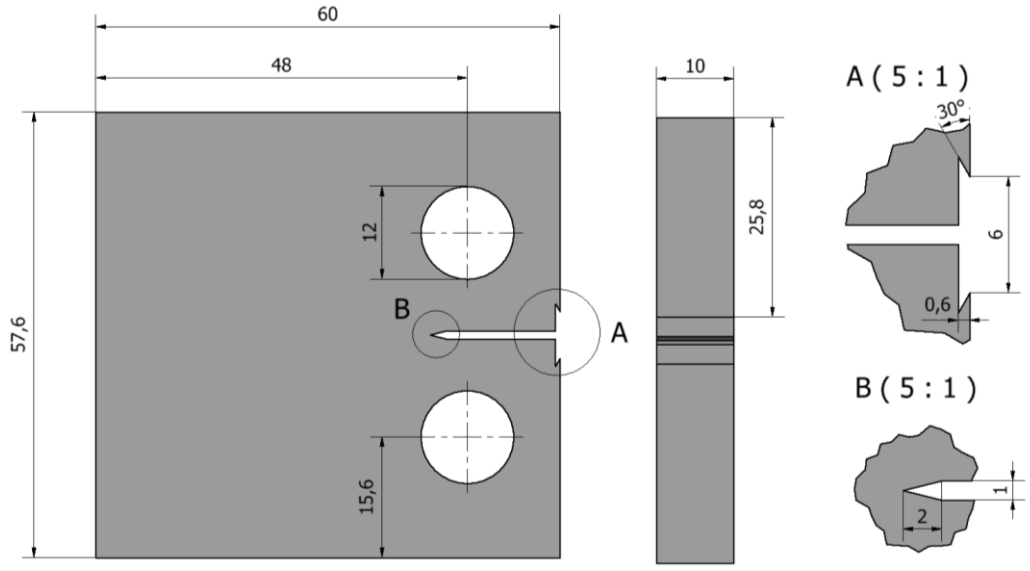

Figure 3.16. Geometry and dimensions (mm) of the CT specimens used in the fatigue crack growth tests.

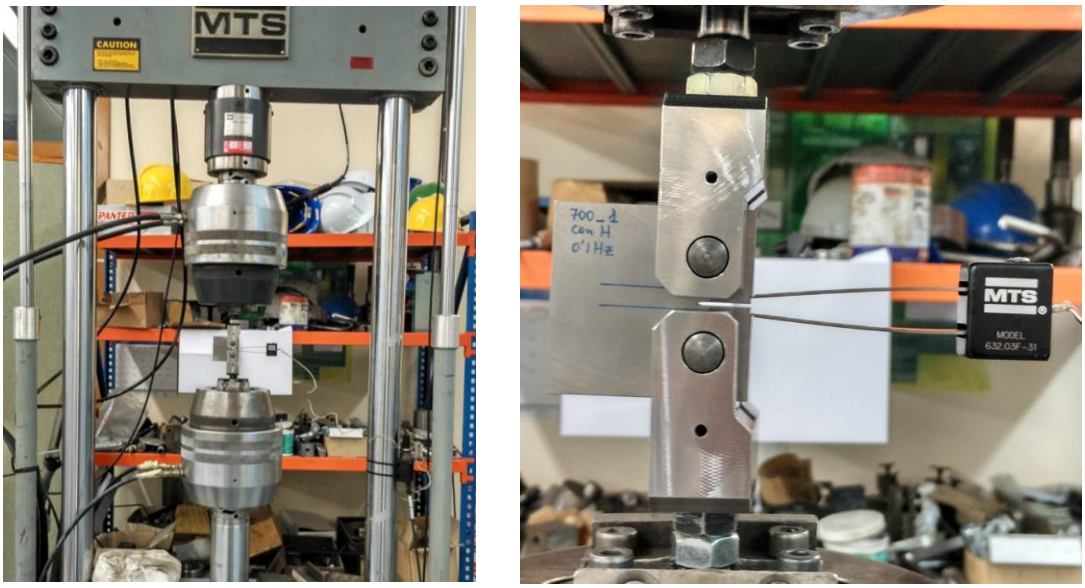

Figure 3.17. Dynamic MTS testing machine (250 kN) and COD gauge used in the fatigue crack growth tests.

These fatigue tests were performed under a constant ΔP load, starting in all cases with an initial, ΔK_0, of approximately 30 MPa$\sqrt{m}$. In the course of the fatigue crack growth tests, the crack length was continuously monitored by means of a CTOD extensometer (Figure 3.17), allowing the representation of the fatigue crack growth rate, da/dN, versus the applied stress intensity factor range, ΔK. After the completion of the test, the specimens were pulled until fracture and the initial

and final crack lengths were measured on the fracture surface of the broken specimen, and ΔK was accordingly corrected.

Regarding the testing parameters, uncharged specimens were always tested at a load ratio, $R=P_{min}/P_{max}$, equal to 0.1 and a frequency, f, of 10 Hz. In the case of hydrogen pre-charged specimens, load ratios of 0.1 and 0.5 and frequencies of 10, 1, 0.5, 0.1, and even 0.05 Hz were applied in order to evaluate the influence of these variables on the fatigue crack growth rate and on the prevailing fracture micromechanisms.

3.9. Observation of fracture surfaces

In order to identify the operative fracture micromechanisms, the fracture surfaces of all the tested specimens in both uncharged and hydrogen pre-charged conditions, were analysed using a scanning electron microscope (SEM JEOL-JSM5600) under an acceleration voltage of 20 kV and different magnifications.

3.10. Summary

As a summary, Figure 3.18 schematically shows the different 42CrMo4 steel grades studied in this thesis along with the particular tests performed on all of them.

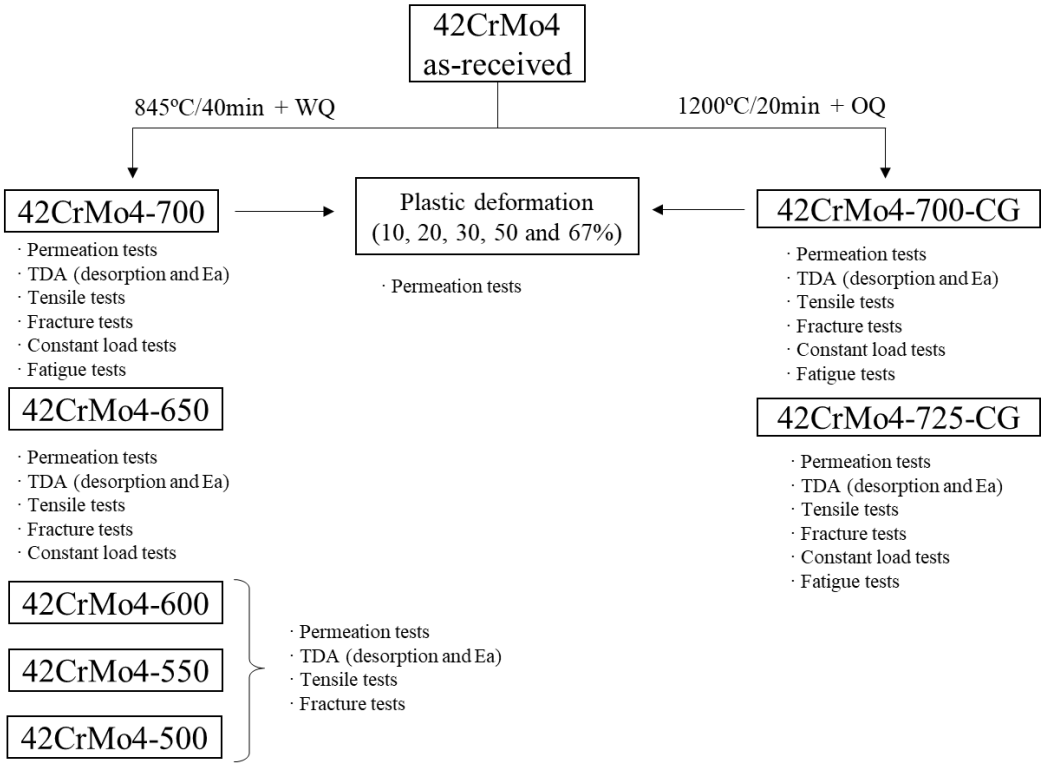

Figure 3.18. Summary of the study performed with the different 42CrMo4 steel grades.

Chapter 4

Results and discussion

Study on hydrogen diffusion and embrittlement of quenched and tempered 42CrMo4 steel

PhD Thesis

4. Results and discussion

4.1. Introduction

This chapter presents the results obtained in the different tests performed in the course of this study. As in the previous chapter, it is divided in 4 sections: microstructural characterization, electrochemical hydrogen permeation tests, thermal desorption analysis, and mechanical testing of hydrogen pre-charged specimens. In addition, to synthetize and facilitate the interpretation of the results, a discussion is included at the end of each aforementioned section.

4.2. Microstructural characterization

4.2.1. Influence of tempering temperature

The SEM microstructures of the five quenched and tempered 42CrMo grades are shown in Figure 4.1 under a magnification of 10000x. Additionally, the microstructure presented in Figure 4.1(a) corresponds to the as-quenched condition (200x), in which a prior austenite grain size of 15-20 μm (it is marked in dotted yellow lines on the image), and a hardness of 559±5 HV30 were determined.

The microstructure of all the quenched and tempered 42CrMo4 grades, Figure 4.1(b-f), was tempered martensite. It is clearly observed that, as the tempering temperature increases, the acicularity of the microstructure decreases, as does the distortion of the crystalline structure [235]. Carbide precipitation also increases with tempering temperature. Elongated carbides precipitated along grain and martensitic lath/packet/block boundaries at low tempering temperatures (500 and 550ºC), and they break up, globulize, and finally grow to yield a more uniform distribution as the tempering temperature increases. This carbide growth is clearly noticed when comparing the microstructures of the steel tempered at 600, 650 and 700ºC.

Furthermore, as the tempering temperature increases, internal residual stresses are released, the dislocation density is reduced and thus hardness and the diffraction peak width (FWHM) likewise decrease [113,209,236,237]. This fact is reflected in Figure 4.2, which shows the excellent linear correlation between the tempering temperature with the Vickers HV30 hardness (R^2=0.98), and with the XRD FWHM parameter (R^2=0.97). The latter is a parameter frequently used as an indicator of the microstructural hardening that alloys submitted to surface treatments undergo and can thus be used as an indirect measure of the dislocation density and the corresponding internal stresses [40,113,209,236,237]. Therefore, due to their linear evolution with the tempering temperature, both HV30 and FWHM can be employed as indicators of the dislocation density present in the steel. From this consideration, the steel hardness will be used with this end in all this work.

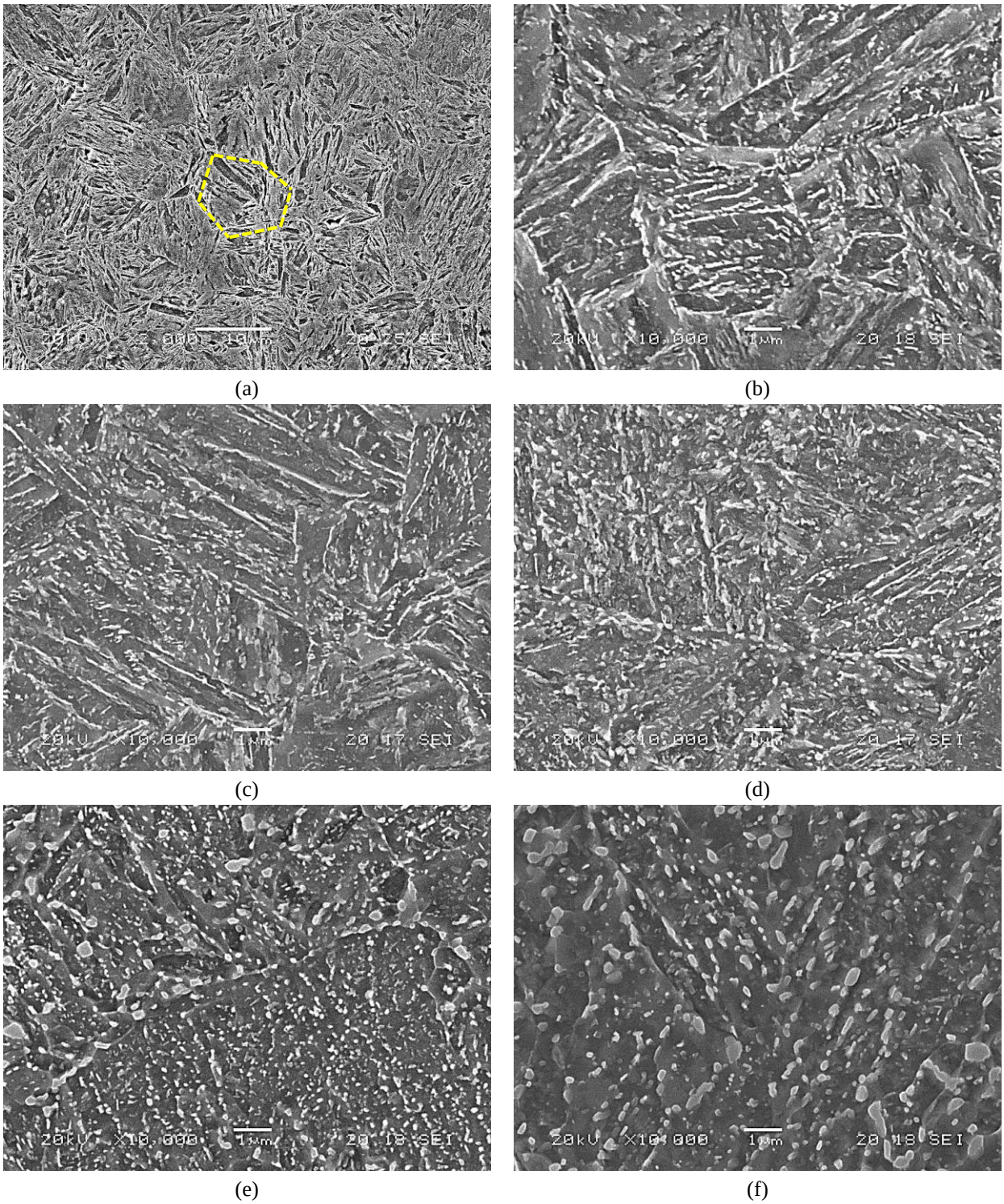

(a) (b)

(c) (d)

(e) (f)

Figure 4.1. SEM microstructures of 42CrMo4 steel, (a) as-quenched (2000x) and quenched and tempered for two hours at (b) 500ºC, (c) 550ºC, (d) 600ºC, (e) 650ºC and (g) 700ºC (10000x).

The aforementioned microstructural differences also give rise to the tensile properties listed in Table 4.1 for uncharged specimens. As expected, yield strength, σ_{ys}, and ultimate tensile strength, σ_{uts}, progressively decrease with increasing tempering temperature, while the opposite occurs with tensile elongation, e, and reduction in area, RA.

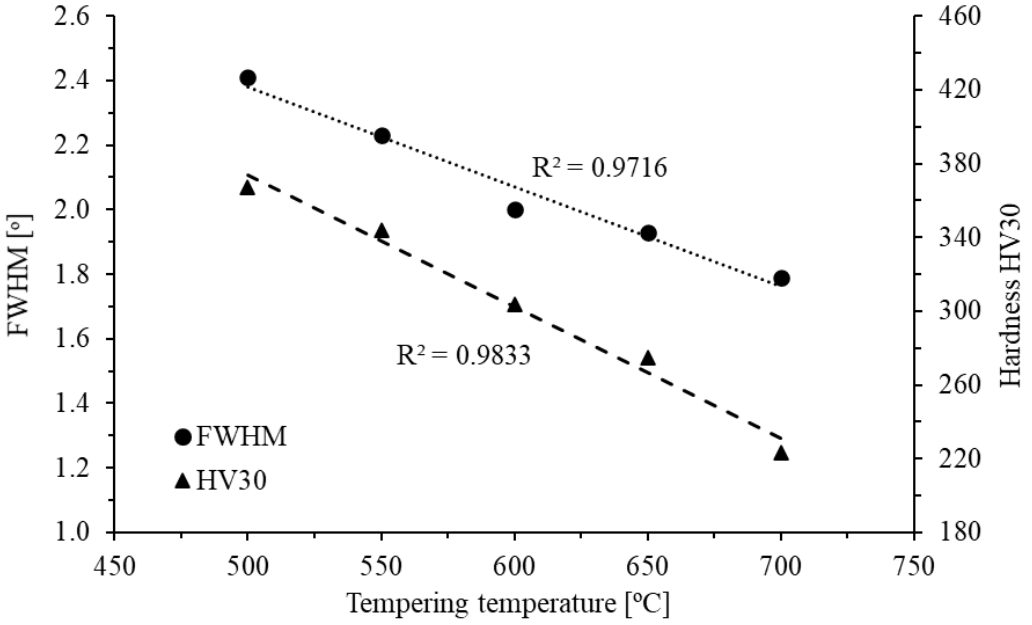

Figure 4.2. XRD FWHM parameter and HV30 hardness versus the tempering temperature.

Steel Grades	Heat treatment	HV30	FWHM [º]	σ_{ys} [MPa]	σ_{uts} [MPa]	e [%]	RA [%]
42CrMo4-700	845ºC+WQ+T700ºC/2h	223±2	1.79±0.05	622±2	710±5	22.6±0.6	62.8±1.7
42CrMo4-650	845ºC+WQ+T650ºC/2h	275±4	1.93±0.04	828±24	913±14	16.1±0.2	57.1±1.4
42CrMo4-600	845ºC+WQ+T600ºC/2h	304±6	2.00±0.05	880±1	985±2	14.6±0.5	55.4±1.0
42CrMo4-550	845ºC+WQ+T550ºC/2h	344±5	2.23±0.04	1023±4	1113±8	13.9±0.4	51.7±0.5
42CrMo4-500	845ºC+WQ+T500ºC/2h	367±8	2.41±0.04	1086±5	1198±4	12.7±0.5	50.6±1.2

Table 4.1 Heat treatments, hardness (HV30), FWHM parameter and tensile properties of the five Q+T 42CrMo4 steel grades.

4.2.2. Replication of the coarse grain heat affected zone of a 42CrMo4 weld

Figure 4.3. Macroscopic view (transversal section) of the weld bead deposited onto a 42CrMo4-700 steel a macroscopic view of the weld bead deposited onto a 42CrMo4-700 steel plate. The size of the heat affected zone has a width of around 1.2 mm. In addition, Figure 4.4 shows a detailed view of the CGHAZ with microhardness impressions on it.

The average microhardness value measured in the real CGHAZ, produced after the deposition of the weld bead, was 571±40 HV1. This corresponds to a fully martensitic microstructure in the 42CrMo4 steel (only a small percentage of bainite was also found). This microstructure (real CGHAZ), with an average PAGS of around 100 μm (a prior austenitic grain size is marked with a yellow dotted line on the image), is shown in Figure 4.5(a, b).

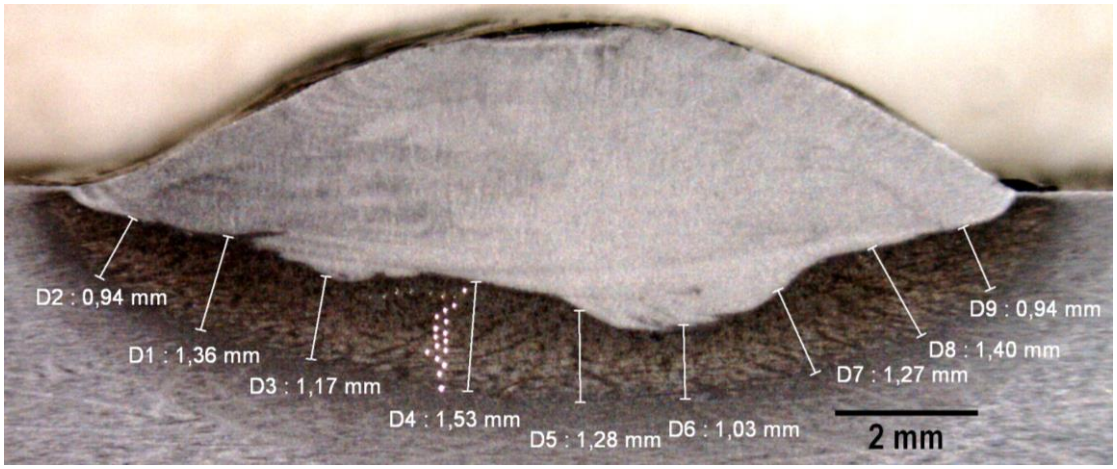

Figure 4.3. Macroscopic view (transversal section) of the weld bead deposited onto a 42CrMo4-700 steel plate.

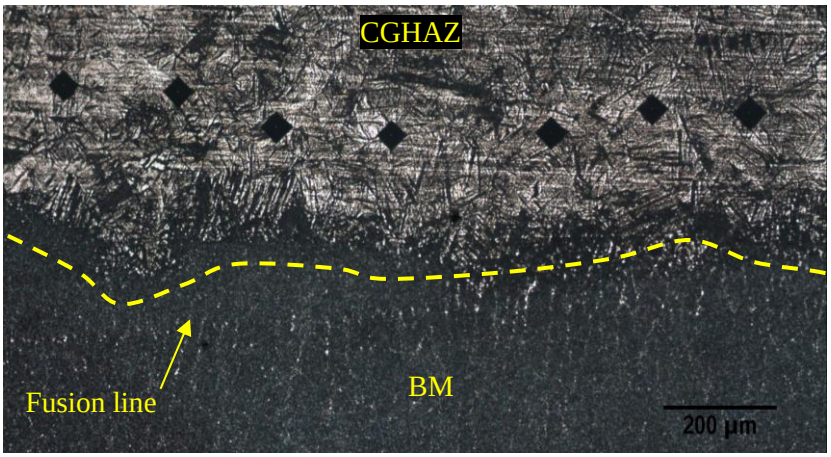

Figure 4.4. Detail of the CGHAZ with microhardness impressions, where the location of the fusion line is indicated.

After the post-welding heat treatment (tempering at 700ºC for 2h), the average microhardness determined on the CGHAZ was 248±6 HV1. The pronounced drop in hardness is a direct consequence of the tempering of the martensite microstructure: internal stress relaxation, with profuse carbide precipitation, along with recovery and recrystallization phenomena affecting the martensite laths and packets [238]. This microstructure is shown in Figure 4.5(c, d).

On the other hand, the average HV30 hardness measured in the steel after performing the simulated heat treatment designed to reproduce the real CGHAZ microstructure (1200ºC/20min+oil quenching) was 585±9HV30. This value is very similar to that measured in the CGHAZ close to the fusion line after the deposition of the weld bead (571±40). Figure 4.6(a, b) shows the obtained microstructure, consisting of nearly 100% martensite (with a small percentage of bainite). Using Vilella's reagent etching, an average prior austenite grain size of around 150 µm was measured in this coarse steel grade (it was marked with a yellow dotted line on Figure 4.6(a)).

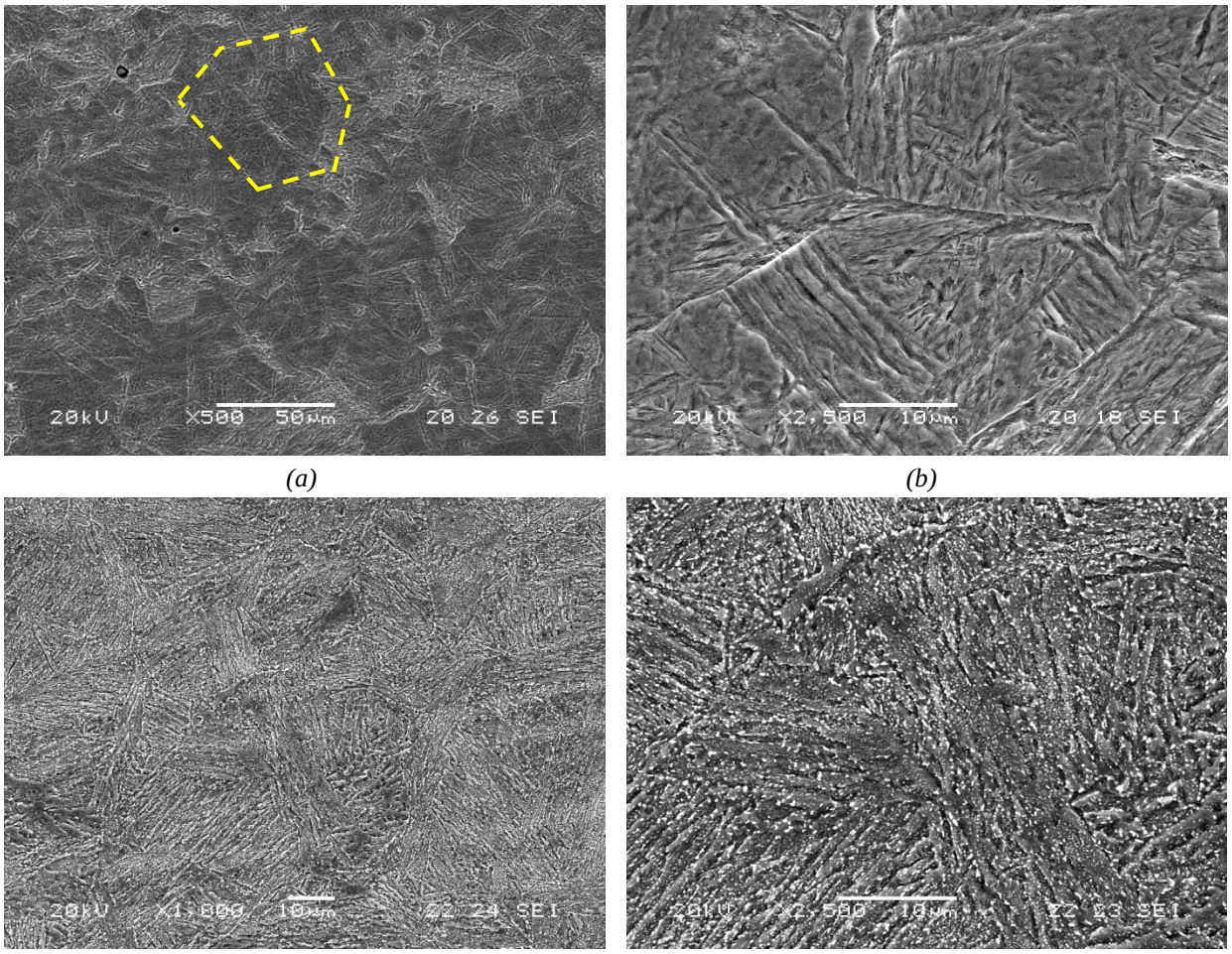

(a) *(b)*

(c) *(d)*

Figure 4.5. SEM microstructures of (a, b) real CGHAZ, and (c, d) real CGHAZ after PWHT (700ºC/2 h).

Finally, the value of the HV30 hardness measured in the replicated CGHAZ after the post-welding heat treatment (700ºC/2h), designated as 42CrMo4-700-CG, was 230±2 (very similar to the hardness value measured in the real CGHAZ after the PWHT, Figure 4.7±6). This microstructure is also shown in Figure 4.6(c, d). The profuse, uniformly distributed carbide precipitation that takes place during the high temperature tempering (700ºC/2h) throughout the microstructure of the steel can be clearly observed in this figure.

Based on the hardness results joined in Figure 4.7, along with the microstructures previously shown in Figure 4.5 and Figure 4.6, it is worth noting that the CGHAZ generated in the deposition of a weld bead onto 42CrMo4-700 steel plates has been successfully reproduced in a large volume with a simulative laboratory heat treatment. Moreover, after the application of a PWHT similar to the tempering treatment applied to the base steel (700ºC for 2 h), quite similar microstructures and hardness were also obtained.

Therefore, in the following sections, it will be possible to evaluate the tensile, fracture and fatigue crack growth behaviour of the CGHAZ of a 42CrMo4 steel weld in the presence of internal hydrogen using standard size specimens (tensile and CT).

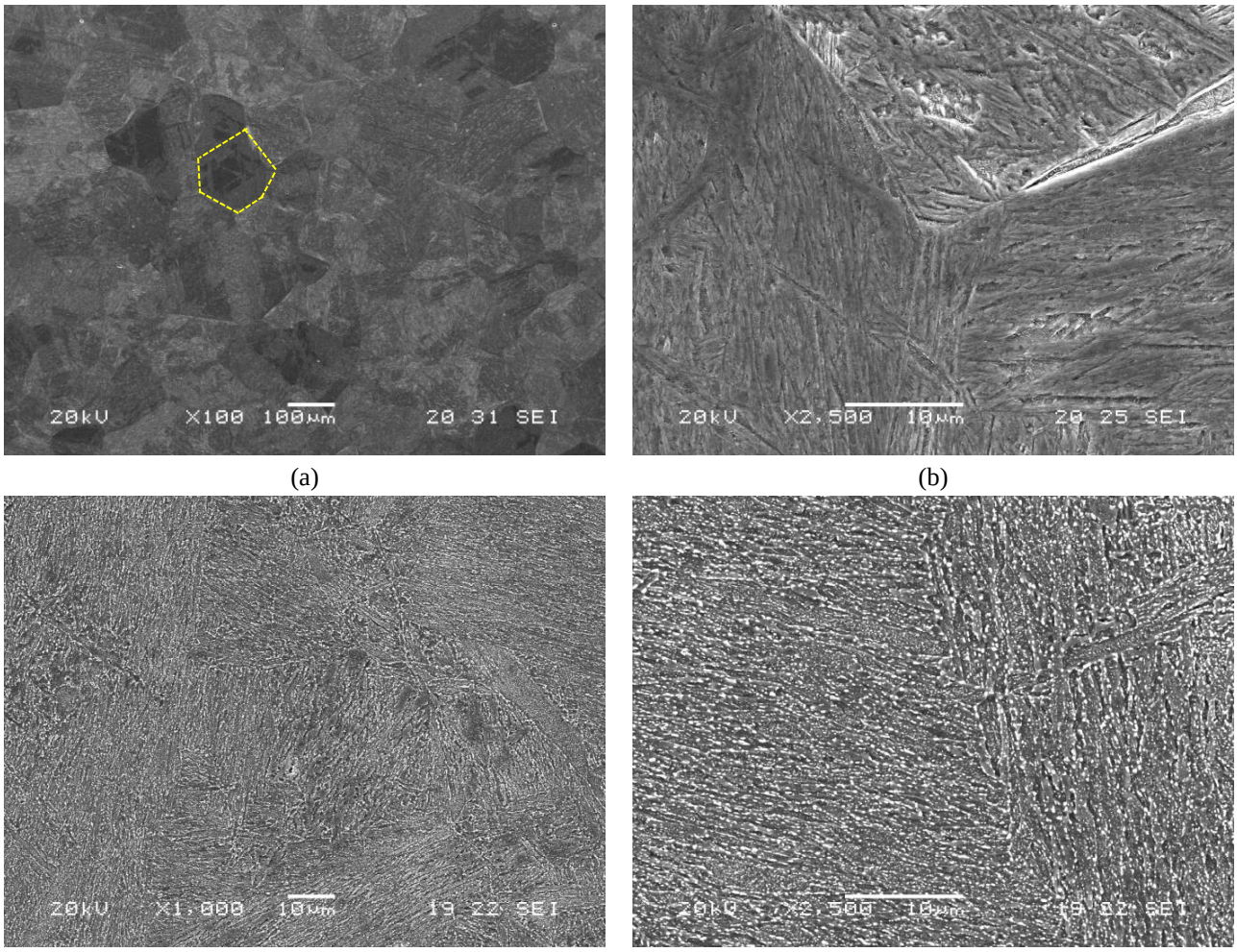

Figure 4.6. SEM microstructures of the coarse grain 42CrMo steel (a, b) as-quenched from 1200ºC and (c, d) quenched and tempered, 42CrMo-700-CG.

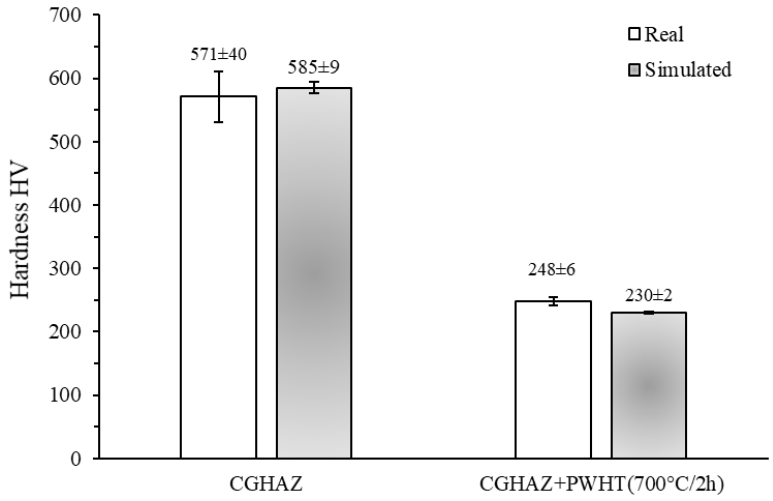

Figure 4.7. Comparison of Vickers hardness measured on the CGHAZ microstructures (real and simulated) before and after the PWHT (700/2h).

4.2.3. Comparison between base steel and simulated CGHAZ (with PWHT)

The hydrogen embrittlement behaviour of the fine grain base steel, 42CrMo4-700, and the simulated CGHAZ after the PWHT (700ºC/2h), with a coarser prior austenite grain size and therefore designated as 42CrMo4-700-CG, are compared in the following chapters of this document. Moreover, an additional post welding heat treatment, consisting of tempering at 725ºC for 4h (42CrMo-725-CG), has been applied to the simulated CGHAZ with the aim to improve its mechanical behaviour in the presence of internal hydrogen, although a lower strength steel grade will be produced.

The microstructures (SEM) of the base steel and both coarse grain grades, shown in Figure 4.8 under 1000x and 10000x, are very similar, tempered martensite. The profuse carbide precipitation that has taken place during the tempering stage can be clearly observed in the three cases. These carbides (Fe, Cr rich carbides [87,106]) are evenly distributed throughout the microstructure, with the larger, elongated carbides (with lengths of between 0.5 and 1 μm) located at interfaces between martensitic laths, and the spherical and smaller carbides (even smaller than 0.5 μm) precipitated inside these laths. No remarkable differences between carbide sizes have been detected among all these steel grades. However, the prior austenitic grain size in the fine-grained base steel is 20 μm and around 150 μm in the coarse-grained steel grades (simulated CGHAZ). For an easier comparison of PAGSs, the as-quenched microstructures are shown in Figure 4.1(a) and Figure 4.6(a). Correspondingly, a significant increase in the average size of martensite laths and packets in the coarse grain microstructures is noticed: an average lath width around 0.4 μm was measured in the base steel and 0.6-0.7 μm in the CG steel grades. On the other hand, the greater thermal drop applied to quench the CG steel grades (quenched from 1200ºC, instead of from 845ºC as in the case of 42CrMo4-700), produces a more distorted martensitic structure, with higher internal stresses and, consequently, higher dislocation density. Distortion differences between the base steel and coarse grain grades can be qualitatively appreciated even after tempering comparing the morphology of martensite lath and block interfaces (yellow dotted lines in Figure 4.8(b, d, f)). The alignment of precipitated carbides is much more evident in the base 42CrMo4-700 grade (more relaxed microstructure).

Finally, Table 4.2 gathers the hardness, PAGS and tensile properties of the base steel, 42CrMo4-700, and the two different coarse grain steel grades, 42CrMo4-700-CG and 42CrMo4-725-CG, studied in this work. The great difference observed in PAGS and the slight differences in hardness and tensile properties between the two steels tempered at the same temperature, base steel and the former CG steel grade, can be explained in terms of the greater austenitization temperature and thus thermal drop applied to quench the coarse grain microstructure. A more distorted martensitic structure is hence produced (see yellow dotted lines of Figure 4.8), with higher internal stresses and, consequently, higher dislocation density [239], which is reflected in its slightly higher hardness and ultimate tensile strength. Regarding now the 42CrMo4-725-CG steel grade, it is observed that its hardness, yield strength and ultimate tensile strength were lower, but its ductility larger, in accordance with the higher tempering temperature and time used with this grade.

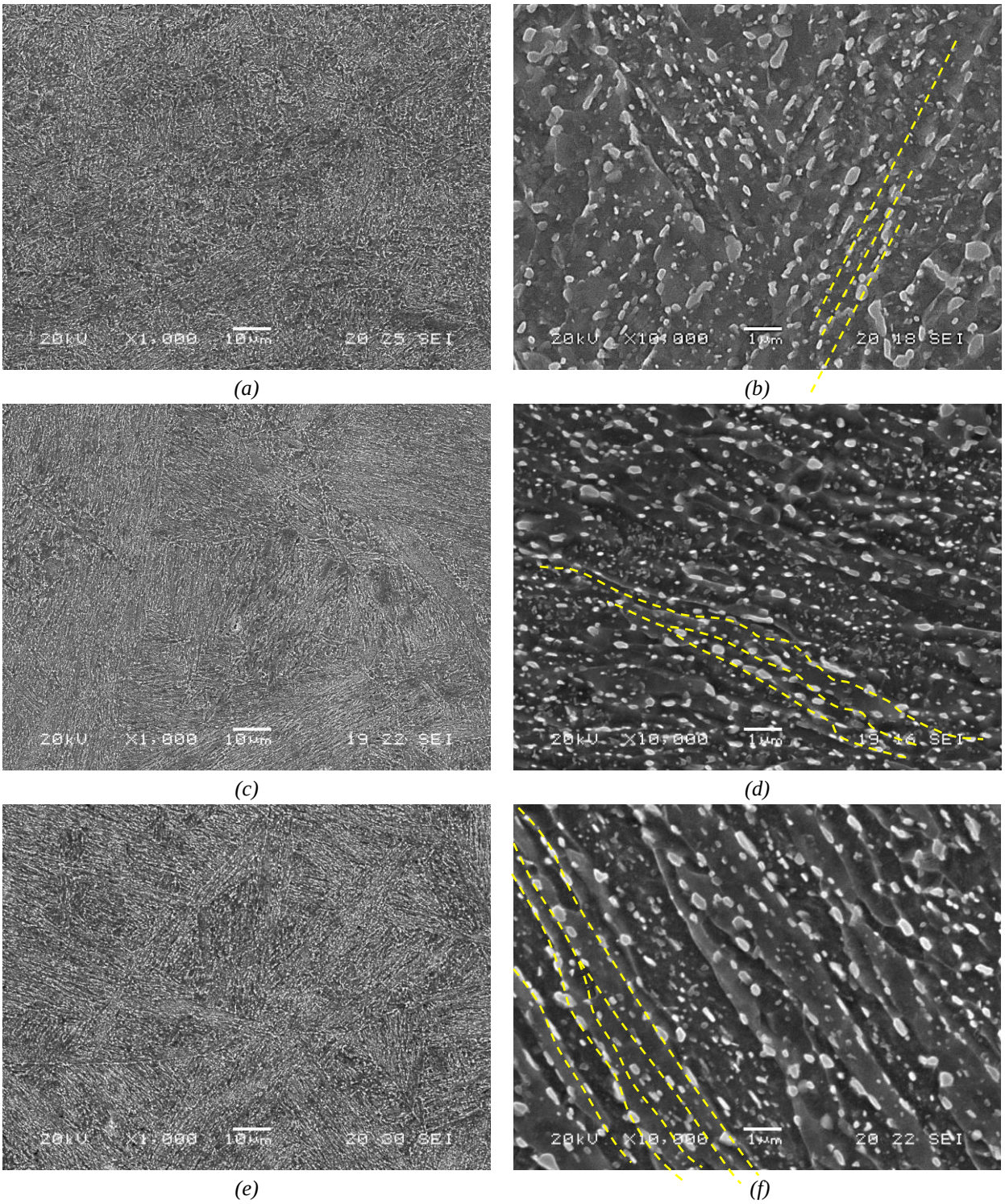

Figure 4.8. SEM microstructures of the 42CrMo4-700 (a ,b) base steel, and the coarse grain steel grades tempered at 700ºC, (c, d) 42CrMo4-700-CG and (e, f) at 725ºC, 42CrMo4-725-CG. Dotted yellow lines show interfaces between martensitic laths.

Steel Grades	Heat treatment	HV30	PAGS [µm]	σ_{ys} [MPa]	σ_{uts} [MPa]	e [%]	RA [%]

42CrMo4-700	845ºC/40min+WQ+T700ºC/2h	223±2	20	622±2	710±5	22.6±0.6	62.8±1.7
42CrMo4-700-CG	1200ºC/20min+OQ+T700ºC/2h	230±2	100-150	602±3	749±1	22.4±1.7	63.9±2.3
42CrMo4-725-CG	1200ºC/20min+OQ+T725ºC/4h	208±2	100-150	498±6	665±7	23.9±0.9	70.2±0.2

Table 4.2. Heat treatment, hardness (HV30), PAGS, and tensile properties of the base steel (42CrMo4-700) and the two different coarse grain steel grades (42CrMo4-700-CG and 42CrMo4-725-CG) studied in this work.

4.2.4. Hardening by cold rolling

The values of Vickers hardness, HV30, measured in the cold rolled samples of 42CrMo4-700 and 42CrMo4-700-CG steel grades are collected in Table 4.3. Note the very low scatter of these hardness results, which indicates that a considerably homogeneous microstructure was obtained after the rolling process. As an example, Figure 4.9 shows the microstructure (longitudinal section) of 42CrMo4-700 after a thickness reduction of 80%, in which a remarkable microstructural distortion is noticed. No significant microstructural difference was observed along the cross-section direction.

Thickness reduction [%]	Equivalent plastic strain ε_{peq}	42CrMo4-700	42CrMo4-700-CG
		HV30	HV30
0	0	223±2	230±2
10	0.11	244±1	257±1
20	0.22	259±2	271±3
30	0.36	270±1	283±2
50	0.69	298±2	311±1
67	1.11	316±1	330±3
80	1.61	335±3	340±1

Table 4.3. Vickers hardness (HV30) and equivalent plastic strain (ε_{peq}) of cold rolled 42CrMo4-700 and 42CrMo4-700-CG steel grades.

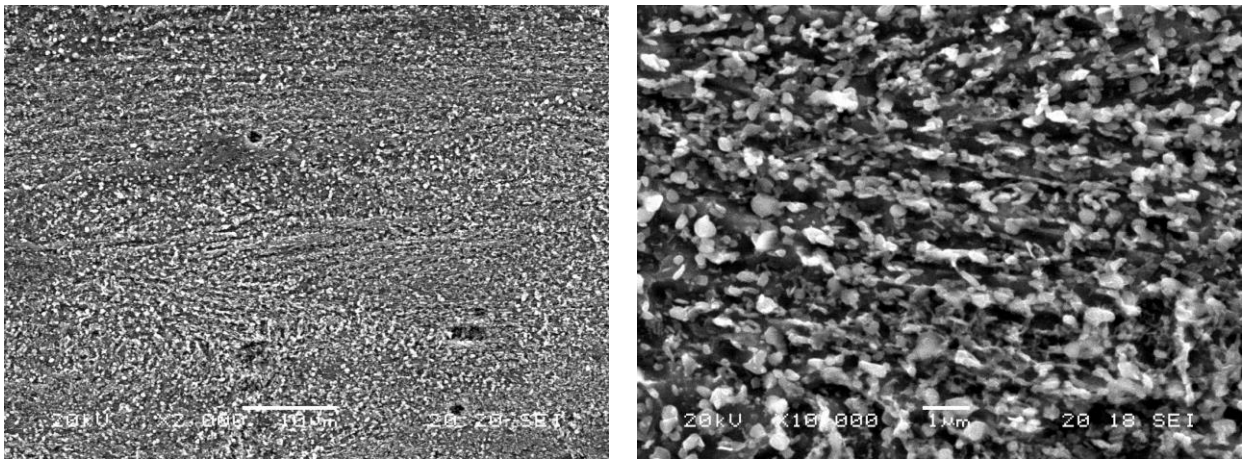

(a) (b)

Figure 4.9. SEM microstructures of 42CrMo4-700 after a thickness reduction of 80% (longitudinal section).

As it can be observed in Figure 4.10, a good linear correlation can be established between HV30 hardness and thickness reduction (plastic deformation). Similarly to the hardness value of the

undeformed samples, the base 42CrMo4-700 steel, presents lower hardness values than the coarse grain steel up to a thickness reduction of 80%, where hardness seem to attain nearly similar values. The significant increase in hardness provided by cold rolling can be mostly associated with an increase in dislocation density (work hardening) [239].

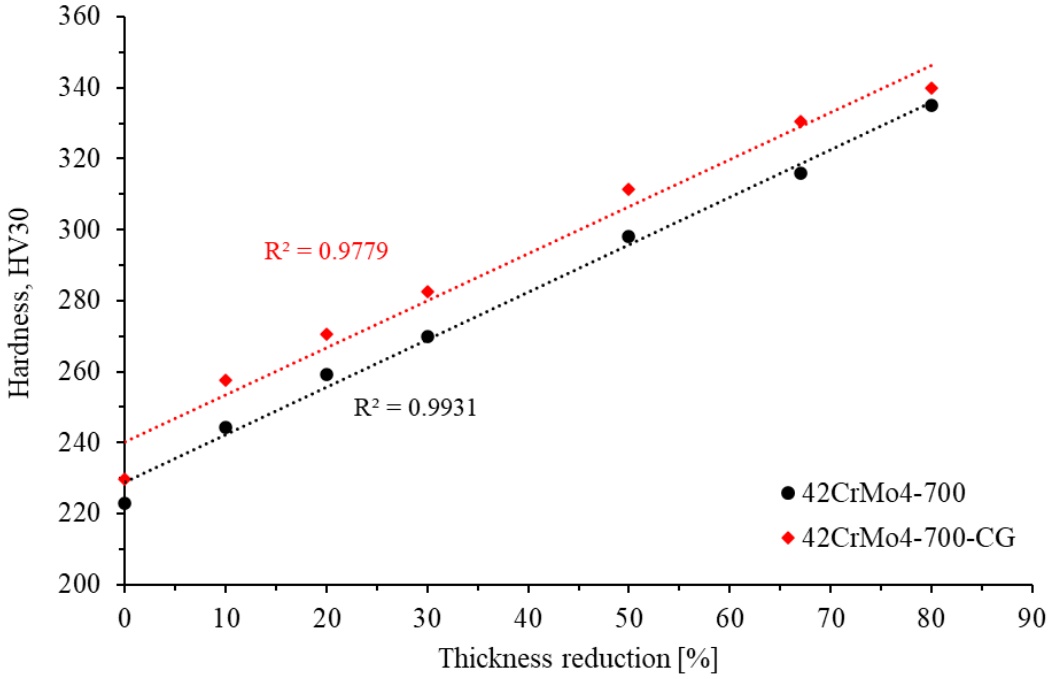

Figure 4.10. Linear correlation between HV30 hardness and applied thickness reduction. Base steel and coarse grain grade both tempered at 700ºC.

In fact, when log(HV30) versus the equivalent plastic strain, ε_{peq}, is represented as shown in Figure 4.11, data follow an exponential function of the form: $log(HV30) = A - B\ exp(C \cdot \varepsilon_{peq})$.

$$Log(HV30) = 2.53 - 0.18\ exp(-1.64 \cdot \varepsilon_{peq}) \quad 42CrMo4 - 700$$

$$Log(HV30) = 2.54 - 0.17\ exp(-2.09 \cdot \varepsilon_{peq}) \quad 42CrMo4 - 700 - CG$$

As it will be shown in the following chapter, this trend is very similar to that observed by some authors [240,241] between log(N_t) and ε_{peq}, (being N_t the density of hydrogen traps), which can confirm hardness to constitute a reliable indicator of the dislocation density present in these steels, associated to hydrogen traps in these specific grades.

It is interesting to point out the hardness tendency to stabilize at high values of the applied equivalent plastic strain ($\varepsilon_{peq} > 1$), which indicates that the steel's hardening capability, and thus, the capacity to increase the dislocation density of the steel and hydrogen trapping has a limit.

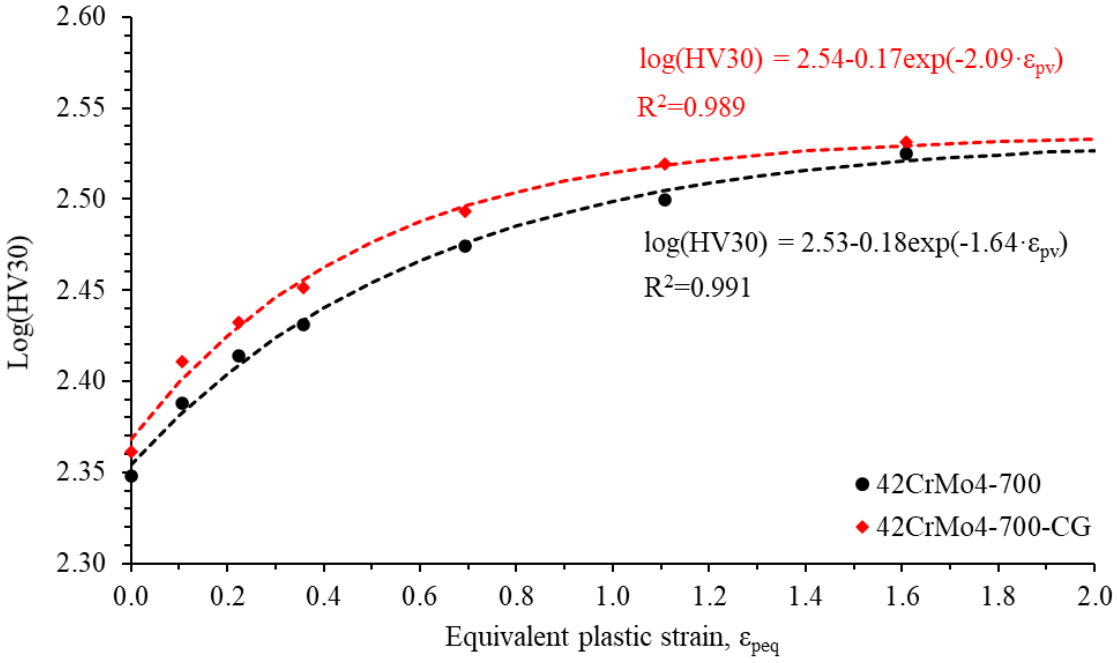

Figure 4.11. Log(HV30) versus ε_{peq} and exponential fits. 42CrMo-700 and 42CrMo4-700-CG steel grades.

4.3. Hydrogen permeation tests

4.3.1. Study on the evolution of the hydrogen diffusion coefficient with the cathodic current density in the 42CrMo4-700 steel grade

Considering 42CrMo4-700 steel grade as an example, Figure 4.12 shows a typical build-up permeation test. The evolution of the permeation current, J_p, obtained in the successive permeation transients produced by sequentially increasing the cathodic current density, J_c, is here shown.

In addition, Table 4.4 provides for this particular test (J_c: 0.5+0.5+1+1+1+1 mA/cm^2), the values of the applied cathodic current density, J_c, and the steady-state permeation current density, J_{ss}, along with the efficiency of the process, η. The apparent hydrogen diffusion coefficient obtained using the time lag value, t_{lag}, (Equation (3.4)) in each transient, D_{app}, and the apparent hydrogen sub-surface cathodic concentration, C_{0app} (Equation (3.5)) are also included in the same table.

Note that an increase in the cathodic current density is always followed by a proportional jump in the steady-state permeation current, reflecting an increase in the subsurface hydrogen concentration on the charging side of the specimen. A fairly uniform D_{app} value was already obtained after the fifth current increment (J_c=4 mA/cm^2).

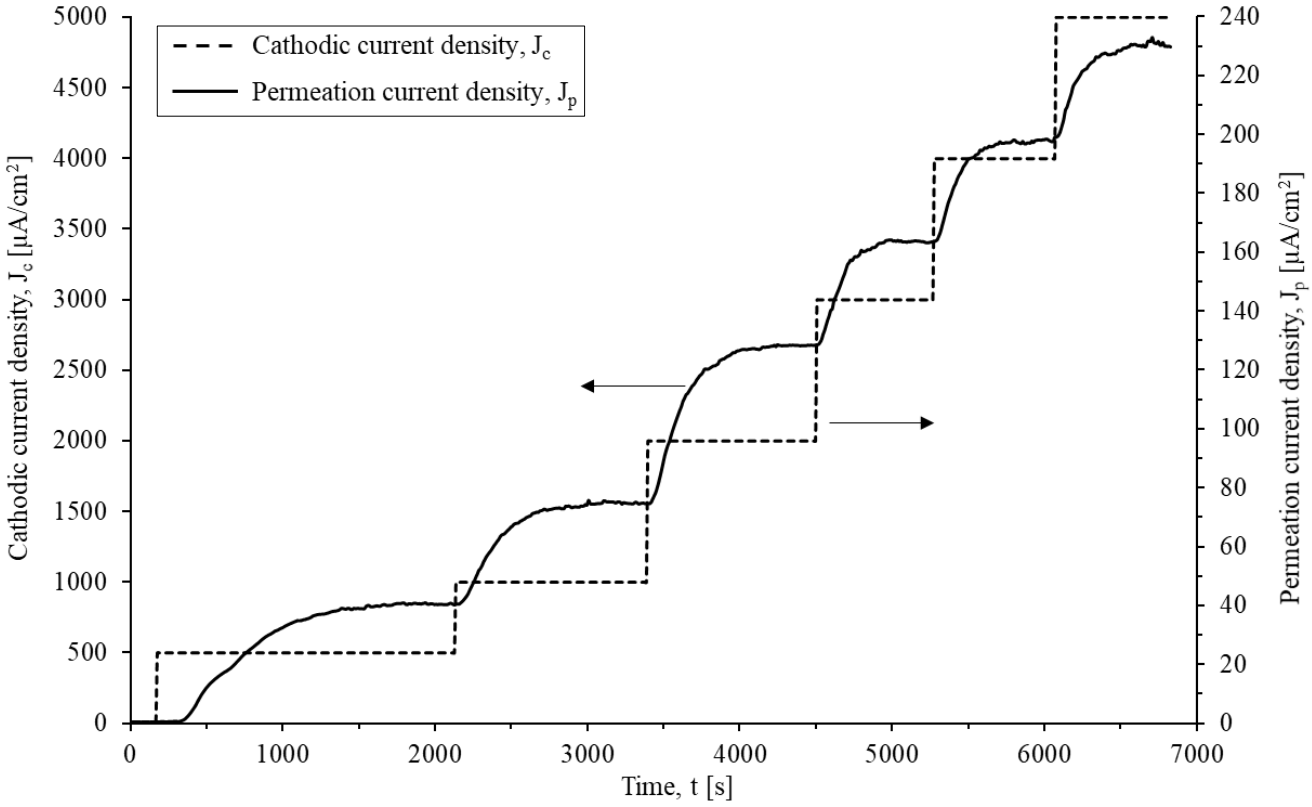

Figure 4.12. Evolution of the permeation current density, J_p, for successive increments of the cathodic current density, J_c, in 42CrMo4-700. Applied J_c: 0.5+0.5+1+1+1+1 mA/cm^2.

Permeation transient	J_c [mA/cm^2]	J_{ss} [µA/cm^2]	η [%]	t_{lag} [s]	D_{app} [m^2/s]	C_{0app} [ppm]
1	0.5	40	7.8	615	2.2×10^{-10}	---
2	1	74	7	270	5.0×10^{-10}	---
3	2	127	6.1	225	6.0×10^{-10}	---
4	3	161	5.2	165	8.2×10^{-10}	2.3
5	4	195	4.7	155	8.7×10^{-10}	2.6
6	5	232	4.5	150	9.0×10^{-10}	3.0

Table 4.4. Values of the cathodic current density, J_c; steady-state permeation current density, J_{ss}; efficiency of the permeation process, η; time lag, t_{lag}; apparent hydrogen diffusion coefficient of each permeation transient, D_{app}; and apparent subsurface hydrogen concentration on the charging side of the specimen, C_{0app}.

The relationship between J_c and J_{ss} represents the efficiency of the permeation process, Equation (3.6), which depends mainly on the hydrogen fugacity in the cathodic face of the specimen. Figure 4.13 provides a graphic representation of the value of η versus the applied cathodic current density. It is noted that the efficiency of the process is considerably low (always below 8%, as an important part of the hydrogen produced, recombines to form the H_2 gas molecule and escapes) and continuously decreases with increasing the applied cathodic current density. This information is useful to establish cathodic charging conditions, where the use of low charging current densities (between 0.5 and 2 mA/cm^2) is the most convenient.

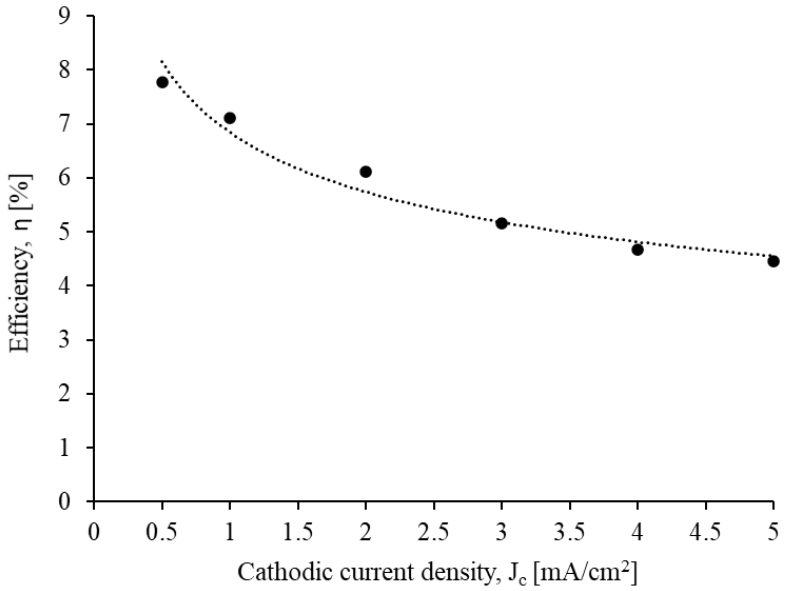

Figure 4.13. Efficiency, η, of the permeation process vs. the applied cathodic current density, J_c. 42CrMo4-700. Applied J_c: 0.5+0.5+1+1+1+1 mA/cm^2.

The results of all the stepped permeation tests carried out under different cathodic current densities with the 42CrMo4-700 steel grade are shown in Figure 4.14, in which the evolution of the apparent hydrogen diffusion coefficient is represented versus the applied cathodic current density.

In accordance with the work carried out by Raina et al. [96], three different regimes can be distinguished depending on trap occupancy: (I) In the first build-up transient, hydrogen traps are empty, and the obtained apparent diffusion coefficient is the lowest. An average value of $2.7\pm0.9\times10^{-10}$ m^2/s was measured under applied J_c values of 0.25-0.5 mA/cm^2, corresponding to hydrogen transport under high interaction of hydrogen atoms with microstructural traps. (II) Hydrogen atoms progressively fill the microstructural traps present in the steel, the effect of traps progressively decreases and, consequently, the D_{app} value increases continuously in this region. (III) Finally, all hydrogen traps become practically saturated and there is no more trapping effect, but only lattice diffusion. Thus, in this last region, the hydrogen diffusion coefficient becomes approximately constant, regardless of the applied cathodic current density. This value corresponds to the lattice hydrogen diffusion coefficient of the steel, D_L. An average D_L value of around 9.0×10^{-10} m^2/s was obtained with the results corresponding to the highest J_c density currents.

It is thus evident that the stepped build-up transient method employed in this study is suitable for studying the hydrogen diffusion evolution with microstructural hydrogen trapping in steels, ultimately allowing the determination of the so-called lattice hydrogen diffusion coefficient, D_L.

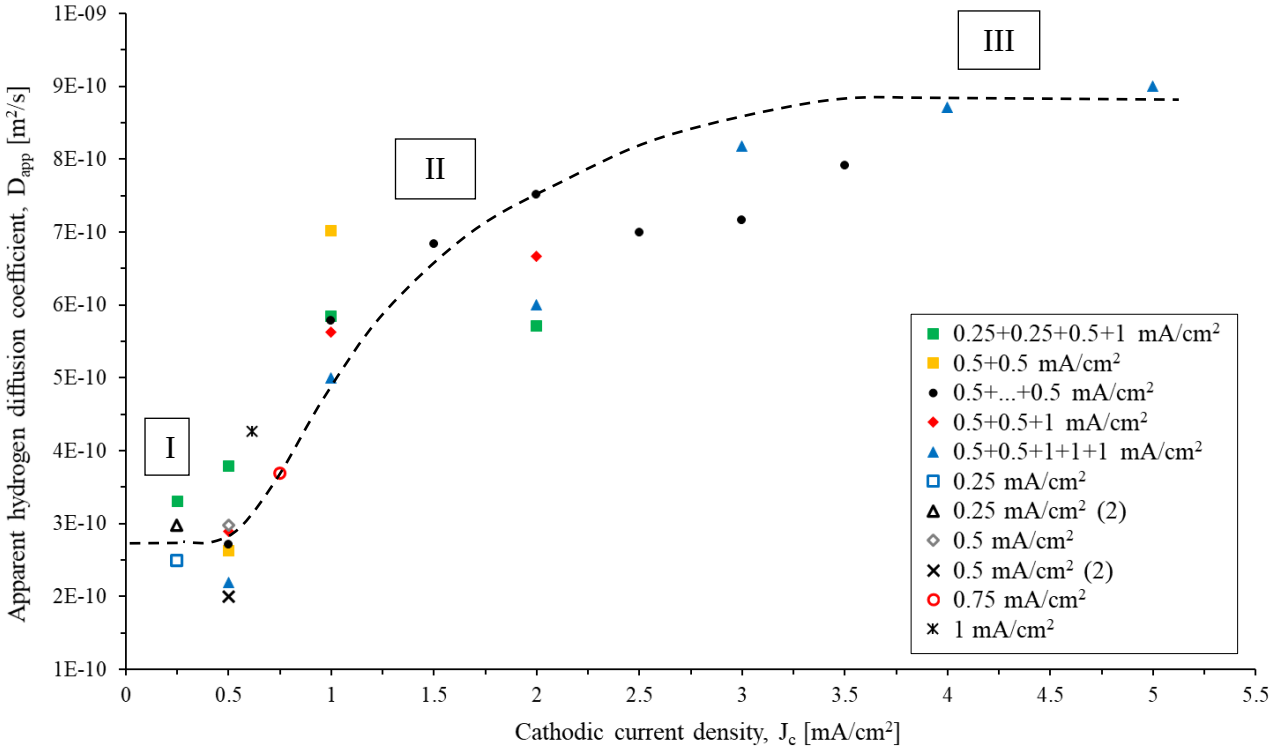

Figure 4.14. Apparent hydrogen diffusion coefficient, D_{app}, vs. the applied cathodic current density, J_c obtained in all the build-up permeation tests performed on 42CrMo4-700 steel grade.

4.3.2. Influence of the tempering temperature

Figure 4.15 shows the results of the stepped build-up permeation tests (J_c = 0.5+0.5+1+1+…+1 mA/cm^2) performed on the different 42CrMo4 steel grades.

Again, the evolution of the permeation current, J_p, in the successive permeation build-up transients obtained when the cathodic current density, J_c, was incrementally increased can be observed in this figure. In the softer grades, tempered at 700ºC and 650ºC, increasing J_c until reaching 5 mA/cm^2 was enough to saturate all their traps; while for the medium-high hardness steel grades, tempered at 600, 550 and 500ºC, it was respectively needed to increase the current density up to 6, 7 and 8 mA/cm^2.

Note that it is difficult to compare the permeation behaviour between steel grades from the curves shown in Figure 4.15, mainly due to the effect of the sample thickness. Different sample thicknesses were tested (between 0.7 and 1 mm) depending on the tempering temperature to avoid excessively long tests. In addition, only the parameters obtained from the first (very low trap occupancy) and last transients (saturation) are used for the determination of the trap density, N_t.

Therefore, in order to compare the permeation behaviour of all these steel grades in the first and last transients, the normalized permeation transients corresponding to an initial cathodic current density of 0.5 mA/cm^2 and the one corresponding to the final applied cathodic current density, when most hydrogen traps were fully filled, are respectively shown in Figure 4.16(a) and (b).

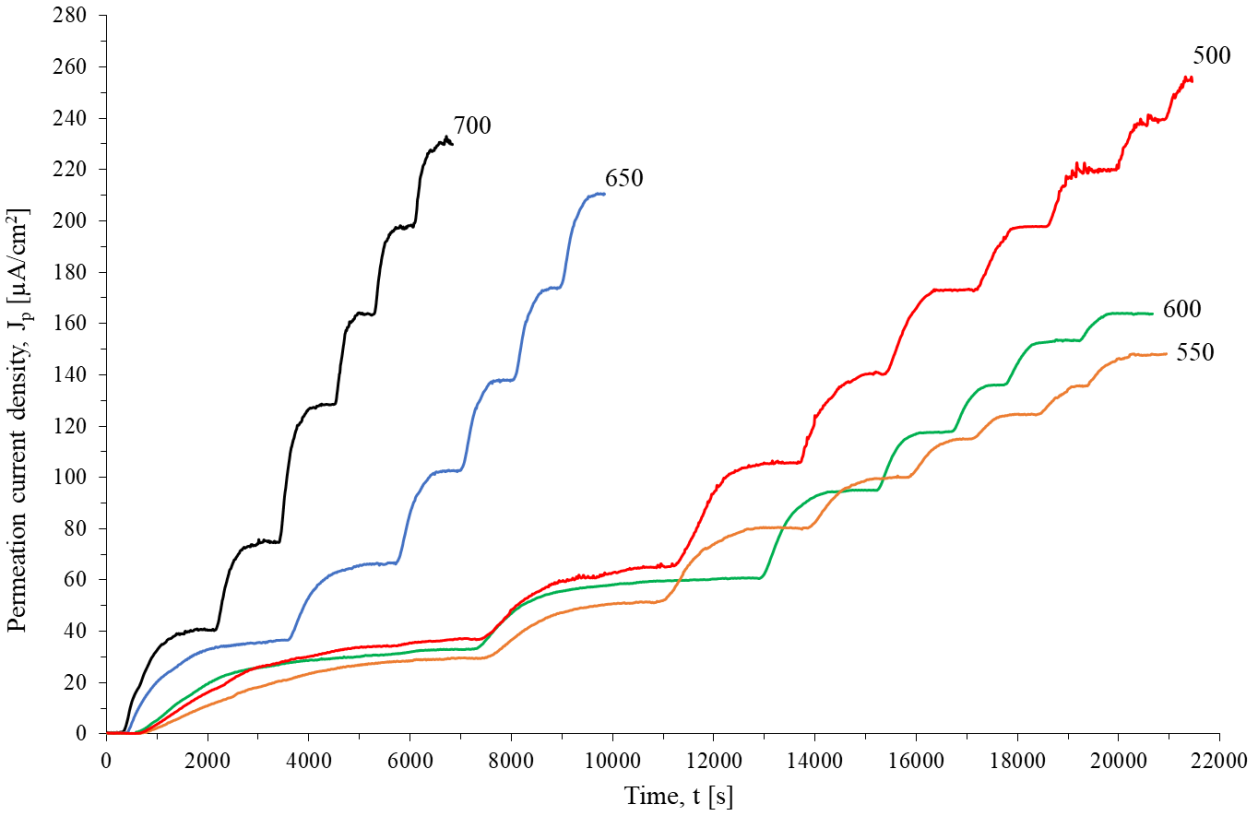

Figure 4.15. Permeation current density measured on the hydrogen stepped build-up transients (J_c: 0.5+0.5+1+1+1+1 mA/cm^2) performed on 42CrMo4 steel quenched and tempered at different temperatures.

In order to remove the dependence of the experimental data on the permeation current density and sample thickness, test results were represented using J_p/J_{ss} vs. t/L^2 coordinates. Thus, the permeation current density was divided by the steady-state permeation current density reached at the end of the respective permeation transient (dimensionless parameter) and time was divided by the square of the sample thickness.

Regarding Figure 4.16(a), it can be clearly observed that the hydrogen permeation flux (hydrogen transport) is progressively delayed as the tempering temperature of the steel decreases (increase in dislocation density and, consequently, hydrogen traps and hardness).

Regarding now the situation when most hydrogen traps are filled, the permeation curves shown in Figure 4.16(b) reveal that the dependence of the hydrogen permeation flux on the tempering temperature is similar but weaker than the former one. When most hydrogen traps are filled, the effect of hydrogen traps on hydrogen transport reduces.

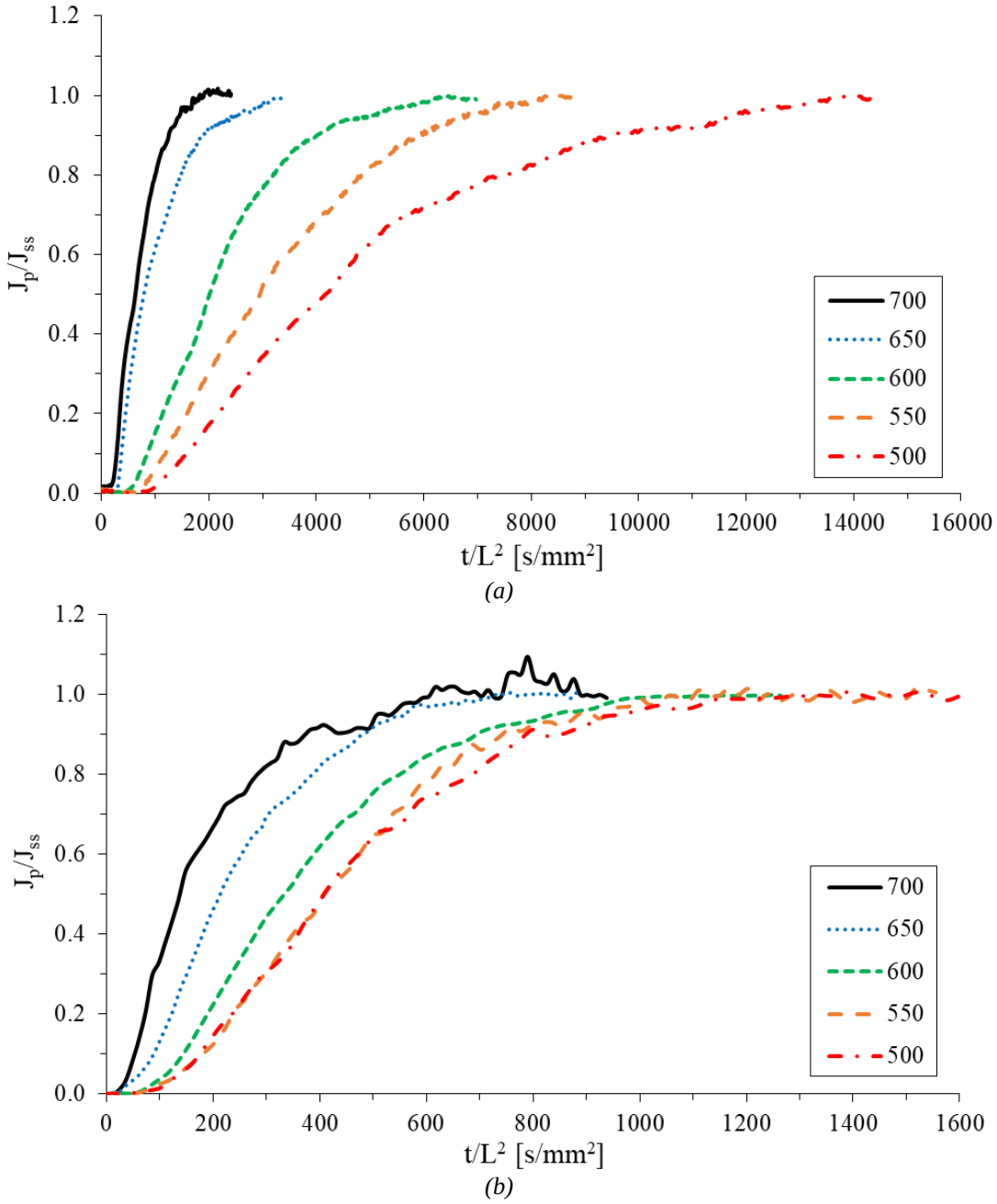

Figure 4.16. Normalized permeation curves of (a) the first (Jc = 0.5 mA/cm^2, empty traps) and (b) the last (traps fully filled) permeation transients in all the 42CrMo4 steel grades.

The permeation parameters t_{lag}, D_{app}, % saturation (based on D_{app}), and C_{0app} calculated on all these transients are jointly presented in Table 4.5.

Moreover, the entire set of data corresponding to all the experimental build-up permeation tests carried out under different cathodic current density transients applied to all the 42CrMo4 steel grades is shown in Figure 4.17, where the evolution of the apparent hydrogen diffusion coefficient, D_{app}, is represented versus the applied cathodic current density, J_c.

Steel Grade	Thickness, L [mm]	Permeation transient	J_c [mA/cm^2]	J_{ss} [μA/cm^2]	t_{lag} [s]	D_{app} [m^2/s]	Saturation [%]	C_{0app} [ppm]
42CrMo4-700	0.90	1	0.5	40	615	2.2×10^{-10}	24	---
		2	1	74	270	5.0×10^{-10}	56	---
		3	2	127	225	6.0×10^{-10}	67	---
		4	3	161	165	8.2×10^{-10}	91	2.3
		5	4	195	155	8.7×10^{-10}	97	2.6
		6	5	232	150	9.0×10^{-10}	100	3.0
42CrMo4-650	1.01	1	0.5	36	1030	1.7×10^{-10}	26	---
		2	1	66	510	3.3×10^{-10}	52	---
		3	2	103	380	4.5×10^{-10}	70	---
		4	3	138	296	5.7×10^{-10}	90	3.2
		5	4	174	268	6.3×10^{-10}	99	3.6
		6	5	210	266	6.4×10^{-10}	100	4.4
42CrMo4-600	0.96	1	0.5	33	1992	7.7×10^{-11}	17	---
		2	1	63	1056	1.5×10^{-10}	32	---
		3	2	98	594	2.6×10^{-10}	57	---
		4	3	121	408	3.8×10^{-10}	82	---
		5	4	140	348	4.4×10^{-10}	97	4.0
		6	5	158	360	4.3×10^{-10}	93	4.7
		7	6	169	336	4.6×10^{-10}	100	4.7
42CrMo4-550	0.90	1	0.5	30	2955	4.6×10^{-11}	13	---
		2	1	51	1192	1.1×10^{-10}	33	---
		3	2	80	870	1.6×10^{-10}	46	---
		4	3	100	638	2.1×10^{-10}	62	---
		5	4	115	480	2.8×10^{-10}	83	---
		6	5	125	398	3.4×10^{-10}	100	4.4
		7	6	136	510	3.2×10^{-10}	100	5.1
		8	7	148	405	3.3×10^{-10}	100	5.3
42CrMo4-500	0.70	1	0.5	37	2430	3.4×10^{-11}	9	---
		2	1	65	1155	7.1×10^{-11}	18	---
		3	2	106	763	1.1×10^{-10}	27	---
		4	3	141	540	1.5×10^{-10}	39	---
		5	4	173	480	1.7×10^{-10}	43	---
		6	5	198	360	2.3×10^{-10}	58	---
		7	6	220	225	3.6×10^{-10}	93	5.6
		8	7	240	215	3.8×10^{-10}	98	5.8
		9	8	255	210	3.9×10^{-10}	100	6.0

Table 4.5. Results obtained from the permeation curves shown in Figure 4.15 for the different 42CrMo4 grades.

As described above for 42CrMo4-700 steel grade, three different hydrogen diffusion regimes may be distinguished in all these steel grades, depending on trap occupancy. Regime I, characterized by low trap occupancy; regime II, in which traps are progressively filled; and regime III, where most traps are saturated with hydrogen.

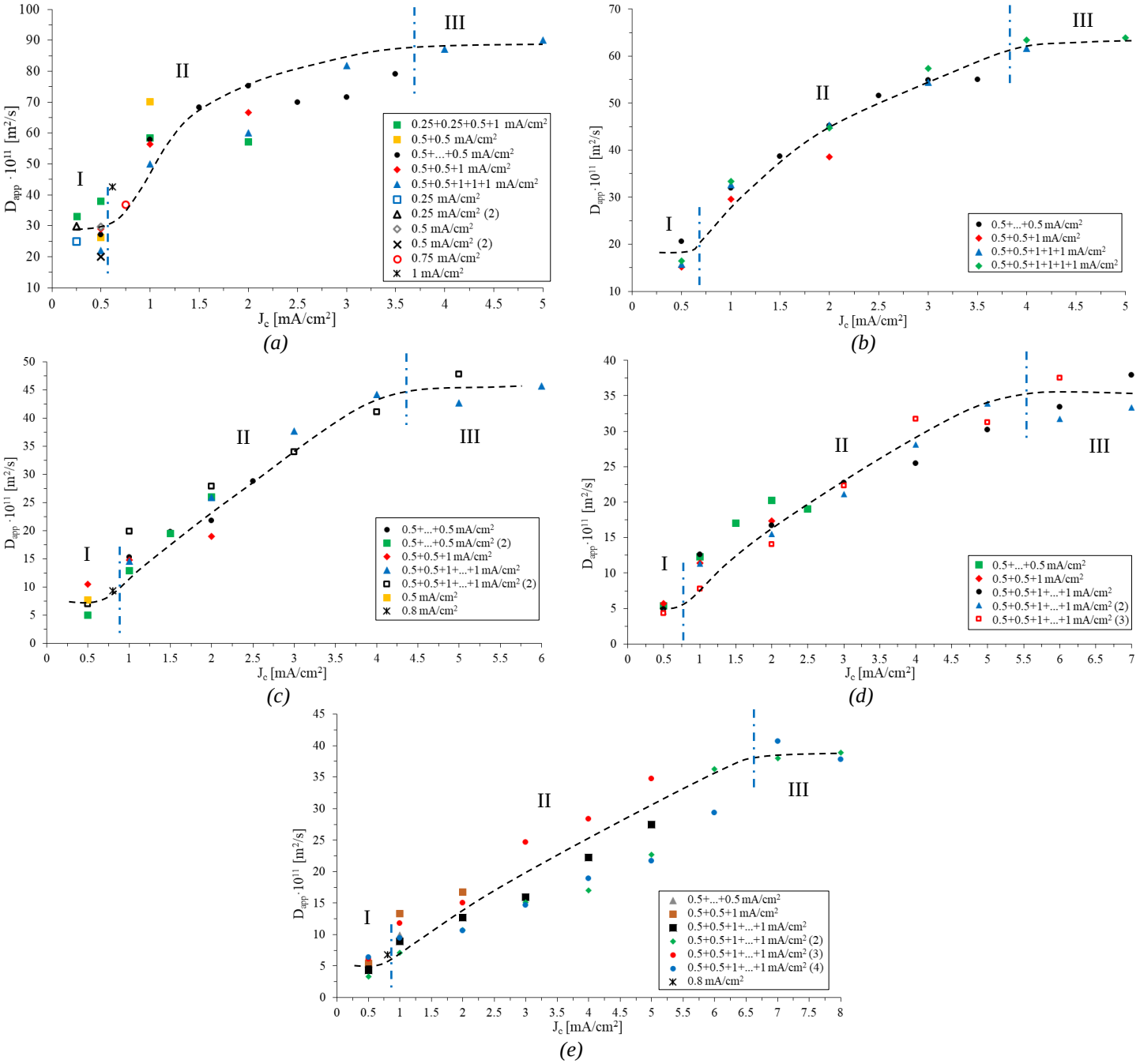

Figure 4.17. Evolution of the apparent hydrogen diffusion coefficient, D_{app}, with the applied cathodic current density, J_c, obtained in all the build-up permeation tests performed on the 42CrMo4 steel grade quenched and tempered at (a) 700, (b) 650, (c) 600, (d) 550 and (e) 500ºC.

Figure 4.18 represents the average values of D_{app} showed in Figure 4.17 on a plot of D_{app} vs. J_c. The apparent diffusion coefficient increases with increasing the applied cathodic current density and, at the same time, it also increases for any current density when the steel is tempered at a higher temperature.

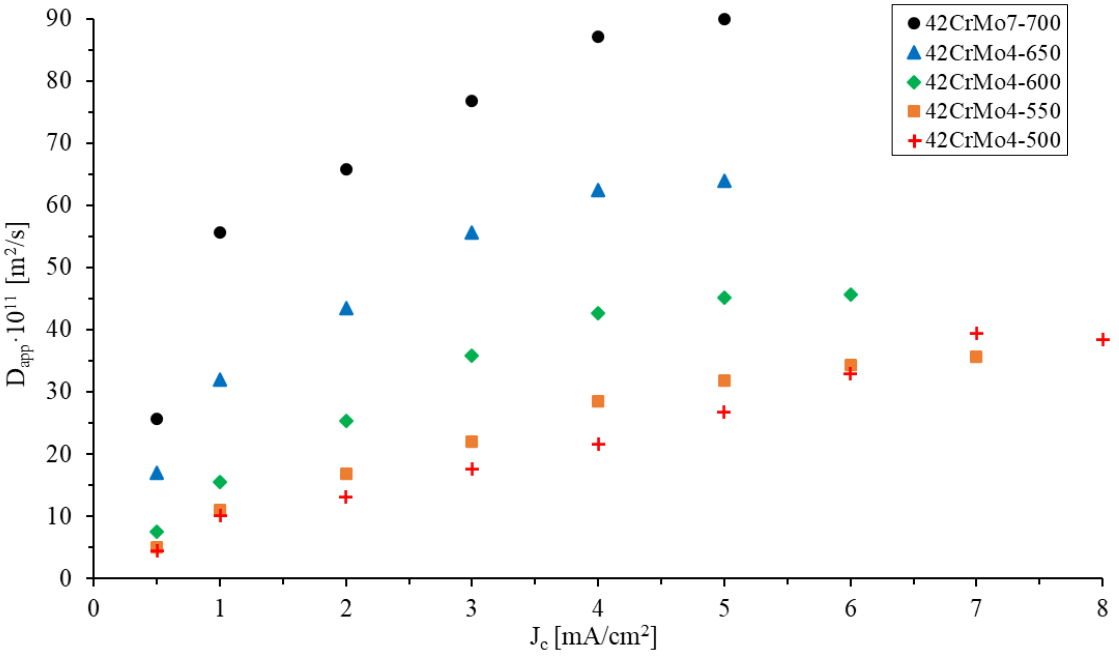

Figure 4.18. Representation of D_{app} vs. J_c for all the studied 42CrMo4 steel grades (average values taken from Figure 4.17).

Finally, in order to provide a summary with a quantitative visualization of the obtained results, Table 4.3 presents the values of D_{app}, determined under a very low cathodic current density, 0.5 mA/cm^2, when most traps are empty and those of the lattice hydrogen diffusion coefficient, D_L, once trap saturation is reached under a certain cathodic current density level. The J_c values needed for hydrogen saturation are also included in this table.

Steel Grade	HV30	D_{app} [m^2/s]	D_L [m^2/s]	J_c saturation [mA/cm^2]	C_{0app} [ppm]
42CrMo4-700	223	$2.7\pm0.9\times10^{-10}$	$8.9\pm0.2\times10^{-10}$	3-4	2.4
42CrMo4-650	275	$1.7\pm0.2\times10^{-10}$	$6.3\pm0.1\times10^{-10}$	4	3.6
42CrMo4-600	304	$7.5\pm1.8\times10^{-11}$	$4.5\pm0.3\times10^{-10}$	4-5	4.3
42CrMo4-550	344	$5.0\pm0.6\times10^{-11}$	$3.5\pm0.3\times10^{-10}$	6	5.1
42CrMo4-500	367	$4.4\pm0.8\times10^{-11}$	$3.9\pm0.1\times10^{-10}$	7	5.8

Table 4.6. Average apparent (D_{app}) and lattice (D_L) hydrogen diffusion coefficients, cathodic current density (J_c) at saturation, and apparent subsurface hydrogen concentration on the charging side of the specimen also at saturation, C_{0app}, of each 42CrMo4 steel grade.

It can be seen that both diffusion parameters, D_{app} and D_L, decrease with decreasing tempering temperature. In fact, the D_{app} and D_L values of the steel grade tempered at 700ºC are respectively around 6 and 2 times greater than those of the steel tempered at 500ºC. Furthermore, the harder steel grades need a significantly higher cathodic current density to reach saturation, i.e., more hydrogen may be generated on the cathodic side of the specimen to fill all their microstructural traps, as indicates the evolution of the average C_{0app} calculated when all traps are saturated.

Table 4.7 presents the density of trapping sites, N_t, determined in all the studied steel grades considering low trap occupancy, Equation (3.7), and high trap occupancy, Equation (3.9).

Dislocations were assumed to be the governing trapping sites in quenched and tempered martensitic steels. Thus, a trap binding energy E_b of 27.4 kJ/mol (the average value of the E_b column obtained with these steel grades), determined in the TDA analysis (see following chapter), was used to calculate N_t by means of Equation (3.7).

In line with the evolution of C_{0app}, a gradual increase in the density of trapping sites, N_t, is observed when the tempering temperature decreased from 700ºC to 500ºC. However, as slightly different values were obtained using both equations, the last column in Table 4.7 shows the average N_t value.

Steel grade	HV30	Low trap occupancy Equation (3.7)		High trap occupancy Equation (3.9),		Trap density (average)
		E_b [kJ/mol]	N_t [sites/m^3]	C_{0app} [ppm]	N_t [sites/m^3]	N_t [sites/m^3]
42CrMo4-700	223	27.2	1.8×10^{25}	2.4	2.7×10^{25}	2.3×10^{25}
42CrMo4-650	275	27.1	2.2×10^{25}	3.6	6.1×10^{25}	4.1×10^{25}
42CrMo4-600	304	27.5	4.0×10^{25}	4.3	1.0×10^{26}	7.2×10^{25}
42CrMo4-550	344	27.6	4.8×10^{25}	5.1	1.6×10^{26}	1.0×10^{26}
42CrMo4-500	367	27.7	6.3×10^{25}	5.8	1.6×10^{26}	1.1×10^{26}

Table 4.7. Density of trapping sites, N_t, calculated on the different steel grades

Figure 4.19 shows the relationship between the steel hardness, HV30, the value of the apparent hydrogen diffusion coefficient, D_{app}, for low trap occupancy (first permeation transient using 0.5 mA/cm^2, in which most traps are empty), the lattice hydrogen diffusion coefficient, D_L, when the microstructural traps were saturated with hydrogen (last permeation transients) and the value of the apparent sub-surface hydrogen concentration on the charging side of the specimen, C_{0app}, when the specimen has reached saturation (J_c saturation).

Note the excellent correlation between the aforementioned permeation properties and the hardness of the different steel grades. Hydrogen diffusivity decreases and hydrogen solubility increases continuously with the hardness of the steels, which is in line with the results reported previously by other authors [49,73]. This behaviour can be explained taking into account the higher density of lattice imperfections, mainly dislocations, associated with hardness in quenched and tempered steels, which constitute the most significant structural parameter governing hydrogen diffusion and trapping in these steels.

Finally, Figure 4.20 shows the relationship between HV30 and the density of hydrogen trapping sites, N_t. Both Equation (3.9), for high trap occupancy, and Equation (3.7), for low trap occupancy, show that N_t values increase with increasing hardness (increase in dislocation density). The average value of trap density, N_t, obtained using the results calculated by means of both equations, was also plotted in Figure 4.20. It is observed the good linear fitting (R^2=0.97) of the average of N_t versus HV30.

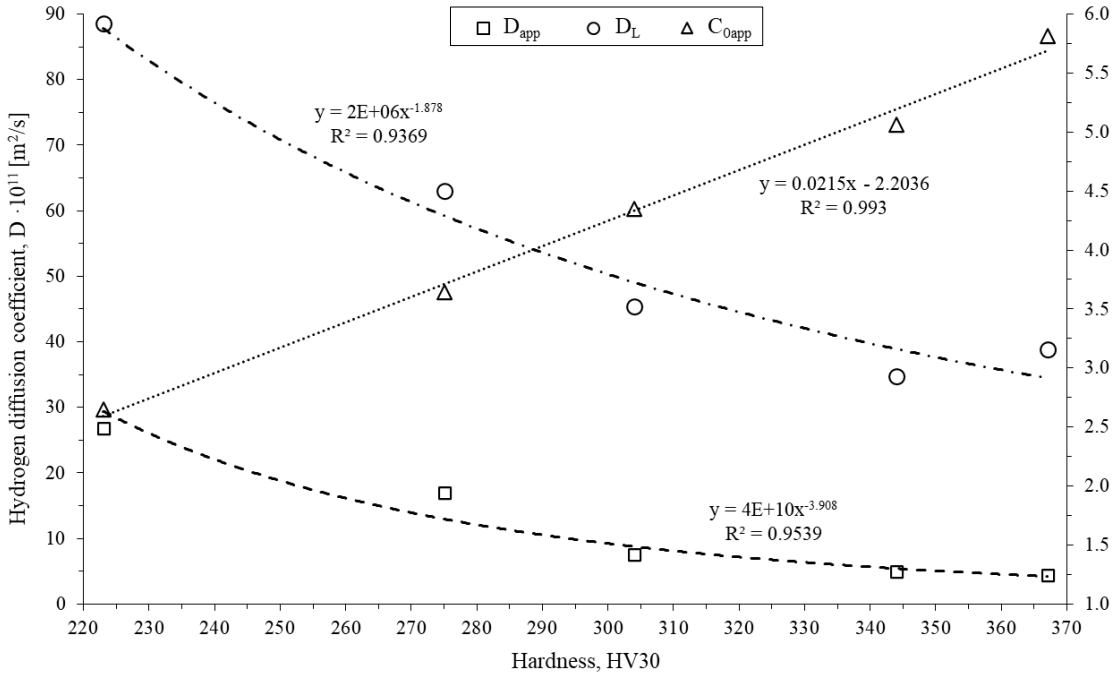

Figure 4.19. Relationship between HV30, lattice and apparent hydrogen diffusion coefficients, D_L and D_{app}, and apparent sub-surface hydrogen concentration, C_{oapp}, for all the 42CrMo4 steel grades.

It is interesting to note as well, that the value of N_t calculated according to Equation (3.9) for the steel tempered at 550 and 550 is exactly the same, which is in line with the diffusion behaviour observed in Figure 4.18, where the curves of these two grades tended to overlap. This means that the hardening degree suffered during the heat treatment of both microstructures is practically the same, and therefore a similar behaviour regarding hydrogen embrittlement is expected.

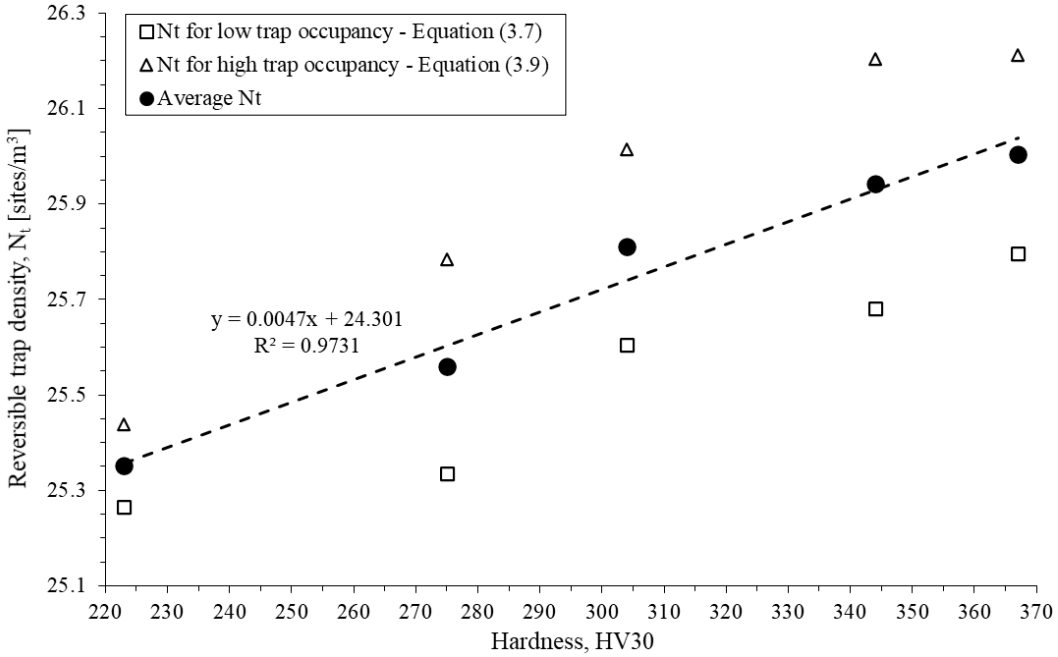

Figure 4.20. Relationship between HV30 and hydrogen trap density sites, N_t. Low trap occupancy (Equation 3.7, E_b=27.4 kJ/mol), high trap occupancy (Equation 3.9) and average trap density.

4.3.3. Hydrogen diffusion and trapping in the CGHAZ of a 42CrMo4 weld

In order to compare the behaviour of the fine grain, 42CrMo4-700, and the two different coarse grain steel grades, 42CrMo4-700-CG and 42CrMo4-725-CG, the permeation curves corresponding to the stepped build-up transients obtained under cathodic current density increments of 0.5+0.5+1+…+1 mA/cm^2 are shown in Figure 4.21. Additionally, Table 4.8 provides the values of the applied cathodic current density, J_c, the steady-state permeation current density, J_{ss}, the apparent hydrogen diffusion coefficient obtained in each transient, D_{app}, and the apparent hydrogen sub-surface cathodic concentration calculated on the charging side of the specimen, C_{0app} (remember that C_{0app} can only be accurately calculated when D_{app} reaches a steady value; that is in the last transients).

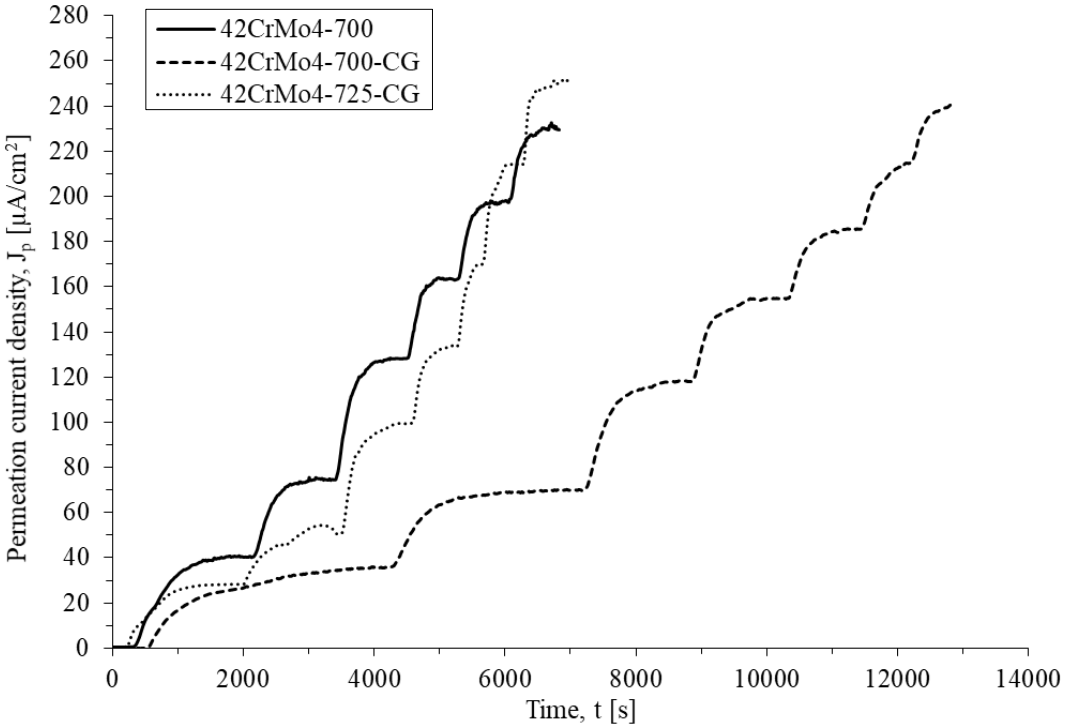

Figure 4.21. Stepped permeation transients of base (42CrMo4-700) and coarse-grained (42CrMo4-700-CG, 42CrMo4-725-CG) steel grades. Applied J_c: 0.5+0.5+1+…+1 mA/cm^2.

Note that the permeation curve of the coarse grain steel 42CrMo4-700-CG is slightly delayed with respect to the other two, the fine grain 42CrMo4-700 and the coarse grain 42CrMo4-725-CG. In fact, the measured value of D_{app} in this particular test is lower in the coarser grain microstructure of 42CrMo4-700-CG for all the applied cathodic current densities, while the C_{0app} values are higher. Quenching the steel from a higher austenitizing temperature (higher thermal drop) yields a coarser, more distorted martensitic structure, with higher internal stresses and hence a higher dislocation density. These differences are maintained after the final tempering treatment, thereby explaining the aforementioned results. In line with our results, Wang et al. [114] also measured a lower hydrogen diffusion coefficient, along with higher dislocation density and structural distortion, as quenching temperature is increased (larger austenite grain size) in a CrMoV steel quenched and tempered at 700ºC. On the other hand, applying a greater temperature

during a longer time in the tempering treatment (42CrMo4-725-CG), over-tempering treatment, seems to bring diffusivity and hydrogen content to similar levels than the ones of the base steel grade (42CrMo4-700).

Steel Grade	Thickness, L [mm]	J_c [mA/cm^2]	J_{ss} [μA/cm^2]	t_{lag} [s]	D_{app} [m^2/s]	Saturation [%]	C_{0app} [ppm]
42CrMo4-700	0.90	0.5	40	615	2.2×10^{-10}	24	---
		1	74	270	5.0×10^{-10}	56	---
		2	127	225	6.0×10^{-10}	67	---
		3	161	165	8.2×10^{-10}	91	2.3
		4	195	155	8.7×10^{-10}	97	2.6
		5	232	150	9.0×10^{-10}	100	3.0
42CrMo4-700-CG	1.07	0.5	36	1232	1.5×10^{-10}	19	---
		1	70	528	3.6×10^{-10}	44	---
		2	117	388	4.9×10^{-10}	60	---
		3	155	288	6.6×10^{-10}	81	---
		4	186	256	7.4×10^{-10}	91	3.5
		5	215	234	8.1×10^{-10}	99	3.7
		6	241	232	8.2×10^{-10}	100	4.1
42CrMo4-725-CG	0.91	0.5	28	500	2.8×10^{-10}	20	---
		1	50	490	3.9×10^{-10}	29	---
		2	99	190	7.3×10^{-10}	53	---
		3	134	140	9.9×10^{-10}	71	---
		4	170	117	1.2×10^{-9}	85	---
		5	214	105	1.3×10^{-9}	95	2.0
		6	251	100	1.4×10^{-9}	100	2.2

Table 4.8. Influence of prior austenite grain size on stepped permeation transients under applied J_c values of 0.5+0.5+1+...+1 mA/cm^2. Current density, J_c; steady-state permeation current density, J_{ss}; apparent hydrogen diffusion coefficient of each permeation transient, D_{app}, and apparent subsurface hydrogen concentration on the charging side of the specimen, C_{0app}.

Figure 4.22, which (similarly to Figure 4.17) shows the evolution of the apparent hydrogen diffusion coefficient in terms of the applied cathodic current density, gathers all the data obtained with all the permeation tests performed on the coarse-grained steel grades, 42CrMo4-700-CG and 42CrMo4-725-CG, using different cathodic current densities. As for the previous studied steel grades, three different hydrogen diffusion regimes can be also distinguished in the coarse grain microstructures, depending on trap occupancy. Regime I, characterized by low trap occupancy; regime II, in which traps are progressively filled; and regime III, where most traps are saturated with hydrogen. Therefore, this is the general behaviour expected in ferritic steels with microstructural hydrogen traps.

Figure 4.23 compares the evolution of D_{app} values with the cathodic current density of the fine grain base steel and the two coarse grain grades. As it was mentioned before, the results relative to 42CrMo4-700-CG fall slightly below those of 42CrMo4-700 steel grade, as this microstructure has a lower diffusivity. On the other hand, D_{app} values of 42CrMo4-725-CG are very similar to those of the base fine grain steel up to 3 mA/cm^2, and from this point on, the diffusivity measured

in this particular coarse grain over-tempered steel (42CrMo4-725-CG) attains considerably greater values, giving rise to considerably higher D_L in this case ($1.4\pm0.1\times10^{-9}$ m^2/s). This result is justified by the more intense tempering treatment (725ºC for 4 hours) performed in this steel grade, which increases defects annihilation, therefore decreasing dislocation density and internal stresses. A qualitative summary of the permeation parameters obtained with these grades is included in Table 4.9 (average values), where the already described behaviour is clearly appreciated.

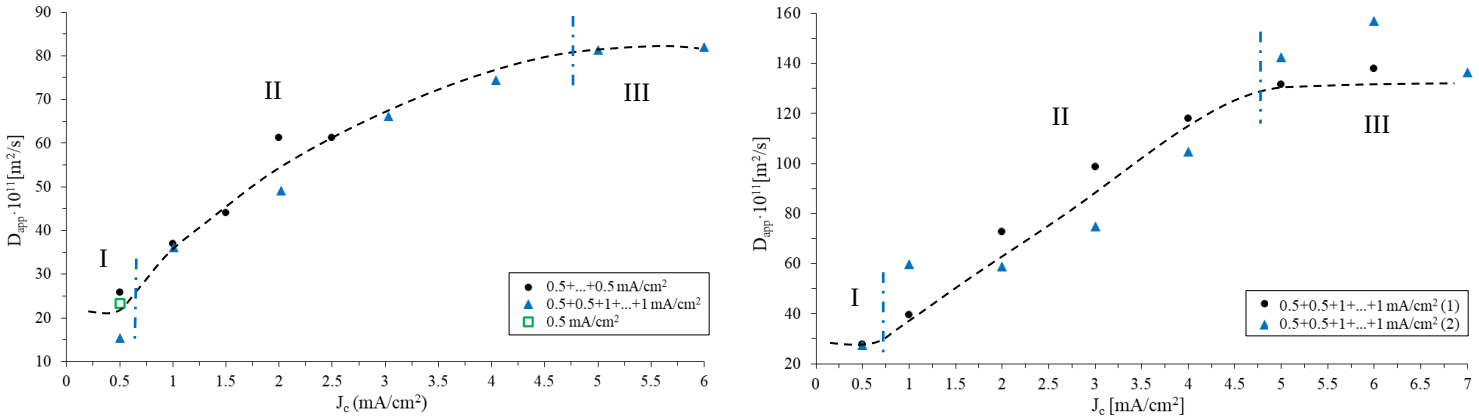

(a) *(b)*

Figure 4.22. Evolution of the apparent hydrogen diffusion coefficient, D_{app}, vs. the applied cathodic current density, J_c. Coarse grain steel grades (a) 42CrMo4-700-CG and (b) 42CrMo4-725-CG.

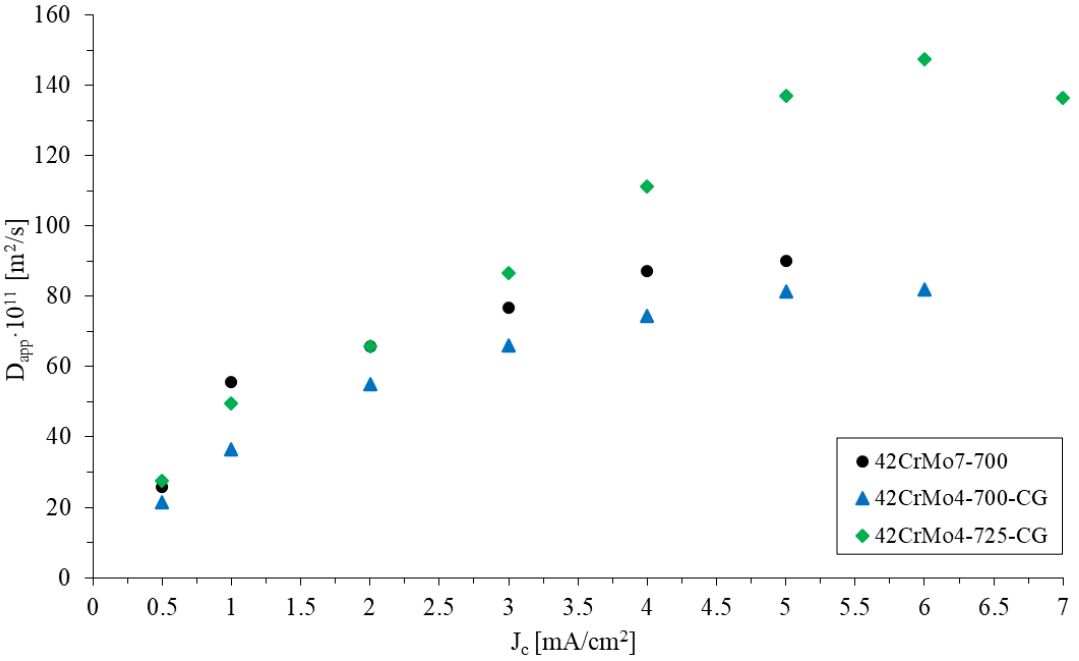

Figure 4.23. Comparison (D_{app} vs. J_c) of the fine (42CrMo4-700) and the coarse grain (42CrMo4-700-CG and 42CrMo4-725-CG) microstructures (average values taken from Figure 4.22).

Steel Grade	HV30	PAGS [µm]	D_{app} [m^2/s]	D_L [m^2/s]	J_c saturation [mA/cm^2]	C_{0app} [ppm]
42CrMo4-700	223	20	$2.7\pm0.9\times10^{-10}$	$8.9\pm0.2\times10^{-10}$	3-4	2.4

42CrMo4-700-CG	230	100-150	$2.2\pm0.5\times10^{-10}$	$8.1\pm0.1\times10^{-10}$	5	3.7
42CrMo4-725-CG	208	100-150	$2.8\pm0.1\times10^{-10}$	$1.4\pm0.1\times10^{-9}$	5	2.1

Table 4.9. Average apparent (D_{app}) and lattice (D_L) hydrogen diffusion coefficients, cathodic current density for saturation (J_c) and apparent subsurface hydrogen concentration on the charging side of the specimen, C_{0app}, of base fine grain and coarse grain steel grades.

Once D_{app}, D_L and C_{0app}, are known, it is now possible to calculate the trap occupancy, or density of trapping sites. Table 4.10 presents the values of N_t determined on the three steel grades using Equation (3.7) and Equation (3.9). An increase in the density of trapping sites in the coarse grain steel (42CrMo4-700-CG) was obtained. Furthermore, taken an approximate and hypothetical single trap binding energy, E_b=26.8 kJ/mol (determined with this steel grade) in Equation (3.7), the density of hydrogen trapping sites obtained using both equations was quite similar. The average value of N_t is also presented in Table 4.10. On the other hand, in the case of 42CrMo4-725-CG, the values of N_t obtained with both methods differ considerably. Considering the approach relative to high trap occupancy (Equation (3.9)), that only make use of the parameters determined in permeation tests, the N_t value is the lowest of the three steel grades, which is in line with the more intense tempering treatment (725ºC for 4h) and associated microstructural recovery. The unrealistic value of N_t obtained with Equation (3.7) in this grade may be due to a limited accuracy of the desorption calculations (as will be explained in the following chapter) carried out for the estimation of E_b. In addition, it should be noted here that most carbides are aligned along martensite lath interfaces (Figure 4.8), where dislocations also concentrate. This makes difficult to separate and differentiate the trapping effects due to carbides, martensite lath, block and packet interfaces and dislocations. The E_b value used here is usually assigned to dislocations but, carbides and internal interfaces co-exist with dislocations on the same location. Therefore, in the case of the over-tempered steel grade, 42CrMo4-725-CG, it also possible that considering a unique trap with E_b of 26.2 kJ/mol may not be accurate enough to obtain a reliable N_t value using the low trap occupancy approach, Equation (3.7).

Steel grade	HV30	PAGS [μm]	Low trap occupancy Equation (3.7)		High trap occupancy Equation (3.9),		Trap density (average)
			E_b [kJ/mol]	N_t [sites/m^3]	C_{0app} [ppm]	N_t [sites/m^3]	N_t [sites/m^3]
42CrMo4-700	223	20	27.4	1.8×10^{25}	2.4	2.7×10^{25}	2.3×10^{25}
42CrMo4-700-CG	230	100-150	26.8	2.8×10^{25}	3.7	4.7×10^{25}	3.8×10^{25}
42CrMo4-725-CG	208	100-150	26.2	5.4×10^{25}	2.1	1.4×10^{25}	3.4×10^{25}

Table 4.10. Density of trapping sites, N_t, calculated for all these steel grades. Influence of the prior austenitic grain size on N_t calculated for low and high trap occupancy levels.

Therefore, in base to these results, in the discussions of the following sections, the value of Nt determined with the high trap occupancy approach (Equation (3.9)) will always be used when comparing the density of trapping sites with any of the mechanical properties.

4.3.4. Influence of plastic deformation

Figure 4.24 shows the evolution of the apparent hydrogen diffusion coefficient versus the applied cathodic current density obtained from permeation tests performed on 42CrMo4-700 and 42CrMo4-700-CG steel grades submitted to plastic deformations of 0%, 10%, 20%, 30%, 50%, 67% and 80%. Additionally, Table 4.11 provides the corresponding values of J_{ss}, D_{app} and C_{0app} obtained in all these permeation tests.

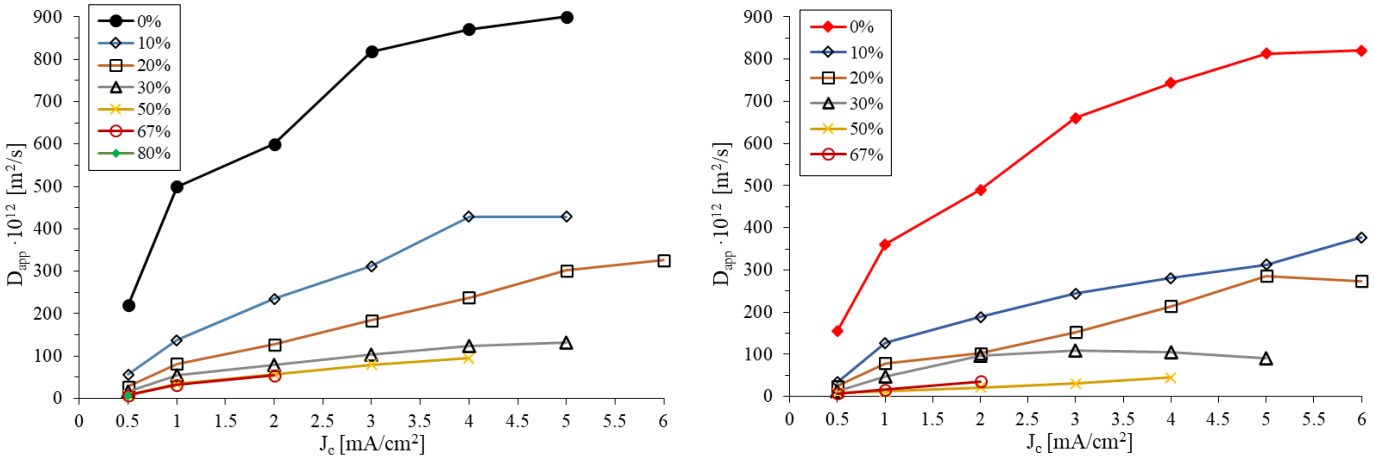

Figure 4.24 D_{app} vs. J_c plots of (a) 42CrMo4-700 and (b) 42CrMo4-700-CG steel grades under different degrees of plastic deformation. Applied J_c: 0.5+0.5+1+…+1 mA/cm².

In both, fine grain and the coarse grain steels, it is observed that the diffusion coefficient D_{app} measured under all the applied cathodic current densities significantly decreases with increasing plastic deformation. The reason is the increase in dislocation density, which hinders diffusion of hydrogen through the steel microstructure. Plastic deformation provides a cellular dislocation distribution, in which the number of dislocations in the cell walls increase and the cell size decreases with the applied deformation [101,242,243]. This effect is very important for the first transient (0.5 mA/cm²), in which hydrogen atoms fill the microstructural traps present in the steel: a decrease of nearly an order of magnitude was observed in D_{app} between the undeformed steel and the 20% plastically deformed one. Moreover, the value of the measured lattice hydrogen diffusion coefficient when most of traps are filled, D_L, also experienced a considerable drop after plastic deformation. Note that for large plastic deformations, above 30%, D_{app} is not able to reach a stable value in the final transients and thus C_{0app} could not be determined. In fact, at a certain point after performing some transients, the permeation current detected in the anodic side of the cell remained invariant (see Table 4.11) despite the increasing of the current in the cathodic side. This could mean that some kind of phenomenon is taking place in the cathodic surface that hinders hydrogen adsorption and diffusion through the steel membrane. Therefore, after completion of the tests corresponding to 42CrMo4-700-CG deformed 50 and 67%, the cathodic surface of the samples was observed using SEM, Figure 4.25. In both cases, cathodic surfaces had a considerable amount of hydrogen blisters, that are typical manifestations of hydrogen induced damage on the surface of metals [46].

Plastic deformation	J_c [mA/cm²]	42CrMo4-700			42CrMo4-700-CG		
		J_{ss} [µA/cm2]	D_{app} [m²/s]	C_{0app} [ppm]	J_{ss} [µA/cm2]	D_{app} [m²/s]	C_{0app} [ppm]

0% (L_1=0.90 mm) (L_2=1.07 mm)	0.5	40	2.2×10^{-10}	---	36	1.5×10^{-10}	---
	1	74	5.0×10^{-10}	---	70	3.6×10^{-10}	---
	2	127	6.0×10^{-10}	---	117	4.9×10^{-10}	---
	3	161	8.2×10^{-10}	2.3	155	6.6×10^{-10}	---
	4	195	8.7×10^{-10}	2.6	186	7.4×10^{-10}	3.5
	5	232	9.0×10^{-10}	3.0	215	8.1×10^{-10}	3.7
	---	---	---	---	241	8.2×10^{-10}	4.1
10% (L_1=0.81 mm) (L_2=0.53 mm)	0.5	43	5.6×10^{-11}	---	74	3.4×10^{-11}	
	1	81	1.4×10^{-10}	---	121	1.3×10^{-10}	
	2	135	2.4×10^{-10}	---	186	1.9×10^{-10}	
	3	173	3.1×10^{-10}	---	238	2.4×10^{-10}	
	4	201	4.3×10^{-10}	5.0	284	2.8×10^{-10}	
	5	230	4.3×10^{-10}	5.7	330	3.1×10^{-10}	---
	---	---	---	---	367	3.8×10^{-10}	6.8
	---	---	---	---	405	3.5×10^{-10}	8.1
20% (L_1=0.84 mm) (L_2=0.68 mm)	0.5	42	2.8×10^{-11}	---	40	2.4×10^{-11}	---
	1	71	8.2×10^{-11}	---	66	7.8×10^{-11}	---
	2	111	1.3×10^{-10}	---	103	1.0×10^{-10}	---
	3	140	1.8×10^{-10}	---	130	1.5×10^{-10}	---
	4	162	2.4×10^{-10}	---	152	2.1×10^{-10}	---
	5	182	3.0×10^{-10}	6.7	170	2.9×10^{-10}	5.3
	6	199	3.3×10^{-10}	6.7	186	2.7×10^{-10}	6.1
	---	---	---	---	200	2.4×10^{-10}	7.5
30% (L_1=0.61 mm) (L_2=0.50 mm)	0.5	44	1.7×10^{-11}	---	40	1.3×10^{-11}	---
	1	62	5.5×10^{-11}	---	60	4.8×10^{-11}	---
	2	83	8.0×10^{-11}	---	75	9.7×10^{-11}	---
	3	101	1.0×10^{-10}	---	87	1.1×10^{-10}	5.3
	4	115	1.2×10^{-10}	7.5	99	1.0×10^{-10}	6.3
	5	125	1.3×10^{-10}	7.7	110	9.0×10^{-11}	8.1
50% (L_1=0.64 mm) (L_2=0.47 mm)	0.5	65	7.9×10^{-12}	---	19	7.6×10^{-12}	---
	1	86	3.4×10^{-11}	---	28	1.2×10^{-11}	---
	2	103	5.7×10^{-11}	---	39	2.1×10^{-11}	---
	3	108	7.9×10^{-11}	---	47	3.0×10^{-11}	---
	4	111	9.5×10^{-11}	9.9	50	4.5×10^{-11}	---
	5	There is no longer J_p increase			There is no longer J_p increase		
67% (L_1=0.65 mm) (L_2=0.60 mm)	0.5	27	7.3×10^{-12}	---	19	6.6×10^{-12}	---
	1	31	3.2×10^{-11}	---	22	1.6×10^{-11}	---
	2	32	5.4×10^{-11}	---	23	3.6×10^{-11}	---
	3	There is no longer J_p increase			There is no longer J_p increase		
80% (L_1=0.80 mm)	0.5	28	6.3×10^{-12}	---	---	---	---
	1	There is no longer J_p increase			---	---	---

Table 4.11. Influence of plastic deformation on the permeation parameters obtained in 42CrMo4-700 (L_1=thickness) and 42CrMo4-700-CG (L_2=thickness) steel grades (Test: 0.5+0.5+1+…+1 mA/cm^2).

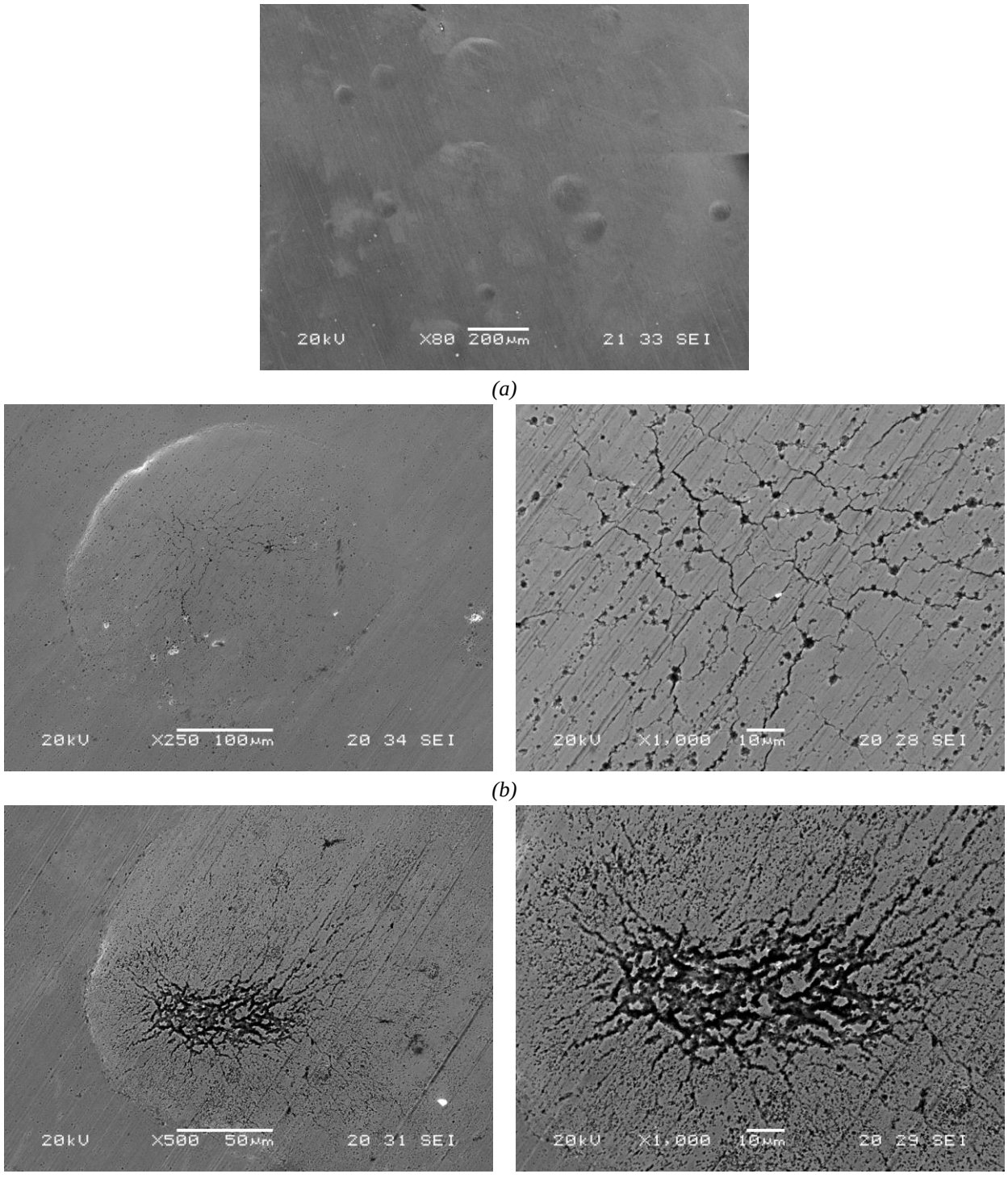

Figure 4.25. SEM observation on the cathodic surface of 42CrMo4-700-CG deformed 50% after the completion of a permeation test (a) general view and (b, c) detailed view of blisters.

The very high dislocation density produced after high plastic deformation promotes the adsorption of great amounts of hydrogen in the cathodic surface of these specimens. This gives rise to very high sub-surface hydrogen concentrations that fosters the recombination of hydrogen atoms into H_2 molecules. A great local pressure is associated to the formation of gaseous hydrogen molecules, which eventually cause extensive cracking, as it was shown in Figure 4.25(b) and (c).

This surface damage may be responsible for hampering the permeation of hydrogen atoms. Li et al. [244] reported this same behaviour when performing permeation tests using a quite similar environment (0.5M H_2SO_4+0.8g/l $Na_4P_2O_7$) under a very high cathodic current density (20 mA/cm^2), on plastically deformed high-strength steel bars.

Table 4.12 presents a summary of these permeation results. The apparent subsurface hydrogen concentration on the charging side of the specimen, C_{0app}, and the trap density, N_t, significantly increase with plastic deformation, due to the aforementioned increment of structural defects, mainly dislocations, which act as hydrogen traps. As the value of the trap binding energy, E_b, in the plastically deformed steels has not been measured in this work, the values of N_t reported in Table 4.12 are those obtained using Equation (3.9), that only depends on the permeation results D_L and C_{0app}. Additionally, due to the aforementioned hydrogen blistering phenomenon, it was not possible to accurately determine the value of N_t after high plastic deformations. However, following the trend observed on D_{app}, it is expected to remain practically constant above a deformation of 50%.

Steel Grade	Plastic deformation	HV30	D_{app} [m^2/s]	D_L [m^2/s]	C_{0app} [ppm]	Nt [sites/m3]
42CrMo4-700	0	223	2.7×10^{-10}	8.9×10^{-10}	2.4	2.7×10^{25}
	10	244	5.6×10^{-11}	4.3×10^{-10}	5.0	1.3×10^{26}
	20	259	2.8×10^{-11}	3.3×10^{-10}	6.7	2.3×10^{26}
	30	270	1.7×10^{-11}	1.3×10^{-10}	7.7	6.6×10^{26}
	50	298	7.9×10^{-12}	9.5×10^{-11}	9.9	1.2×10^{27}
	67	316	7.3×10^{-12}	---	---	---
	80	335	6.3×10^{-12}	---	---	---
42CrMo4-700-CG	0	230	2.2×10^{-10}	8.1×10^{-10}	3.7	4.7×10^{25}
	10	257	3.4×10^{-11}	3.6×10^{-10}	6.8	2.1×10^{26}
	20	271	2.5×10^{-11}	2.8×10^{-10}	7.5	3.2×10^{26}
	30	283	1.3×10^{-11}	1.0×10^{-10}	8.1	9.2×10^{26}
	50	311	7.6×10^{-12}	---	---	---
	67	330	6.6×10^{-12}	---	---	---

Table 4.12. Summary table. Apparent (D_{app}) and lattice (D_L) hydrogen diffusion coefficients, apparent subsurface hydrogen concentration on the charging side of the specimen, C_{0app}, and trap density (using Equation (3.9)), N_t, of plastically deformed 42CrMo4-700 and 42CrMo4-700-CG steel grades

In order to contextualize these results, Figure 4.26 shows the relationship between the true plastic strain, ε_{peq}, and the average density of hydrogen trap sites, log (N_t), obtained in this thesis along with those reported by different authors. The works performed by Kumnick and Johnson [82] and Huang et al. [240] are based on electrochemical permeation tests, while Sofronis et al. [241] obtained their results assuming one trap per atomic plane threaded by a dislocation. It is worth to note that different steels have different trap densities based on their specific microstructures, as can be appreciated when, for example, the initial value at $\varepsilon_{peq}=0$ is compared (data from [82] correspond to refined iron, while [241] used a carbon steel).

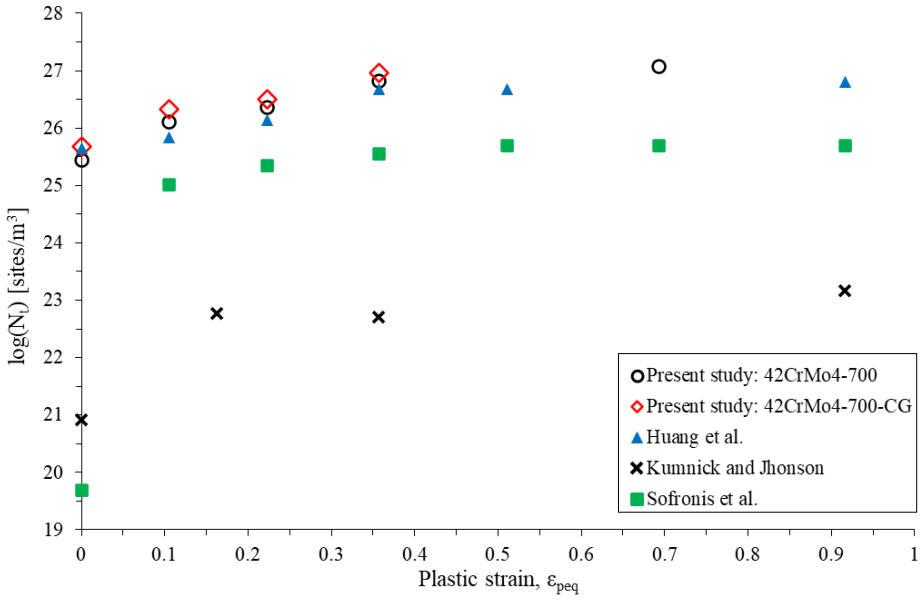

Figure 4.26. Trap density, N_t, versus plastic strain, ε_p, for 42CrMo4-700 and 42CrMo4-700-CG steel grades. Also rresults from Kumnick and Johnson [82], *Huang et al.* [240] *and Sofronis et al.* [241].

Another interesting observation, common to all the results shown in Figure 4.26, is the stabilization of the N_t value after a certain degree of plastic deformation ($\varepsilon_{peq} \approx$ 0.4-0.5). In fact, these authors suggest fitting these data following an exponential function of the form: $log(N_t) = A - B\ exp(C \cdot \varepsilon_{peq})$.

Therefore, for the shake of clarity, Figure 4.27 represents only the results obtained with the 42CrMo4-700 and 42CrMo4-700-CG grades, along with their respective exponential fittings.

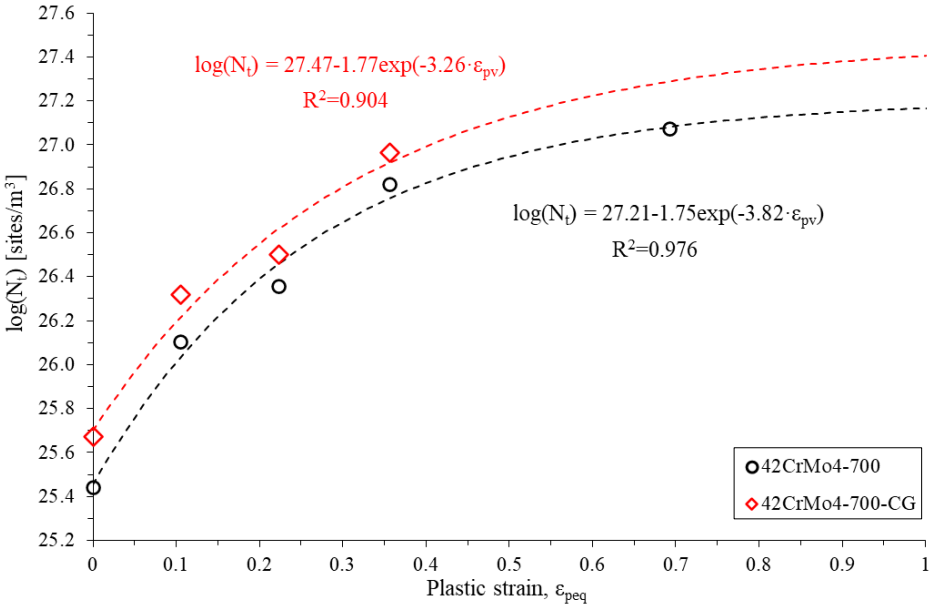

Figure 4.27. Trap density, N_t, versus plastic strain, ε_p, for 42CrMo4-700 and 42CrMo4-700-CG steel grades.

It is worth noting the very good fitting attained by means of such exponential function, a little bit lower however in the case of 42CrMo4-700-CG due to less experimental data available.

$$Log(N_t) = 27.21 - 1.75\ exp\left(-3.82 \cdot \varepsilon_{peq}\right)\ \ (R^2 = 0.976\,,\ \ 42CrMo4 - 700)$$

$$Log(N_t) = 27.47 - 1.77\ exp\left(-3.26 \cdot \varepsilon_{peq}\right)\ \ \ (R^2 = 0.904\,,\ \ 42CrMo4 - 700 - CG)$$

In general, and according to the behaviour of the underfomed steels (ε_{peq}=0), it is observed that the trapping density of the fine grain 42CrMo4-700 steel always lies below that of the coarse grain 42CrMo4-700-CG one. Indeed, the shape of the fitting function is barely similar but with just a small offset.

4.3.5. Summary

As a summary of the permeation results, Figure 4.28 shows the relationship between the steel hardness, HV30, and the value of the apparent hydrogen diffusion coefficient, D_{app}, for low trap occupancy (first permeation transient using 0.5 mA/cm^2), for all the steel grades studied in this thesis. In first place, it is observed that the apparent diffusion coefficient decreases considerably when increasing the hardness, as this basic mechanical property provides an indirect measure of the dislocation density present in the steel, as it is the structural parameter that governs hydrogen diffusion and trapping in martensitic steels.

However, it is clearly observed that all these data can be gathered in two groups: one corresponding to those steel grades submitted exclusively to quench and tempering heat treatments (black triangles), where a really good potential fitting was obtained; and another relative to steel grades 42CrMo4-700 and 42CrMo4-700-CG submitted to different degrees of plastic deformation, where an exponential fitting was the best option. Same behaviour is also observed in Figure 4.29, representing in this case log(Nt) versus HV30.

As mentioned previously, hydrogen trapping in quenched and tempered steels is mainly due to dislocations. Therefore, if the unique effect of heat treatment hardening and cold work hardening were the multiplication of dislocations, the results obtained through both hardening procedures would tend to overlap. However, a much higher decrease of D_{app} and increase of N_t are experienced for the same hardness level when cold rolling is applied. For example, 42CrMo4-650 (quenched and tempered at 650ºC for 2h, 275HV30) has a similar hardness as 42CrMo4-700 plastically deformed 30% (270HV30), but the apparent diffusion coefficient of the former is one order of magnitude greater and its trap density one order of magnitude lower (see blue arrows in Figure 4.28 and Figure 4.29). Anyway, it is well known that cold work hardening is really produced via dislocation multiplication, but heat-treating hardening (in this case, quenching and tempering) is produced not only by the increase in the dislocation density, but it is also justified by other multiple structural modifications (solid phase transformation, carbides precipitation, restauration phenomena, etc.).

In the following sections, only those steel grades hardened via heat treatments will be studied.

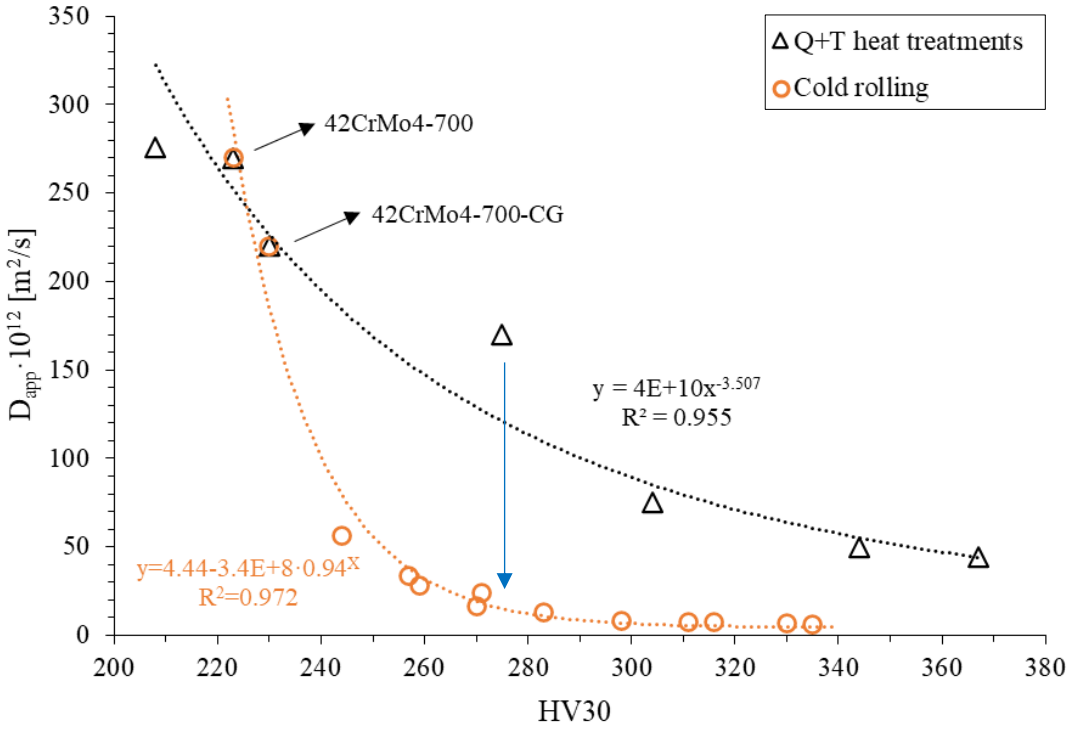

Figure 4.28. Relationship between the apparent hydrogen diffusion coefficient, D_{app}, and HV30 hardness for all the steel grades studied in this thesis.

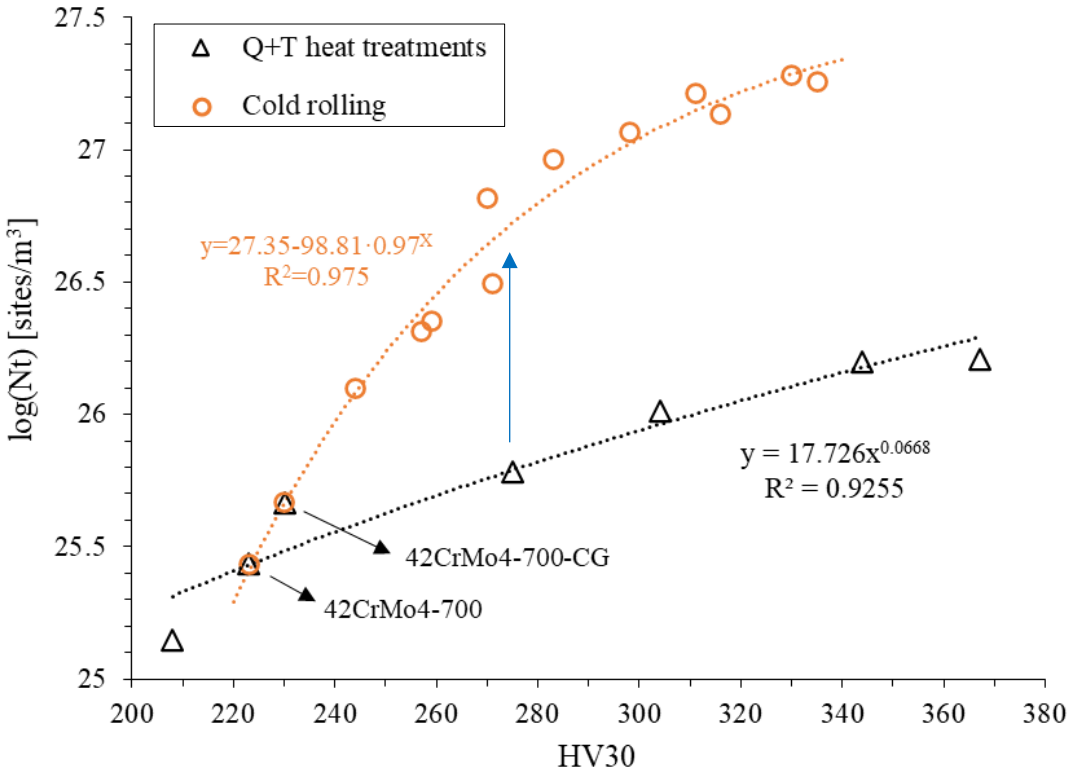

Figure 4.29. Relationship between log(N_t) (trap density calculated with Equation (3.9)) and HV30 hardness for all the steel grades studied in this thesis.

4.4. Hydrogen desorption curves

4.4.1. Influence of tempering temperature

The hydrogen desorption data experimentally obtained at room temperature for each steel grade after gaseous charging at high pressure and temperature are shown in Figure 4.30 along with the fitted FEM simulated curves. These curves represent the evolution of the hydrogen content (ppm) versus the exposure time in air (hours) at room temperature. As the hydrogen content measured in uncharged specimens on these steel grades is 0.1 ppm, a significant hydrogen uptake took place during the charging process. In addition, a good fitting between the experimental data and the numerical simulation results was obtained in all the cases.

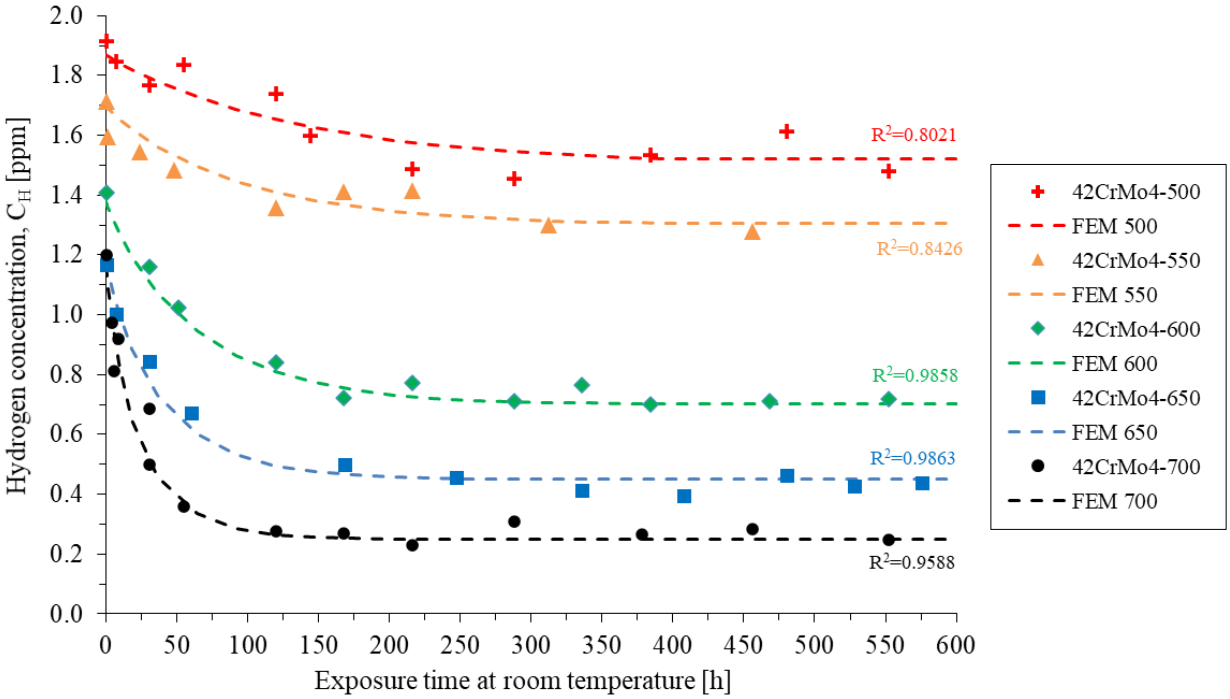

Figure 4.30. Influence of the tempering temperature in the hydrogen desorption curve after gaseous hydrogen charging. Experimental data (points) and numerical fitting (lines).

As mentioned above, data fitting of the experimentally determined desorption data was used to estimate the apparent hydrogen diffusion coefficient, D_{app}, in all the studied steel grades. As an example, the homogeneous hydrogen concentration at the end of hydrogen pre-charging (the same for all the steel grades, 4.1 ppm, as traps do not affect hydrogen absorption at 450ºC) is shown in Figure 4.31(a). The initial hydrogen distribution at the end of the cooling phase (from 450 to 85ºC inside the high-pressure reactor), in the case of the 42CrMo4-700 steel grade, is also shown in Figure 4.31(b). This hydrogen distribution corresponds to the first data point of the desorption curve (t=0), where an average hydrogen content of 1.2 ppm was experimentally measured. However, at this moment, while the specimen surface retains only the deep trapped, or residual hydrogen concentration (0.3 ppm in this steel grade, which represents our surface boundary condition), a hydrogen content as high as 2.2 ppm is still present in the centre of the specimen. Figure 4.31(c) corresponds to the final situation, after a sufficiently long time at room temperature, where all the diffusible hydrogen has diffused out, and the microstructure only

preserves the deep trapped hydrogen (0.3 ppm in this steel grade). The diffusion coefficient which provides the best fit to the experimental data was taken as the apparent diffusion coefficient of the steel. In this case (42CrMo4-700 steel grade) the estimated D_{app} value was 4.2×10^{-10} m^2/s.

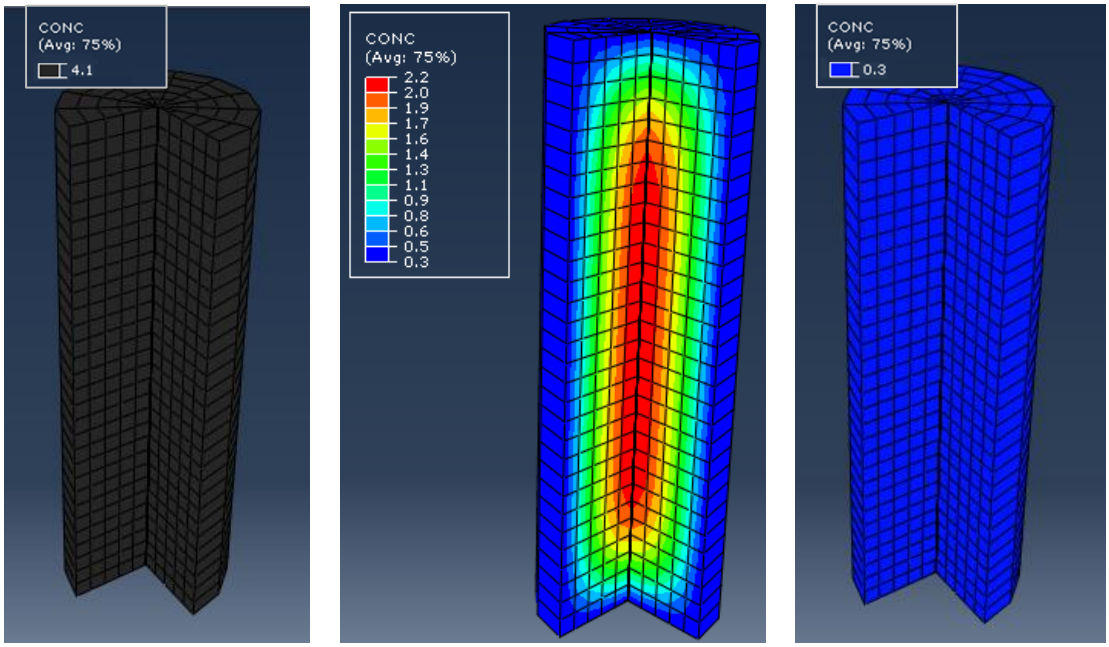

(a) *(b)* *(c)*

Figure 4.31. Hydrogen distribution (ppm) in cylindrical samples (R=5mm and L=30mm) of 42CrMo4-700 steel grade. (a) Homogeneous hydrogen concentration at the end of the hydrogen pre-charge (4.1 ppm). (b) Distribution of hydrogen in the specimen at the beginning of the desorption curve at RT (average hydrogen concentration of 1.2 ppm). (c) Residual hydrogen concentration (0.3 ppm) after 48 h at RT.

The results obtained from the analysis of hydrogen desorption performed on all the steel grades, are summarized in Table 4.13.

Steel Grade	HV30	C_{H0} [ppm]	C_{Hr} [ppm]	C_{Hdiff} [ppm]	D_{app} [m^2/s]
42CrMo4-700	223	1.20	0.30	0.90	4.3×10^{-10}
42CrMo4-650	275	1.20	0.45	0.75	2.5×10^{-10}
42CrMo4-600	304	1.40	0.70	0.70	1.5×10^{-10}
42CrMo4-550	344	1.70	1.30	0.40	9.0×10^{-11}
42CrMo4-500	367	1.85	1.50	0.35	6.6×10^{-11}

Table 4.13. Initial (C_{H0}), residual (C_{Hr}) and diffusible $C_d = C_{H0}-C_{Hr}$ hydrogen concentrations. Apparent diffusion coefficient at room temperature, D_{app}, estimated on the different 42CrMo4 steel grades.

The initial hydrogen content, C_{H0}, corresponds to the first point of the desorption curve (hydrogen content at the end of the cooling phase following thermal pre-charging in the hydrogen reactor). The deep trapped or residual hydrogen, C_{Hr}, is the hydrogen strongly trapped in the steel microstructure, i.e., the hydrogen content after a long exposure at room temperature (in this case after nearly one month). The diffusible hydrogen, C_{Hdiff}, defined as the amount of hydrogen that

is able to overcome traps and diffuse out of the steel when sufficient time is available, was calculated as the difference between the initial and residual hydrogen contents (C_{H0} - C_{Hr}).

After plotting the values showed in Table 4.13, a good correlation was obtained between the steel tempering temperature (or the steel hardness) with the different hydrogen contents and the apparent diffusion coefficient, Figure 4.32. As the steel tempering temperature decreases (hardness increases), initial and residual hydrogen significantly increase and the apparent hydrogen diffusion coefficient decreases. It is also worth noting here that the D_{app} values obtained from fitting the desorption curves, are in accordance with the D_{app} values obtained in permeation experiments (red triangles in Figure 4.32). As D_{app} calculation from the desorption curves shows the egress of hydrogen from partially filled traps, it was compared in this figure with the D_{app} determined in permeation tests under a cathodic current density of 1 mA/cm^2 (hydrogen entrance), assuming that hydrogen contents on both type of tests should not be very different. In fact, the potential fit determined for both set of data is very similar.

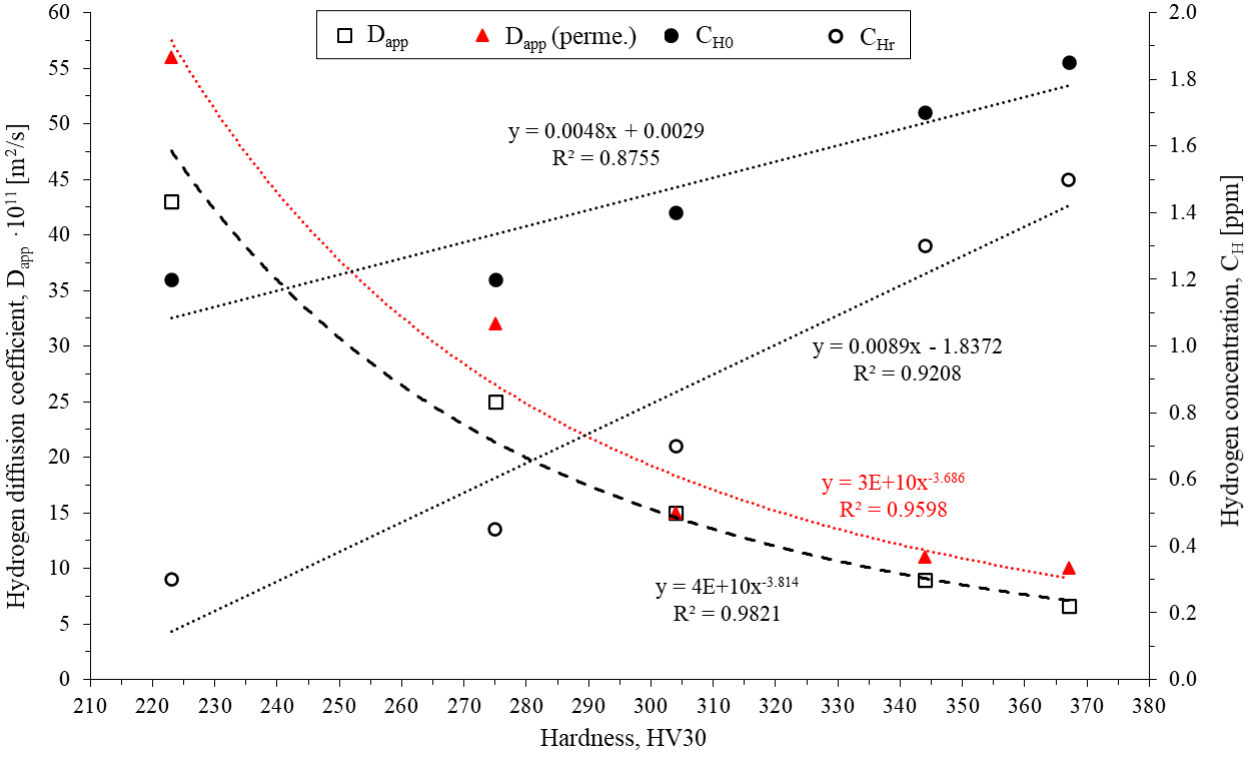

Figure 4.32. Influence of the steel hardness on the apparent hydrogen diffusion coefficient, D_{app}, and initial, C_{H0}, and residual, C_{Hr}, hydrogen concentrations in hydrogen pre-charged pins of 42CrMo4 steel grades. Comparison with permeation data (D_{app} measured at 1 mA/cm^2).

The tempered martensite microstructure of the quenched and tempered 42CrMo4 grades is especially dependent on the tempering temperature. As tempering temperature increases from 500 to 700ºC (tempering time was always two hours), carbide precipitate, internal residual stresses relax, and dislocation density reduces. According to results exposed in Table 4.13 and Figure 4.32, the initial hydrogen content, measured in samples pre-charged under high temperature and high hydrogen pressure, increased with decreasing steel tempering temperature, due to the fact that hydrogen microstructural trapping is greater in distorted, high energy martensitic microstructures (with higher dislocation densities). Moreover, the final hydrogen content

(residual hydrogen), hydrogen strongly trapped in the steel microstructure, is even more dependent on the steel microstructure, decreasing with increasing tempering temperature, mainly due to stress relaxation and the reduction in dislocation density and internal interphases (martensite laths, blocks and packets).

4.4.2. Hydrogen trapping in the CGHAZ of a 42CrMo4 weld

Figure 4.33 compares the hydrogen desorption curves obtained at room temperature with the 42CrMo4-700 fine grain steel grade and the coarse grain, 42CrMo4-700-CG and 42CrMo4-725-CG, steel grades (the numerical fits used to calculate the apparent hydrogen diffusion coefficient are also included in the same figure). The desorption results (C_{H0}, C_{Hr} and C_{Hdiff}) are summarized in Table 4.14, along with the numerically estimated hydrogen diffusion coefficient, D_{app}, obtained in these tests.

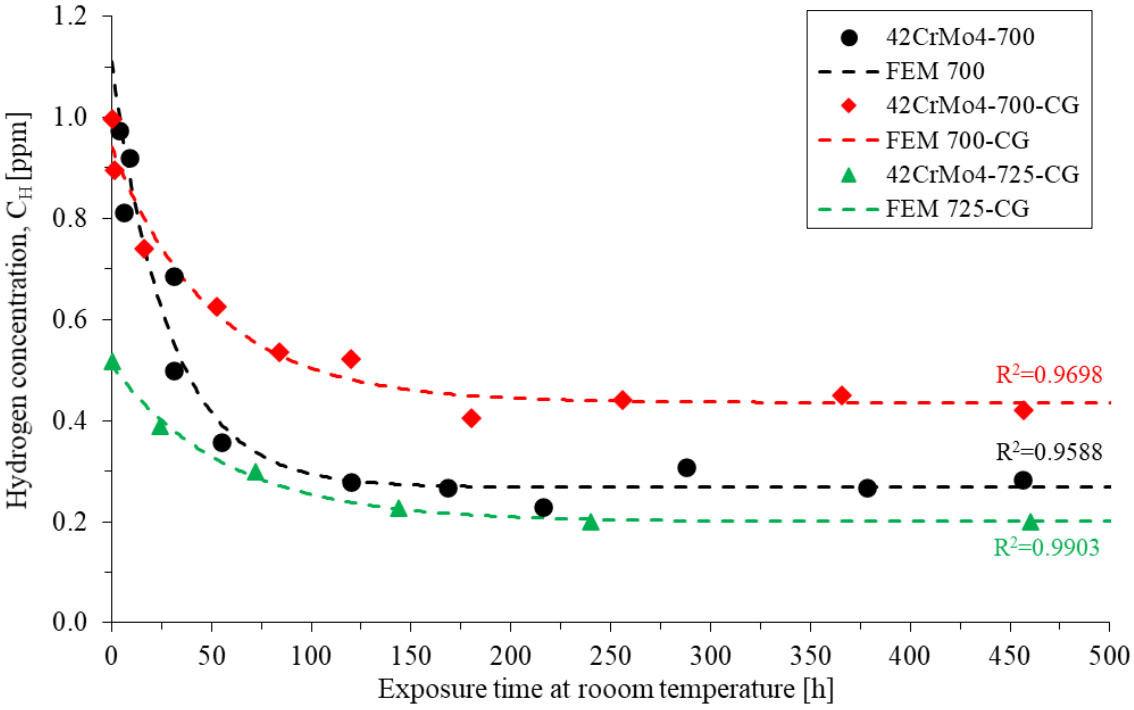

Figure 4.33. Hydrogen desorption curves of the 42CrMo4-700, 42CrMo4-700-CG and 42CrMo4-725-CG steel grades at room temperature and numerical fitting using Abaqus.

It is noted the steeper fitting of the fine grain steel in comparison with the coarse grain one tempered at the same temperature, reflecting its higher hydrogen diffusion coefficient. On the other hand, diffusion is slower in both coarse grain steels, whose fitting curves are very similar except that in 42CrMo4-725-CG (lower hardness) it is shifted downwards to lower C_H levels. On the other hand, the initial hydrogen content, C_{H0}, was respectively 1.2 and 1.0 ppm in 42CrMo4-700 and 42CrMo4-700-CG steels, but it drops to approximately 0.5 ppm for 42CrMo4-725-CG.

Steel Grade	HV30	PAGS [µm]	C_{H0} [ppm]	C_{Hr} [ppm]	C_{Hdiff} [ppm]	D_{app} [m^2/s]
42CrMo4-700	223	20	1.20	0.30	0.90	4.3×10^{-10}

42CrMo4-700-CG	230	100-150	1.00	0.45	0.55	2.5×10^{-10}
42CrMo4-725-CG	208	100-150	0.52	0.20	0.32	2.2×10^{-10}

Table 4.14. Initial (C_{H0}), residual (C_{Hr}) and diffusible $C_{Hdiff} = C_{H0}$-C_{Hr} hydrogen concentrations. Apparent diffusion coefficient at room temperature, D_{app}, estimated on the different 42CrMo4 steel grades.

When the austenitizing temperature increases from 845 to 1200ºC, a significant increase in the prior austenite grain size occurs (from 20 to 100-150 μm), a similar increase in martensite lath and packet sizes also takes place and the initial hydrogen content decreases from 1.2 to 1 ppm in the steel grades tempered at 700ºC. These results can be explained in terms of trapping phenomena in the prior austenitic grain and martensitic lath boundaries, where profuse carbide precipitation (Fe- and Cr-rich carbides [106]) takes place during tempering, as shown in Figure 4.8. When the size of the aforementioned features increases, the density of the austenitic grain boundaries and lath interfaces decreases, as does the accumulated hydrogen content in these regions. This drop of the initial hydrogen content is even more evident in the softer coarse grain steel grade, 42CrMo4-725-CG (0.5 ppm), due to its higher tempering temperature and time (lower hardness and therefore lower microstructural defects able to trap hydrogen). Moreover, all internal interfaces act as weak hydrogen traps, with activation trapping energies typically below 20 kJ/mol [21,56,57,59,74]. Hence, a major fraction of the initial hydrogen accumulated in these traps will escape when kept at room temperature.

On the other hand, the residual hydrogen content, C_{Hr}, which represents the deep trapped hydrogen, comprises the hydrogen strongly trapped and retained in the steel microstructure after a long time at room temperature (more than a month in this case). For the same tempering temperature, the value of C_{Hr} was greater in the coarse grain steel grade, 0.45 ppm versus 0.3 ppm, a result that can be attributed to the greater microstructural distortion and higher hardness of this steel grade (230HV30) compared to the base steel (223HV30). In quenched and high temperature tempered medium-carbon low-alloyed steels like this one, most of the deep trapped hydrogen concentrates along dislocations, generated during the quenching stage. The greater thermal drop applied to quench the 42CrMo4-700-CG steel grade (quenched from 1200ºC, instead of 845ºC in the case of the base steel) gives rise to a more distorted martensitic structure, with higher internal stresses and hence a higher dislocation density [239]. A similar explanation likewise justifies the slightly lower value of the hydrogen diffusion coefficient calculated with the coarse-grain steel (2.5×10^{-10} m^2/s) compared to the fine grain base steel (4.3×10^{-10} m^2/s). The diffusible hydrogen content, C_{Hdiff} (which constitutes the hydrogen able to move freely within the steel microstructure at room temperature, overcome traps and escape from the steel), is substantially higher in the fine-grain base steel, once again demonstrating that the density of weak traps (E_a<30 kJ/mol) is greater in this case.

On the other hand, in the case of 42CrMo4-725-CG steel grade, the aforementioned high temperature austenitization effect (and thus grain coarsening), seems to be compensated with the higher tempering temperature and time (725ºC for 4h) applied during the heat treatment, as the residual hydrogen concentration (0.2 ppm) drops below that of the original, fine grain steel. This tempering stage reduces the hardness of the steel to 208HV30 and, consequently, its dislocation density. However, in this case, the diffusion coefficient does not seem to increase to a similar level of the one calculated for the fine grain steel (42CrMo4-700), as it was previously observed

in permeation tests. It is possible that the accuracy of the desorption calculations is limited in this case because we had only access to a quite small length of the desorption curve (hydrogen contents between 0.52 to 0.2 ppm). In fact, this value is even lower than that obtained in permeation tests (2.8×10^{-10} m^2/s) for a current density of 0.5 mA/cm^2, when traps occupancy is very low. Remember than in the rest of the steel grades the value estimated from the desorption curves was comparable to that calculated in permeation tests at approximately 1 mA/cm^2. This suggests that hydrogen concentration in 42CrMo4-725-CG at the end of the hydrogen charge was already very low.

4.5. Determination of the trap binding energies

4.5.1. Influence of tempering temperature

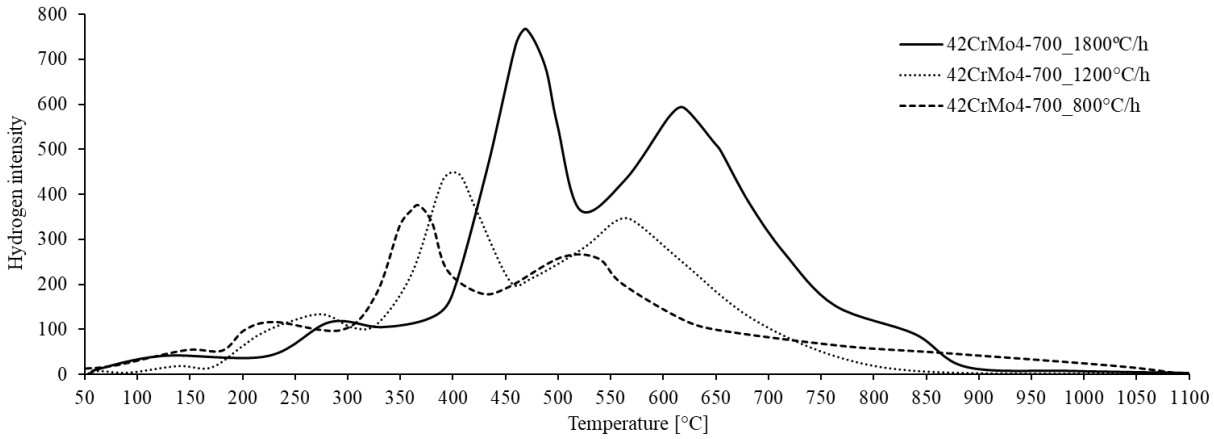

Figure 4.34 shows an example of hydrogen evolution during the thermal desorption analysis (TDA) performed on the 42CrMo4 steel tempered at 700ºC under three different heating rates: 1800, 1200 and 800ºC/h. Three desorption peaks, associated with three different hydrogen traps, are clearly detected in all cases, shifting to higher temperatures as the heating rate increases. It is worth noting that the second and third peaks were much more intense than the first one, meaning that a greater volume of hydrogen is trapped in their corresponding traps.

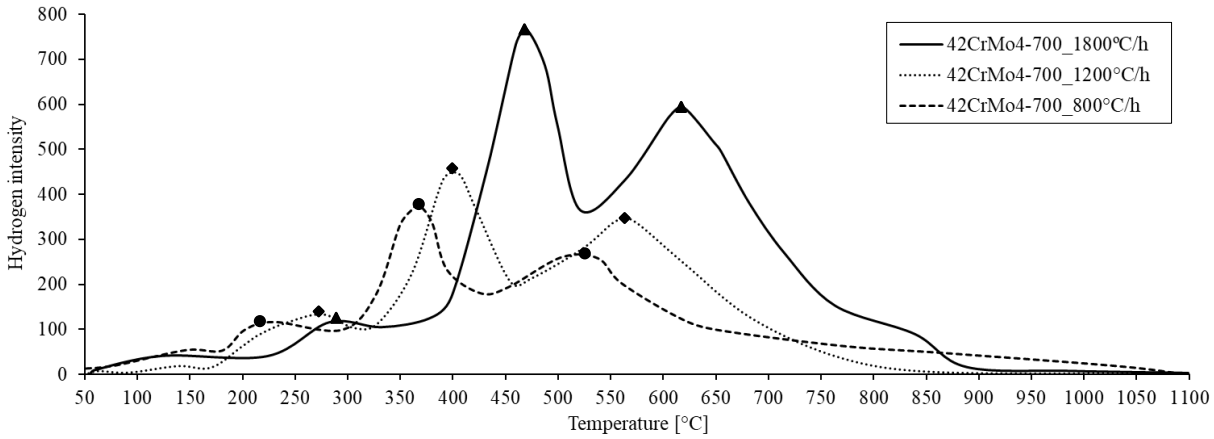

Figure 4.34. Thermal desorption analysis of the 42CrMo4-700 grade under three different heating rates.

Considering now all the applied heating rates, Figure 4.35 shows the linear regression obtained between $\ln(\phi/T_p^2)$ and $(1/T_p)$, for the same steel tempered at 700ºC. Excellent regressions (R^2

above 0.95) were obtained for the three peaks, corresponding respectively to activation energies, E_a, of 21, 25 and 35 kJ/mol.

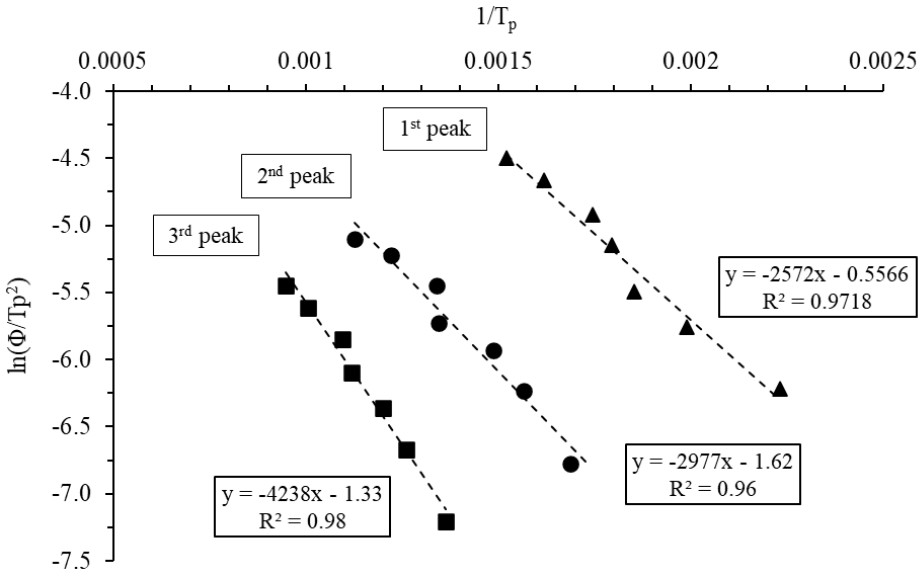

Figure 4.35. Linear regressions for the determination of trap activation energies in 42CrMo4-700 steel grade.

Thermal desorption analysis was also applied to the other 42CrMo4 steel grades. In fact, Figure 4.36 compares the desorption profiles of the 42CrMo4 steel grades tempered at 700, 650, 600, 500 and 500ºC, under the same heating rate of 2400ºC/h.

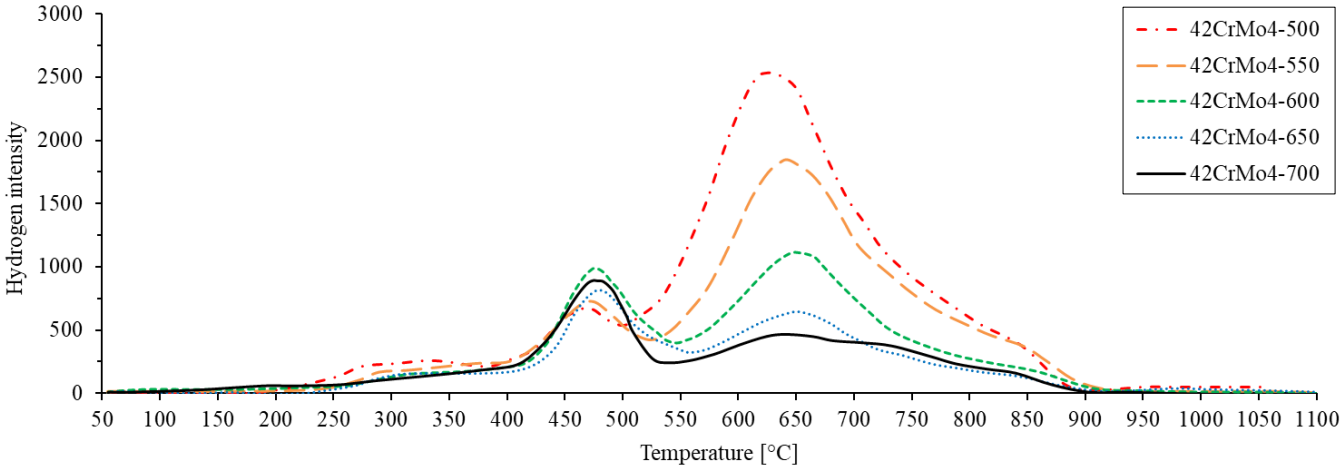

Figure 4.36. Thermal desorption analysis of 42CrMo4 steel quenched and tempered at 500, 550, 600, 650 and 700ºC under a heating rate of 2400ºC/h.

Three peaks were also identified in all these grades. Note that the intensities of the first and second peaks were quite similar for the five tempering temperatures, while the intensity of the third peak increases considerably when the tempering temperature decreases.

Table 4.15 shows the slope, m, of the $\ln(\phi/T_p^2)$ versus $(1/T_p)$ plots, the R^2 determination coefficient and the activation energy, E_a, calculated from the TDA analysis performed on all the 42CrMo4 steel grades. The excellent regressions obtained in all these analyses are also worth noting, with determination coefficients, R^2, above 0.9 in all cases.

Steel Grade	1st Peak			2nd Peak			3rd Peak		
	E_a [kJ/mol]	m	R^2	E_a [kJ/mol]	m	R^2	E_a [kJ/mol]	m	R^2
42CrMo4-700	21.4	-2572	0.97	24.8	-2977	0.96	35.2	-4238	0.98
42CrMo4-650	19.9	-2391	0.90	26.0	-3125	0.98	35.1	-4222	1.00
42CrMo4-600	17.7	-2133	0.97	24.0	-2886	0.98	35.5	-4265	0.99
42CrMo4-550	19.3	-2324	0.93	25.2	-3033	0.97	35.6	-4286	0.98
42CrMo4-500	20.1	-2413	0.94	25.1	-3016	0.98	35.7	-4288	0.97

Table 4.15. Trap activation energies, E_a, and determination coefficient, R^2, associated with the three desorption peaks determined in all the 42CrMo4 steel grades.

However, the trap binding energy, E_b, (instead of E_a) is the trapping parameter usually reported in literature (it is also the parameter used in Equation (3.7)). Therefore, Table 4.16 shows the trap binding energies, E_b, determined for each steel grade ($E_b = E_a - E_L$, taking E_L, the activation energy of hydrogen diffusion in an iron lattice, equal to 8 kJ/mol). According to these results, the binding energy associated with each desorption peak is practically the same in all the steel grades, regardless of the tempering temperature, a finding in line with the results reported by Wei and Tsuzaki [77]. Consequently, three different hydrogen traps with average binding energies of 11.8, 17.0 and 27.4 kJ/mol were identified in the 42CrMo4 steel quenched and tempered at 500-700ºC.

Steel Grade	1st Peak	2nd Peak	3rd Peak
	E_b [kJ/mol]	E_b [kJ/mol]	E_b [kJ/mol]
42CrMo4-700	13.4	16.8	27.2
42CrMo4-650	11.9	18.0	27.1
42CrMo4-600	10.2	16.0	27.5
42CrMo4-550	11.3	17.2	27.6
42CrMo4-500	12.1	17.1	27.7
Average	11.8±1.2	17.0±0.7	27.4±0.2

Table 4.16. Trap binding energies, E_b, determined in 42CrMo4 steel grades

Assuming that most vacancies are removed in the course of tempering [245], the first peak, with a binding energy of 11.8 kJ/mol, may be associated with interfaces between the alloyed carbides $(Fe, Cr, Mo)_3C$ and the ferritic matrix [17,56], and the second peak, with a binding energy of 17.0 kJ/mol, to hydrogen trapped in lath, block and packet martensite interphases [49,84,246]. The third peak, with a binding energy of 27.4 kJ/mol is identified with dislocations [21,49,246]. A significant, continuous increase in the intensity of this peak with decreasing tempering temperature can be observed in Figure 4.36, reflecting the well-known fact that dislocation density strongly increases with decreasing tempering temperature. In fact, many authors [73,77] have considered that dislocations are the governing trap site responsible for hydrogen trapping in quenched and tempered CrMo steels, and trapping energies in the range of 26-30 kJ/mol are

usually assumed for dislocations in steels [21,57,64,65,67–72]. The average E_b value of 27.4 kJ/mol calculated in this thesis is in line with all these previous studies.

Furthermore, in order to confirm that the aforementioned third peak corresponds to hydrogen trapped in dislocations, two additional TDA analyses were performed:

- First, several 42CrMo4-500 hydrogen pre-charged samples were exposed to air at room temperature (RT) for 400 h (17 days) in order to release the reversible trapped hydrogen. TDA analysis at 1200ºC/h of these samples, shown in Figure 4.37 , revealed that the first and second desorption peaks virtually disappeared (weakly trapped hydrogen). Moreover, the activation energy associated with the third peak increased to 39.8 kJ/mol (E_b=31.8 kJ/mol). This slight increase in binding energy may be due to the RT release of hydrogen trapped in the weakest locations within dislocations [49].
- A similar TDA analysis was subsequently performed on samples of the 42CrMo4-700 steel which had been previously submitted to a small tensile plastic deformation of 0.5%. The results are shown in Figure 4.38, which compares the TDAs of the un-deformed and the plastically strained samples under the same heating rate, 1200ºC/h. In both cases, a small first peak and two successive larger peaks were detected, the third peak being more intense for the strained sample, where a binding energy value of 29.8 kJ/mol was calculated, slightly higher than that of the undeformed sample (27.4 kJ/mol). It is well known that the main effect induced by plastic deformation is dislocation multiplication (increase in dislocation density) [112,246–248]; hence the third peak may undoubtedly be related to dislocations.

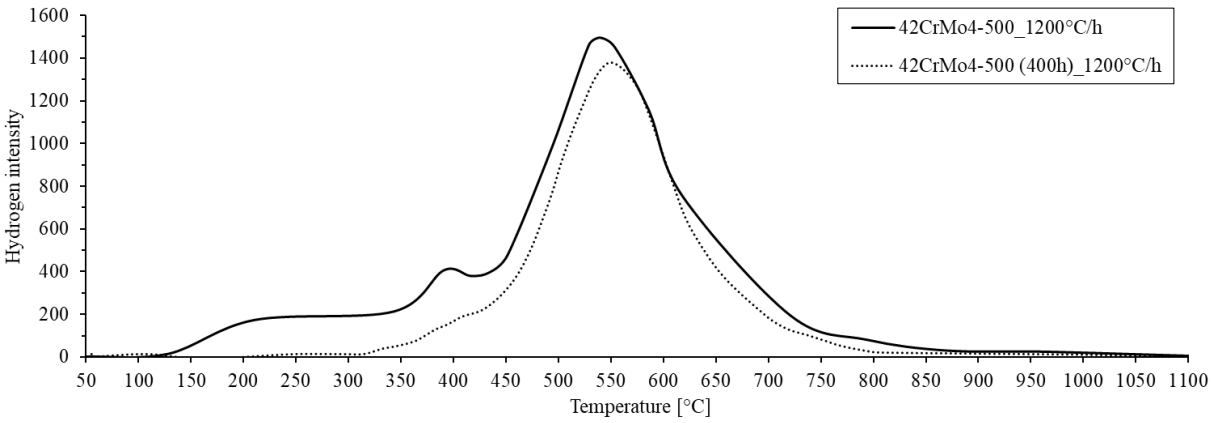

Figure 4.37. Thermal desorption analysis of 42CrMo4-500 just after extraction from liquid nitrogen (t=0) and after 400h of air exposure, under a heating rate of 1200ºC/h.

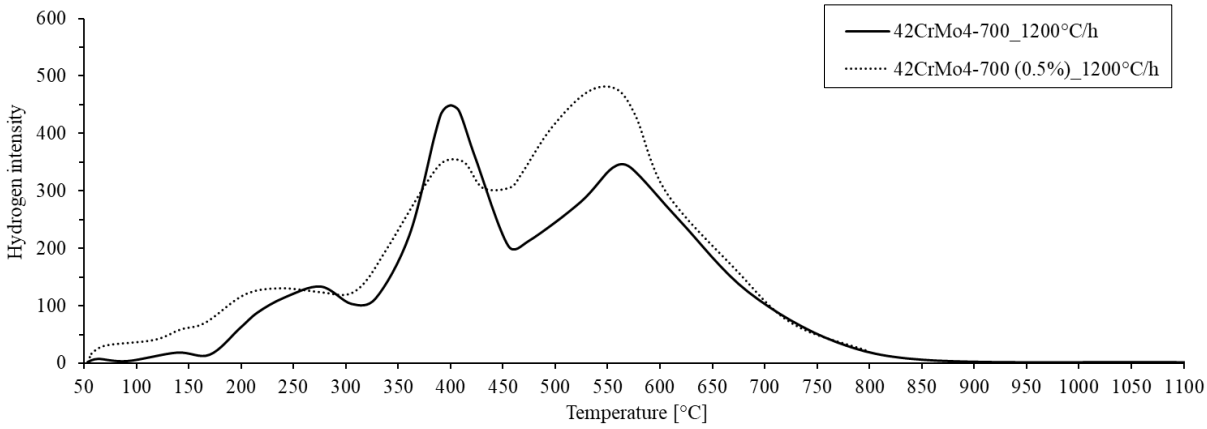

Figure 4.38. Thermal desorption analysis of undeformed and 0.5% strained samples of 42CrMo4 steel quenched and tempered at 700ºC under a heating rate of 1200ºC/h.

4.5.2. Trapping behaviour in the CGHAZ of a 42CrMo4 weld

In order to compare the trapping behaviour of the fine grain steel grade, 42CrMo4-700, and the coarse grain steel grades, 42CrMo4-700-CG and 42CrMo4-725-CG, Figure 4.39 shows their desorption profiles under a heating rate of 2400ºC/h.

Again, three temperature peaks can be distinguished, each associated to a different hydrogen trap. Table 4.17 shows the slope, m, of the $\ln(\phi/T_p^2)$ versus $(1/T_p)$ plots, the R^2 determination coefficient and the activation energy, E_a, calculated from all the TDA analysis performed on both coarse grain steel grades (fine grain steel is included for comparison). In this case, good regressions were also obtained for all the peaks ($R^2 > 0.88$).

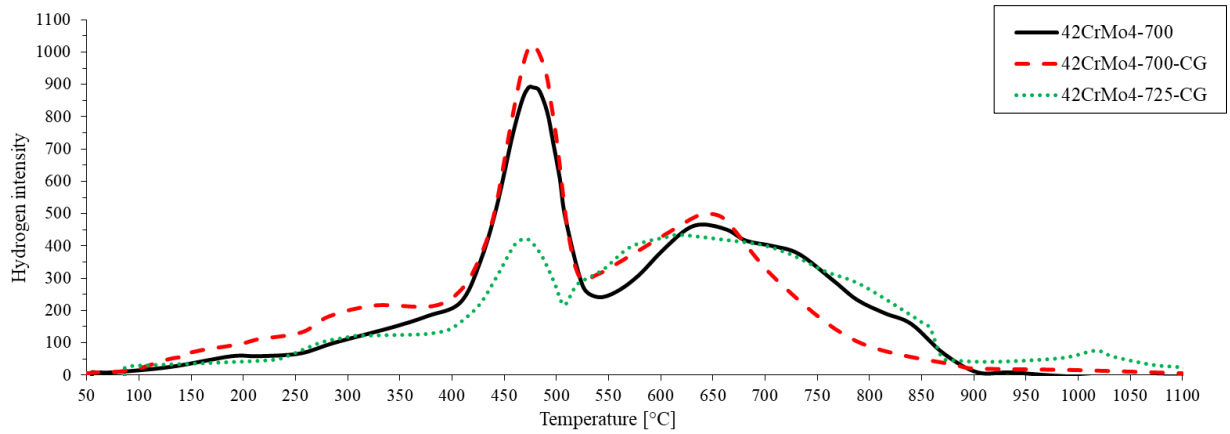

Figure 4.39. Thermal desorption analysis of fine grain (42CrMo4-700) and coarse grain (42CrMo4-700-CG, 42CrMo4-725-CG) steel grades under a heating rate of 2400ºC/h.

Steel Grade	1st Peak			2nd Peak			3rd Peak		
	E_a [kJ/mol]	m	R^2	E_a [kJ/mol]	m	R^2	E_a [kJ/mol]	m	R^2

42CrMo4-700	21.4	-2572	0.97	24.8	-2977	0.96	35.2	-4238	0.98
42CrMo4-700-CG	18.9	-2273	0.88	27.1	-3254	0.98	34.8	-4188	0.99
42CrMo4-725-CG	18.4	-2218	0.94	27.9	-3357	0.96	34.2	-4108	0.92

Table 4.17. Trap activation energies, E_a, and determination coefficient, R^2, associated with the three desorption peaks determined in fine grain (42CrMo4-700) and coarse grain (42CrMo4-700-CG, 42CrMo4-725-CG) steel grades.

Finally, the trap binding energy, E_b, determined as $E_b=E_a-E_L$ (E_L=8 kJ/mol), is shown in Table 4.18 for each steel grade. Considering that the only microstructural difference between the fine and the coarse grain steel grades is the prior austenitic grain size (their microstructure also consists of tempered martensite), the same peak-trap assignation than that suggested for 42CrMo4-700 steel grade (fine grain) can be applied. Therefore, as previously said, the first peak is associated with hydrogen trapped in carbide-matrix interfaces; the second peak to hydrogen in lath, block, and packet martensite interphases and the third to hydrogen in dislocations.

Steel Grade	HV30	PAGS [μm]	1st Peak	2nd Peak	3rd Peak
			E_b [kJ/mol]	E_b [kJ/mol]	E_b [kJ/mol]
42CrMo4-700	223	20	13.4	16.8	27.2
42CrMo4-700-CG	230	100-150	10.9	19.1	26.8
42CrMo4-725-CG	208	100-150	10.4	19.9	26.2

Table 4.18. Trap binding energies, E_b, determined in fine grain (42CrMo4-700) and coarse grain (42CrMo4-700-CG, 42CrMo4-725-CG) steel grades.

Although major E_b differences are not noticed between these three steel grades, it is interesting to observe that the binding energy associated to the second peak have slightly increased in the coarser microstructures (other differences are not relevant). This behaviour may be related to the greater distortion of the martensitic laths observed in the coarse grain steels, see Figure 4.8. Having a greater E_b value, distorted internal interfaces are able to trap more hydrogen. However, remember that most of the carbides generated during tempering precipitate in these interfaces and also dislocations tend to accumulate in these same boundaries, making it very difficult to find a sound explanation.

4.6. Effect of internal hydrogen in the mechanical properties of steels

This part of the thesis aims to assess the effects of internal hydrogen on the mechanical properties of all the studied steel grades. To do so, tensile tests (both on smooth and notched specimens), fracture toughness tests, constant K tests and also fatigue crack growth tests (pre-cracked CT specimens) were performed using hydrogen gas pre-charged specimens.

4.6.1. Effects of internal hydrogen on the tensile properties

4.6.1.1. Influence of tempering temperature

4.6.1.1.1. Tensile tests on smooth specimens

Table 4.22 shows the results obtained in the tensile tests performed in uncharged and hydrogen pre-charged (at 0.4 and 0.04 mm/min) smooth specimens of 42CrMo4 steel quenched and tempered at different temperatures. The duration of the tests and the average hydrogen concentration, C_H, extrapolated from the desorption curves are also included in this table.

Steel grade	v_{test} [mm/min]	Test duration [h]	C_H [ppm]	σ_{ys} [MPa]	σ_{uts} [MPa]	e [%]	RA [%]
700	0.4	0.33	-	622±2	710±5	22.6±0.6	62.8±1.7
	0.4	0.35	1.2	585±7	694±1	22.8±1.6	63.9±0.4
	0.04	2.7	1.2	590	689	21.7	62.6
650	0.4	0.25	-	828±24	913±14	16.1±0.2	57.1±1.4
	0.4	0.26	1.2	800	897	14.8	56.1
	0.04	2.6	1.2	796	891	13.9	58.9
600	0.4	0.28	-	880±1	985±2	14.6±0.5	55.4±1.0
	0.4	0.30		860±28	984±1	15.9±0.1	55.6±2.9
	0.04	2.7		838±11	960±12	13.7±2.9	55.7±0.4
550	0.4	0.27	-	1023±4	1113±8	13.9±0.4	51.7±0.5
	0.4	0.25		960	1094	10.8	49.3
	0.04	2.3		974±16	1094±3	9.0±1.5	42.7±3.3
500	0.4	0.26	-	1086±5	1198±4	12.7±0.5	50.6±1.2
	0.4	0.32		1083	1199	11.2	47.8
	0.04	2.6		1060	1178	10.8	46.3

Table 4.19. Results of the tensile tests performed at different displacement rates on smooth specimens (uncharged and hydrogen pre-charged) of the 42CrMo4 steel quenched and tempered at different temperatures.

It should be born in mind that C_H values showed in Table 4.22 are approximate, as the desorption curves were obtained with cylindrical samples of 10 mm in diameter and the smooth tensile specimens had a diameter of 5 mm in the calibrated region. In addition, as an example, Figure 4.40 shows the stress-strain curves obtained with the steel grades respectively tempered at the highest and lowest temperatures, 700ºC and 500ºC.

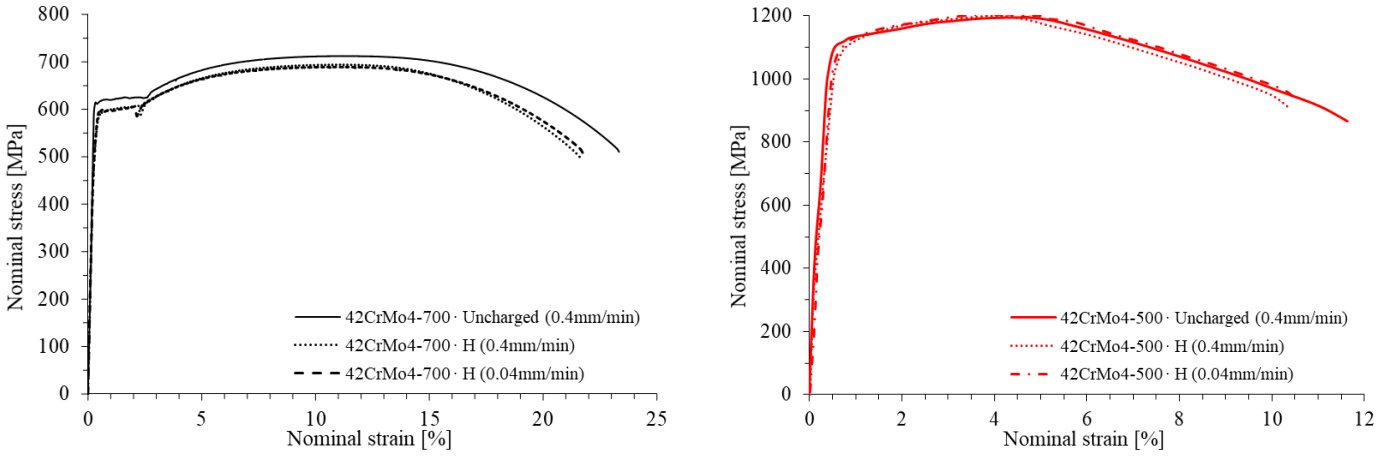

(a) *(b)*

Figure 4.40. Stress-strain curves of the uncharged and hydrogen pre-charged smooth tensile specimens (a) 42CrMo4-700 and (b) 42CrMo4-500 grades.

Regarding 42CrMo4 tempered at 700ºC, no significant differences were observed between the stress-strain tensile curves of the tests carried out on uncharged and on hydrogen pre-charged samples at different displacement rates (Figure 4.40(a)). In fact, the embrittlement indexes (EI), shown in Figure 4.41, relative to all the tensile parameters were always below 6% in this grade (steel with the lowest hardness, 223HV30).

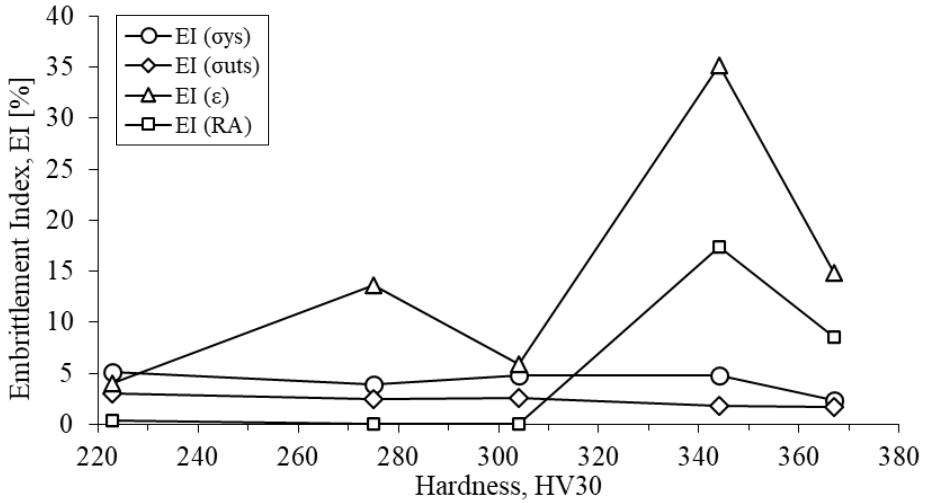

Figure 4.41. Influence of the steel hardness (tempering temperature) on the embrittlement index (EI) calculated for the tensile parameters (σ_{ys}, σ_{uts}, e and RA) of hydrogen pre-charged smooth tensile specimens. Displacement rate: 0.04 mm/min.

Quite similar embrittlement indexes were found in the steel grades tempered at 650 and 600ºC (275 and 304HV30). However, the EI associated to ductility parameters (reduction in area and elongation), increase significantly for tempering temperatures of 550 and 500ºC, i.e., the hardest steel grades. Nonetheless, it is worth noting that the embrittlement index for strength remains almost constant at approximately 2% for all these grades, which means that hydrogen has little influence on the tensile strength of them, irrespective of the hardness of the steel.

It could then be stated that tensile properties measured on smooth specimens pre-charged with gaseous hydrogen remained practically unaffected in the steel grades tempered at high temperature (above 600ºC). However, in the hardest grades, tempered at 500 and 550ºC, a slight decrease in tensile elongation and reduction in area was noticed under the lowest displacement rates. In line with this behaviour, the fracture micromechanism observed under the scanning electron microscope on the failure surfaces of the uncharged and hydrogen pre-charged smooth tensile specimens of all these grades was always fully ductile, characterized by microvoids coalescence (MVC), as it is illustrated in Figure 4.42 for the hardest steel grade, 42CrMo4-500.

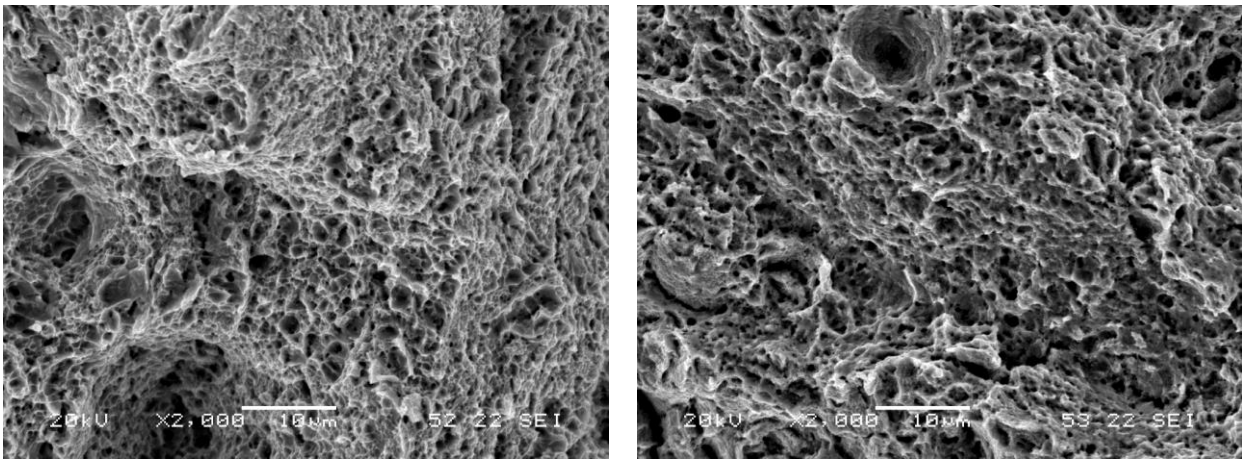

(a) *(b)*

Figure 4.42. Fracture micromechanisms (SEM) of (a) uncharged and (b) hydrogen precharged smooth tensile specimens of 42CrMo4-500 steel.

4.6.1.1.2. Tensile tests on notched specimens

Table 4.20 summarizes the results obtained in the tensile tests performed on the notched specimens (K_t=4.25) for the different 42CrMo4 steel grades. The values of the notch tensile strength, σ_{uts}, and reduction in area, RA, are shown for each grade, uncharged and hydrogen pre-charged under different displacement rates. Note that the values of the maximum deformation ε_{max} are not provided in this case because these specimens were tested without extensometer (in any case, it is not very relevant, as deformation concentrates in the notch region). EI calculated for the aforementioned mechanical properties are also presented in Table 4.20. Moreover, the test duration and approximate average hydrogen content, C_H, of the specimens in the course of the tests are also provided in this table. It is worth noting that test duration barely affected the hydrogen content in these specimens, except at the lowest displacement rates. Nonetheless, the values of C_H in Table 4.20 should be considered to be approximate, as they were derived from the desorption curves (Figure 4.30) of cylindrical pins whose geometry was not exactly the same as the one of the notched specimens. Moreover, local hydrogen concentrations are expected to be much greater in the region close to the notch tip, where the hydrostatic stress reaches maximum values [36].

Beginning with the grade tempered at 500ºC (σ_{ys}=1086 MPa), it can be noticed that as the test displacement rate decreases, hydrogen embrittlement increases considerably. In fact, the fracture strength of this grade decreased almost 60%, and the reduction in area more than 90%, when the H-precharged specimen was tested at the lowest displacement rate (0.004 mm/min). However, quite different behaviour was observed on the softer 42CrMo4-700 steel grade. In this case, due to the much lower yield strength of the steel (σ_{ys}= 622 MPa), the effects of hydrogen were rather small. Furthermore, for displacement rates lower than 0.004 mm/min, embrittlement indexes seems to be barely affected by this test parameter (significant hydrogen losses during the test are expected). The amount of pre-charged hydrogen in this steel grade was also the lowest (1.2 ppm). Due to this fact and its low yield strength, hydrogen accumulation in the notched region of this grade was limited and the embrittlement phenomenon was minimised. The steel grades submitted to the other tempering temperatures (650, 600 and 550ºC) produced intermediate behaviours.

Steel Grade	v_{test} [mm/min]	Test duration [h]	C_H [ppm]	σ_{uts} [MPa]	RA [%]	$EI_{(\sigma uts)}$ [%]	$EI_{(RA)}$ [%]
700	0.4	0.20	-	1330±29	12.5±0.4	-	-
	0.4	0.15	1.2	1273±21	11.8±0.1	4	6
	0.04	1.3	1.2→1.1	1258±20	10.3±1.6	5	18
	0.004	13.5	1.2→0.8	1294	9.6	3	23
	0.002	35.9	1.2→0.5	1250±61	9.8±0.6	6	21
650	0.4	0.28	-	1566±22	11.9±0.1	-	-
	0.4	0.25	1.2	1527±73	11.8±0.3	3	1
	0.04	1.8	1.2	1508	8.9	4	25
	0.004	16	1.2→0.9	1487±43	7.9±0.6	5	34
	0.002	23	1.2→0.8	1506	4.2	4	65
600	0.4	0.2	-	1717±10	8.4±0.1	-	-
	0.4	0.2	1.4	1604	7.6	7	9
	0.04	1.4	1.4	1384	6.0	19	28
	0.004	14	1.4→1.0	1336±65	3.4±0.6	22	59
550	0.4	0.13	-	1800±18	7.5±0.1	-	-
	0.4	0.15	1.7	1602	6.3	11	16
	0.04	1.1	1.7	1303	4.9	28	35
	0.004	11	1.7→1.6	1248±47	2.7±0.2	31	64
500	0.4	0.25	-	1833±32	6.4±0.3	-	-
	0.4	0.22	1.9	1534	4.7	16	27
	0.04	1.3	1.9	1050	3.1	43	51
	0.004	6	1.9→1.8	771±25	0.5±0.2	58	92

Table 4.20. Results of tensile tests performed on uncharged and hydrogen pre-charged notched specimens (K_t=4.25) of all the 42CrMo4 grades. Influence of the displacement rate.

To clarify the results presented in Table 4.20, Figure 4.43 shows the evolution of the notch tensile strength and reduction in area versus the hardness of the steels. For a complete comparison, uncharged and hydrogen pre-charged notched tensile specimens, the latter under displacement rates of 0.04 and 0.004 mm/min, are included. It is noticed that the presence of hydrogen barely modifies the notched tensile strength (σ_{uts}) of the grades with the lowest hardness (223 and 275HV30, respectively tempered at 700 and 650ºC) but produces a significant strength decrease in the case of the grades with the highest hardness (i.e., lowest tempering temperatures). Furthermore, it seems that this strength drop is barely dependent of the displacement rate except for the hardest steel grade. On the other hand, the behaviour is not the same for the reduction in area (RA): the embrittling effect of hydrogen is evident in all the grades, from the softest to the hardest, and significantly dependent on the displacement rate, especially in the hardest grades.

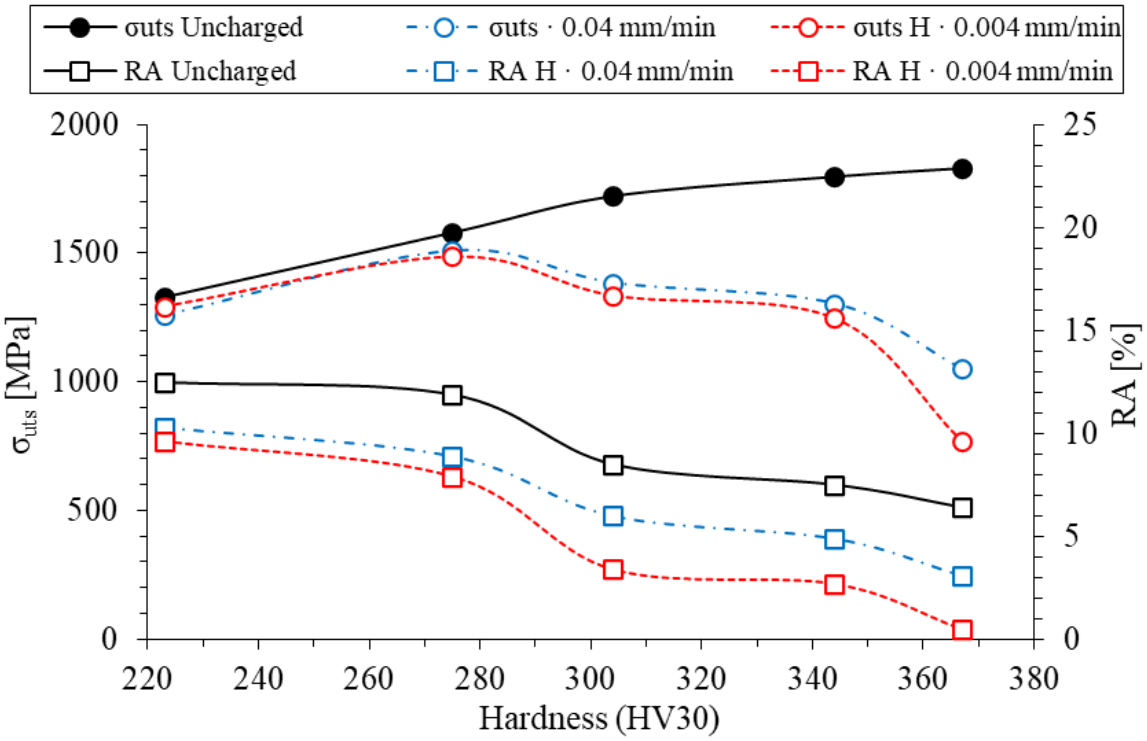

Figure 4.43. Evolution of the tensile strength (σ_{uts}) and reduction in area (RA) versus HV30 hardness of notched specimens (K_t=4.25) without hydrogen and hydrogen pre-charged at 0.04 and 0.004 mm/min.

The fracture surfaces corresponding to the notched specimens of the different grades under study were analysed using SEM and the main operative fracture micromechanisms were identified. They are summarized in Table 4.21. As happened in the smooth specimens, the fracture micromechanism of all the steel grades tested without internal hydrogen was fully ductile, microvoid coalescence (MVC), as can be respectively seen in Figure 4.44(a) and (b) for the softest and hardest grades.

Steel Grade	v_{test} [mm/min]	C_H [ppm]	Fracture Micromechanisms*	
			Periphery	Internal region
700	0.4	-	MVC	
	0.4	1.2	MVC	
	0.04	1.2→1.1	MVC (elongated)	
	0.004	1.2→0.8	CMD (175 μm)	MVC (elongated)
	0.002	1.2→0.5	MLD (20 μm) + CMD (120 μm)	MVC (elongated)
650	0.4	-	MVC	
	0.4	1.2	MVC	
	0.04	1.2	MLD (40 μm)	MVC (elongated)
	0.004	1.2→0.9	MLD (75 μm)	MVC (elongated)
	0.002		MLD (100 μm)	MVC (elongated)
600	0.4	-	MVC	

	0.4	1.4	CMD (200 µm)	MVC (elongated)
	0.04	1.4	MLD (75-90 µm) + CMD (275 µm)	MVC (elongated)
	0.004	1.4→1.0	MLD + IG (200-300 µm)	MVC (elongated) + MLD + IG
550	0.4	-	MVC	
	0.4	1.7	MLD + IG	MVC (elongated) + MLD + IG
	0.04	1.7	MLD + IG	MVC (elongated) + MLD + IG
	0.004	1.7→1.6	MLD + IG	MVC (elongated) + MLD + IG
500	0.4	-	MVC	
	0.4	1.9	IG + MLD	MVC (elongated) + MLD + IG
	0.04	1.9	IG + MLD	MVC (elongated) + MLD + IG
	0.004	1.9→1.8	IG + MLD	MVC (elongated) + MLD + IG

*Table 4.21. Operative fracture micromechanisms identified in the fracture surfaces of the uncharged and hydrogen pre-charged notched tensile specimens. *MVC: microvoid coalescence; CMD: carbide-matrix interface decohesion; MLD: martensitic lath interface decohesion; IG: intergranular fracture.*

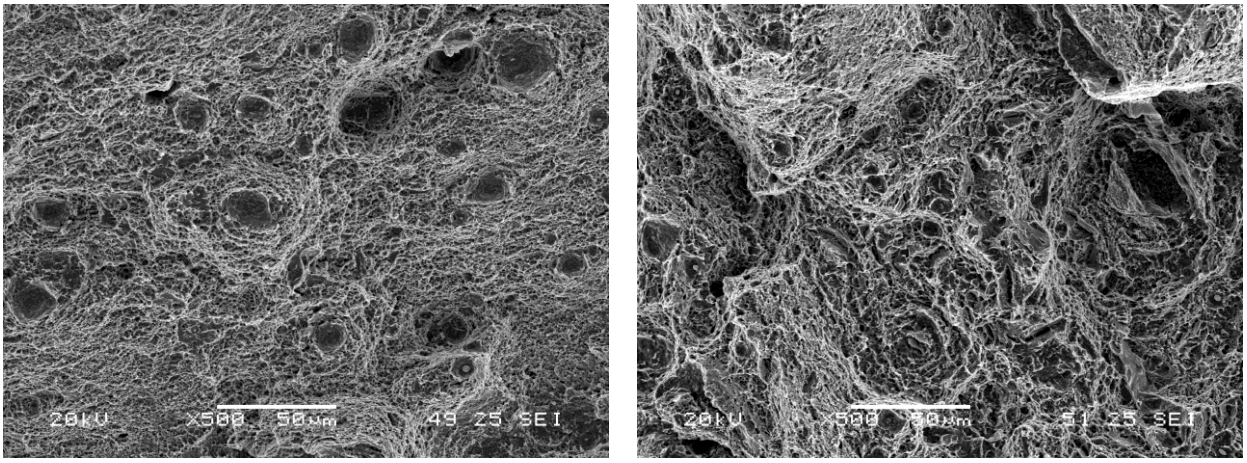

(a) *(b)*

Figure 4.44. Fracture micromechanism (SEM) detected in uncharged notched specimens of (a) 42CrMo4-700 and (b) 42CrMo4-500 grades.

Regarding the steel tempered at 700ºC, Figure 4.45 shows the fracture surfaces of the notched tensile specimens tested with internal hydrogen at different displacement rates. In the case of the fastest test, carried out at the same displacement rate as that used with the uncharged specimens (0.4 mm/min), hydrogen has not modified the operative fracture micromechanism, which is MVC (Figure 4.45(a)). However, when the applied displacement rate was 10 times lower (0.04 mm/min), the effects of hydrogen begin to appear in the form of flattened and elongated areas, like those indicated by black arrows in Figure 4.45(b). These singular zones are generally associated with strain localization ahead of the notched region due to local accumulation of hydrogen, following the mechanism described as hydrogen enhanced localized plasticity (HELP) [39,40]: the accumulation of hydrogen in front of the notch, due to the high triaxiality existing in this region, facilitates dislocation movement, plastic deformation localised and extended, giving rise to shallow and elongated dimples.

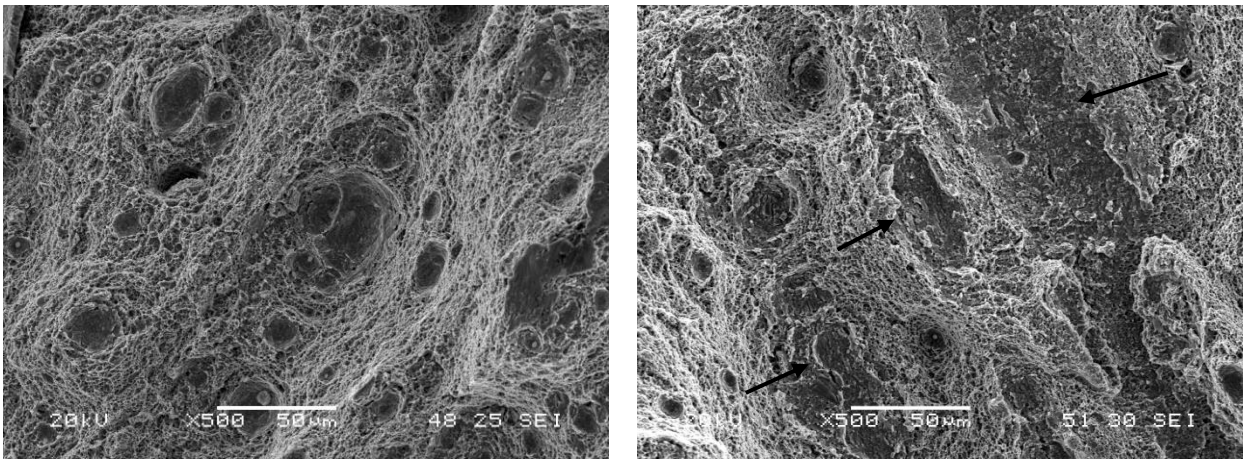

(a) *(b)*

Figure 4.45. Fracture micromechanism of notched tensile specimens of the softer grade (42CrMo4-700) tested with internal hydrogen at (a) 0.4 mm/min and (b) 0.04 mm/min.

When the specimens were tested with internal hydrogen at a displacement rate of 0.004 mm/min, apart from the presence of elongated microvoids in the bulk of the specimen (Figure 4.46(a)), a narrow band ahead of the notch (with an average extension of about 175 µm) characterized by a flatter topography was observed (Figure 4.46 (b, c)). A closer look at this area (Figure 4.46(d)) revealed the presence of very small microvoids, with an approximate diameter of around 0.5 µm. These microvoids are produced by decohesion along matrix-carbide interfaces, a micromechanism denominated carbide-matrix interface decohesion (CMD) in this study, which is promoted by the high local hydrogen concentration accumulated in these particular interfaces (weak hydrogen traps). In line with the embrittlement index stabilization, the fracture micromechanisms of the specimens tested at the lowest displacement rate (0.002 mm/min) are quite similar to those already observed at 0.004 mm/min. Once again, elongated microvoids in the bulk of the specimens and a peripheral belt of approximately 120 µm characterized by CMD were clearly observed. The only difference is that in this case, a very narrow band of around 20 µm, shown in Figure 4.47, characterized by decohesion along martensitic lath boundaries, called martensitic lath decohesion (MLD) in this thesis, was found in the most peripheral region of the specimen, just ahead of the notch tip. This micromechanisms will be better described further in the text. However, it is worth noting that the extremely small area where this mechanism took place was not enough to decrease more the notched tensile properties under this condition.

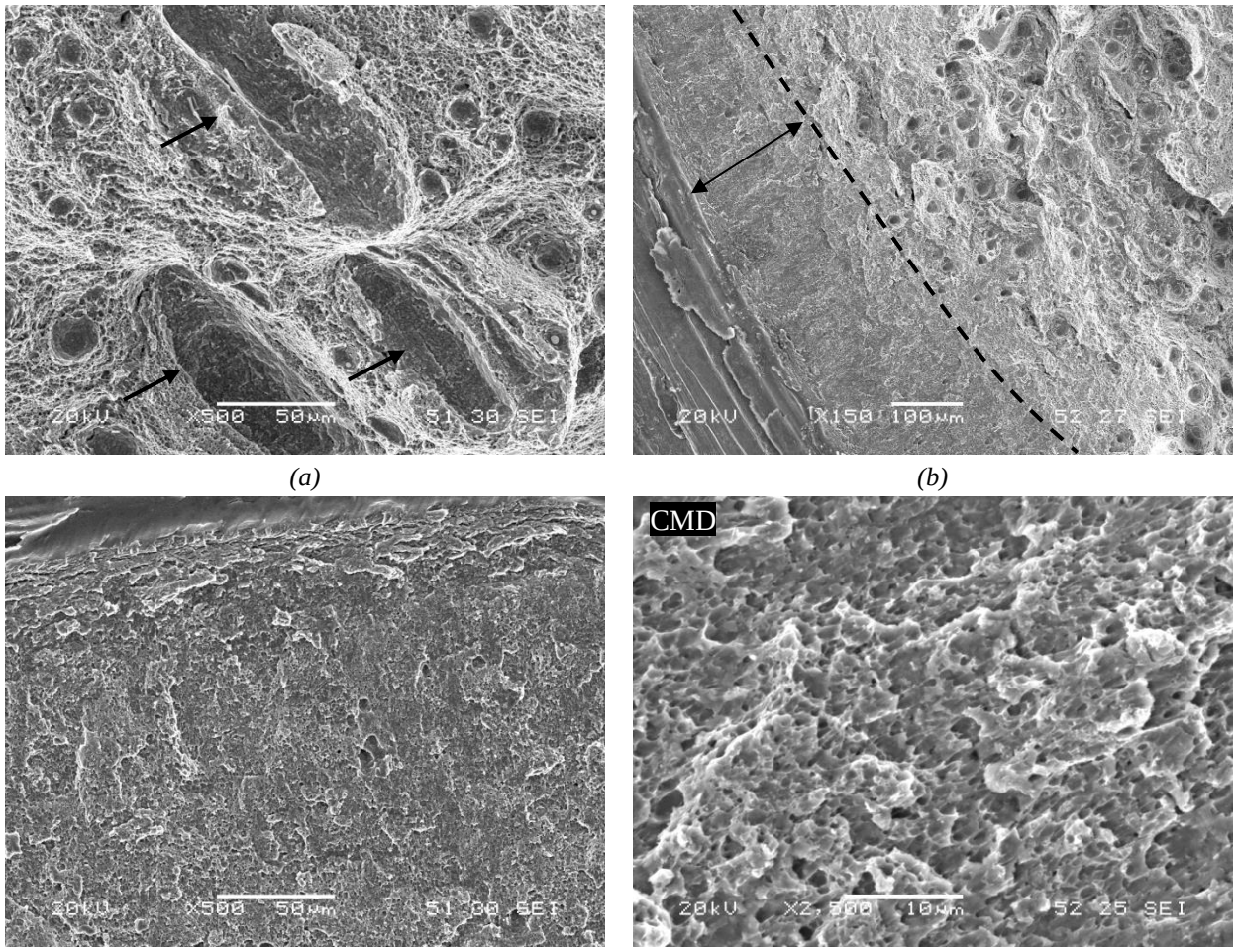

(a) *(b)*

(c) *(d)*

Figure 4.46. Fracture micromechanism of notched tensile specimens of 42CrMo4-700 grade tested with internal hydrogen at 0.004 mm/min. (a) Elongated microvoids in the bulk of the specimen, and (b, c, d) CMD (carbide-matrix interface decohesion) fracture in the periphery.

In the case of 42CrMo4-650 grade, two different regions were also observed in those specimens tested under displacement rates below 0.4 mm/min: a central region with microvoids, some of which were also enlarged, and a narrow peripheral region characterized by MLD micromechanism. The width of this region increased when decreasing the test displacement rate (see Table 4.21). This mechanism is clearly observed in Figure 4.48, where a region of around 100 µm exhibiting the martensite lath decohesion mechanism (MLD) is observed in the specimen tested under a displacement rate of 0.004 mm/min.

MLD micromechanism has the appearance of a transgranular fracture surface or quasi-cleavage and is usually referred to as plasticity-related hydrogen induced cracking (PRHIC) in martensitic steels [39]. The PRHIC mechanism was first described by Takeda and McMahon [249] in reference to the fracture mechanism observed in a low alloy quenched and tempered steel in hydrogen gas. It is sometimes called tearing topography surface (TTS), which is described as a fracture surface characterised by ductile micro-plastic tearing on a very fine scale, along martensite lath interfaces [39,249]. It is here highlighted that the size of the characteristic features observed in Figure 4.48(b) is comparable to the microstructure units (martensite laths) shown in (Figure 4.1). The use of low displacement rates (longer testing times) allows more hydrogen to

diffuse from the bulk of the specimen and to accumulate at the most strained area, in the vicinity of the notch tip [138,141]. These hydrogen atoms are trapped in this region at the martensitic lath interfaces, thus promoting their decohesion under the applied load when a critical hydrogen concentration is reached.

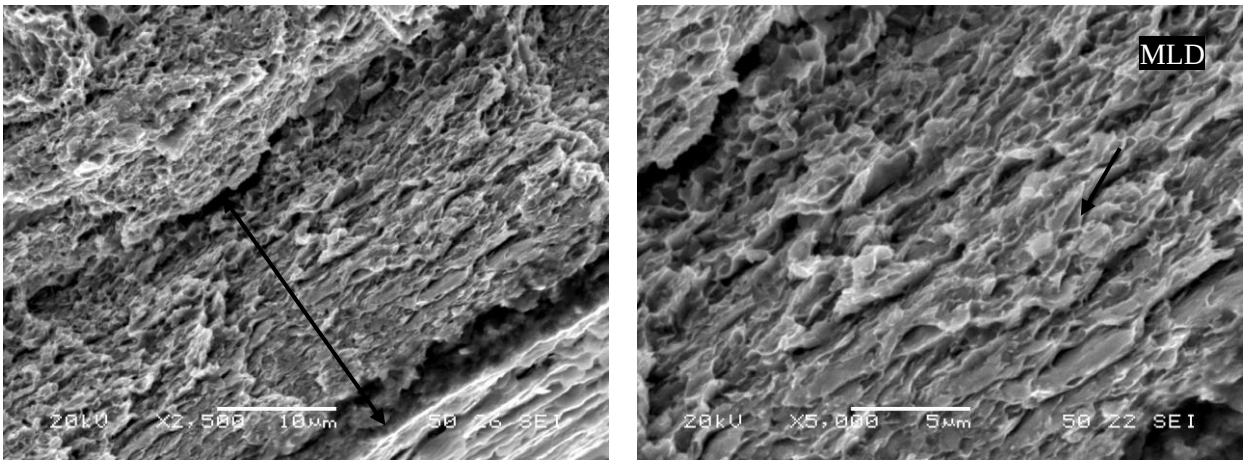

(a) *(b)*

Figure 4.47. (a) General view and (b) detail of martensite lath decohesion mechanism (MLD) detected in the most peripheral region ahead of the notch tip (20 µm) in notched tensile specimens of 42CrMo4-700 grade tested with internal hydrogen at 0.002 mm/min.

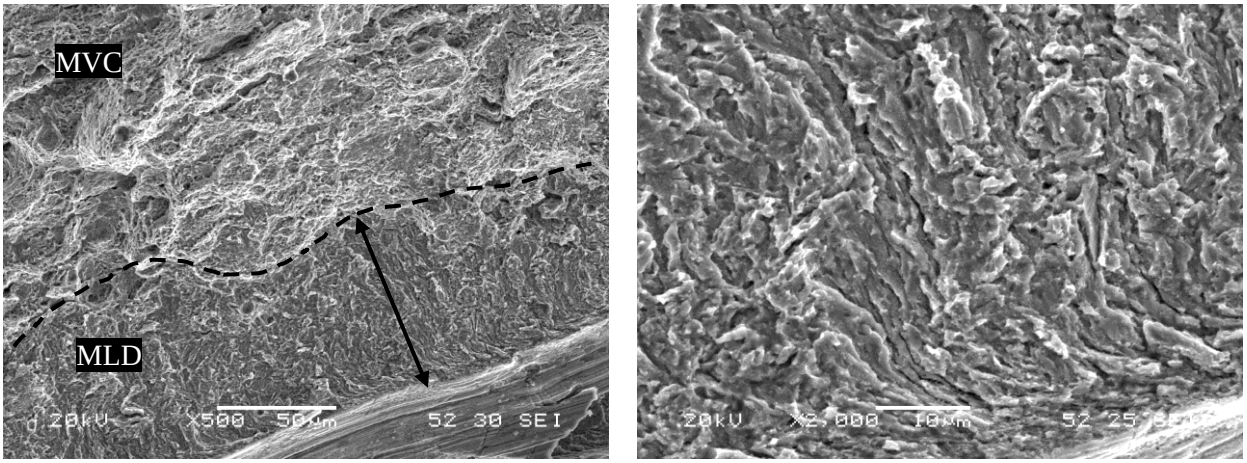

(a) *(b)*

Figure 4.48. MLD fracture micromechanism (a) general and (b) detailed picture, observed in the peripheral region ahead of the notch tip in notched tensile specimens of 42CrMo4-650 grade tested with internal hydrogen at 0.004 mm/min.

The fracture surfaces corresponding to the steel grades tempered at lower temperatures (600, 550 and 500ºC) are shown in Figure 4.49.

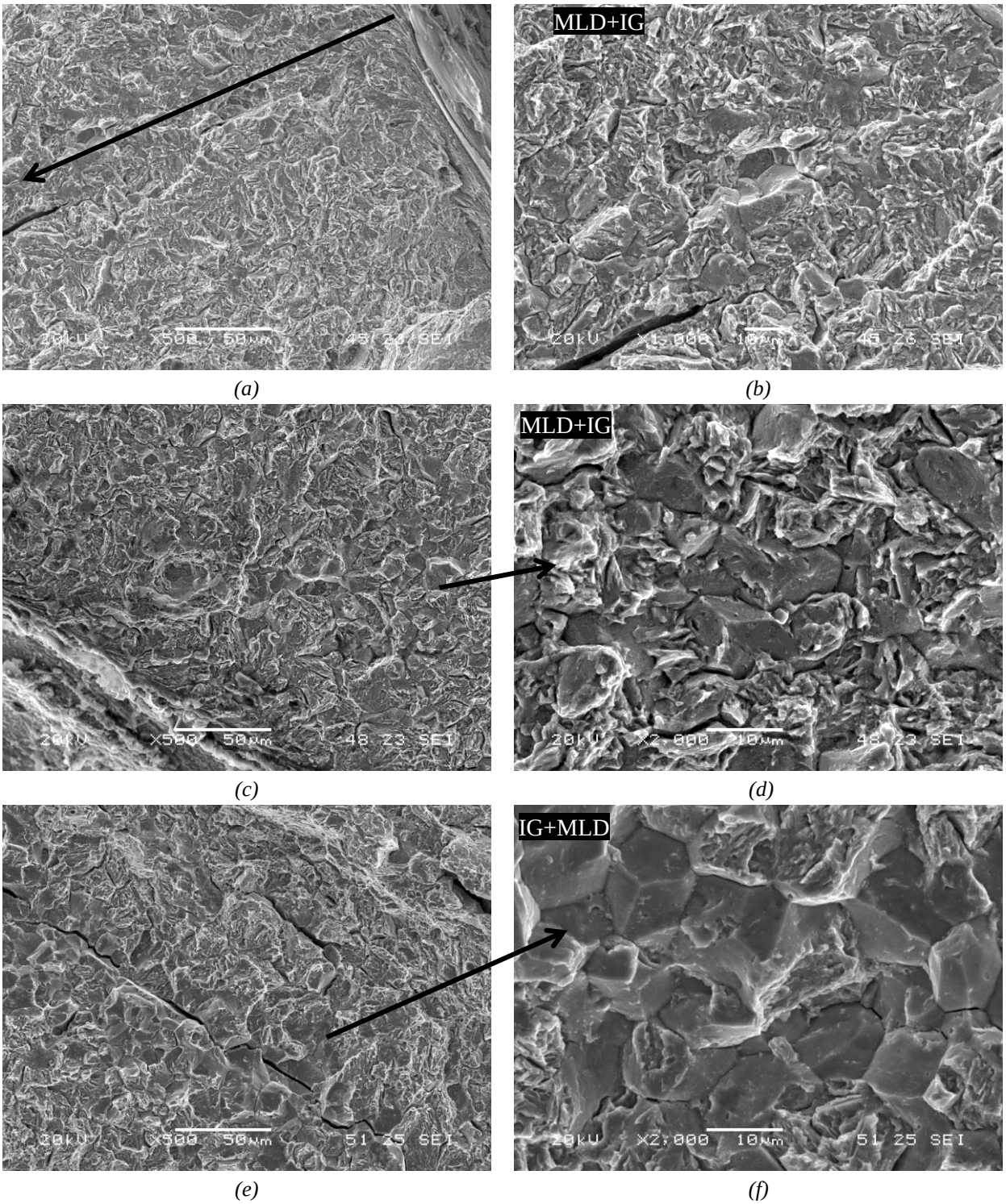

(a) *(b)*

(c) *(d)*

(e) *(f)*

Figure 4.49. Fracture micromechanisms (MLD and IG) of notched tensile specimens tested with hydrogen at a displacement rate of 0.004mm/min. 42CrMo4 steel quenched and tempered for two hours at (a, b) 600ºC, (c, d) 550ºC and (e, f) 500ºC.

In these steel grades the observed fracture micromechanism (pre-charged specimens) was always a mixture of MVC, MLD and intergranular fracture (IG). While in the bulk of the specimens, MVC (with elongated microvoids) was the predominant micromechanism, a combination of MLD and IG were the characteristic features observed at the periphery and also along some radial

"paths" leading from the periphery to the centre of the specimen. The extension of this outer region increases with the hardness of the steel (i.e., decreasing tempering temperature), being greater than 250 μm in all cases. Examples of these characteristic brittle failed surfaces are shown in Figure 4.49. Furthermore, the extent of the intergranular fracture region (clean facets) is larger in the grade with the highest hardness, 42CrMo4-500, which also gave rise to the highest embrittlement indexes, as was seen in Table 4.20. Additionally, the estimated grain size directly measured on these fractographs was around 15-20 μm, which corresponds to the prior austenite grain size measured on the polished and etched sections of these steels (Figure 4.1(a)).

Now, in order to explain the aforementioned experimental results, the distribution of the local normal stress, stress perpendicular to the notch plane, σ_{22}, the hydrostatic stress, σ_h, and the Von Mises stress, σ_{VM}, were simulated along a radial path, defined from the free surface at the tip of the notch (x=0) to the centre of the specimen in the notched section (x=2.5 mm). The σ_{VM}/σ_{ys} ratio versus distance from notch tip at an applied stress equal to the notch tensile strength corresponding to the five analysed steel grades is shown in Figure 4.50. The extension of the plastic region ($\sigma_{VM}/\sigma_{ys} > 1$) varies between 100 and 180 μm, increasing when decreasing the yield strength of the steel (higher tempering temperature). It is then worth noting that, in all the cases, most of the specimen is only elastically strained, except for a very small region close to the stress concentrator.

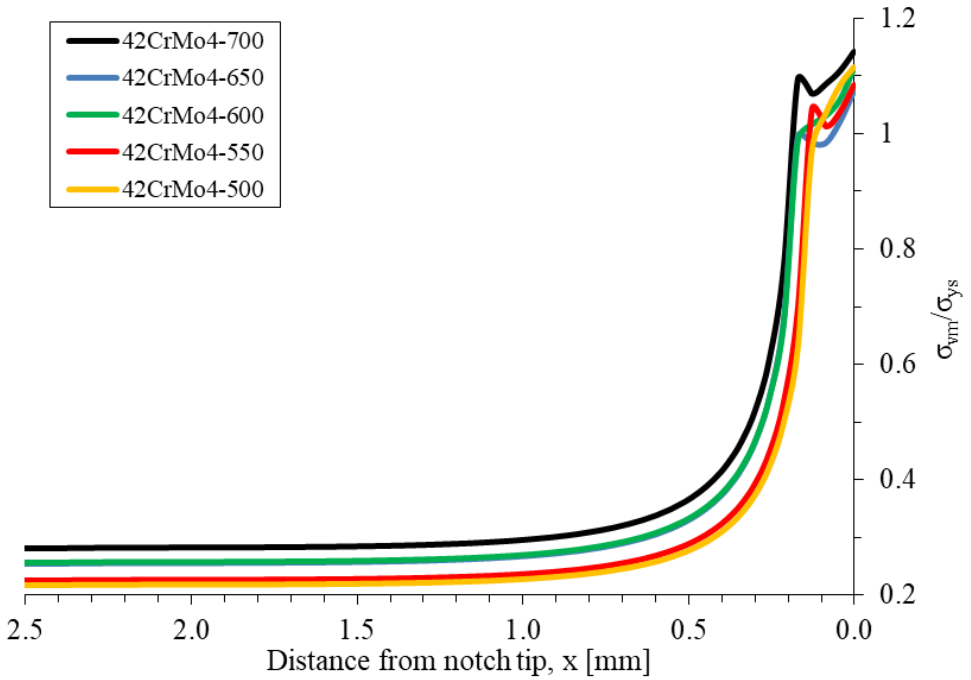

Figure 4.50. Distribution of σ_{VM}/σ_{ys} along the radial direction when the applied net stress is equal to the notch tensile strength. 42CrMo4 steel quenched and tempered at different temperatures.

Figure 4.51 shows the evolution of σ_{VM}, σ_h, and σ_{22} during the application of the load for one of the grades (42CrMo4-650). The two lowest stress profiles correspond to essentially full elastic loadings ($\sigma_{VM} \leq \sigma_{ys}$ = 880 MPa). When a higher load is applied, a plastic zone develops in the front of the notch and the last represented stress profile corresponds to the instant of the specimen

failure. It is also noted that once a plastic zone is developed ($\sigma_{VM} > \sigma_{ys}$), a peak in the Von Mises and in the hydrostatic stress profiles is produced at a certain depth of the notch tip. The location of this peak displaces to larger depths when loading is increased.

Finally, Figure 4.52 shows, for the five grades, the evolution of σ_h, and σ_{22} versus distance from the notch tip, x, at an applied stress equal to the notch tensile strength. The level of the normal stress and hydrostatic stress increases, especially in the region closer to the notch tip, as the yield strength of the steel is increased and, at the same time, it is also worth noting the displacement of the maximum of both aforementioned stresses to a lower depth.

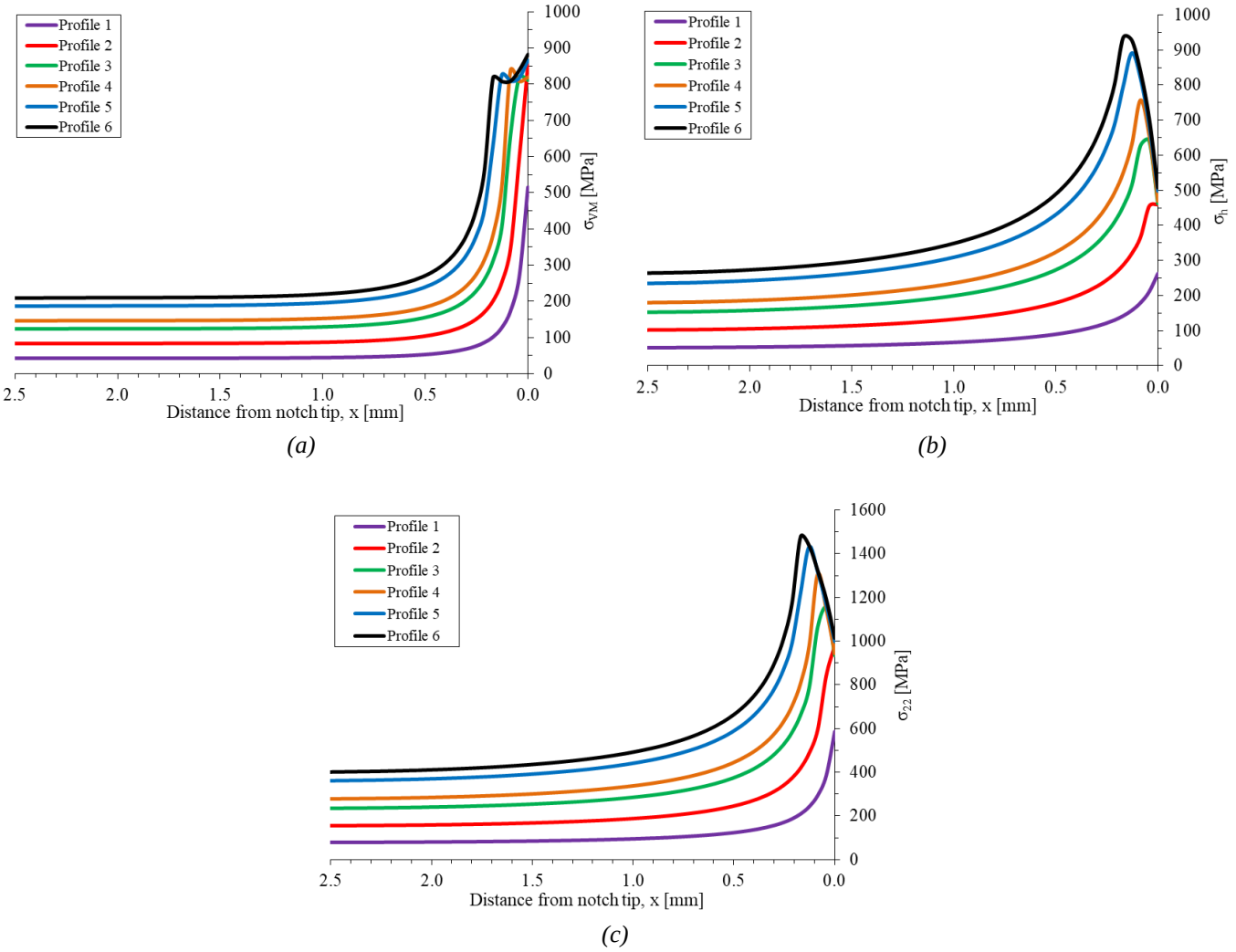

Figure 4.51. Distribution of (a) σ_{VM}, (b) σ_h and (c) σ_{22} along the radial direction for six different loading steps in 42CrMo4-650 steel grade. Applied load increases from 1 to 6.

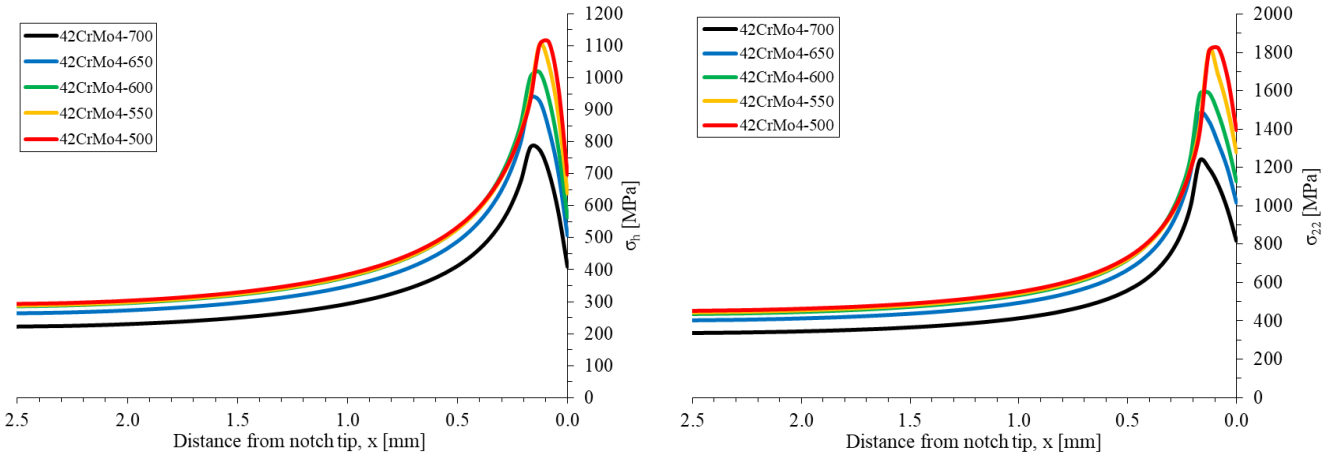

Figure 4.52. Distribution of (a) σ_h, and (b) σ_{22} along the radial direction when the applied net stress is equal to the notch tensile strength. 42CrMo4 steel quenched and tempered at different temperatures.

4.6.1.2. Discussion related to steels tempered at different temperatures

It is well known that the internal hydrogen distribution in medium-high strength steels submitted to external loads is governed by the local hydrostatic stress [36]. Due to this phenomenon, hydrogen atoms diffuse along the steel microstructure (assisted by dislocation motion when a plastic zone is present) to reach the region submitted to the highest hydrostatic stress, located near the notch tip (see Figure 4.51 and Figure 4.52). As a result of the accumulation of hydrogen in this region, a critical hydrogen concentration is reached, leading to premature failure of the specimen under the applied load [44].

As a summary of the results presented so far, Figure 4.53 shows the embrittlement indexes calculated for the notch tensile strength and the reduction in area (for a displacement rate of 0.004 mm/min) versus the Vickers hardness of the steels (inversely related to the tempering temperature, Figure 4.2). The fracture micromechanisms predominant in the peripheral region of the failed specimen and their approximate hydrogen evolution along the test are also included on this figure.

A significant increase of both embrittlement indexes with increasing steel hardness is noted. This trend is consistent with the change appreciated in the fracture micromechanisms acting in the peripheral region just ahead of the notch (where the specimen failure is triggered). MVC with a small fraction of CMD was the predominant failure micromechanism in the grade with the lowest hardness (tempered at 700ºC), while MLD and a combination of MLD+IG were the operative failure micromechanisms in the case of the steel grades with intermediate and highest hardness, respectively. Now, it should be recalled that hydrogen embrittlement is controlled by local stress and local hydrogen concentration, and only occurs when the critical combination of both factors is satisfied in some specific microstructure units.

The MVC micromechanism was always the only failure mechanism observed in the uncharged specimens of all grades, while the presence of hydrogen in the interior regions of the pre-charged specimens of the grades with the lowest hardness, 42CrMo4-700 and 42CrMo4-650, although maintaining the same operative micromechanism, gave rise to larger and shallower dimples (see

Figure 4.46(a)), as already stated in [250]. According to the hydrogen-enhanced localized plasticity mechanism (HELP) [35,251], the presence of internal hydrogen increases the mobility of dislocations enabling them to move under lower stresses, providing plasticity localization on the notch region, where shallow dimples are produced and grow, given rise to very large voids, as the ones already shown in Figure 4.46(a). When this was the operative micromechanism in the peripheral region of the specimen, although mixed with some matrix-carbide interface decohesion (42CrMo4-700), the effect of hydrogen was the lowest (this steel also had the lowest hydrogen content, 1.2-0.8 ppm, and lowest density of trapping sites), being the embrittlement index non-significant for the strength and around 20% for the reduction of area.

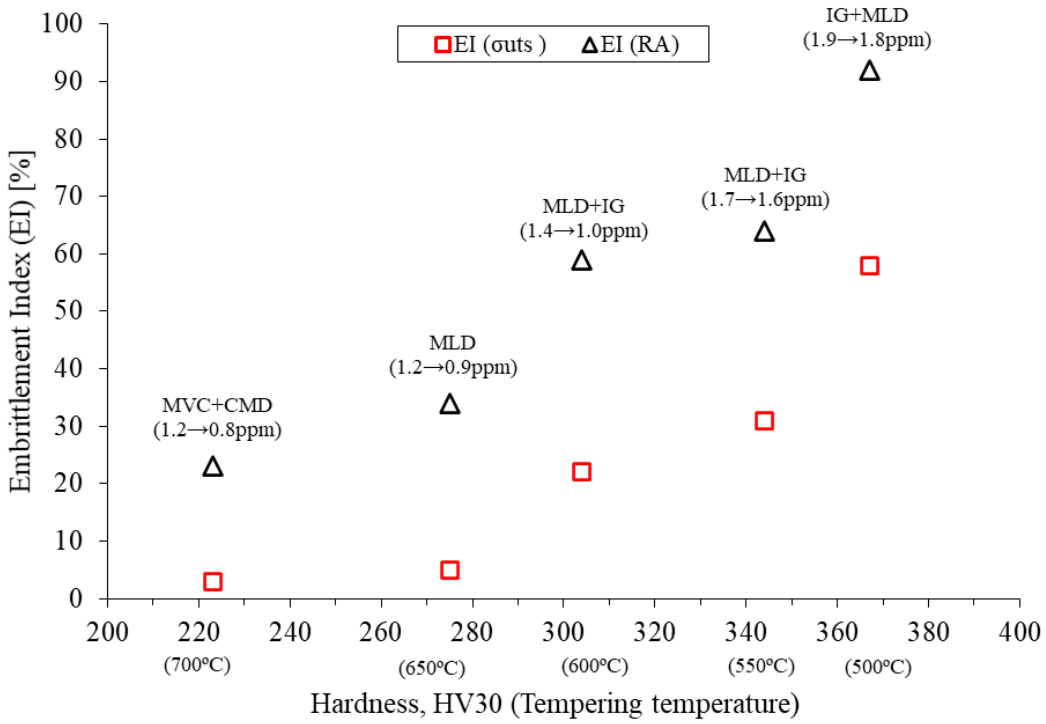

Figure 4.53. Influence of the steel hardness (tempering temperature) on the embrittlement indexes for notched tensile strength and reduction in area (displacement rate: 0.004mm/min). The operative fracture micromechanisms in the peripheral region and approximate hydrogen evolution are included.

In all the other grades, ductile features (MVC) are only observed in the interior of the specimens and brittle areas were present at the notch tip region [139,252], due to the stress profiles described in Figure 4.50 and Figure 4.51. Failure initiates at the plastic zone at the tip of the notch, where normal and hydrostatic stresses are larger, and hydrogen accumulates driven by the high hydrostatic stress. By the contrary, in the centre of the specimen and due to the relatively low level of the local hydrostatic stress, hydrogen does not reach critical values and failure took always place in a ductile manner (MVC).

In the case of the steel grade tempered at 650ºC the existence of MLD was detected in the region just ahead of the notch. As it was observed in Figure 4.52, hydrostatic stress reaches its peak value at a depth around 150 μm. This region suffered the greatest embrittlement, as it was shown in Figure 4.48, where this decohesion micromechanism (HEDE) was observed at a narrow peripheral region, with an extension of approximately 40-100 μm. This mechanism is related to

hydrogen accumulation in martensite block, packet and lath interphases, decreasing the necessary energy for their decohesion. The occurrence of MLD requires a higher accumulation of hydrogen in the notch region and, in this case, it was attained due to the existence of a higher density of hydrogen traps and a higher local hydrostatic stress, which led to higher local hydrogen concentrations. The embrittlement produced by MLD (failure initiates just ahead of the notch under this mechanism and MVC takes place only afterwards in the centre of the specimen) was evident in Figure 4.53, when the measured embrittlement indexes of the two grades with the lowest hardness are compared.

A combination of MLD and intergranular fracture (IG) was observed in the steel grades with the highest hardness (tempered below 600ºC), giving rise to the highest embrittlement indexes. Indeed, a 50% embrittlement of the notched strength was surpassed in the grade with the highest hardness. This is a direct consequence of: (I) the notched specimens of these steels had higher initial hydrogen content and trap density and (II) they were subject to higher local hydrostatic stress due to its higher strength. Therefore, the accumulation of hydrogen ahead of the notch front was the highest, giving also rise to decohesion along the prior austenitic grain boundaries (IG micromechanism). The area covered by this combined mechanism (MLD+IG) was the largest in the grades with the highest hardness, in accordance with the increment of their corresponding embrittlement indexes. Moreover, when comparing Figure 4.49(b), (d) and (f), it is worth noting that the fraction of IG micromechanism increases with steel hardness, being predominant in the grade tempered at 500ºC.

Recent studies have shown that intense slip bands (deformation bands) are present beneath intergranular (IG) and quasi-cleavage (MLD) fracture surfaces as a consequence of the dislocation activity enhancement prompted by hydrogen (according to the HELP mechanism) [40,253]. The notch area reduction measured in all our tests under the lowest displacement rate (except for the steel grade with the highest strength), is the best evidence of the existence of certain plasticity in the process region before failure. Therefore, hydrogen redistribution takes place among the microstructural traps existing in the process region submitted to high hydrostatic stress (notch tip region). This hydrogen accumulation on internal interfaces (martensite laths and prior austenite grain boundaries) takes place until hydrogen concentration is enough that a crack initiates and propagates by interface decohesion driven by the action of the applied local stress [23]. Nagao et al. [40] explain this mechanism as a concerted action of HELP and HEDE mechanisms whose action is assisted by the hydrogen accumulated on the internal boundaries and called it hydrogen-enhanced-plasticity mediated decohesion.

As a summary of all this discussion, the main effects of the steel microstructure on the hydrogen embrittlement of quenched and tempered CrMo steels are graphically depicted in Figure 4.54.

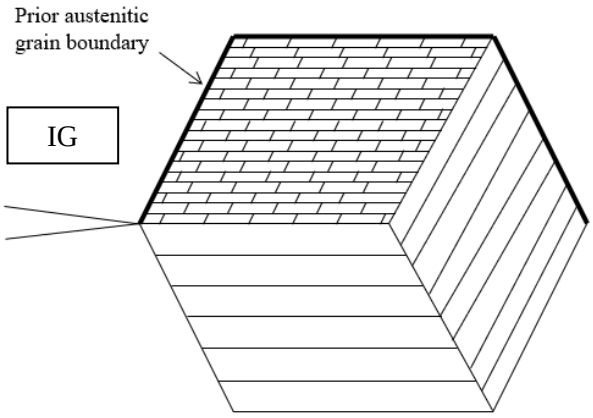

LOW TEMPERING TEMPERATURE

High hardness and yield strength
Strongly distorted interphases
High dislocation density
High local hydrogen content
High local stresses

(a)

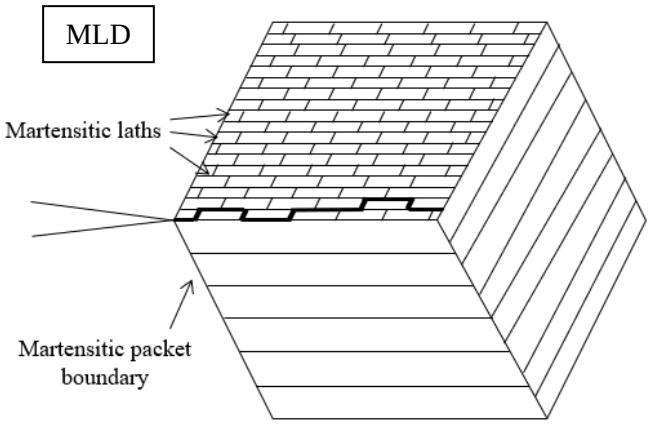

MEDIUM TEMPERING TEMPERATURE

Medium hardness and yield strength
Distorted interphases
Medium dislocation density
Medium local hydrogen content
Medium local stresses

(b)

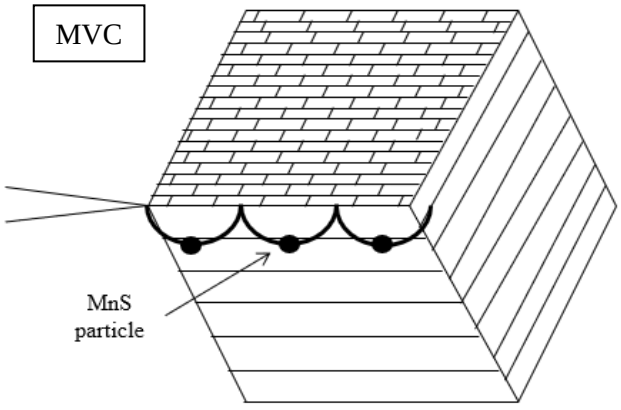

HIGH TEMPERING TEMPERATURE

Low hardness and yield strength
Relaxed interphases
Low dislocation density
Low local hydrogen content
Low local stresses

(c)

Figure 4.54. Failure micromechanisms acting ahead of a mechanically loaded notch in hydrogen pre-charged quenched and tempered steels. Influence of tempering temperature. (a) IG, (b) MLD and (c) MVC.

It should be recalled that after low temperature tempering, relaxation of the quenched microstructure is still quite low and a lot of structural defects with a large capacity to accumulate hydrogen atoms can be found at the prior austenitic grain boundaries. In this situation, when a normal load is applied in presence of internal hydrogen, hydrogen accumulates preferentially at the prior austenitic grain boundaries existing in the notch front region submitted to high hydrostatic stress, giving rise to decohesion of these interfaces when a high enough local stress is attained. As a result, intergranular fracture takes place under a much lower tensile stress than the stress required to collapse the same specimen without hydrogen.

As the tempering temperature increases, the steel microstructure relaxes, the distortion of the austenitic grain boundaries progressively diminishes and their capacity to accumulate hydrogen, i.e., density of hydrogen traps, decreases at the same time. In this case, the interfaces between martensite blocks, packets and laths are now the sites where hydrogen accumulation is more abundant and the predominant fracture micromechanism changes from IG to MLD, decreasing the corresponding embrittlement indexes. It should also be noted that the surface per unit volume of all these interfaces is much greater than those related to the austenitic grain boundaries. As the yield strength of the steels quenched and tempered at higher temperatures decreases, local normal stress and hydrostatic stress in the process zone also decrease, contributing to improve the embrittlement indexes.

Only when the tempering temperature is high enough, microstructure relaxation reach a level at which hydrogen accumulation in the aforementioned interfaces is low and not sufficient to produce decohesion at large scale. In this situation, hydrogen distributes more uniformly in the notch front region, local accumulation is not important, and HELP becomes the predominant mechanism. Dislocations move easily in the process zone just ahead of the notch, plastic deformation is enhanced, and finally fracture takes place by means of a fully ductile micromechanism (nucleation on MnS inclusions, growth, and coalescence of microvoids, MVC). Failure takes place now under only a slightly lower level of stress than in the absence of hydrogen. Note that carbide-matrix interface decohesion (CMD) can be seen as a particular case of MVC (decohesion takes place at small carbides precipitated during tempering, instead that at larger MnS inclusions) in which this particular decohesion is enhanced by the accumulation of hydrogen.

4.6.1.3. Effects of hydrogen on the CGHAZ of a 42CrMo4 weld

4.6.1.3.1. Tensile tests on smooth specimens

Figure 4.55 and Table 4.22 show the stress-strain curves and the associated tensile parameters obtained for the coarse grain steel grades (42CrMo4-700-CG and 42CrMo4-725-CG) in the absence of hydrogen. Fine grain steel (42CrMo4-700) is also included for comparison. It is noted that the steel with the largest austenitic grain size (100-150μm) exhibits a slightly higher strength when tempered at the same temperature and time, justified by its greater hardness. On the other hand, the ductility parameters were approximately similar in both steel grades. When the tempering temperature and time are increased in the coarse grain steel, 42CrMo4-725-CG, both the yield strength and the tensile strength are significantly reduced, and tensile elongation slightly increased.

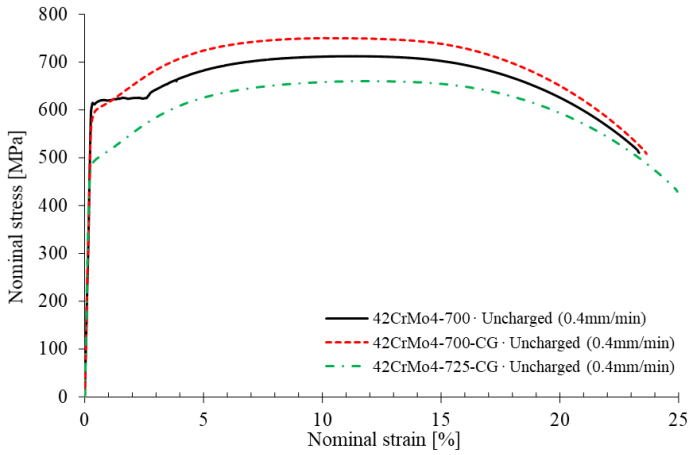

Figure 4.55. Stress-strain curves obtained with uncharged smooth tensile specimens (0.4 mm/min) of 42CrMo4-700, 42CrMo4-700-CG and 42CrMo4-725-CG grades.

Steel grade	v_{test} [mm/min]	Test duration [h]	C_H [ppm]	σ_{ys} [MPa]	σ_{ut} [MPa]	e [%]	Z [%]
700	0.4	0.33	-	622±2	710±5	22.6±0.6	62.8±1.7
	0.4	0.35	1.2	585±7	694±1	22.8±1.6	63.9±0.4
	0.04	2.7	1.2→1.1	590	689	21.7	62.6
700-CG	0.4	0.35	-	600	750	23.6	65.5
	0.4	0.35	1.0	610	755	22.5	67.8
	0.04	3.3	1.0→0.9	593	731	20.2	67.6
	0.004	29.4	1.0→0.8	580	710	18.1	65.7
725-CG	0.4	0.37	-	498±6	665±7	24.4±0.8	70.2±0.2
	0.004	33.5±0.1	0.5→0.4	489±1	642±2	23.3±1.2	67.7±0.5

(a)

Steel grade	v_{test} [mm/min]	$EI_{(\sigma ys)}$ [%]	$EI_{(\sigma ut)}$ [%]	$EI_{(e)}$ [%]	$EI_{(Z)}$ [%]
700	0.4	-	-	-	-
	0.4	5.6	2.2	0	0
	0.04	5.1	3.0	4.0	0.3
700-CG	0.4	-	-	-	-
	0.4	0	0	4.7	0
	0.04	1.2	2.5	14.4	0
	0.004	3.3	5.3	23.3	0
725-CG	0.4	-	-	-	-
	0.004	1.7	3.5	4.5	3.5

(b)

Table 4.22. (a) Results of the tensile tests performed at different displacement rates on smooth specimens (uncharged and hydrogen pre-charged) of the fine grain (42CrMo4-700) and the coarse grain (42CrMo4-700-CG and 42CrMo4-725-CG) grades. (b) Corresponding embrittlement indexes.

Table 4.22(a) also shows the results relative to the tensile tests performed on smooth hydrogen pre-charged specimens under different displacement rates, along with the test duration and approximate hydrogen content. The values of the embrittlement indexes associated with the

different tensile properties are reported in Table 4.22(b). Additionally, Figure 4.56 shows for both coarse grain steels, the stress-strain curves obtained using uncharged and hydrogen pre-charged specimens.

As previously mentioned, in the case of the fine grain steel (showed in Figure 4.40(a)), with a smaller prior austenite grain size and lower hardness, minor differences were detected between tests carried out on uncharged and on hydrogen pre-charged specimens, regardless the applied displacement rate (in this case, all the embrittlement indexes remained below 6%). However, in the case of the coarse grain steel tempered at the same temperature, Figure 4.56(a), although the effects of hydrogen were also negligible in terms of yield strength and ultimate tensile strength, a certain reduction in ductility was observed, specially reflected in the tensile elongation. In fact, the embrittlement index associated to this parameter, $EI_{(e)}$, gradually increases as the displacement rate decreases.

Therefore, an additional ultra-low displacement rate test (0.004 mm/min) was performed, in which an $EI_{(A)}$ value over 20% was reached. Regarding the curves shown in Figure 4.56(b), the application of a more intense tempering treatment (725ºC for 4h) on the coarse grain microstructure results in a complete ductility restauration, being now the $EI_{(e)}$ below 5% for a displacement rate of 0.004 mm/min. Nevertheless, is should be born in mind that the yield strength of this steel was reduced from 622 MPa to 498 MPa.

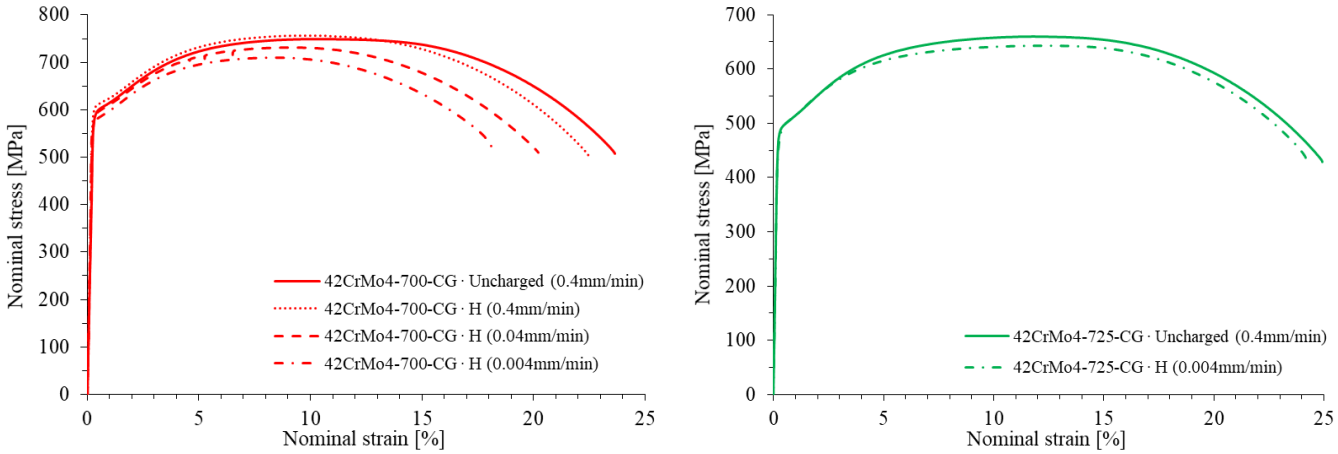

Figure 4.56. Stress-strain curves obtained with uncharged and hydrogen pre-charged smooth tensile specimens of (a) 42CrMo4-700-CG and (b) 42CrMo4-725-CG grades.

The fracture micromechanism observed by means of SEM on the failure surfaces of the hydrogen uncharged smooth tensile specimens of both coarse grain steels was always fully ductile, being characterized by microvoid coalescence (MVC), as can be seen in Figure 4.57.

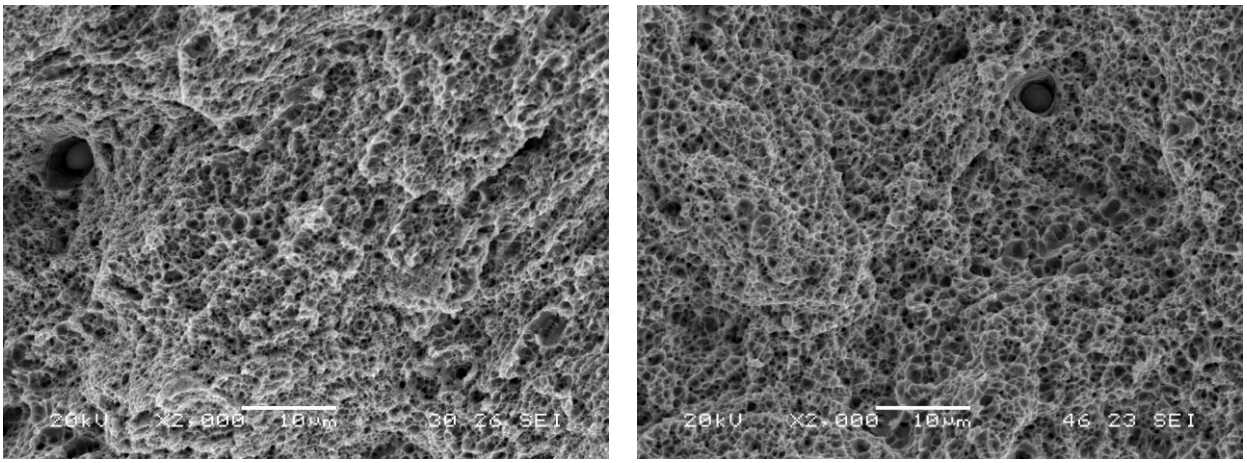

(a) *(b)*

Figure 4.57. Fracture micromechanism of smooth uncharged tensile specimens (0.4 mm/min) of (a) 42CrMo4-700-CG and (b) 42CrMo4-725-CG.

No significant changes in the failure micromechanism were either observed in the fracture surface of the tensile specimens of both coarse grain grades tested under internal hydrogen, Figure 4.58. Indeed, microvoid coalescence (MVC) is the only failure micromechanism detected in the fracture surfaces of both steels. The only remarkable aspect related to the fracture surface of 42CrMo4-700-CG steel tested with internal hydrogen under the lowest displacement rate (Figure 4.58(a)) is the larger size of their microvoids (compare images presented in Figure 4.58(a) and (b)). In fact, the maximum embrittlement index was reported for this specimen.

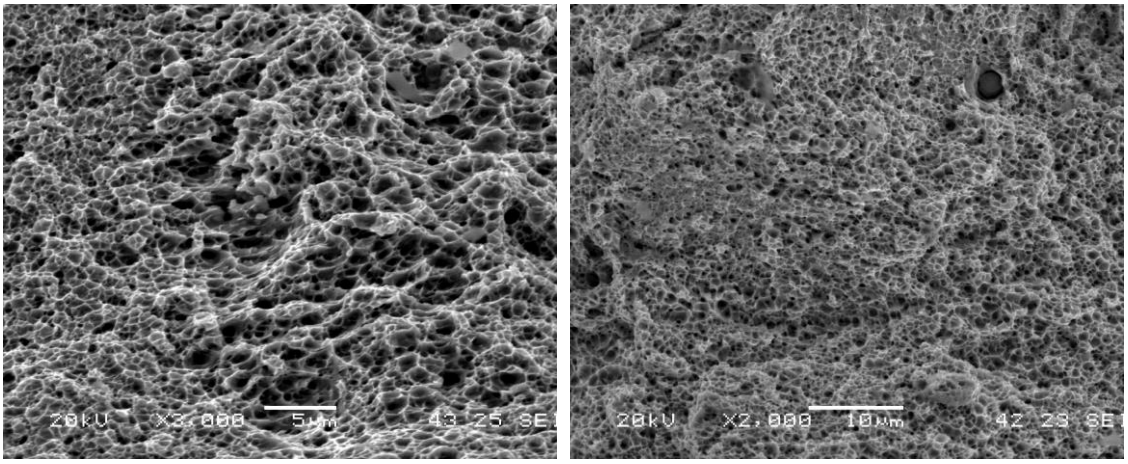

(a) *(b)*

Figure 4.58. Fracture micromechanism of hydrogen pre-charged smooth tensile specimens (0.004 mm/min) of (a) 42CrMo4-700-CG and (b) 42CrMo4-725-CG.

4.6.1.3.2. Tensile tests on notched specimens

The stress-strain curves obtained with uncharged and hydrogen pre-charged notched specimens (K_t=4.25) on the fine (42CrMo4-700) and both coarse grain grades, tested at different displacement rates (only tests at 0.004 mm/min were performed with the H-charged 42CrMo-725-CG), are shown in Figure 4.59.

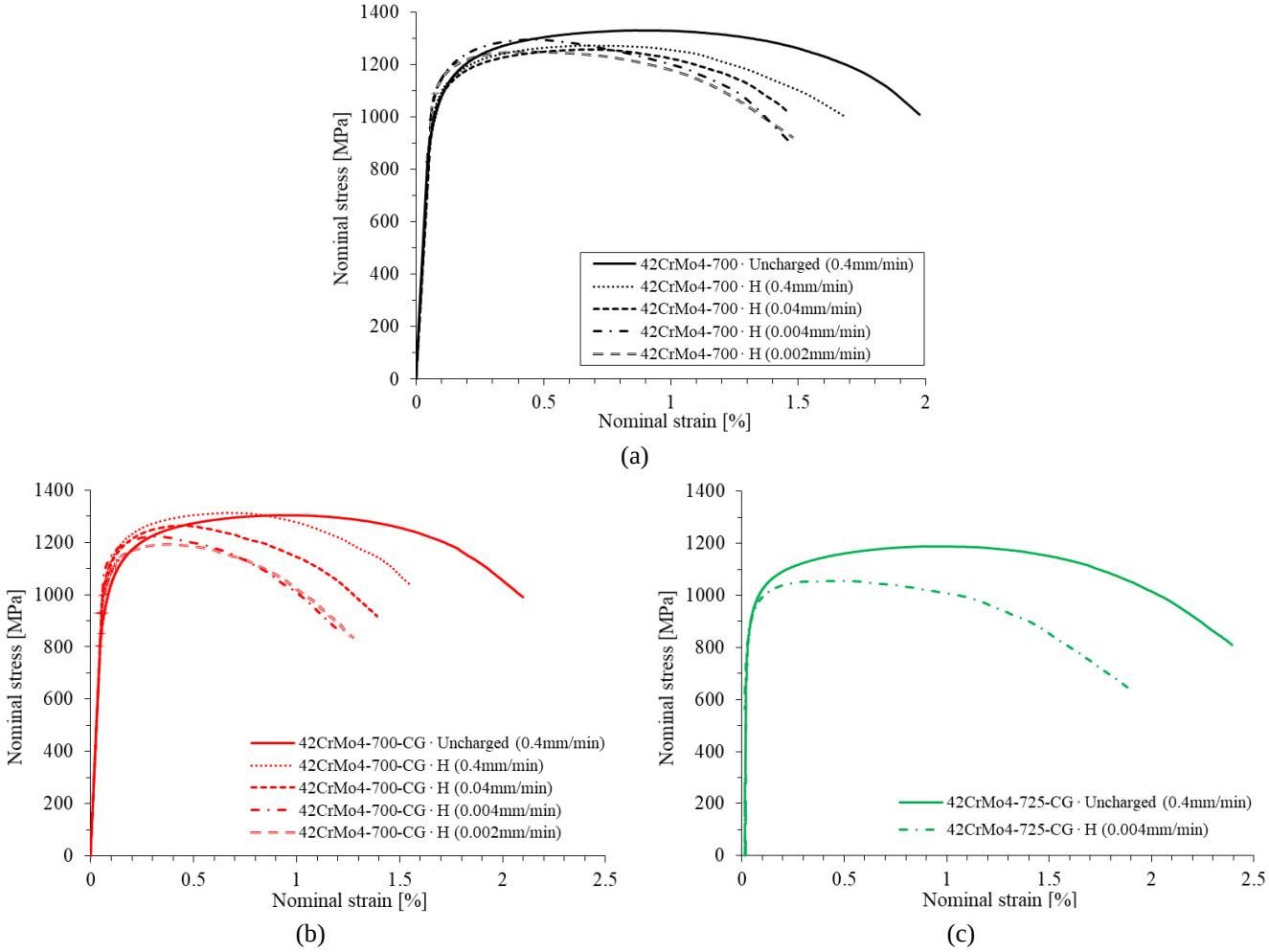

Figure 4.59. Stress-strain curves of the uncharged and hydrogen pre-charged notched tensile specimens (K_t=4.25) of (a) 42CrMo4-700-CG and (b) 42CrMo4-725-CG steel. Influence of the applied displacement rate.

Additionally, Table 4.23(a) shows the values obtained for the notch tensile strength (σ_{uts}), maximum deformation (ε_{max}) and reduction in area (RA) using uncharged and hydrogen pre-charged specimens tested under different displacement rates. As in previous tables, the embrittlement indexes calculated for the aforementioned mechanical properties, test duration and the approximate evolution of the average hydrogen content (C_H) in the specimens during the test are also included in the table. Furthermore, the prevailing fracture micromechanisms and their extension measured on the failed surfaces, which was fully analysed afterwards, are also presented in Table 4.23(b).

Regarding the 42CrMo4-700 (previously explained) and 42CrMo4-700-CG grades, it is worth pointing out that, as the test displacement rate decreases, ductility (ε_{max} and RA) also decreases, being this drop especially remarkable in the coarse grain version of the steel (42CrMo4-700-CG). However, under the slowest displacement rate (0.002 mm/min), the negative effect of hydrogen seems to finally stabilize, due most probably to relevant hydrogen losses in the course of the test (the duration of these tests were 25-35 hours). In addition, 42CrMo4-725-CG exhibits a significant reduction of both embrittlement indexes related to ductility, but similar to the ones corresponding to the fine grain steel, that is much lower than those of the other coarse grain grade.

Steel Grade	v_{test} [mm/min]	Test duration [h]	C_H [ppm]	σ_{uts} [MPa]	ε_{max} [%]	RA [%]	$EI_{(\sigma uts)}$ [%]	$EI_{(\varepsilon max)}$ [%]	$EI_{(RA)}$ [%]
700	0.4	0.20	-	1330	2.0	12.5	-	-	-
	0.4	0.15	1.2	1273±21	1.7	11.8±0.1	4.3	14.7	5.6
	0.04	1.3	1.2→1.1	1258±20	1.5	10.3±1.6	5.4	25.9	17.9
	0.004	13.5	1.2→0.8	1294	1.5	9.6	2.7	24.9	23.1
	0.002	35.9	1.2→0.5	1250±61	1.5±0.3	9.8±0.6	6.1	24.9	21.2
700-CG	0.4	0.22	-	1304	2.1	13.3	-	-	-
	0.4	0.18	1.0	1313	1.6	10.8	0	23.8	18.5
	0.04	1.6	1.0→0.9	1238±35	1.4	8.7±0.8	5.8	33.3	34.8
	0.004	13.3	1.0→0.8	1206±23	1.2	7.4±0.3	8.3	42.9	44.2
	0.002	25.7	1.0→0.7	1193	1.3	6.1	9.3	38.1	54.0
725-CG	0.4	0.2	0.5	1166±11	2.4±0.1	14.4±0.2	-	-	-
	0.004	13.9	0.5→0.45	1057±1	1.9±0.1	11.7±0.1	9.4	21.1	19.0

(a)

Steel Grade	v_{test} [mm/min]	C_H [ppm]	Fracture Micromechanisms*	
			Periphery	Internal region
700	0.4	-	MVC	
	0.4	1.2	MVC	
	0.04	1.2→1.1	MVC (elongated)	
	0.004	1.2→0.8	CMD (175 μm)	MVC (elongated)
	0.002	1.2→0.5	MLD (20 μm) + CMD (120 μm)	MVC (elongated)
700-CG	0.4	-	MVC	
	0.4	1.0	MLD (10 μm) + CMD (150 μm)	MVC (elongated)
	0.04	1.0→0.9	MLD (10 μm) + CMD (165 μm)	MVC (elongated)
	0.004	1.2→0.8	MLD (75 μm) + IG (250 μm)	MVC (elongated)
	0.002	1.2→0.7	MLD (75 μm) + IG (375 μm)	MVC (elongated)
725-CG	0.4	-	MVC	
	0.004	0.5→0.45	MVC+CMD+MLD (150 μm)	MVC

(b)

*Table 4.23. (a) Results of tensile tests performed on notched specimens (Kt=4.25) of uncharged and hydrogen pre-charged 42CrMo4-700, 42CrMo4-700-CG and 42CrMo4-725-CG steel grades loaded at different displacement rates. (b) Operative fracture micromechanisms. *MVC: microvoid coalescence; CMD: carbide-matrix interface decohesion; MLD: martensitic lath interface decohesion; IG: intergranular fracture.*

Figure 4.60 provides a summary of all these results. It shows the evolution of the embrittlement indexes associated to the reduction in area (RA), maximum deformation (ε_{max}) and ultimate notch strength (σ_{uts}) in terms of the applied displacement rate (plotted in logarithmic scale). Firstly, it is worth noting that the coarse grain steel tempered at 700ºC suffered in all cases the greatest embrittlement. Nonetheless, regarding the notched strength, only a slight decrease in the embrittlement index (always below 10%) took place, which is a common point in the three grades. As stated previously, the properties related to ductility were those most affected by hydrogen. In fact, under the lowest displacement rates, the embrittlement index related to the reduction in area, $EI_{(RA)}$, reached values over 20% and 50% for the fine and coarse grain size steels respectively tempered at 700ºC. And finally, the worst behaviour of the coarse grain steel tempered at 700ºC

seems to improve to levels similar to the ones of the fine grain steel, when a more intense tempering treatment (in time and temperature) is applied to the coarse grain microstructure.

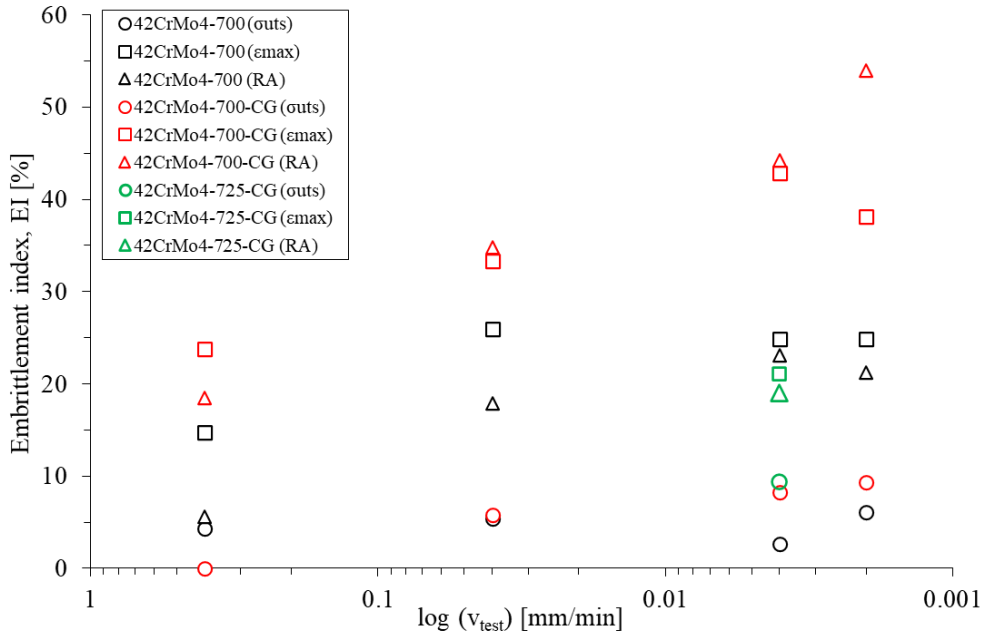

Figure 4.60. Embrittlement indexes associated with the reduction in area (RA), maximum elongation (ε_{max}) and ultimate notch strength (σ_{uts}) versus displacement rate. Hydrogen pre-charged notched tensile specimens.

The fracture surfaces corresponding to the notched tensile specimens of both coarse grain steels were analysed using SEM and the main operative fracture micromechanisms were identified (Table 4.23(b)). Again, the fracture micromechanism acting on both coarse grain steels tested without internal hydrogen was fully ductile, characterized by microvoid coalescence (MVC). An example relative to 42CrMo4-700-CG (the more sensitive to hydrogen of the two coarse grain grades) is presented in Figure 4.61. The fracture surfaces observed in the notched specimens of the 42CrMo4-700 coarse grain steel tested with internal hydrogen at 0.4 mm/min are shown in Figure 4.62. The bulk of the specimen was characterized by the MVC micromechanism, where elongated microvoids due to the HELP mechanism are appreciated (black arrows in Figure 4.62(a)). Moreover, a flattened peripheral area ahead of the notch tip with an extension of around 150 µm can also be seen in Figure 4.62(b). Apart from the CMD (carbide-matrix interface decohesion mechanism) observed in this region, detail A (Figure 4.62(c)), a small belt (with an extension of about 10 µm) characterized by the decohesion of martensitic lath interfaces (MLD) was also observed, detail B (Figure 4.62(d)). Similar failure micromechanisms were also observed in the specimens tested at 0.04 mm/min.

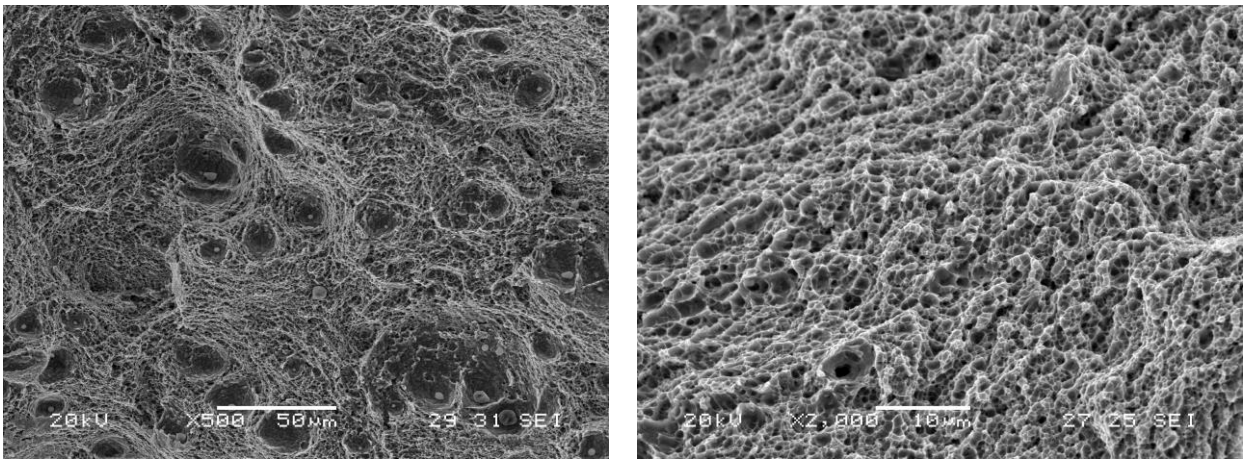

(a) *(b)*

Figure 4.61. Fracture micromechanism in uncharged 42CrMo4-700-CG observed at different magnifications.

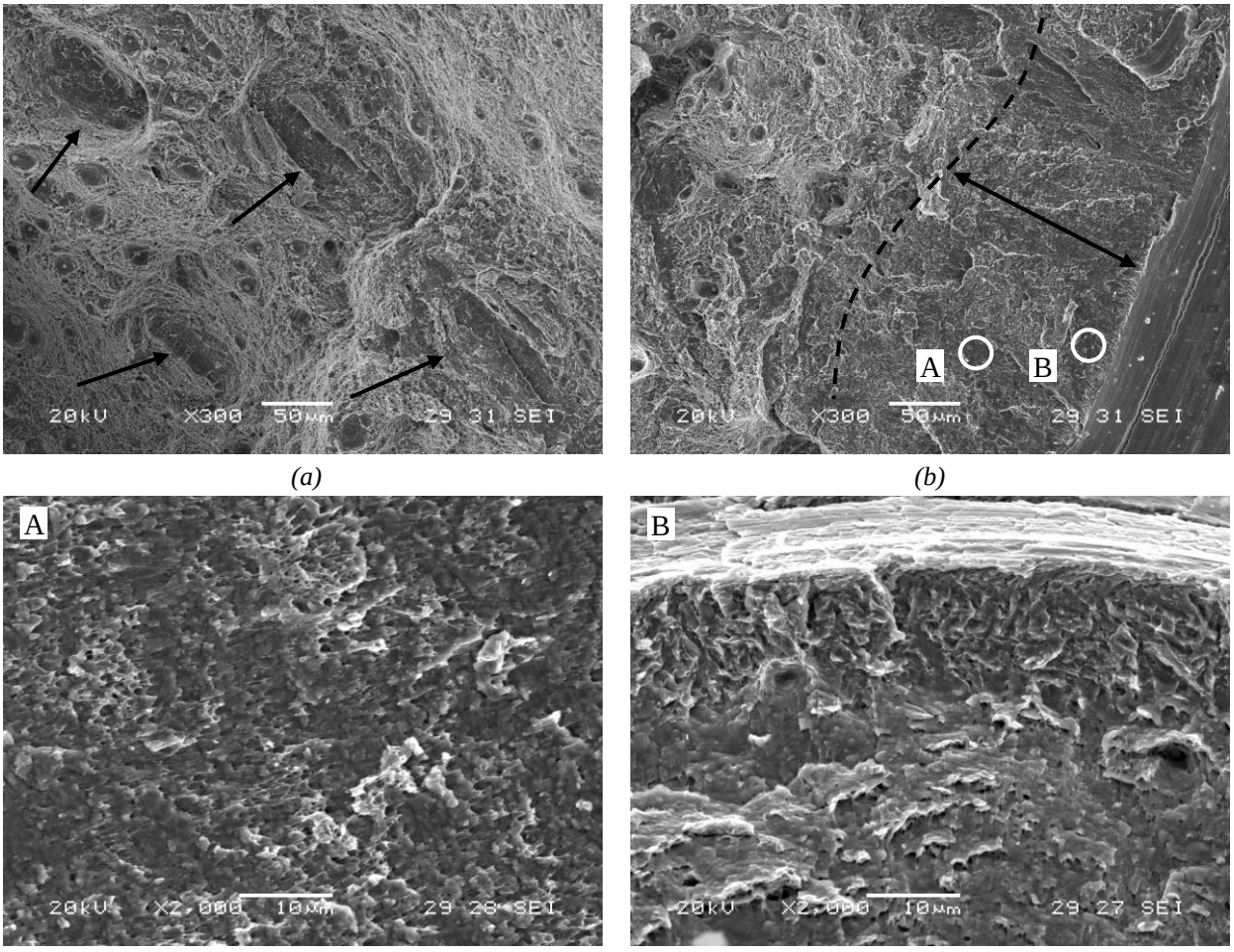

(a) *(b)*

(c) *(d)*

Figure 4.62. Fracture micromechanism of notched tensile specimens of the 42CrMo4-700-CG steel grade tested with internal hydrogen at 0.4 mm/min. (a) Elongated microvoids in the bulk of the specimen, (b, c) CMD (carbide-matrix interface decohesion) at the peripheral belt, and (d) MLD (martensitic lath decohesion) in the most peripheral region ahead of the notch tip.

The fracture surfaces corresponding to the hydrogen pre-charged 42CrMo4-700-CG notched tensile specimens tested at 0.004 mm/min are now shown in Figure 4.63 (similar failure micromechanisms were also observed at the lowest displacement rate of 0.002 mm/min).

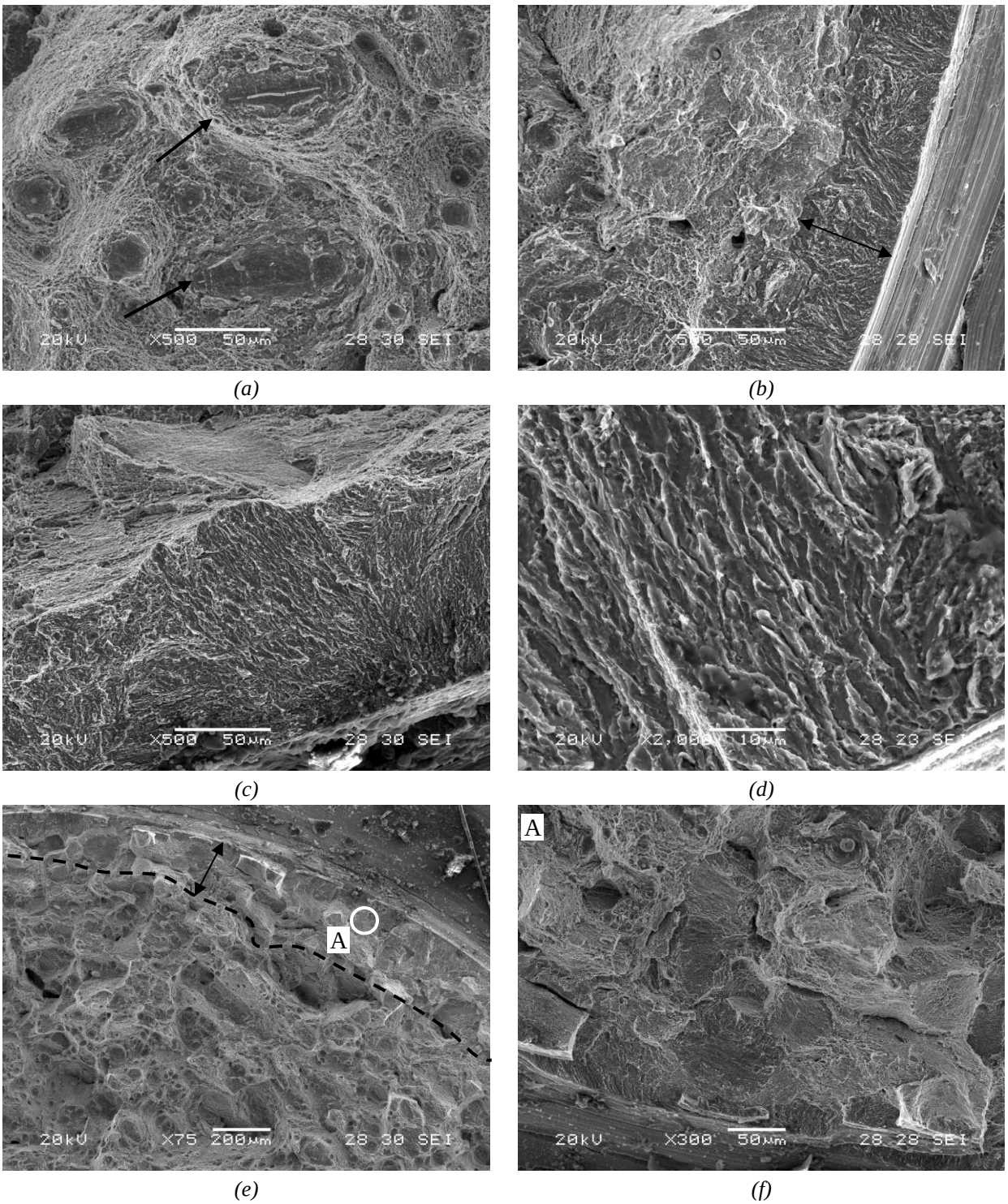

(a) *(b)*

(c) *(d)*

(e) *(f)*

Figure 4.63. Fracture micromechanism of notched tensile specimens of the 42CrMo4-700-CG steel grade tested with internal hydrogen at 0.004 mm/min. (a) Elongated microvoids in the bulk of the specimen, (b, c, d) MLD (martensitic lath decohesion) in the most peripheral region ahead of the notch tip and (e, f) IG fracture also active in some areas of the peripheral region.

Again, as in the previous cases, the operative fracture micromechanism in the interior regions of the specimen was MVC with flat elongated areas, as shown in Figure 4.63(a). A belt with a depth around 50-100 μm, characterized by decohesion along martensitic lath interfaces (MLD), was also detected in the periphery of the specimen (notch tip region). It is shown at different magnifications in Figure 4.63(b, c, d). As expected, the fracture features observed here (martensitic laths) are larger than those observed on the fine grain base steel (see for example Figure 4.48) due to the much greater austenitic grain size present in the 42CrMo4-700-CG grade. Moreover, intergranular fracture mechanisms (IG) were also active in some specific regions of the peripheral region, with depths that can attain even 250 μm from the notch tip (see Figure 4.63(e, f)). The estimated size of the grains directly measured on these fractographies was around 100-150 μm, which corresponds to the prior austenite grain size measured on the polished and etched sections of the steel.

Finally, the fracture surfaces of the hydrogen pre-charged 42CrMo4-725-CG notched tensile specimens tested at the same displacement rate of 0.004 mm/min are shown in Figure 4.64.

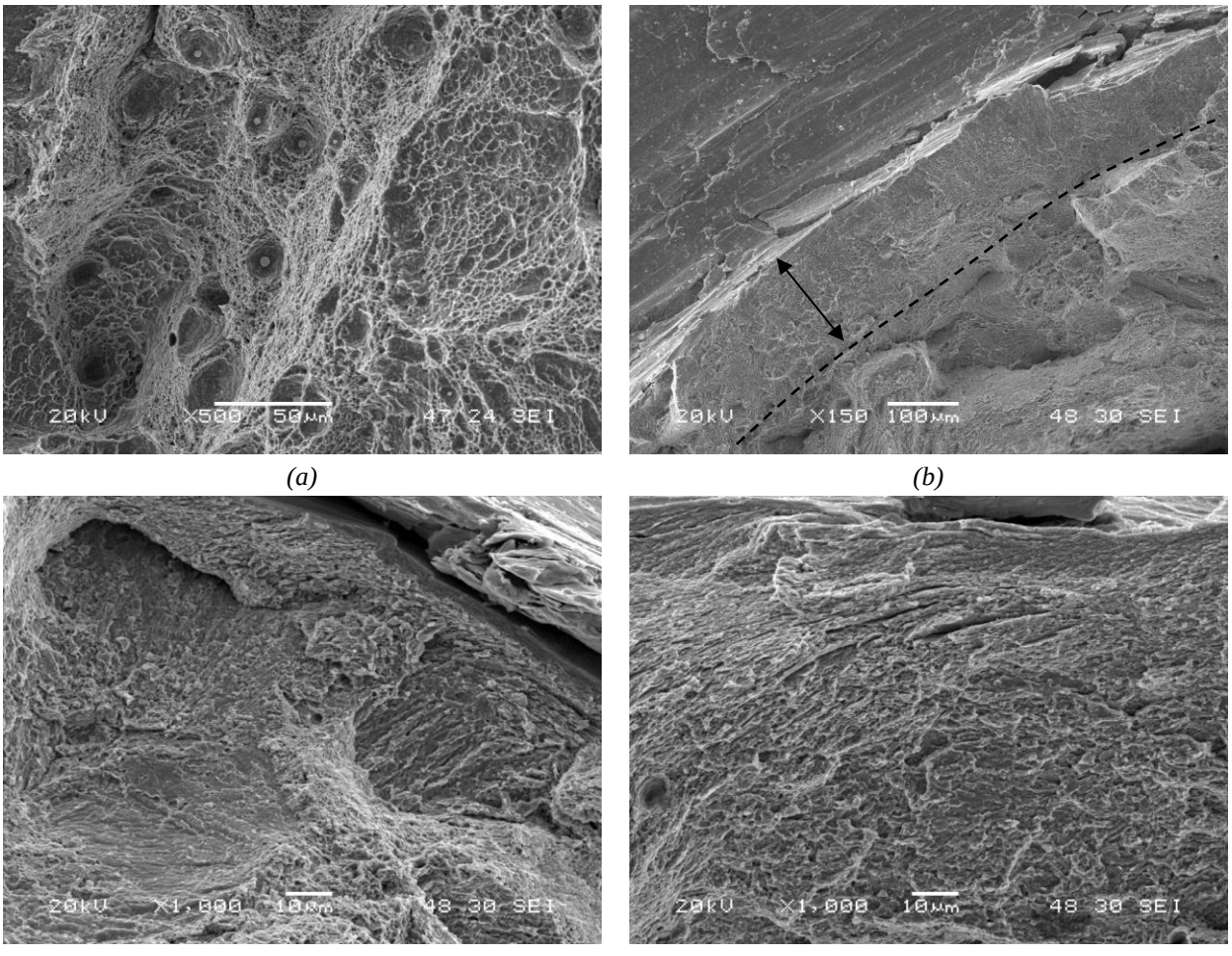

(a) *(b)*

(c) *(d)*

Figure 4.64. Fracture micromechanism of notched tensile specimens of the 42CrMo4-725-CG grade tested with internal hydrogen at 0.004 mm/min. (a) MVC in the inner region of the specimen, (b) flat peripheral region and (c, d) mixture of MVC, CMD and MLD micromechanisms present in the peripheral region.

As expected, based on the previous observations, the operative fracture micromechanism in the inner regions of the specimen was MVC, being in this case the elongated and flat areas rarely present, Figure 4.64(a). In this case, the observations made in the peripheral area match really well with the observed decrease in the elongation and reduction in area embrittlement indexes. As shown in Figure 4.64(b), a flat area of around 150 μm in depth was observed in certain areas of the sample periphery (it was not generalized).The flat topography of this area was characterized by a mix of MVC, CMD and to a lesser extent MLD (no IG fracture was detected), as exemplified in Figure 4.64(c, d). Nevertheless, the existence of this region, where the embrittling effects of hydrogen are still noticeable, explains the 20% drop in ε_{max} and RA. Anyway, the embrittlement indexes of this coarse grain steel grade are now at the same level (or even below) of those relative to the fine grain steel (see Figure 4.60). However, it may be taken into account that this grade also has a reduced strength.

4.6.1.4. Discussion related to fine and coarse grain steels

In order to explain the experimental results described in the previous section, Figure 4.65 shows the distribution of σ_{22}, σ_h and σ_{VM} versus the distance measured from the notch tip calculated on the fine-grained base steel at an applied stress equal to the notch tensile strength.

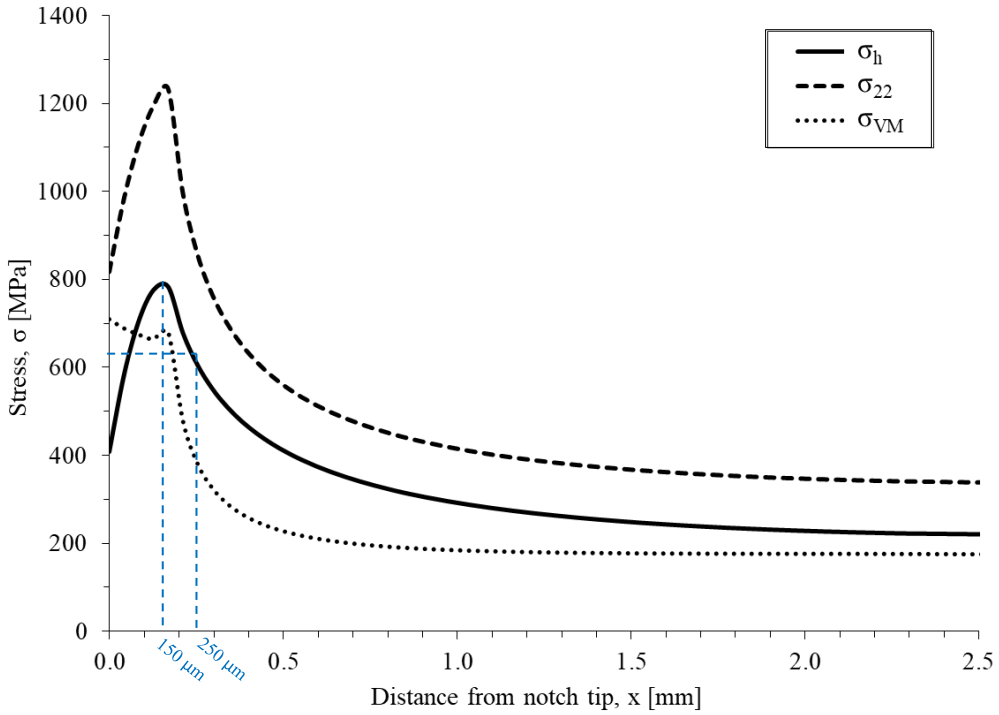

Figure 4.65. Distribution of σ_h, σ_{22} and σ_{VM} along the radial direction when the applied net stress is equal to the notch tensile strength. 42CrMo4-700 base steel grade (fine grain).

As mentioned previously, it is now well known that the hydrogen distribution in a steel specimen with internal hydrogen submitted to an external load is governed by the hydrostatic stress [134][59]. Hydrogen located in the surroundings of the notch tip will diffuse up to the process zone located just ahead of the notch root (driven by the high hydrostatic stress existing in this region, where it is trapped by dislocation entanglements produced in the plastic strained zone), where hydrogen atoms will accumulate and thereby give rise to embrittlement phenomena.

Returning to Figure 4.65, a plastic zone ($\sigma_{VM} > \sigma_{ys}$ = 622 MPa) with a depth of about 180 μm was predicted. Moreover, maximum values of both the normal stress and the hydrostatic stress are also predicted at a certain distance from the notch tip. Specifically, the maximal hydrostatic stress observed in Figure 4.65 reaches 780 MPa at 150 μm from the notch tip and high hydrostatic stresses greater than the yield stress of the steel (σ_{ys}=622 MPa) are found at depths lower than 250 μm. The extension of the region submitted to high hydrostatic stress at the moment of failure of the different notched tensile specimens coincides quite well with the depth of the peripheral belt observed in those specimens in which hydrogen embrittlement micromechanisms (carbide-matrix interface decohesion, CMD, martensite lath interface decohesion, MLD, and intergranular fracture, IG) were observed (Table 4.23(b)). However, martensite lath interface decohesion, MLD, was observed to take place only at very low depths, (between 20 and 75 μm depending on the steel grade) under the most demanding conditions (lowest displacement rates). At such small depths within the plastic zone, the local plastic strain is maximal. Therefore, dislocation density will have significantly increased, and hydrogen will have accumulated on the highly dislocated martensite lath interfaces, where this particular hydrogen embrittlement phenomenon takes place.

On the other hand, the available effective hydrogen diffusion distance, x_H, for the movement of hydrogen atoms during the tensile tests can be approximated by *Equation (4.1*) [45], considering unidirectional hydrogen diffusion towards the notch root (hydrogen transport by dislocations from the bulk into the process zone was not taken into account). Therefore, *Equation (4.1*) can then be used to calculate the effective diffusion distance for hydrogen diffusion in each particular test, in which D_{app} is the apparent hydrogen diffusion coefficient in the steel and t is the elapsed time (total duration of the notched tensile test).

$$x_H = 2\sqrt{D_{app} \cdot t} \qquad \textit{Equation (4.1)}$$

The total duration of the notched tensile tests was given in Table 4.23(a), and the apparent diffusion coefficients of these steels (estimated from the desorption curves) were shown in Table 4.14. Table 4.24 shows these calculated effective hydrogen diffusion distances.

Displacement rate [mm/min]	Diffusion distance, x_H [mm]		
	Fine grain steel (42CrMo4-700)	Coarse grain steel (42CrMo4-700-CG)	Coarse grain steel (42CrMo4-725-CG)
0.4	1.6	0.7	---
0.04	2.8	4.2	---
0.004	9.2	6.8	6.6
0.002	15	9.6	---

Table 4.24. Available effective hydrogen diffusion distance (in mm) in the hydrogen pre-charged notched tensile tests performed at different displacement rates.

It is worth noting that, for a given steel, as the time available for hydrogen to reach the notch tip region increases (tests performed under lower displacement rates) the diffusion distance also increases. Therefore, more hydrogen accumulates in the process zone ahead of the notch root (submitted to high normal stresses) until the aforementioned embrittlement micromechanisms develop once a critical hydrogen concentration is reached.

Figure 4.66 shows a plot of the embrittlement index related to the reduction in area determined for the three steels versus the effective hydrogen diffusion distance; the most important embrittlement mechanisms observed in the process zone in each case were also reported in the same figure.

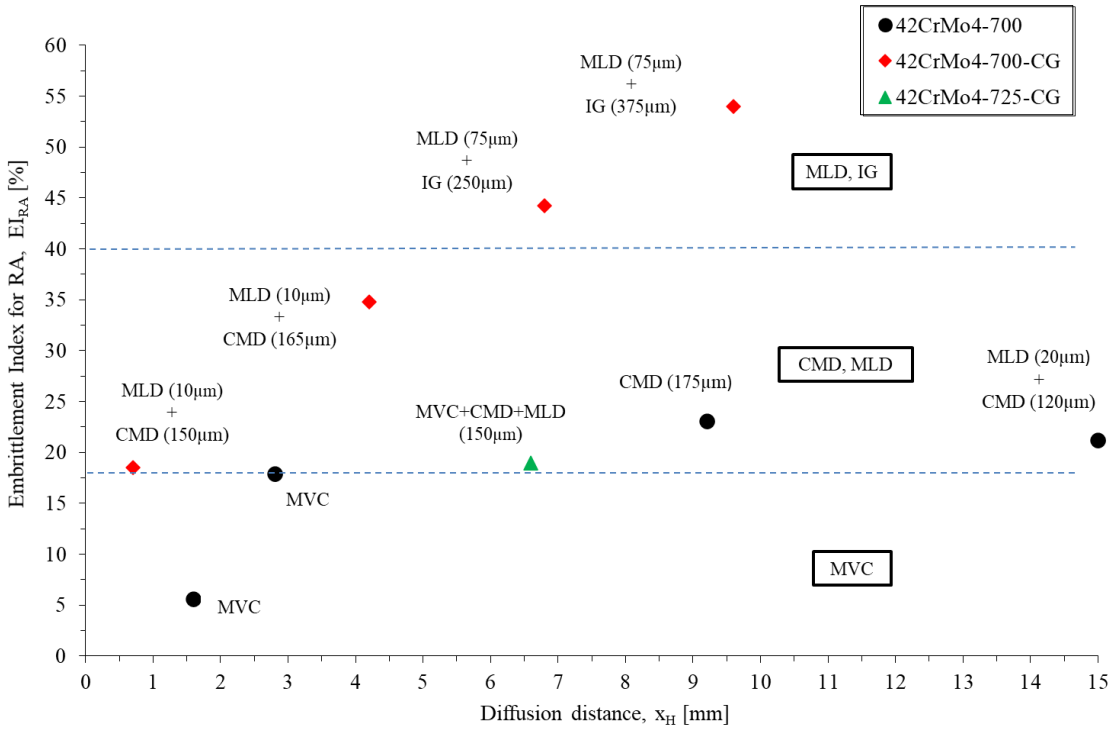

Figure 4.66. Embrittlement index associated with the reduction in area (RA) versus the effective hydrogen diffusion distance (x_H). Operative fracture micromechanisms in the peripheral region of the specimens. Hydrogen pre-charged notched tensile specimens loaded at different displacement rates.

The magnitude of the embrittlement index can now be related to the operative failure micromechanism in these 42CrMo4 grades. When this embrittlement index is lower than 18%, only the HELP mechanism operates, and failure takes place via microvoid coalescence (MVC), where only the presence of very enlarged voids evidences the presence of internal hydrogen. In the case of embrittlement indexes between 18% and around 40%, HEDE mechanisms already take place, namely carbide-matrix interface decohesion (CMD) and martensite lath interface decohesion (MLD). Finally, intergranular fracture (IG) was only observed when this embrittlement index was greater than 40%. It should be borne in mind that, as the effective diffusion distance increases, hydrogen accumulation in the process zone ahead of the notch also increases, giving rise to the modification of the main failure mechanism: from MVC to CMD, MLD and, finally, to IG.

¡Error! No se encuentra el origen de la referencia. also shows the effect of the prior austenite g rain size on the hydrogen embrittlement of this 42CrMo4 steel. At small diffusion distances (high displacement rates), the embrittlement index measured in the fine grain steel, 42CrMo4-700, is quite low (<20%) and a characteristic predominant ductile micromechanism (MVC) was observed. However, under the same testing conditions, and even for lower values of the diffusion distance, MLD and CMD embrittlement mechanisms are already operative in the coarse grain

42CrMo4-700-CG steel and the corresponding embrittlement indexes increase. These same micromechanisms operate in the fine grain steel under significantly larger effective diffusion distances, giving rise to slightly higher embrittlement indexes (but always below 25%). However, under these same testing conditions, the most important failure mechanism in the case of the coarse grain 42CrMo4-700-CG steel was intergranular failure (IG) and the embrittlement index increases significantly (EI>40%).

Regarding now the coarse grain steel tempered at 725ºC for 4 hours (42CrMo4-725-CC), it is noted that the corresponding embrittlement index plotted in **¡Error! No se encuentra el origen de la referencia.** lies within the trend of the fine grain steel and the fracture micromechanisms observed under this testing condition was a combination of MVC, CMD and MLD. It can be then concluded, that applying a more intense tempering treatment on a coarse grain microstructure (produced, for example, in welding), the deleterious effects of hydrogen in the tensile properties of the steel is considerably minimized, although it also reduces the yield strength of the steel (in this particular case from 622 to 489 MPa).

4.6.2. Effects of internal hydrogen on the fracture toughness

4.6.2.1. Influence of tempering temperature

The fracture toughness results obtained with the steel grades tested without hydrogen are shown in Figure 4.67 and Table 4.25. Figure 4.67 shows the load versus the load line displacement (LLD) curves and also the J-resistance curves, J toughness versus crack growth, J-Δa curves, derived from the former ones. The potential law from the fitted experimental data, $J=C_1\Delta a^{C2}$, is also included in Table 4.25, allowing to estimate the J value corresponding to any value of crack growth.

The J value for the onset of crack growth, $J_{0.2/BL}$ (Δa=0.2 mm), was calculated using the corresponding blunting line, also represented in the same figure. It is also worth noting that two different specimens were tested with some grades and data dispersion was always very low.

As expected, the value of $J_{0.2/BL}$ decreases as the tempering temperature decreases (higher yield strength and ultimate tensile strength), and also does the C_2 parameter, which means a flatter crack propagation curve.

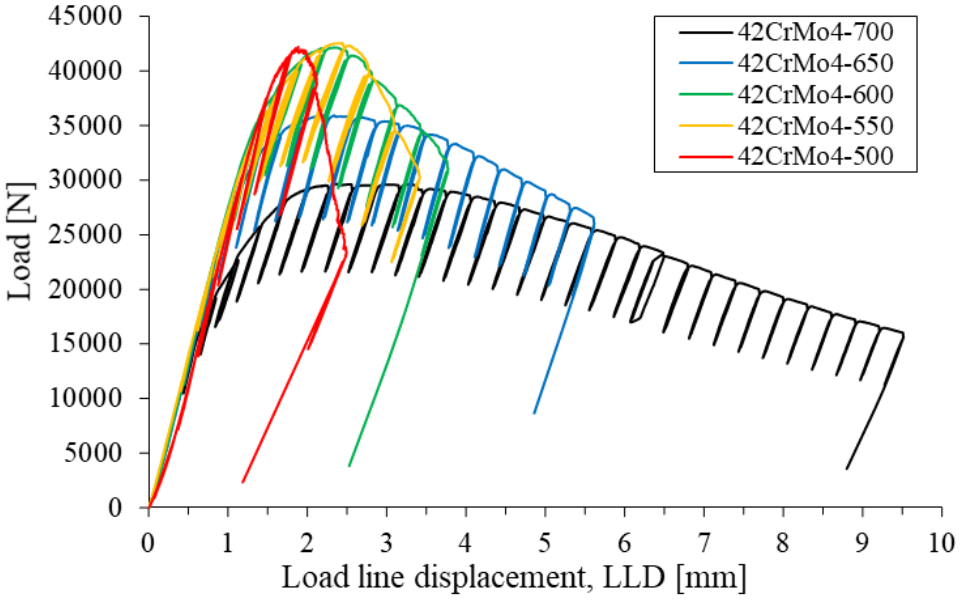

(a)

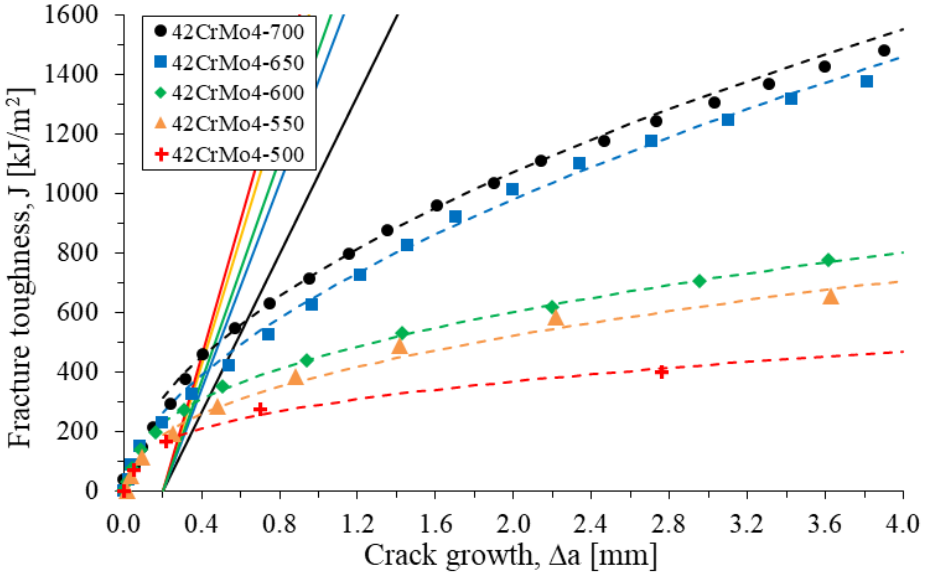

(b)

Figure 4.67. (a) Load-Load line displacement (LLD) and (b) J-resistance (J-Δa) curves corresponding to 42CrMo4 steel quenched and tempered at different temperatures obtained with uncharged specimens.

Steel Grade	σ_{ys} [MPa]	σ_{uts} [MPa]	v_{test} [mm/min]	P_{max} [N]	$J_{0.2/BL}$ [kJ/m^2]	$J=C_1\Delta a^{C2}$	
						C_1	C_2
42CrMo4-700	622	710	1	29636±112	580±10	739±12	0.54±0.02
42CrMo4-650	828	913	1	35924	396	670	0.62
42CrMo4-600	880	985	1	42134	292	456	0.43
42CrMo4-550	1023	1113	0.1	42650±144	225±13	421±18	0.53±0.01
42CrMo4-500	1086	1198	0.1	41892±434	189±17	270±20	0.28±0.03

Table 4.25. Fracture toughness results of the different quenched and tempered 42CrMo4 grades. Uncharged specimens.

As happened with the notched tensile specimens, the operative fracture micromechanism in the fracture surfaces of uncharged CT specimens were fully ductile in all the cases. Microvoids coalescence (MVC) can be clearly seen in Figure 4.68 for the specimens respectively tempered at 700, 600 and 500ºC.

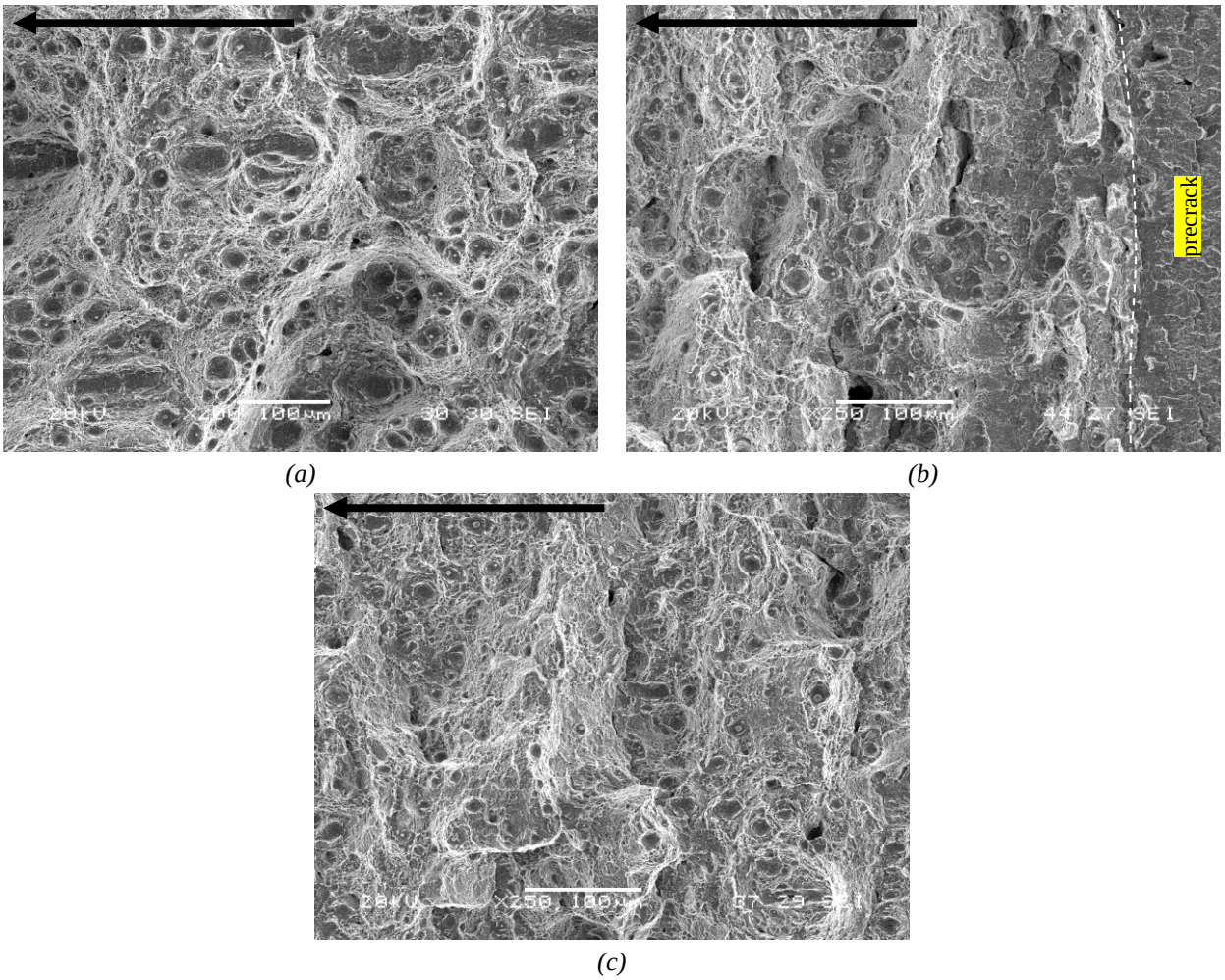

Figure 4.68. Fracture surfaces (SEM) of uncharged CT specimens of (a) 42CrMo4-700, (b) 42CrMo4-600 and (c) 42CrMo4-500 steel grades. Black arrows show the crack propagation direction.

Figure 4.69 shows the J-Δa curves of 42CrMo4 steel quenched and tempered at 700, 650 and 600ºC obtained with uncharged (1 mm/min) and hydrogen pre-charged specimens, at 1, 0.1 and 0.01 mm/min.

The results of these fracture toughness tests are summarized in Table 4.26. The J value for the onset of crack growth, $J_{0.2/BL}$, and the J value corresponding to a crack growth of 1 mm, from 0.2 to 1.2 mm, $J_{0.2\text{-}1.2/BL}$, are also reported. The fracture toughness increment, $\Delta J_{0.2\text{-}1.2/BL}$, measures the slope of the crack propagation curve in the first part of the curve (J increase needed to induce 1 mm of crack growth).

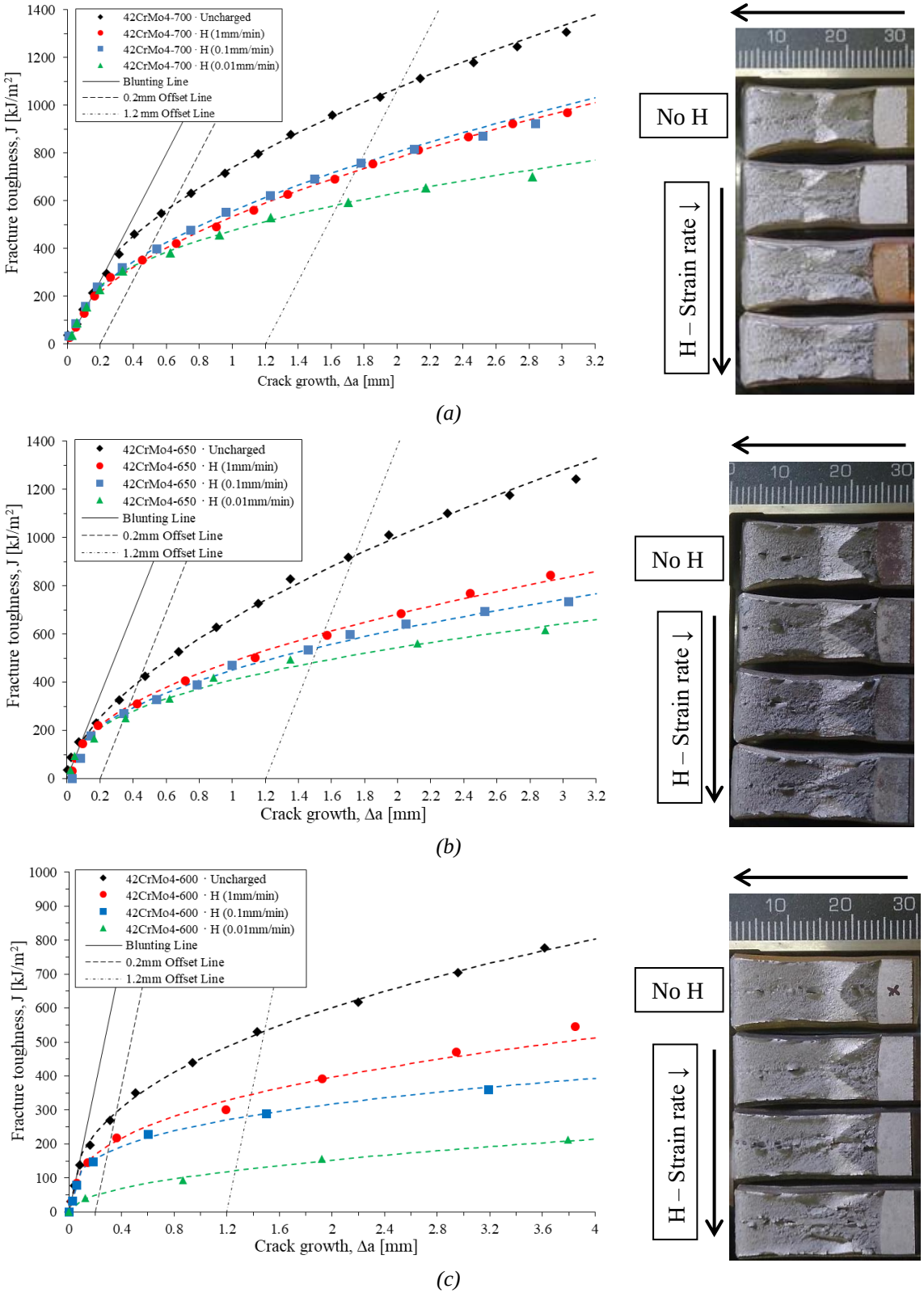

Figure 4.69. J-Δa curves and macroscopic fracture surfaces of uncharged and hydrogen pre-charged specimens tested at different displacement rates. (a) 42CrMo4-700, (b) 42CrMo4-650 and (c) 42CrMo4-600.

In addition, the embrittlement indexes (EI) associated to these parameters as well as the total duration of the tests and the evolution of hydrogen content, $C_{H0} \rightarrow C_{Hf}$, in the specimens along the tests are also included in Table 4.26. The provided C_H values are only approximate and should be taken with caution as they were derived from the desorption curves (Figure 4.30) obtained with samples with the same thickness (10 mm) but different geometry. Hydrogen desorption in CT specimens should be slower and therefore hydrogen contents something higher. Finally, Table 4.26(b) summarises the prevailing fracture micromechanisms, further discussed below, for both the initiation and propagation stages of crack growth.

Steel Grade	v_{test} [mm/min]	t_{test} [h]	$C_{H0} \rightarrow C_{Hf}$ [ppm]	$J_{0.2/BL}$ [kJ/m^2]	$J_{1.2/BL}$ [kJ/m^2]	$\Delta J_{0.2\text{-}1.2/BL}$ [kJ/m^2]	EI ($J_{0.2/BL}$) [%]	EI ($\Delta J_{0.2\text{-}1.2/BL}$) [%]
42CrMo4-700	1	0.7	-	580±10	1073±19	493±15	-	-
	1	0.5	1.2	350	724	374	40	24
	0.1	1.6	1.2→1.1	380	757	377	34	24
	0.01	8.3	1.2→0.85	345	582	237	41	52
42CrMo4-650	1	0.47	-	396	850	454	-	-
	1	0.36	1.2	303	600	297	23	35
	0.1	1.3	1.2	273	544	271	31	40
	0.01	6.7	1.2→1	249	505	256	37	44
42CrMo4-600	1	0.41	-	292	545	253	-	-
	1	0.23	1.4	205	340	135	30	47
	0.1	0.5	1.4	175	280	105	40	58
	0.01	2.6	1.4→1.3	66±18	139±28	73±9	77	71

(a)

Steel Grade	v_{test} [mm/min]	$C_{H0} \rightarrow C_{Hf}$ [ppm]	Fracture Micromechanisms*	
			Crack growth initiation	Crack Propagation
42CrMo4-700	1	-	MVC	
	1	1.2	MLD+CMD (150 μm)	MVC+localized MLD
	0.1	1.2→1.1	MLD+CMD (200 μm)	MVC+localized MLD
	0.01	1.2→0.85	MLD (300 μm)	MVC+localized MLD
42CrMo4-650	1	-	MVC	
	1	1.2	MLD (250 μm)	MVC+localized MLD
	0.1	1.2	MLD (350-400 μm)	MVC+localized MLD
	0.01	1.2→1	MLD	
42CrMo4-600	1	-	MVC	
	1	1.4	MLD+IG (200 μm)	MVC+localized MLD and IG
	0.1	1.4	MVC+MLD+IG	
	0.01	1.4→1.3	MLD+IG	

(b)

*Table 4.26. (a) Results of the fracture toughness tests performed on uncharged and hydrogen pre-charged CT specimens of 42CrMo4 steel quenched and tempered at 700, 650 and 600ºC. (b) Operative fracture micromechanisms in order of importance. *MVC: microvoid coalescence; CMD: carbide-matrix interface decohesion; MLD: martensitic lath interface decohesion; IG: intergranular fracture.*

Already in the steel grade tempered at 700ºC (Figure 4.69(a)), corresponding to the steel with the lowest yield strength, the effect of hydrogen is clearly noticeable, giving rise to a clear decrease of the whole curve, which can also be appreciated in the values of $J_{0.2/BL}$ and $J_{1.2/BL}$ parameters

showed in Table 4.26(a). Maximum embrittlement occurred under the lowest displacement rate, 0.01 mm/min. This behaviour, a decrease in fracture toughness when decreasing the displacement rate, was also noted in the grades quenched and respectively tempered at 650 and 600ºC (see Figure 4.69(b, c)), being the fracture drop especially remarkable in the latter grade: its $J_{0.2/BL}$ parameter was reduced near 80% when tested with internal hydrogen at 0.01 mm/min.

In the course of these fracture toughness tests, mobile or diffusible hydrogen move towards the region located ahead of the crack tip, attracted by the local hydrostatic stress, σ_h, which according to continuum plasticity theory reaches a maximum at a distance x from the crack tip, $x=J/\sigma_{ys}$. At the same time, local plastic strain exhibits a singularity at the crack tip, reaching very high values (ε_{eq}>10%) at distances lower than x/2 ($J/2\sigma_{ys}$), where the dislocation density multiplies, giving rise to high local hydrogen mobility and accumulation [254,255].

Having this in mind, Figure 4.70 shows the fracture surface corresponding to the hydrogen pre-charged specimens of 42CrMo4-700 steel, tested at 0.01 mm/min. Figure 4.70(a) shows a general view of the fractured surface, where two different regions can be clearly distinguished. Region 1, with an extension of between 250-300 μm, corresponds to the onset of crack growth from the fatigue pre-crack. Region 2 corresponds to the propagation of the growing crack. Considering the value of $J_{0.2/BL}$ measured on this specimen (345 kJ/m^2) along with the yield strength of the steel (622 MPa), the extension of the aforementioned region submitted to large plastic strains is 280 μm. Region 1, which can be seen at a higher magnification in Figure 4.70(b, c), shows decohesion along martensitic lath interfaces, MLD micromechanism.

In fact, as it was already noticed in notched tensile specimens, the size of the characteristic features observed in Figure 4.70(c) is comparable to the microstructure units (martensite laths) present in this steel. As the applied J increases, the plastic zone extends (using the K value calculated from J, the plastic zone size is soon larger than 10 mm), and mobile hydrogen distributes in a larger volume submitted to high stresses. Moreover, as these tests have been performed in air, hydrogen is continuously lost along the test (the maximum hydrogen concentration is located in the middle of the specimen). As a matter of fact, the total local hydrogen content in the process zone decreases in the so-called crack propagation region, and MLD is no longer the unique failure micromechanism, but MVC also takes place (see Table 4.26(b))).

Consequently, region 2, shown in Figure 4.70(d), is now characterized by a mixed fracture micromechanism composed of distinctive zones of circular appearance embedded in a general MVC micromechanism. These circular areas represent zones where localized MLD micromechanism took place, as it is shown in Figure 4.70(e, f). This figure also shows very small

microvoids, which could be attributed to the action of a CMD micromechanism (carbide-matrix decohesion).

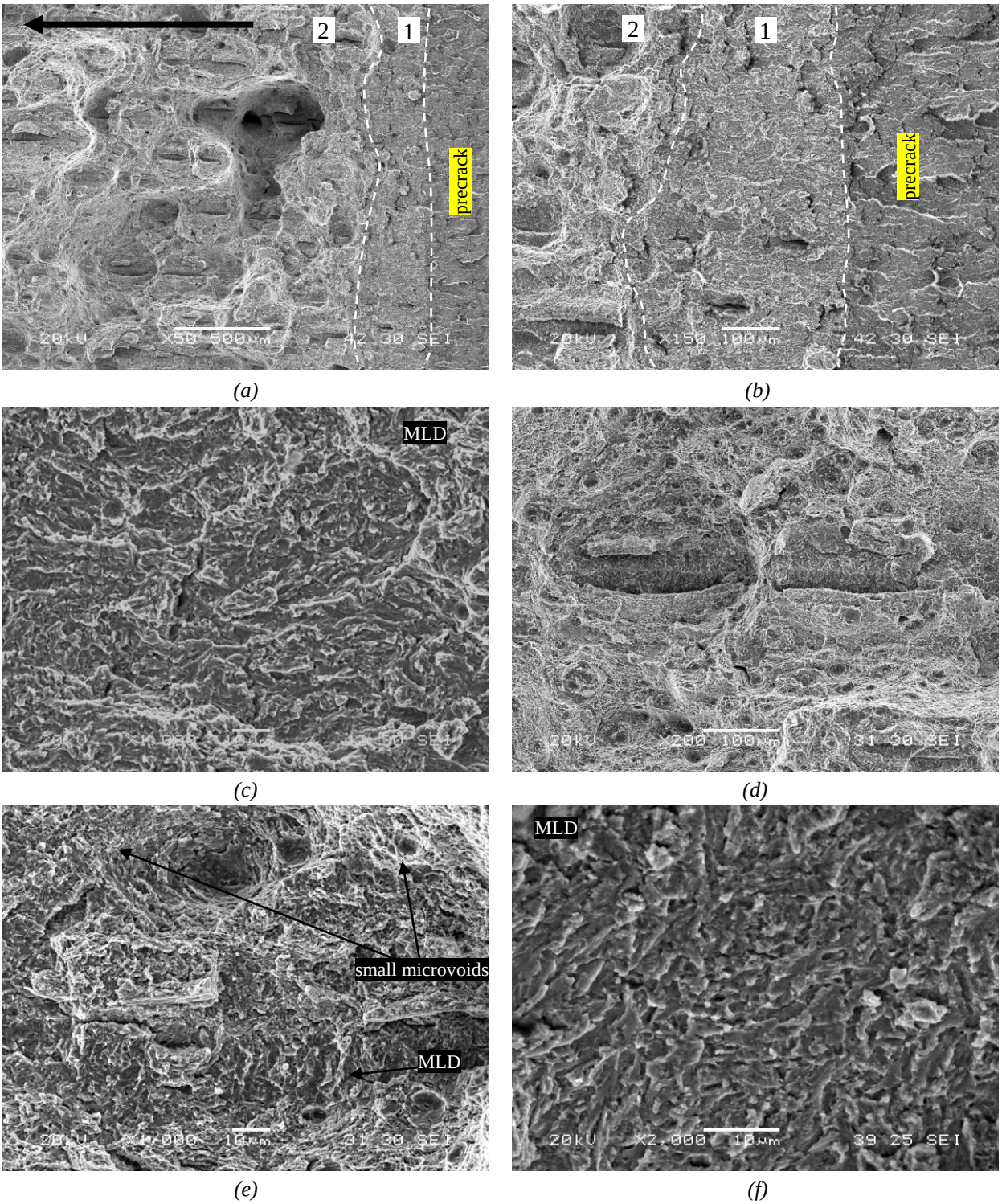

Figure 4.70. SEM fracture surfaces of hydrogen pre-charged specimens of 42CrMo4-700 steel tested at 0.01 mm/min. (a) General view, (b, c) crack initiation region and (d, e, f) crack propagation region. Black arrow shows the crack propagation direction.

The embrittlement indexes and predominant fracture micromechanisms corresponding to the grade quenched and tempered at 650ºC for the different displacement rates, also shown in Table 4.26, are not very different from those observed in the steel tempered at 700ºC. As indicated in Table 4.26(b), the fracture micromechanisms evolved from a fully ductile mechanism (MVC), in the absence of hydrogen, to predominant MLD under internal hydrogen at the lowest displacement rate. In fact, in this case, MLD was observed in all the fracture surface of the broken specimen (both at initiation and at propagation stages) in the test performed at the lowest displacement rate, as shown in Figure 4.71. These differences can be justified due to the higher hydrostatic stress developed in front of the crack in this grade (with a higher yield strength), which enables greater local hydrogen accumulations. As observed in Table 4.26(b), a combination of MLD and MVC micromechanisms were observed in those hydrogen pre-charged specimens tested at intermediate displacement rates.

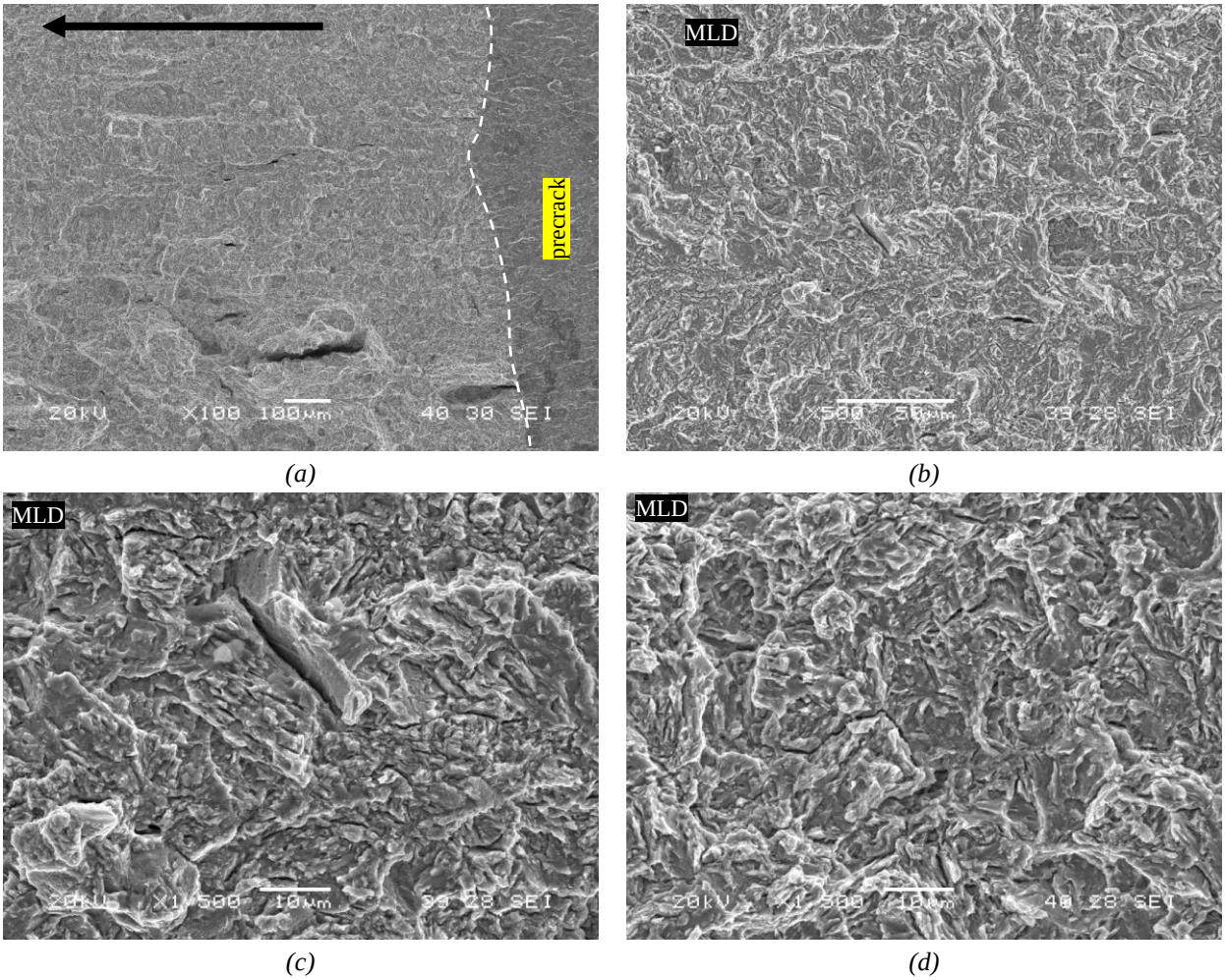

Figure 4.71. SEM fracture surfaces of hydrogen pre-charged specimens of 42CrMo4-650 steel tested at 0.01 mm/min. (a, b) General views, (c) detail of the crack initiation region and (d) detail of the crack propagation region. Black arrow shows the crack propagation direction.

The hydrogen pre-charged grade quenched and tempered at 600ºC tested at 1 mm/min already shows traces of IG fracture that, finally, when tested at the lowest displacement rate (0.01 mm/min), gives rise to a generalised combination of MLD and IG that extended along all the crack extension, from the initiation to the propagation stages, as it can be seen in Figure 4.72.

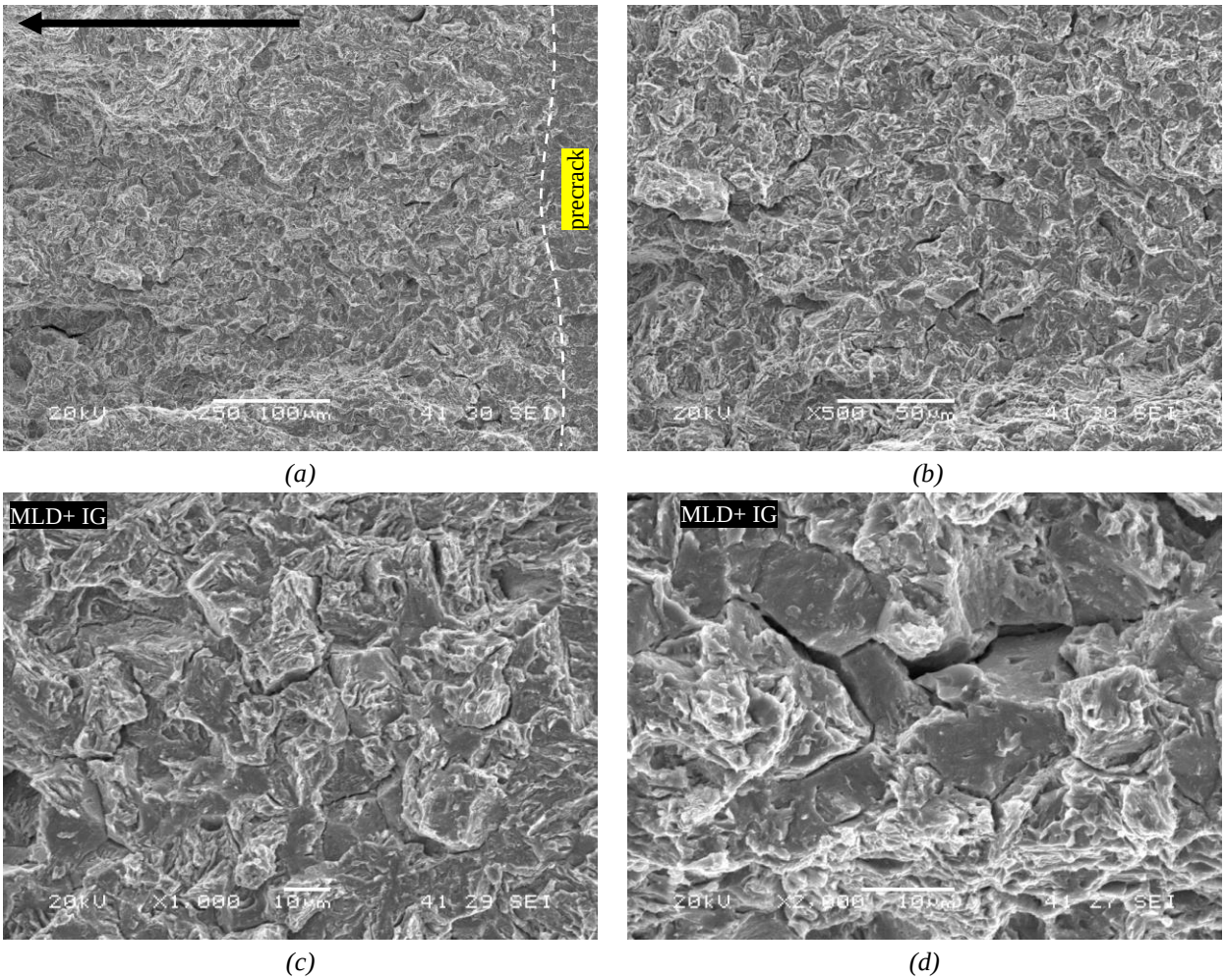

(a) *(b)*

(c) *(d)*

Figure 4.72. SEM fracture surfaces of hydrogen pre-charged specimens of 42CrMo4-600 steel tested at 0.01 mm/min. (a, b) General views and (c, d) details at 0.2 mm from the pre-crack. Black arrow shows the crack propagation direction.

Finally, the extreme brittleness of the hydrogen pre-charged 42CrMo4 grades quenched and tempered at the lowest temperatures (550 and 500ºC) precluded obtaining valid J-Δa curves, so K_Q at instability was used as the characteristic fracture toughness parameter (it was calculated from P_Q determined with the 95% secant line methodology as specified in [256]). In this case, the J_Q value was derived from K_Q ($J_Q = K_Q^2(1-\nu^2)/E$), as it was explained in the experimental section.

The load vs. load line displacement (LLD) curves of the steel grades quenched and tempered at 550 and 500ºC, along with their macroscopic fracture surfaces are presented in Figure 4.73. In both grades, a clear drop of the load, and therefore also on the derived fracture toughness, J_Q, is observed as the displacement rate is decreased, being the bearing capacity of both grades almost null under the lowest displacement rate. In fact, the embrittlement is maximum in the case of the hardest grade (tempered at 500ºC) tested with internal hydrogen at 0.001mm/min: the load at failure, P_Q, drops 80% and the embrittlement index relative to J_Q is nearly 100% (Table 4.27(a

Indeed, Table 4.27 summarizes the fracture toughness results along with the test duration and the approximated hydrogen content in the specimens in the course of the tests. The operative fracture mechanisms are indicated in order of importance in Table 4.27(b) as well. Again, it is worth noting

the low dispersion of results observed in those cases where two specimens were tested under the same conditions.

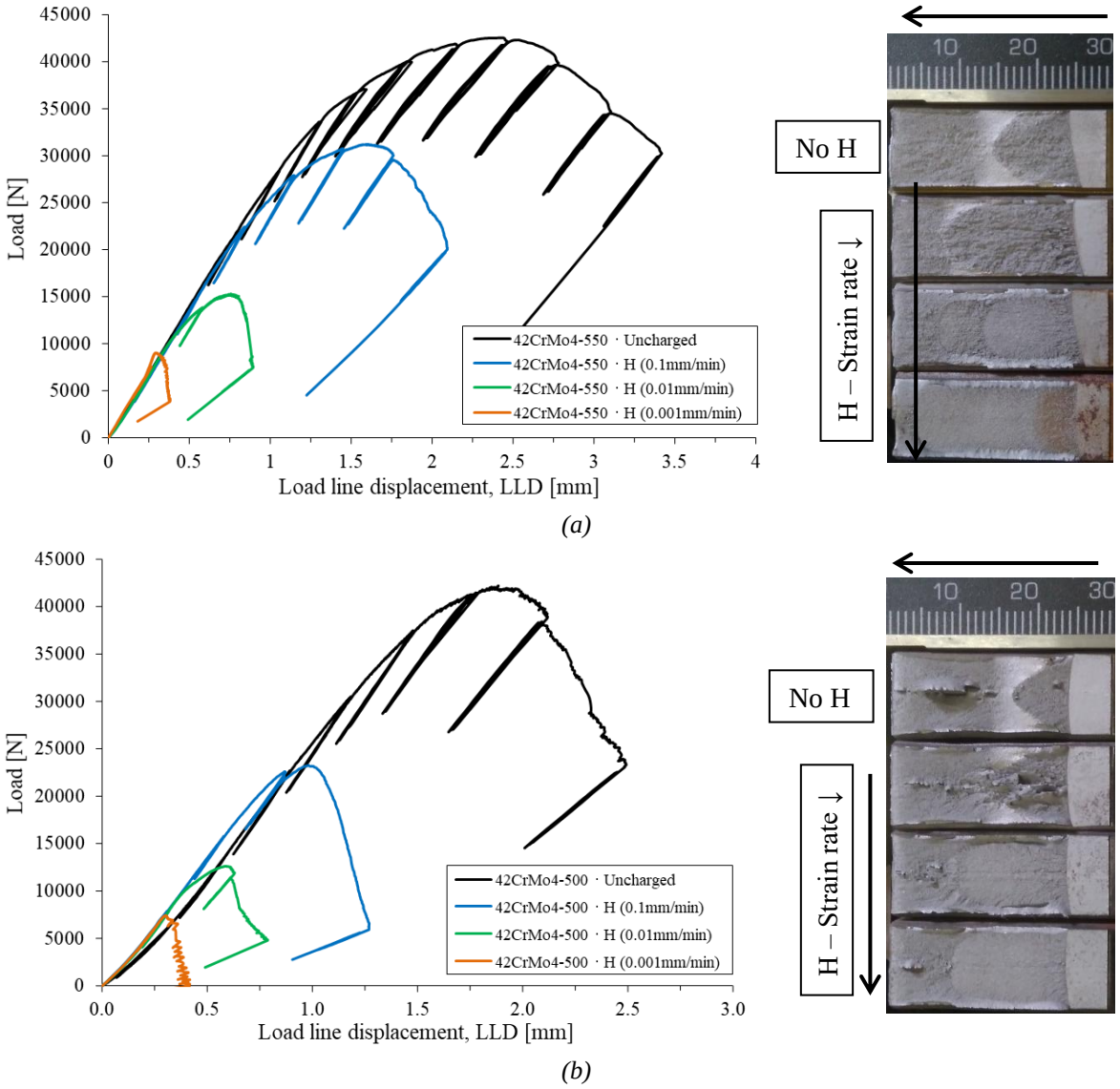

Figure 4.73. Load versus load line displacement (LLD) curves and macroscopic fracture surfaces corresponding to the 42CrMo4 steel quenched and tempered at (a) 500ºC and (b) 550ºC. Uncharged specimen and H pre-charged specimens tested at 0.1, 0.01 and 0.001mm/min.

In line with the embrittlement indexes values, as the displacement rate decreases, a clear evolution can be appreciated in the fracture micromechanisms, see Table 4.27(b). Quite similar observations were performed in both grades. In the case of steel quenched and tempered at 550ºC, the fracture micromechanism evolves from MVC for the uncharged specimens to IG in combination with MLD for the hydrogenated specimen tested at the lowest displacement rate, Figure 4.74. The main difference observed in the grade tempered at 500ºC was the greater extension of the IG fracture, in this case with only faint remnants of MLD features, in the case of the specimens tested at the lowest displacement rate, as shown in Figure 4.75.

Steel Grade	v_{test} [mm/min]	t_{test} [h]	$C_{H0} \rightarrow C_{Hf}$ [ppm]	P_Q [kN]	K_Q [MPa$\sqrt{m}$]	J_Q [kJ/m^2]	EI (P_Q) [%]	EI (J_Q) [%]
42CrMo4-550	0.1	0.3	-	30.7±1.1	143±6	89±7	-	-
	0.1	0.42	1.7	22.4	113	55	27	38
	0.01	1	1.7	12.5	66	19	59	79
	0.001	1.7	1.7	8.9	43	8	71	91
42CrMo4-500	0.1	0.67	-	36.6±0.6	157±1	107±2	-	-
	0.1	0.2	1.85	20.7	85	31	43	71
	0.01	0.78	1.85	10.3	42	8	72	93
	0.001	1.8h	1.85	7.3±0.1	23±4	2.5±0.8	80	98

(a)

Steel Grade	v_{test} [mm/min]	$C_{H0} \rightarrow C_{Hf}$ [ppm]	Fracture Micromechanisms*	
			Crack growth initiation	Crack Propagation
42CrMo4-550	0.1	-	MVC	
	0.1	1.7	MLD+IG (180 μm)	MVC+MLD+IG
	0.01	1.7	IG+MLD+MVC	
	0.001	1.7	IG+MLD	
42CrMo4-500	0.1	-	MVC	
	0.1	1.85	MVC+MLD+IG	
	0.01	1.85	IG+MLD	
	0.001	1.85	IG+MLD	

(b)

*Table 4.27. Results of the fracture toughness tests performed on uncharged and hydrogen pre-charged CT specimens of 42CrMo4 steel quenched and tempered at 550 and 500ºC ($J_Q = K_Q^2(1-\nu^2)/E$). Operative fracture micromechanisms in order of importance. *MVC: microvoid coalescence; MLD: martensitic lath interface decohesion; IG: intergranular fracture.*

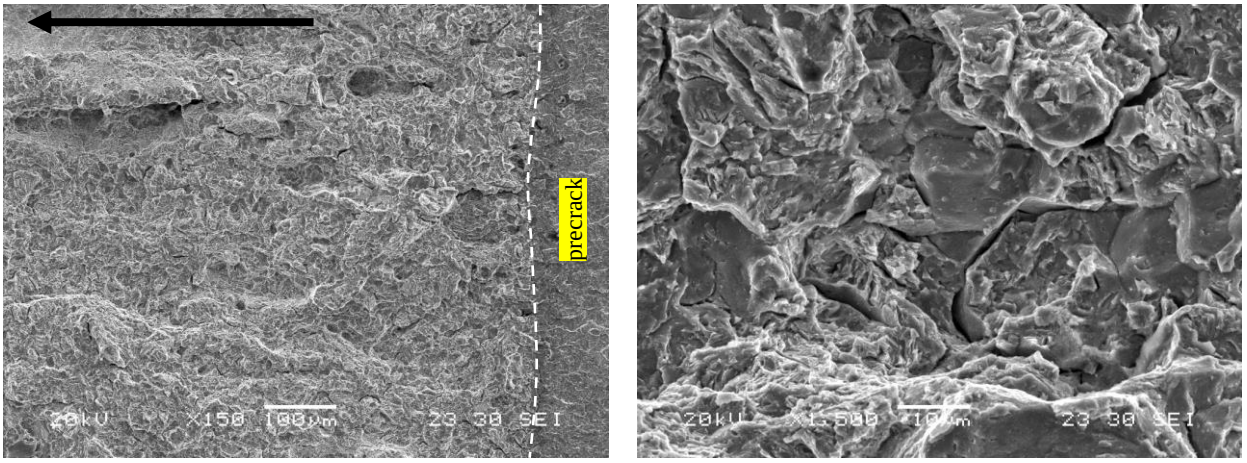

(a) *(c)*

Figure 4.74. SEM fracture surfaces of hydrogen pre-charged specimens of 42CrMo4-550 steel tested at 0.001 mm/min. (a) General view and (b) detail of IG+MLD fracture. Black arrow shows the crack propagation direction.

This behaviour is in line with the macroscopic observations made on the broken specimens (Figure 4.73), where a completely flat propagation area, without any sign of plastic deformation is noticed in the specimens tested with internal hydrogen at the lowest displacement rates.

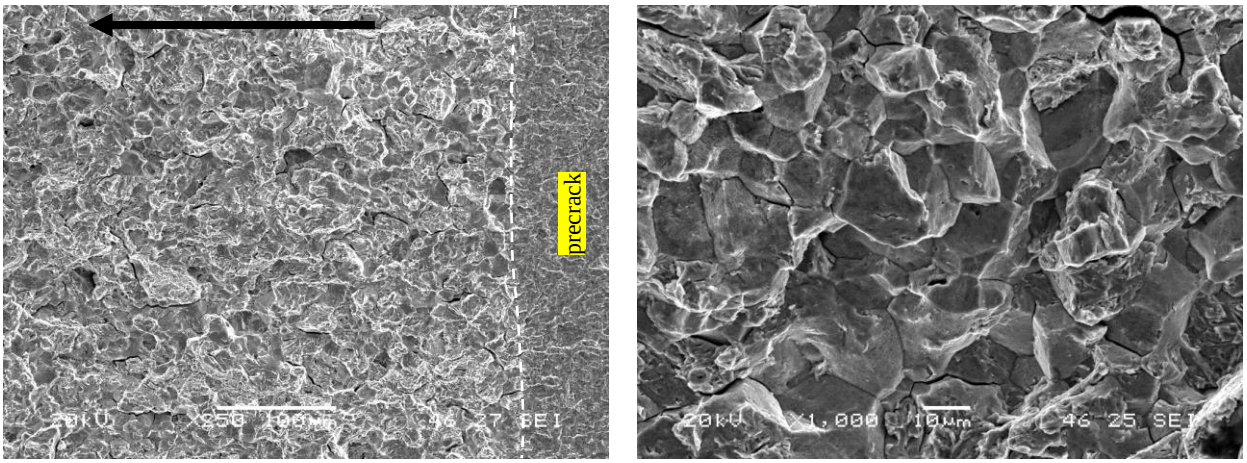

(a) *(b)*

Figure 4.75. SEM fracture surfaces of hydrogen pre-charged specimens of 42CrMo4-500 steel tested at 0.001 mm/min. (a) General view and (b) detail of IG fracture. Black arrow shows the crack propagation direction.

4.6.2.2. Room temperature de-embrittlement of 42CrMo4-500 steel grade

The aim of this sub-section was to follow the recovery of fracture toughness by leaving hydrogen pre-charged specimens to degas in air at room temperature. Therefore, Figure 4.76(a) shows the load vs. LLD curves obtained from fracture toughness tests performed on hydrogen pre-charged 42CrMo4-500 steel (the most brittle grade) after degassing the CT specimens at room temperature during different times (3, 6, 15 and 25 days). The curves obtained with the uncharged specimen and just after hydrogen pre-charging are also included. All these tests were performed at a displacement rate of 0.01mm/min. Additionally, the corresponding J-Δa curves, along with their macroscopic fracture surfaces are also shown in Figure 4.76(b). Only the test performed just after hydrogen pre-charging was unable to provide a J-Δa curve so, in this case, the J_Q value already shown in Table 4.27 was represented in the same plot as a single green triangle.

Firstly, as mentioned previously, a great difference was observed between the behaviour of the uncharged specimen (black curves) and the hydrogen pre-charged specimen tested immediately after hydrogen pre-charging (green curve and green triangle). However, an intermediate behaviour was obtained after leaving the specimen to degas in air at room temperature during 3 and 6 days (red and blue curves respectively). Finally, those specimens degassed for 15 and 25 days already show a behaviour almost identical to that of the uncharged specimen. All the fracture toughness values, $J_{0.2/BL}$, their embrittlement indexes, the degassing times (elapsed time in air at RT), test duration, approximate hydrogen concentration in the specimen at the beginning of the test, C_H, and the operative fracture micromechanisms (in order of importance) are gathered in Table 4.28.

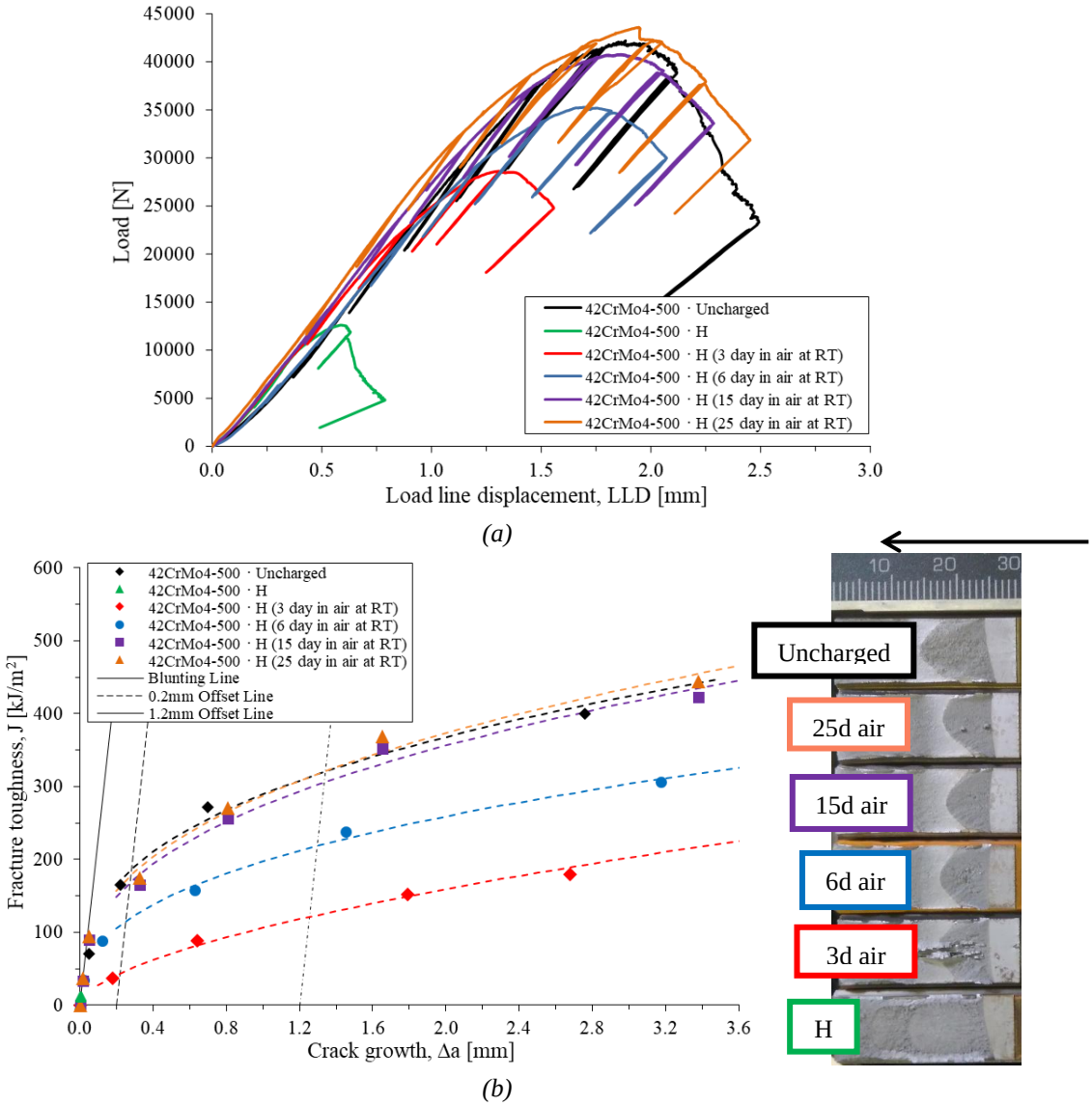

Figure 4.76. Effect of degassing time in (a) Load – LLD and (b) J-Δa curves (with macroscopic fracture surfaces). 42CrMo4 steel quenched and tempered at 500ºC and tested at 0.01mm/min.

Steel Grade	Time in air at RT [days]	Test duration [h]	C_H [ppm]	$J_{0.2/BL}$ [kJ/m^2]	EI ($J_{0.2/BL}$) [%]	Fracture Micromechanisms*	
						Initiation	Propagation
500	-	0.67	-	189	---	MVC	
	-	0.78	1.85	8 (J_Q)	97	IG+MLD	
	3	2.2	1.71	43	78	IG+MLD	
	6	3.2	1.62	115	40	MLD+IG (2.5 mm)	MVC
	15	3.5	1.55	168	11	MLD (50 µm)	MVC
	25	3.8	1.50	178	6	MVC	

*Table 4.28. Fracture toughness recovery observed on CT specimens of 42CrMo4-500 steel grade after degassing for different times. Displacement rate of 0.01 mm/min. Operative fracture micromechanisms in order of importance. *MVC: microvoid coalescence; MLD: martensitic lath interface decohesion; IG: intergranular fracture.*

The fracture micromechanisms observed on these specimens are presented in Figure 4.77, 4.78 and 4.79. The specimen tested after degassing for 3 days in air at RT, Figure 4.77(c, d), with an embrittlement index of 78%, still shows the typical mixed IG+MLD fracture micromechanisms already observed in the hydrogen pre-charged and non-degassed specimen (Figure 4.77(a, b)).

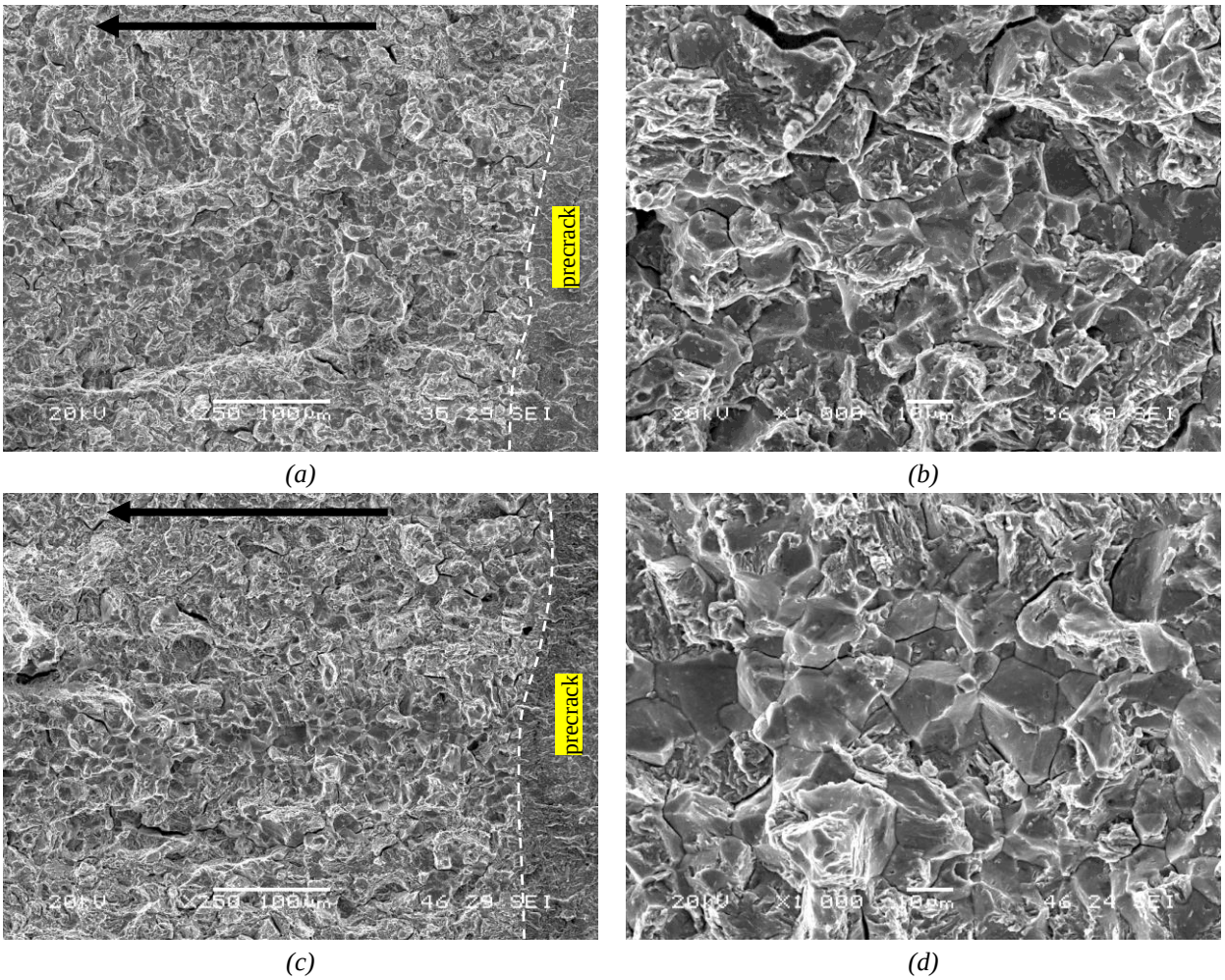

(a) *(b)*

(c) *(d)*

Figure 4.77. Fracture micromechanisms observed in CT specimens (tested at 0.01mm/min) of 42CrMo4-500 grade (a, b) just after hydrogen pre-charging and (c, d) after degassing for 3 days in air at RT.

After 6 days of air exposure (Figure 4.78), the embrittlement index decayed until 40% and the operative fracture micromechanism started to change: an initiation crack growth area of approximately 2.5 mm, region denoted as "1" in the figure, characterized by a mixture of MLD and IG fracture is observed; followed by region "2", where MVC is now the prevalent failure micromechanism. Detailed views of these two regions are shown in Figure 4.78(b, c) respectively.

After 15 days of degassing, fracture toughness restauration was nearly complete and the main fracture micromechanism is now MVC, except in a very narrow band (of around 50 μm) at the beginning of crack propagation where MLD was still detected (Figure 4.79(a, b)). A fracture toughness of 168 kJ/m^2 was measured in this specimen (yield strength 1086 MPa), so the theoretical extension of the high strained process region ($x=J/2\sigma_{ys}$) is around 77 μm, very similar to the extension of the MLD region.

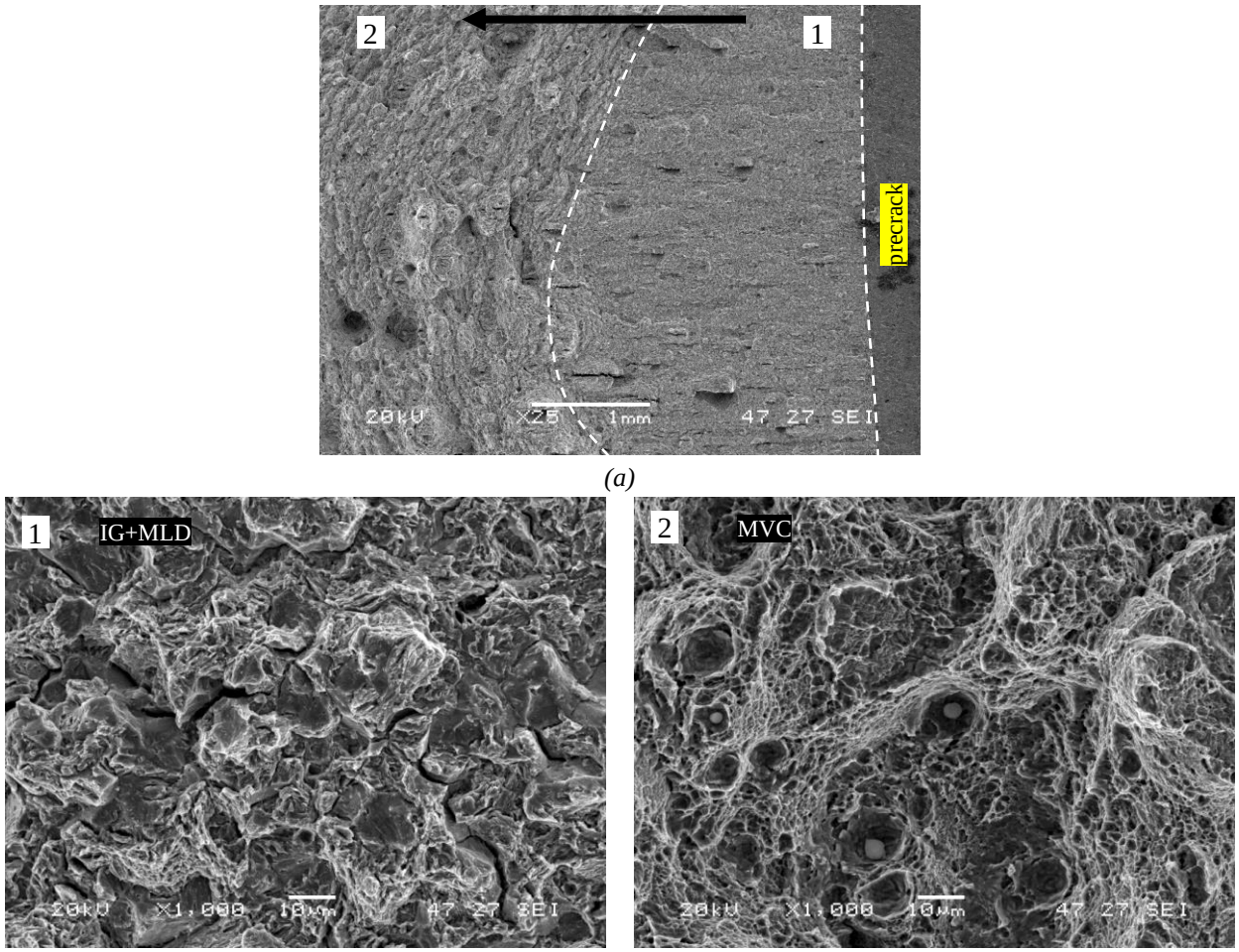

(a)

(b) *(c)*

Figure 4.78. Fracture micromechanisms observed in CT specimens (tested at 0.01mm/min) of 42CrMo4-500 grade after degassing for 6 days in air at RT.

Finally, the specimen left for 25 days in air at RT already shows complete restauration of its fracture toughness, exhibiting only the ductile MVC micromechanism (along all the extension of the crack), as can be seen in Figure 4.79(c, d) and exactly as it was already observed in the uncharged specimen (Figure 4.68(c)).

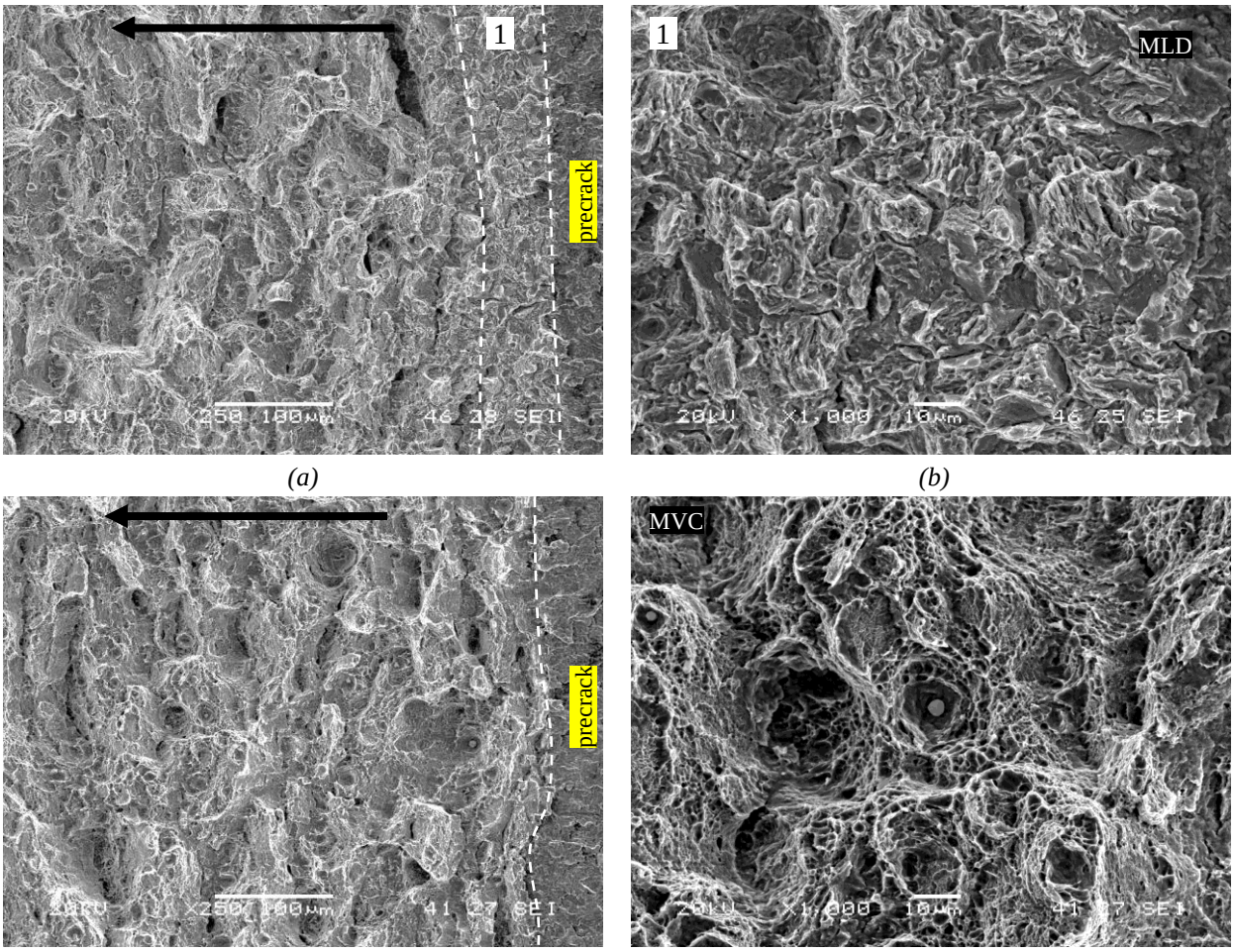

Figure 4.79. Fracture micromechanisms observed in CT specimens (tested at 0.01mm/min) of 42CrMo4-500 grade after degassing for (a, b) 15 days and (c, d) 25 days in air at RT.

4.6.2.3. Discussion on the effects of hydrogen in fracture toughness

As shown in previous sections, the tempered martensite microstructure of the quenched and tempered 42CrMo4 steel is especially dependent on the tempering temperature. As tempering temperature increases from 500 to 700ºC (two hours), carbides break up and grow, internal residual stresses relax and dislocation density decreases. In fact, the initial and residual (deep-trapped) hydrogen contents, measured in gaseous pre-charged cylindrical pins, increased with decreasing the steel tempering temperature, due to the fact that hydrogen microstructural trapping is higher in distorted, high energy martensitic microstructures (with high dislocation densities). This is also reflected in a greater density of hydrogen traps (determined by means of permeation tests) and a lower apparent hydrogen diffusion coefficient.

On the other hand, the fracture toughness reduction due to the presence of internal hydrogen in the steel microstructure is noticeable in all these grades, giving rise to a clear decrease of the whole J-resistance curve and particularly of the critical J parameter for the onset of crack growth, $J_{0.2/BL}$ or J_Q. Maximum embrittlement occurred in the steels tempered at the lowest temperatures (higher yield strength), with greater density of hydrogen traps (mainly dislocations, $E_b \approx 27.4$ kJ/mol), when they are tested under the lowest displacement rates.

In order to justify the fracture toughness results obtained in this section, it should be recalled the aforementioned stress and strain distribution existing ahead of a cracked, stress loaded, elasto-plastic metal (CT specimen). The stress reaches a peak that, according with the continuum plasticity theory, is located at a distance *x* from the crack tip, $x=J/\sigma_{ys}$ [257,258]. Moreover, local strain exhibits a singularity at the crack tip, reaching very high values ($\varepsilon_{eq}>10\%$) at approximately half this distance ($J/2\sigma_{ys}$), where the dislocation density multiplies, giving rise to high local hydrogen accumulation. The maximum levels of the normal opening stress, σ_{yy}, and the hydrostatic stress, σ_H, ahead of the crack front are respectively about $3.5\sigma_{ys}$ and $2.5\sigma_{ys}$. Moreover, hydrogen in the surroundings of the crack will diffuse up to the process zone located just ahead of the crack tip, driven by the high hydrostatic stress existing in this area, where hydrogen is also trapped by dislocations entanglements produced in the plastic strained zone. In practice, hydrogen atoms will accumulate in the crack front giving rise to the embrittlement phenomenon (namely hydrogen enhanced decohesion, HEDE) once a critical hydrogen concentration is reached. According to Oriani theory [18], hydrogen atoms are attracted by the hydrostatic stress, σ_H, existing ahead of the crack until an equilibrium hydrogen concentration, C_H, given by Equation (4.2), is attained.

$$C_H = c_0 \cdot e^{\left(\sigma_H V_H / RT\right)} \qquad \textit{Equation (4.2)}$$

Where, c_0 is the hydrogen concentration at zero stress and V_H is the partial molar volume of hydrogen, which can be approximated by 2×10^{-6} m^3/mol H in a ferritic microstructure.

Hence, the influence of the steel strength (yield strength) in the fracture toughness embrittlement is explained by its effect on the level of the hydrostatic stress produced ahead of the crack tip, σ_H ($\sigma_H = 2.5\ \sigma_{ys}$), and consequently, on the hydrogen content, c_H, accumulated in the process zone, according to expression Equation (4.2). On the other hand, the displacement rate applied during the fracture toughness test will influence on the time that hydrogen atoms have to diffuse and accumulate in the aforementioned process zone until reaching a critical concentration (see Figure 4.80).

Taking all of these considerations into account, and as explained before in the text, an area of around 280 μm from the crack tip becomes highly strained in the 42CrMo4-700 steel grade ($J/2\sigma_{ys}$), which corresponds to the initiation of crack extension characterized by MLD micromechanisms in the test performed at 0.01 mm/min (Figure 4.70(a, b)). The dislocation increment produced in this region, increases hydrogen trapping, and hydrogen atoms accumulate mainly along internal interphases, such as martensite lath, blocks and packets, increasing the c_H value in such region and promoting HEDE mechanism. Similar behaviour was also observed in the grades quenched and tempered at 650ºC and at 600ºC, although due to their higher yield strengths (820 and 880 MPa respectively), hydrogen accumulation in the crack front process region increases and embrittlement phenomena also does. It may be also remembered that the density of hydrogen traps, i.e., dislocation density, is greater in these grades, as was observed in Table 4.7. In the case of the grade quenched and tempered at 600ºC, the hydrogen concentration attained in the process zone when tested at low displacement rates (0.1 and 0.01 mm/min) are high enough to trigger the intergranular fracture mechanism (IG), that is decohesion along the

prior austenite grain boundaries. Tempering at 600ºC is not enough to relax the austenite grain boundaries and to avoid intergranular decohesion when hydrogen is present.

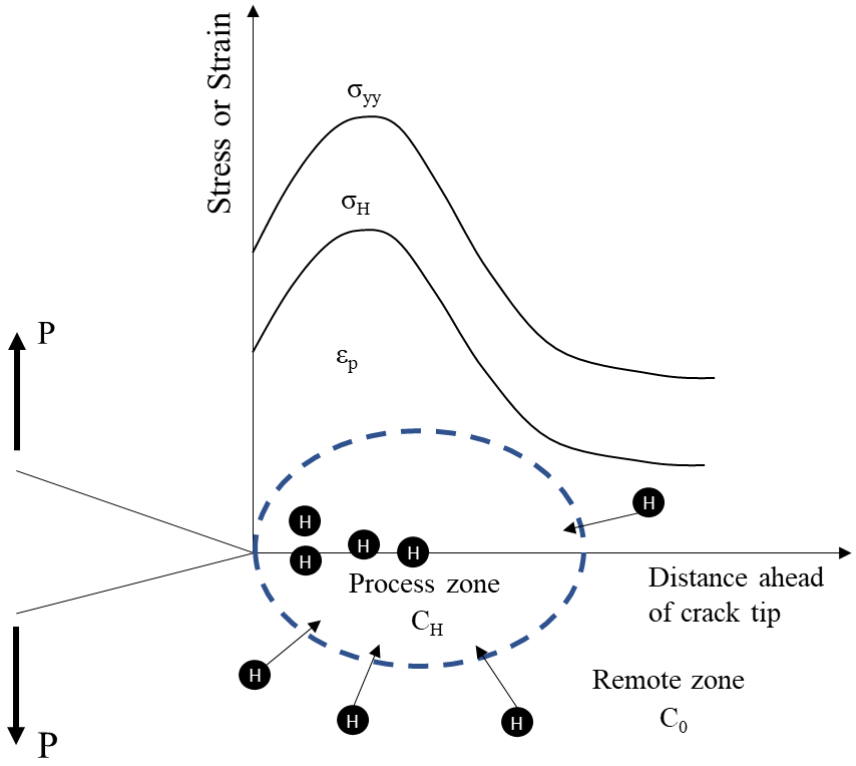

Figure 4.80. Atomic hydrogen diffusion towards the process zone ahead of an opened crack tip. σ_{yy}, σ_H and ε_p are respectively the opening stress, hydrostatic stress, and plastic strain.

Finally, the extreme brittleness of the hydrogen pre-charged 42CrMo4 grades quenched and tempered at the lowest temperatures, 550 and 500º, is justified by their significantly higher yield strengths (1023 and 1086 MPa, respectively) and much higher density of hydrogen traps. Hence, the number of hydrogen traps (dislocations) increases and therefore the hydrogen concentration present in the strained region just ahead of the crack tip (especially in the specimens tested under low displacement rates) attains such values that the cohesion energy between internal interfaces (prior austenite grain boundaries and martensite lath boundaries) is drastically reduced as an unmistakable manifestation of HEDE micromechanism.

Figure 4.81 represents the critical stress intensity factor for the onset of crack growth ($J_{0.2/BL}$ or J_Q), measured with hydrogen pre-charged specimens under a low displacement rate of 0.01 mm/min, versus the tempering temperature (the yield strength is also indicated) for the quenched and tempered 42CrMo4 grades. In a second vertical axis, the evolution of density of trapping sites, N_t, determined in permeation tests, is also represented. Additionally, in order to justify the behaviour of each grade, the predominant fracture micromechanisms are also shown in this figure.

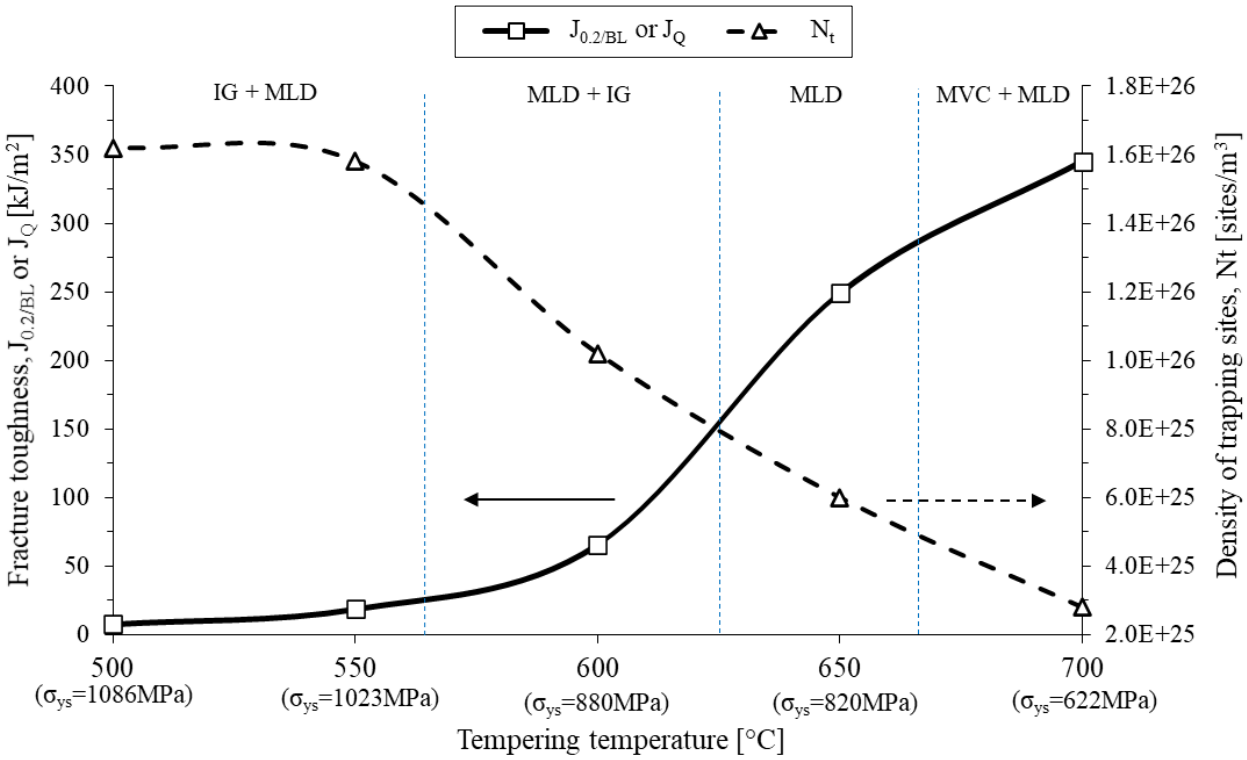

Figure 4.81. Fracture toughness for the onset of crack growth (J0.2/BL or JQ) with internal hydrogen (displacement rate of 0.01 mm/min) versus the tempering temperature (yield strength) in quenched and tempered 42CrMo4 steel. Evolution of trap density, N_t, and predominant operative failure micromechanisms.

At first place, it is worth noting the sudden drop in fracture toughness when intergranular failure micromechanism appears (grade quenched and tempered at 600ºC, σ_{ys} = 880 MPa). As can be seen in Figure 4.1, the quenched and tempered microstructure of this steel still shows elongated carbides precipitated along prior austenite grain boundaries and block and packet martensite boundaries, resembling low tempering microstructures (grades tempered at 550ºC and 500ºC). These distorted internal interfaces are able to trap and retain a lot of hydrogen, whose diffusible fraction is able to move and accumulate in the process zone ahead of the crack tip in the CT specimen (within the plastic zone at the region submitted to high hydrostatic stress, with high dislocation density), giving rise to a HEDE failure micromechanism (hydrogen-enhanced decohesion, MLD and intergranular fracture, IG). However, the 42CrMo4 steels quenched and tempered at 650 and at 700ºC already have sufficiently relaxed quenched and tempered microstructures with a more uniform dispersion of globular carbides (Figure 4.1), so that hydrogen distributes in a more uniform manner along the crack front process region, giving rise to certain decohesion of packet, block and lath martensite boundaries (MLD) only after significant previous plastic deformation (high fracture toughness for the onset of crack growth).

On the other hand, the extreme brittleness of 42CrMo4 grades tempered at the lowest temperatures (500, 550ºC) excludes the use of these grades when toughness in the presence of internal hydrogen is an important design requirement.

Finally, regarding the effect of room temperature degassing during several days measured in the CT specimens of the 42CrMo4 steel quenched and tempered at 500ºC (the grade most susceptible to hydrogen embrittlement), a very good correlation was obtained between the measured fracture toughness and the diffusible hydrogen present in the steel, as it can be appreciated in Figure 4.82. Diffusible hydrogen was obtained using the desorption curve presented in Figure 4.30. As it was already mentioned, these diffusible hydrogen data are only a qualitative approximation, as they were obtained using samples with the same thickness but different geometry than the CT ones.

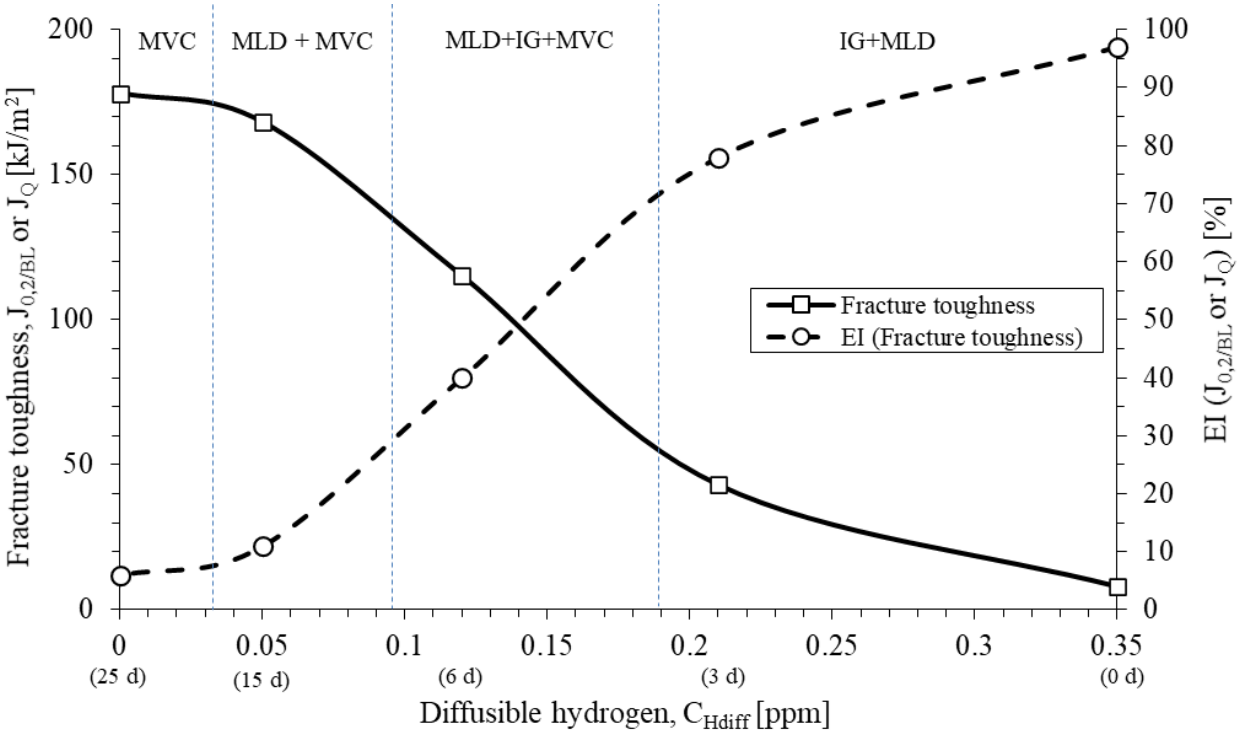

Figure 4.82 Critical fracture toughness ($J_{0.2/BL}$ or J_Q) and its associated embrittlement index versus diffusible hydrogen (days in air at RT). Operative fracture micromechanisms. 42CrMo4-500 steel grade.

Anyway, these results lead us to the conclusion that only diffusible hydrogen, hydrogen which is able to move through the microstructure, overcome traps and finally to accumulate in specific internal interfaces on the process region, is able to damage the steel microstructure and trigger hydrogen-related fracture micromechanisms, such as MLD and IG. When only the strongly trapped hydrogen remains in the microstructure and diffusible hydrogen approaches to zero, the so-called residual hydrogen (1.5 ppm, after a degassing treatment of 25 days in this case, Figure 4.30), the behaviour of the steel is the same already observed in the hydrogen free specimen. The recovery of fracture toughness through sample degassing is also clearly observed in the evolution of the operative fracture micromechanisms, from IG+MLD in the most brittle state (just after hydrogen pre-charging) until a fully ductile one (MVC) after complete degassing (although having a total internal hydrogen content of 1.5 ppm).

4.6.2.4. Effects of hydrogen in the fracture toughness of the CGHAZ of a 42CrMo4 weld

The Load-Load line displacement (LLD) and the J-Resistance, J-Δa, curves corresponding to the uncharged specimens (tested at 1 mm/min) of the fine grain (42CrMo4-700) and coarse grain (42CrMo4-700-CG and 42CrMo4-725-CG) grades are shown in Figure 4.83(a, b). The fitted potential law determined from the experimental data, $J=C_1\Delta a^{C2}$, along with the J value for the onset of crack growth, $J_{0.2/BL}$, are included in Table 4.29.

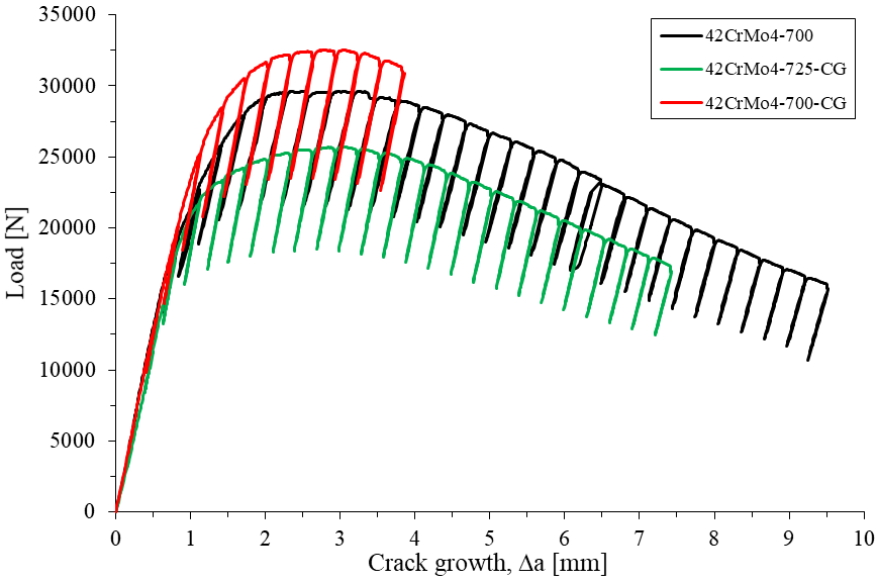

(a)

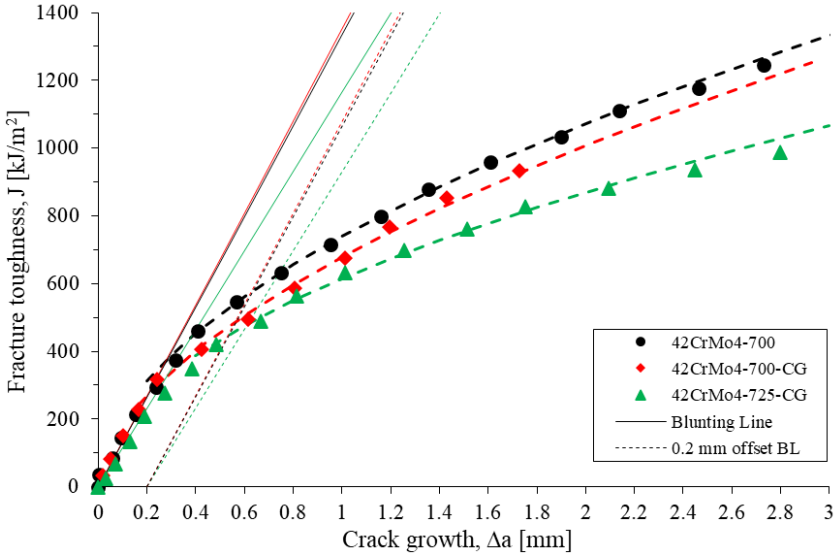

(b)

Figure 4.83. (a) Load- LLD and (b) J-Δa curves corresponding to uncharged specimens (1 mm/min) of the fine grain (42CrMo4-700) and coarse grain (42CrMo4-700-CG and 42CrMo4-725-CG) grades.

It is worth noting that the fracture toughness at the onset of crack growth decreases in the coarse grain grades, which can be justified by their larger prior austenitic grain size. This microstructural characteristic increases brittleness in the non-hydrogenated specimens. On the other hand, the 42CrMo4-725-CG grade shows a fracture toughness value, $J_{0.2/BL}$, very similar to that of 42CrMo4-700-CG, but with a lower strength. The fracture surfaces corresponding to the

uncharged specimens of both coarse grain grades, 42CrMo4-700-CG and 42CrMo4-725-CG, are shown in Figure 4.84 (crack propagation direction is indicated with arrows).

Steel Grade	HV30	PAGS [μm]	σ_{ys} [MPa]	σ_{uts} [MPa]	P_{max} [N]	$J_{0.2/BL}$ [kJ/m^2]	$J=C_1\Delta a^{C2}$	
							C_1	C_2
42CrMo4-700	223	20	622	710	29636±112	580±10	739±12	0.54±0.02
42CrMo4-700-CG	230	150	600	750	32525	488	678	0.57
42CrMo4-725-CG	208	150	498	665	25947±350	461±28	607±10	0.53±0.04

Table 4.29. Elasto-plastic fracture toughness results relative to uncharged specimens of fine grain (42CrMo4-700) and coarse grain (42CrMo4-700-CG and 42CrMo4-725-CG) grades.

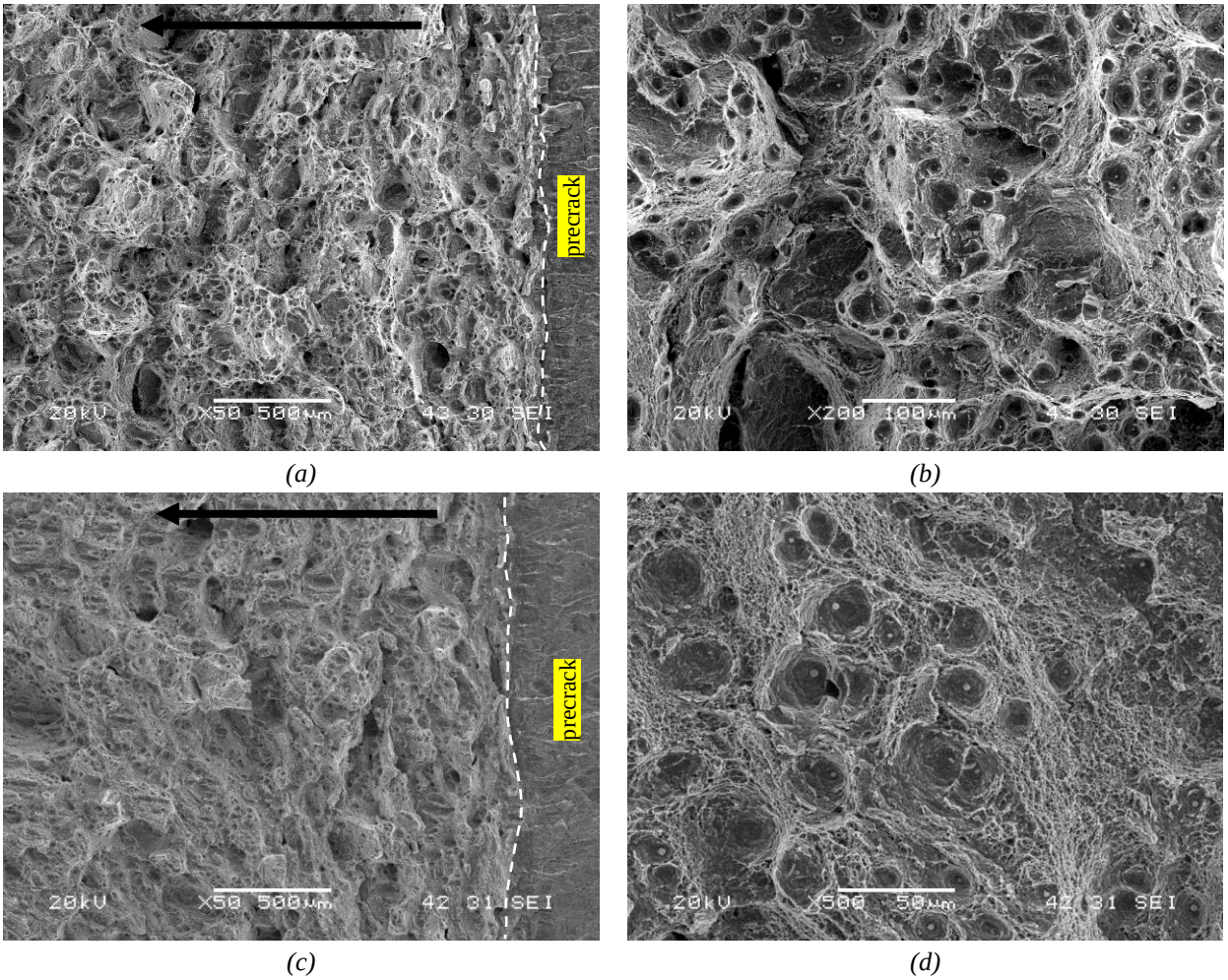

(a) *(b)*

(c) *(d)*

Figure 4.84. SEM fracture surfaces of uncharged specimens (1 mm/min) of (a, b) 42CrMo4-700-CG and (c, d) 42CrMo4-725-CG steel grades. Black arrow shows the crack propagation direction.

As in the fine grain grade (see Figure 4.68(a)), the operative fracture micromechanism was fully ductile in both cases, characterized by microvoid coalescence (MVC) along the whole crack extension, both at initiation and at propagation stages of crack growth.

Figure 4.85(a, b) show respectively the Load- LLD and the J-Δa curves obtained with hydrogen pre-charged CT specimens of the fine grain (42CrMo4-700) and the two coarse grain grades (42CrMo4-700-CG and 42CrMo4-725-CG).

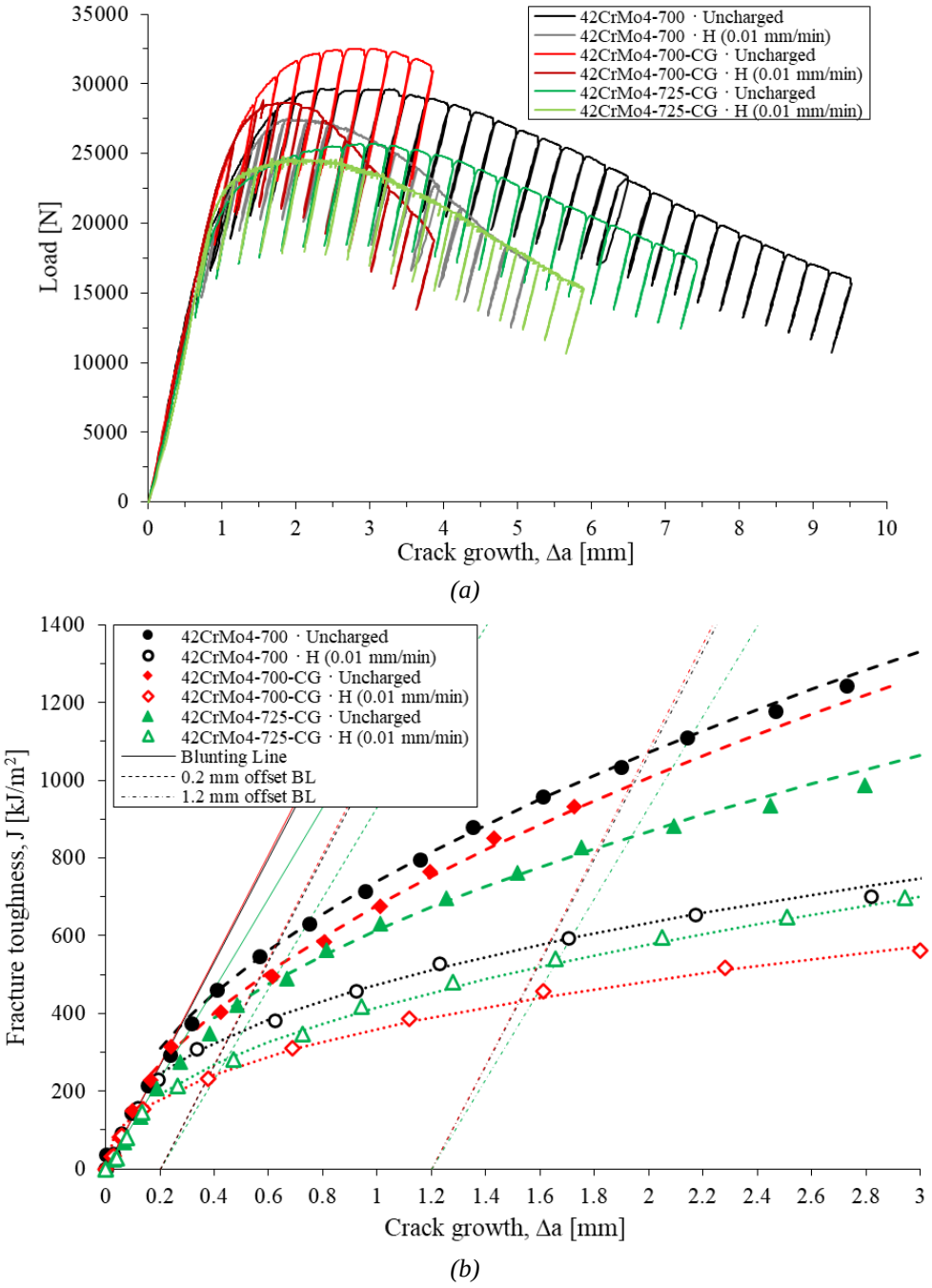

Figure 4.85. (a) Load-LLD and (b) J-Δa curves corresponding to uncharged (1 mm/min) and hydrogen pre-charged (0.01 mm/min) specimens of the fine grain (42CrMo4-700) and coarse grain (42CrMo4-700-CG and 42CrMo4-725-CG) grades.

Based on the results obtained with the 42CrMo4 steel quenched and tempered at different temperatures, the latter were tested only at a displacement rate of 0.01 mm/min, where hydrogen embrittling effects are expected to maximize due to greater hydrogen accumulation at the crack tip region. Results corresponding to uncharged specimens are also included in these figures for an easier comparison.

In a similar way to Table 4.26 and Table 4.27, Table 4.30(a) reports now the results corresponding to the coarse grain grades (42CrMo4-700 is included for comparison): J value at the onset of crack

growth, $J_{0.2/BL}$, at a crack growth of 1 mm, $J_{1.2/BL}$, and the difference between these two values, $\Delta J_{0.2\text{-}1.2/BL}$, along with their corresponding embrittlement indexes (EI). Test duration and evolution of hydrogen contents are also given in the table. Finally, Table 4.30(b) summarises the prevailing fracture micromechanisms, further discussed below, for both the initiation and propagation stages of crack growth.

Steel Grade	v_{test} [mm/min]	t_{test} [h]	$C_{H0} \rightarrow C_{Hf}$ [ppm]	$J_{0.2/BL}$ [kJ/m^2]	$J_{1.2/BL}$ [kJ/m^2]	$\Delta J_{0.2\text{-}1.2/BL}$ [kJ/m^2]	EI ($J_{0.2/BL}$) [%]	EI ($\Delta J_{0.2\text{-}1.2/BL}$) [%]
700	1	0.7	-	580±10	1073±19	493±15	-	-
	0.01	8.3	1.2→0.85	345	582	237	41	52
700-CG	1	0.3	-	488	991	503	-	-
	0.01	6.2	1.0→0.9	233	430	197	52	61
725-CG	1	0.5	-	461±28	865±14	404±42	-	-
	0.01	9.4	0.5	265±13	540±1	276±15	43	32

(a)

Steel Grade	v_{test} [mm/min]	$C_{H0} \rightarrow C_{Hf}$ [ppm]	Fracture Micromechanisms*	
			Crack growth initiation	Crack Propagation
700	1	-	MVC	
	0.01	1.2→0.85	MLD (300 µm)	MVC+localized MLD
700-CG	1	-	MVC	
	0.01	1.0→0.9	MLD+IG (500 µm)	MVC+IG
725-CG	1	-	MVC	
	0.01		MLD (330 µm)	MVC

(b)

*Table 4.30. (a) Results of the fracture toughness tests performed on uncharged and hydrogen pre-charged CT specimens (only at 0.01 mm/min) of fine grain (42CrMo4-700) and coarse grain (42CrMo4-700-CG and 42CrMo7-725-CG) grades. (b) Operative fracture micromechanisms in order of importance. *MVC: microvoid coalescence; MLD: martensitic lath interface decohesion; IG: intergranular fracture.*

It should be pointed out that, as it was also noticed on the notched tensile properties, the presence of internal hydrogen manifests in a significant drop in the fracture toughness (around 40%) already in the fine grain steel. Nevertheless, under the same tempering conditions, hydrogen effects are even greater in the coarser microstructure, as the embrittlement index related to $J_{0.2/BL}$ attains a value higher than 50%. In fact, the quick fall of the Load-LLD curve of the hydrogen pre-charged 42CrMo4-700-CG steel (Figure 4.85(a)) gives rise to a flattened J-Δa propagation curve. It can then be said that the CGHAZ region is significantly more prone to hydrogen embrittlement than its corresponding fine grain grade. On the other hand, after the application of a more intense tempering treatment (higher temperature and longer time), the deleterious impact of coarser microstructure is minimized to attain levels quite similar to the fine grain one.

In the case of 42CrMo4-700 and 42CrMo4-700-CG, it is also worth noting that the embrittlement index associated to crack propagation, $\Delta J_{0.2\text{-}1.2/BL}$ (J increment for crack growth from 0.2 to 1.2 mm), is higher than that associated to crack initiation ($J_{0.2/BL}$): once cracks have started to grow in the presence of hydrogen, crack propagation takes place under quite low energy requirements, because of hydrogen accumulation onto the process zone (first mm ahead of the crack front) where hydrogen embrittlement micromechanisms easily develop. However, on this respect, the

behaviour of the coarse grain steel tempered at a higher temperature (42CrMo4-725-CG) is different, possibly due to its lower yield strength (less hydrogen accumulation in the process zone).

Although a thorough analysis of the fracture surfaces relative to the fine grain, 42CrMo4-700 grade, was already presented in a previous section (see explanation relative to Figure 4.70), the fracture micromechanisms operative in the CT specimen tested with internal hydrogen at 0.01 mm/min are again summarized in Table 4.30(b). The main manifestation of hydrogen embrittlement to be mentioned here is the presence of MLD micromechanism in the first 300 μm of crack growth (initiation region), apart from some isolated MLD areas in the propagation region.

Figure 4.86 shows the fracture surface of the hydrogen pre-charged 42CrMo4-700-CG specimen tested at 0.01 mm/min. Initiation and propagation zones are again easily differentiated in the general view presented in Figure 4.86(a). However, in this case, the crack initiation region extends around 500 μm, where a combination of IG and MLD micromechanisms prevails, as can be seen in detail in Figure 4.86(b, c). In fact, these figures manifest the coarse prior austenitic grain size of this grade (with a metallographically measured PAGS of 150 μm) and, correspondingly, quite long martensitic laths, also matching previous observations regarding its microstructure. When the facets of the fractured grains (IG fracture) are observed under greater magnifications, Figure 4.86(d, e), a decohesion mechanism along interfaces between matrix and very small carbides (carbide-matrix interface decohesion, CMD) is clearly seen. This failure mechanism implies certain localised plasticity at the microscale. With a $J_{0.2/BL}$ toughness and a yield strength of 233 kJ/m^2 and 600 MPa respectively, the maximum hydrostatic stress is located at ≈390 μm from the crack tip, approximating the extension of the crack initiation region measured in this specimen. Further away from those first 500 μm, a mixed fracture micromechanism prevails, constituted in this case by a combination of IG and MVC, as it is seen in Figure 4.86(f).

Lastly, the fracture surface of the analogous specimen of 42CrMo4-725-CG is shown in Figure 4.87. Having measured in this specimen a $J_{0.2/BL}$ toughness and a yield strength of 265 kJ/m^2 and 498 MPa respectively, the location of the maximal hydrostatic stress and the highly strained region are expected to be respectively at around 540 and 270 μm from the crack tip, which is a good approximation to the 330 μm initiation region where MLD was noticed (Figure 4.87(b, c)). It is interesting to note that intergranular mechanisms were not visible in this grade, that is, the applied tempering (725ºC for 4 hours) was able to relax these interfaces avoiding their decohesion when hydrogen is present. Figure 4.87(d) shows that MVC was now the predominant micromechanisms in the propagation region, justifying in this way the higher slope of the J-Δa curve observed in this grade.

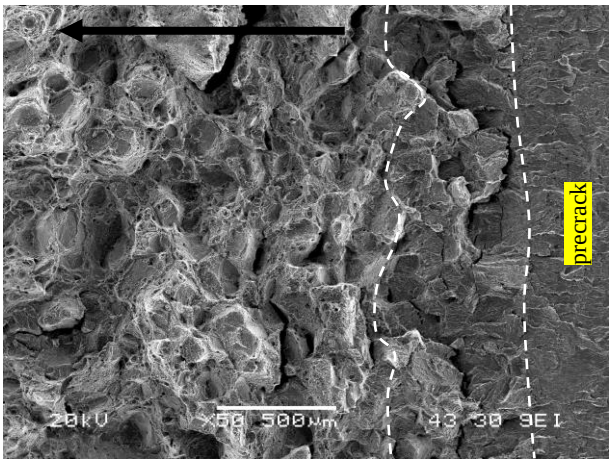

(a)

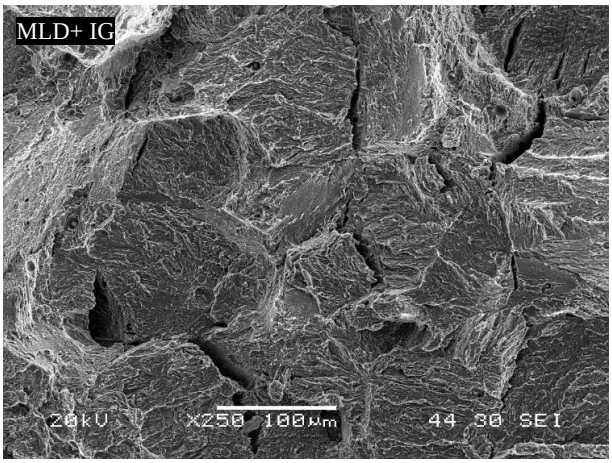

(b)

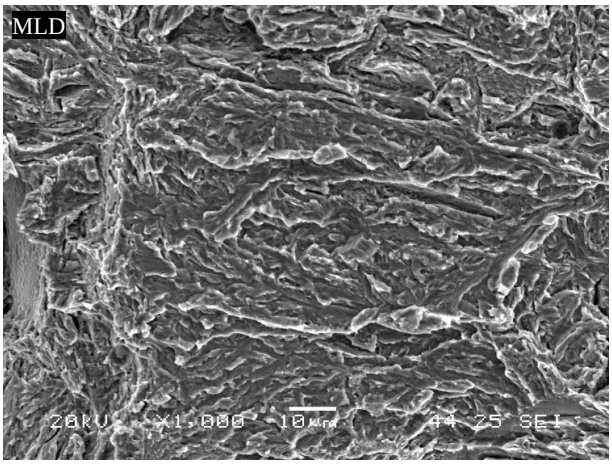

(c)

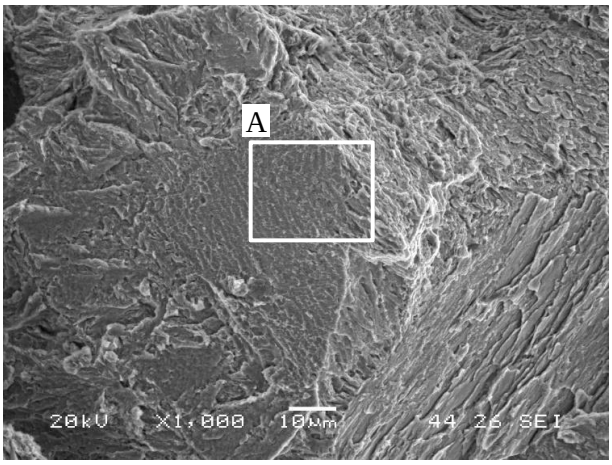

(d)

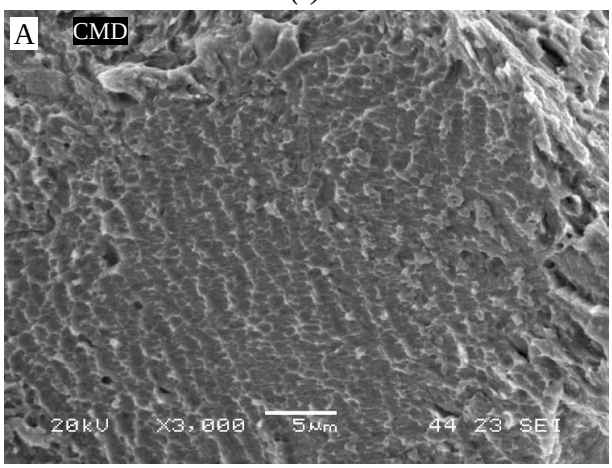

(e)

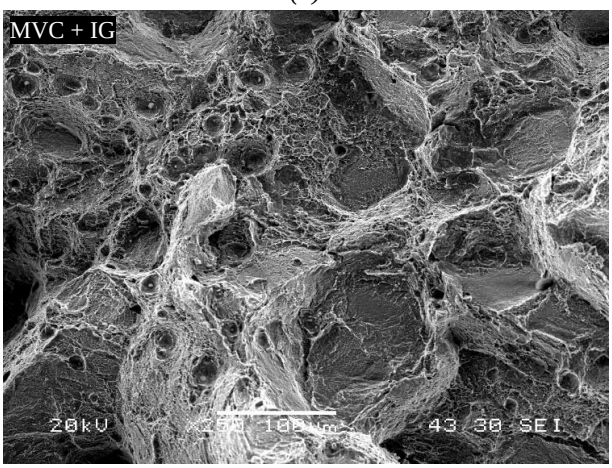

(f)

Figure 4.86. SEM fracture surfaces of hydrogen pre-charged specimens of 42CrMo4-700-CG steel tested at 0.01 mm/min. (a) General view, (b, c, d, e) crack initiation region and (f) crack propagation region. Black arrow shows the crack propagation direction.

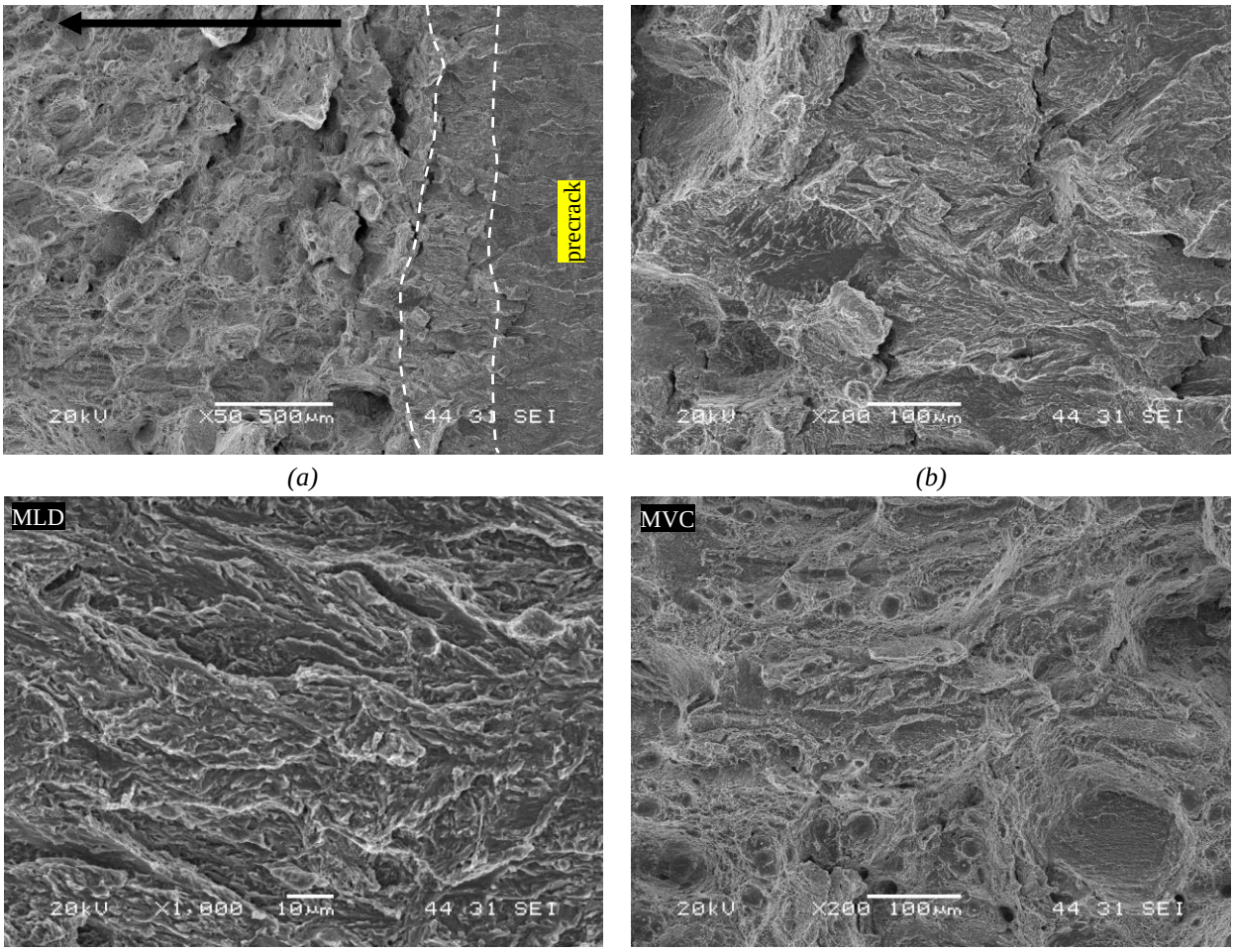

(a) *(b)*

(c) *(d)*

Figure 4.87. SEM fracture surfaces of hydrogen pre-charged specimens of 42CrMo4-725-CG steel tested at 0.01 mm/min. (a) General view, (b, c) crack initiation region and (f) crack propagation region. Black arrow shows the crack propagation direction.

4.6.2.5. Discussion on the fracture toughness of the coarse grain grades

Figure 4.88 shows the embrittlement indexes corresponding to $J_{0.2/BL}$ and $\Delta J_{0.2\text{-}1.2/BL}$ fracture toughness parameters of the fine grain and coarse grain steels. The operative fracture mechanisms at crack growth initiation are also indicated in the same figure. Fracture micromechanisms at the onset of crack growth always changed from microvoids coalescence (MVC) in the absence of hydrogen to martensite lath decohesion, MLD, in the case of the fine grain 42CrMo4-700 grade, and to a mixture of MLD and intergranular failure (IG) in the coarse grain grade also tempered at 700ºC. The development of IG fracture is associated to an increase of the embrittlement indexes. Regarding now the 42CrMo4-725-CG steel, when a higher tempering temperature and a longer time was applied to the as-quenched coarse grain microstructure, embrittlement indexes significantly reduced, and IG fracture completely disappeared. The fracture toughness susceptibility to hydrogen embrittlement decreases to the levels (or even below) of the fine grain steel.

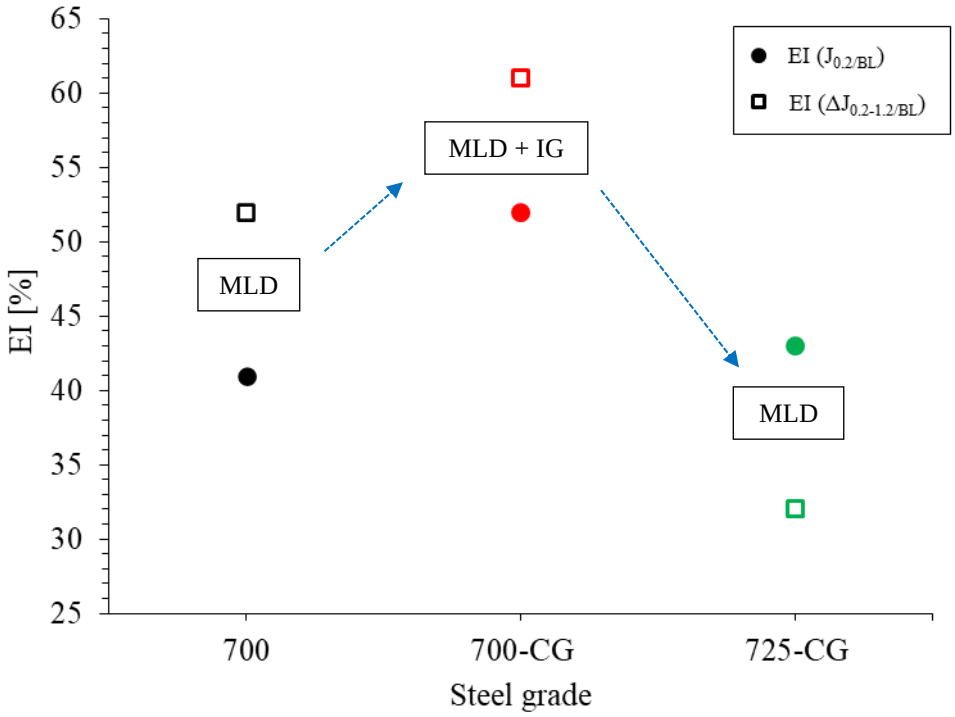

Figure 4.88. $J_{0.2/BL}$ and $\Delta J_{0.2\text{-}1.2/BL}$ embrittlement indexes of fine grain (42CrMo4-700) and coarse grain (42CrMo4-700-CG and 42CrMo4-725-CG) grades. Main fracture micromechanisms.

The extensive microfractography study performed in this section of the thesis supports the hydrogen-enhanced-plasticity mediated decohesion (HELP mediated HEDE) model proposed by Nagao [40], based on previous works of the same research group [253,254]. In fracture toughness tests performed with internal hydrogen, hydrogen atoms diffuse and accumulate in the process region located ahead of the crack tip attracted by the local high hydrostatic stress. The high concentration of hydrogen present in this region facilitates dislocation movements, hydrogen accumulates in internal interfaces, which include interfaces between martensitic laths, matrix-carbides, and prior austenitic grain interfaces and dislocation pile-ups against these same internal interfaces develop. The separation distance between dislocations in pile-ups is reduced due to the presence of hydrogen, thus increasing local pile-up stresses. Then, internal decohesion phenomena are triggered, assisted by the weakening of the aforementioned internal boundaries.

The results previously presented in this work show that there are two main decohesion mechanisms at the onset of crack growth in the studied steel grades provided with internal hydrogen, martensite lath decohesion, MLD, and intergranular fracture, IG. Fractographic details of the MLD mechanism were already shown, for example, in Figure 4.86(c) and Figure 4.87(c). The ductile micro-plastic tearing on a very fine scale with characteristic lath-like features are comparable in dimensions to the martensite laths present in the microstructure of the corresponding grades. In addition, these figures show serrated markings and some secondary cracks, which reveal active plastic deformation beneath the failed surface. Similar morphologies were also observed by [254,255] in single-notched bend tests performed with martensitic steels pre-charged with high pressure hydrogen. Heavily deformed microstructures with intense slip bands (deformation bands) were observed by these authors just beneath the surface of the failed martensitic laths. Figure 4.86(d, e) also show signs of a decohesion mechanism along the prior

austenite grains (intergranular fracture), activated by decohesion between the steel matrix and small precipitated carbides in the coarse grain 42CrMo4-700-CG grade.

A closer vision of the intergranular facets present in 42CrMo4-700-CG steel (remember this is the grade with the lowest fracture toughness) is presented in Figure 4.89(a). The same MLD mechanism with ductile micro-plastic tearing is observed in one of the grain facets and very small dimples, associated to decohesion phenomena along the interfaces between the steel matrix and small carbides precipitated during tempering are also observed in the enlarged vision of the other grain facet (Figure 4.89(b)). In this case, dislocation pile-ups impinging on grain boundary carbides lead to decohesion at the carbide-matrix interface and finally to the complete decohesion of the whole boundary. This failure mechanism follows the hydrogen-enhanced-plasticity mediated decohesion model explained above.

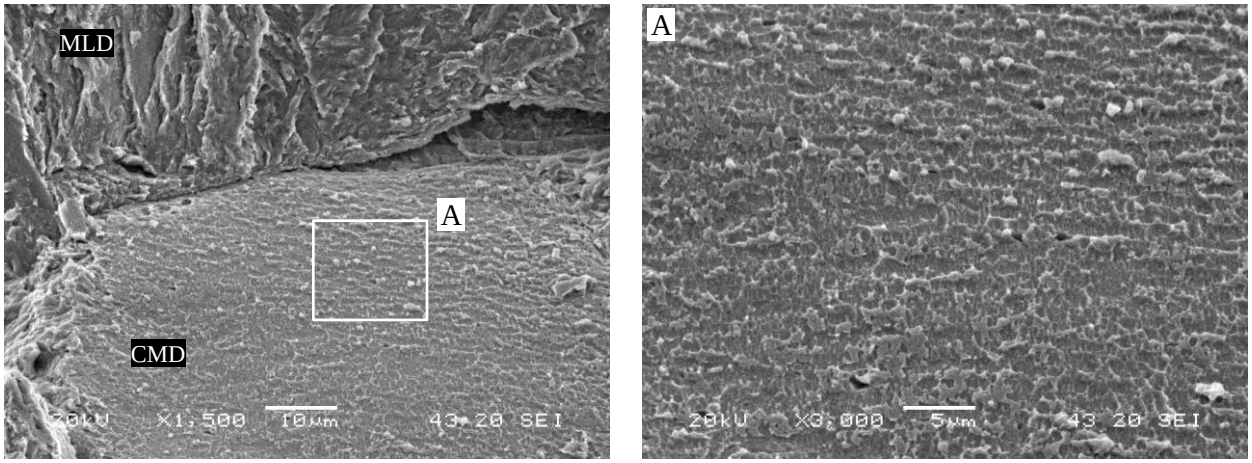

(a) *(b)*

Figure 4.89. (a) Detail of the intergranular fracture at crack initiation region in 42CrMo4-700-CG grade and (b) enlarged vision of the area marked in (a).

The coarser microstructure of the 42CrMo4-700-CG steel was seen to be more sensitive to hydrogen embrittlement and also more prone to intergranular failure than the corresponding base, fine grain, steel. When the austenitizing temperature increases from 845ºC to 1200ºC, a significant increase of the prior austenite grain size occurs, from 20 to 100-150 µm. The strongly trapped hydrogen retained in the steel microstructure after very long times at room temperature (Table 4.14) and the density of trapping sites also increase (Table 4.10). These facts are justified based on the greater thermal drop applied for quenching, which gives rise to a much more distorted martensitic structure, with higher internal stresses and, consequently, higher dislocation density. As these differences are maintained after the same tempering, the coarse grain microstructure have more distorted prior austenite grain boundaries becoming more susceptible to intergranular failure in the presence of internal hydrogen. On the other hand, coarse-grain austenitic microstructures are also more susceptible to temper embrittlement (intergranular fracture) because the concentration of residual elements in prior austenitic grain boundaries increases due to the lower extension of such boundaries. Nevertheless, these effects can be counterbalanced when a more intense tempering treatment is applied to the coarse-grain microstructure.

In fact, Figure 4.90 represents the evolution of the embrittlement indexes of $J_{1.2/BL}$ and $\Delta J_{0.2\text{-}1.2/BL}$ versus the density of hydrogen trapping sites, which had been determined with permeation tests. Considering that dislocations are the governing trap in these microstructures, as it was demonstrated in sub-sections 4.3 and 4.5, the density of trapping sites in the studied steels is directly related to their dislocation density. Remember that dislocations play an essential role in the HELP mediated HEDE failure mechanism and, therefore, the greater density of trapping sites, the greater hydrogen embrittlement indexes are expected. The more intense tempering applied to the coarse grain microstructure of the 42CrMo4 steel was able to reduce the density of hydrogen traps, reducing the toughness hydrogen embrittlement indexes, although a lower yield strength was also produced.

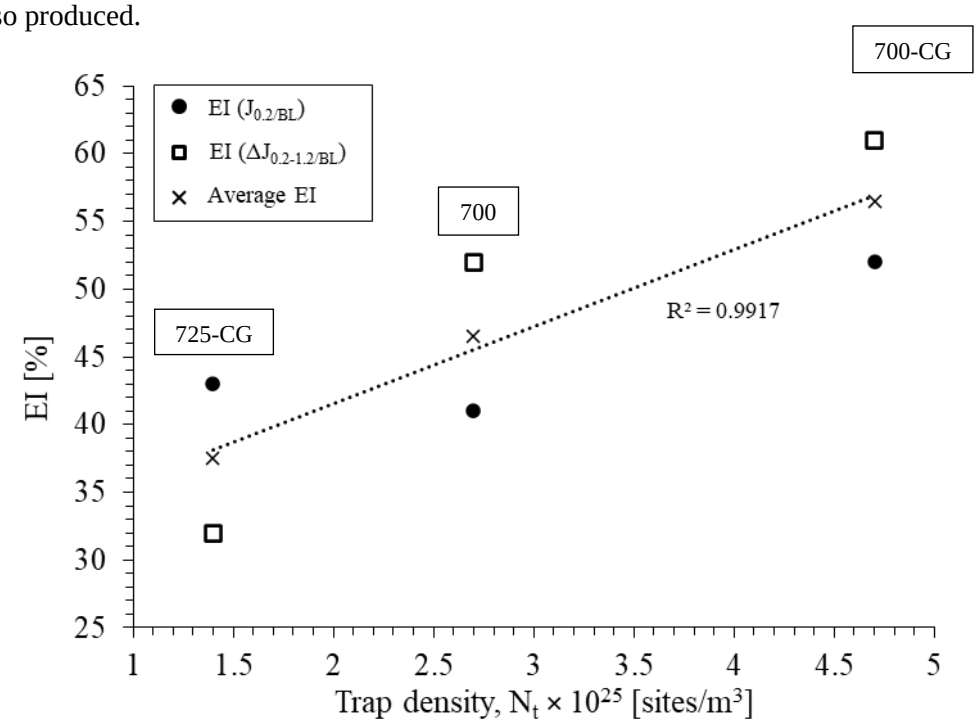

Figure 4.90. Evolution of the embrittlement indexes related to $J_{0.2/BL}$, $\Delta J_{0.2\text{-}1.2/BL}$ (and the average value of both indexes) with the density of trapping sites, N_t, determined in permeation tests.

4.6.3. Effects of internal hydrogen on tests performed under constant K

According to the fracture toughness results exposed in the previous section, those grades tempered at the lower temperatures (500, 550 and even 600ºC), where IG fracture was clearly manifested in the failure surfaces of hydrogen pre-charged fracture toughness specimens tested at low displacement rates, were considered not suitable for the manufacture of gaseous hydrogen high-pressure vessels. Therefore, they were excluded from further analysis in this and in the following subchapter. The remaining grades (42CrMo4-700, 42CrMo4-650, 42CrMo4-700-CG and 42CrMo4-725-CG), less susceptible to hydrogen embrittlement, were also submitted to hydrogen-assisted cracking by means of constant K tests performed on hydrogen pre-charged CT specimens.

As explained in the experimental chapter, the aim of these tests, which had a total duration of 24 hours (longer times were excluded to avoid hydrogen losses), was to determine if the initial crack (a_0=25 mm) was able to grow under a certain constant applied load, P_{app}, i.e. under a certain stress

intensity factor, K_{app}, due exclusively to the accumulation of hydrogen in the highly stressed region (process zone) located just ahead of the crack tip [234]. Considering the hydrogen diffusion coefficients of these particular steels, a total test duration of 24 hours assures hydrogen saturation of the most stressed region located ahead of the crack front. For example, under an applied K_{app} factor of 100 MPa$\sqrt{m}$, the peak hydrostatic stress, where a maximum hydrogen concentration is attained, is located below 0.1 mm from the crack front, and diffusion distances are much higher.

4.6.3.1. Influence of tempering temperature

The results obtained in these tests with the 42CrMo4 steel quenched and tempered at 700 and 650ºC for two hours, are first compared. The crack growth, Δa, measured in these tests versus the different applied load, P_{app}, or stress intensity factors, K_{app}, are shown in Table 4.31, The stress intensity factor acting on the specimen at the end of the test, K_{final}, is also indicated, although in general is very similar to the first applied K_{app}, as crack growth was always very small. The operative fracture micromechanisms identified in the crack growth region are also included in Table 4.31 in order of importance.

Steel grade	$C_{H0} \rightarrow C_{Hf}$ [ppm]	P_{app} [kN]	K_{app} [MPa$\sqrt{m}$]	K_{final} [MPa$\sqrt{m}$]	Δa [mm]	Fracture Micromechanisms*
42CrMo4-700	1.2→0.5	19.46	81	81	0.07	MLD
		22.73	92	93	0.13	
		27.35	113	117	0.46	
		29.84	124	127	0.47	
42CrMo4-650	1.2→0.8	12.25	51	51	0.07	MLD+IG
		15.44	64	65	0.27	
		19.27	80	85	0.85	

*Table 4.31. Results of the 24h constant load, or K, tests performed on 42CrMo4 steel quenched and tempered at 700 and 650ºC. Operative fracture micromechanisms in order of importance. * MLD: martensitic lath interface decohesion; IG: intergranular fracture.*

It is also interesting to comment that hydrogen concentrations ($C_{H0} \rightarrow C_{Hf}$) provided in this table are merely illustrative (they were derived, as in the previous sections, from desorption analysis, Figure 4.1), as the local hydrogen concentration reached in the crack tip region will be much higher and dependent on the local hydrostatic stress developed in each case.

A progressive increase of crack length when the applied stress intensity factor is increased was observed in both steels. Nevertheless, for the same applied K_{app} the grade tempered at higher temperature always showed a smaller crack growth. For example, for an applied stress intensity factor of about 80 MPa$\sqrt{m}$, crack growth was negligible (0.07 mm) in the 42CrMo4-700 grade, but around 0.85 mm in the 42CrMo4-650 grade. This fact is clearly appreciated in Figure 4.91, that shows the crack extension in the centre of the CT specimens (where hydrogen concentration is maximum) after being submitted to different stress intensity factors for 24h.

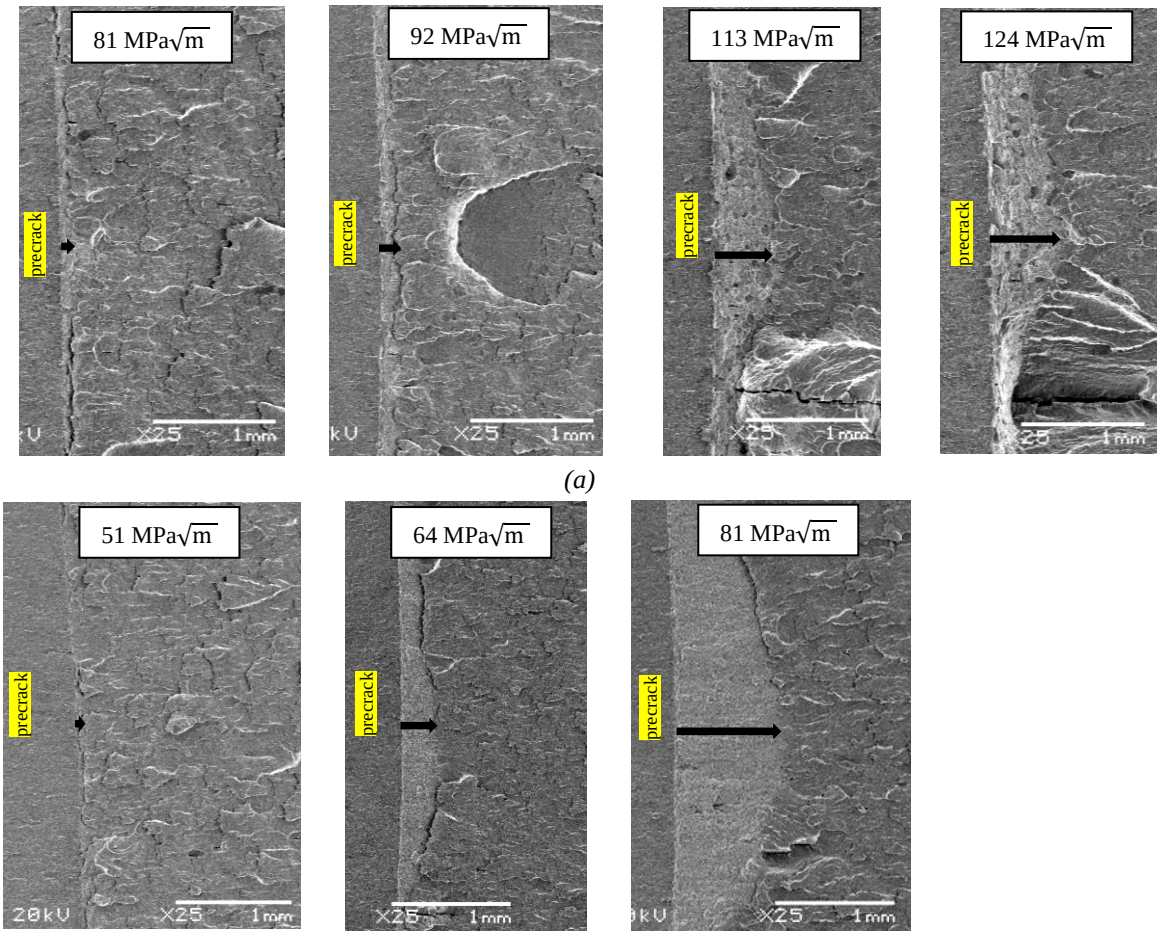

Figure 4.91. Crack growth (SEM) observed at mid-thickness under different stress intensity factors, K_{app}, applied during 24h in (a) 42CrMo4-700 and (b) 42CrMo4-650 steels. Maximum crack growth is indicated by a black arrow.

As already advanced in Table 4.31, considering a certain grade, the operative fracture micromechanisms were similar in all the tests, regardless of the applied K_{app}. Figure 4.92 and Figure 4.93 were selected as examples.

The crack growth fracture surfaces corresponding to 42CrMo4-700 tested under a K_{app}=92 MPa$\sqrt{m}$ (Figure 4.92) reveal the same operative fracture micromechanism along all the crack length (in this case, maximum Δa was 0.13 mm), that corresponds to martensite lath decohesion, MLD, already described in previous sections.

On the other hand, when a K_{app} equal to 80 MPa$\sqrt{m}$ was applied to a CT specimen of the 42CrMo4-650 grade (see Figure 4.93), although the primary micromechanism observed in the crack growth region was also MLD, a small fraction of intergranular cracking, IG, was also detected. This finding is in agreement with the fracture behaviour showed in the previous section and also with the observations made by Somerday and Nibur [180]. These authors detected a change from MLD to MLD with certain amounts of intergranular secondary cracking when the yield strength of the steel increased from 641 to 900 MPa.

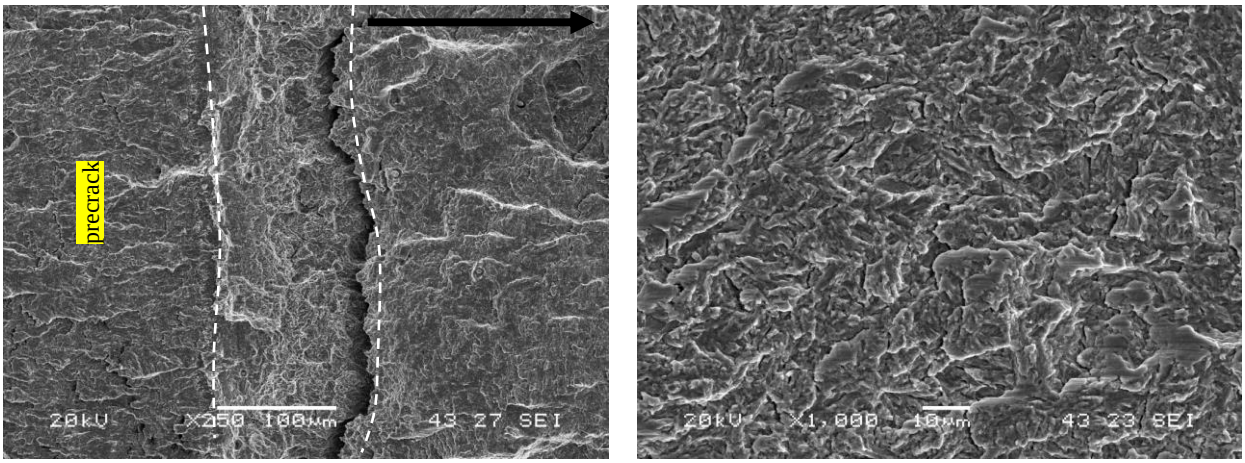

(a) *(b)*

Figure 4.92. Fracture surface (SEM) of hydrogen pre-charged CT specimen of 42CrMo4-700 steel submitted to K_{app} = 92 MPa$\sqrt{m}$ for 24 h. (a) General view (mid-thickness) and (b) detail of the crack growth region.

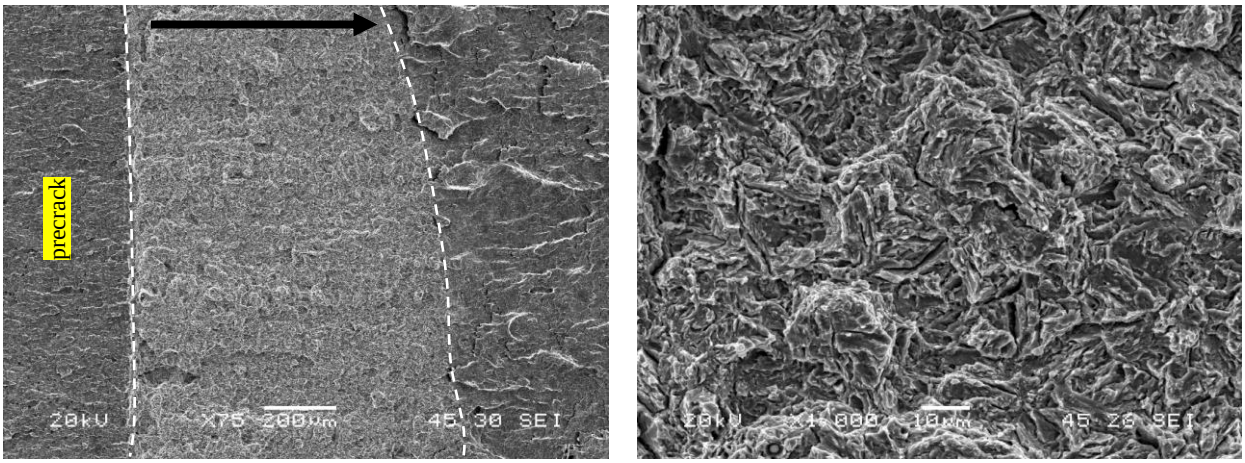

(a) *(b)*

Figure 4.93. Fracture surface (SEM) of hydrogen pre-charged CT specimen of 42CrMo4-650 steel submitted to K_{app} = 80 MPa$\sqrt{m}$ for 24 h. (a) General view (mid-thickness) and (b) detail of the crack growth region.

4.6.3.2. Influence of the austenitic grain size

The results obtained in the constant load tests performed on pre-cracked and pre-charged specimens of the coarse grain steels, 42CrMo4-700-CG and 42CrMo4-725-CG, are presented in Table 4.32. These results may be compared with the results relative to the corresponding base, fine grain steel, already shown in Table 4.31. Again, crack growth increases were observed after 24h of constant loading in both steels.

The fracture surfaces of these specimens observed at low magnifications are shown in Figure 4.94. Note that crack growth always increases with the applied K_{app}.

Steel grade	$C_{H0} \rightarrow C_{Hf}$ [ppm]	P_{app} [kN]	K_{app} [MPa$\sqrt{m}$]	K_{final} [MPa$\sqrt{m}$]	Δa [mm]	Fracture Micromechanisms*
700-CG	1.0→0.75	19.34	85	86	0.14	MLD
		20.39	90	92	0.23	MLD+IG
		24.22	93	95	0.36	
		27.50	105	108	0.82	
725-CG	0.5→0.4	20.23	83	83	0.03	-
		19.60	90	90	0.12	MVC+MLD
		21.88	100	103	0.48	
		23.34	107	116[(1)]	---[(1)]	

*Table 4.32. Results of the 24h constant load tests performed on the coarse grain 42CrMo4 grades. [(1)] Run-out: this specimen failed in two parts after 7 hours testing. Operative fracture micromechanisms in order of importance. * MLD: martensitic lath interface decohesion; IG: intergranular fracture.*

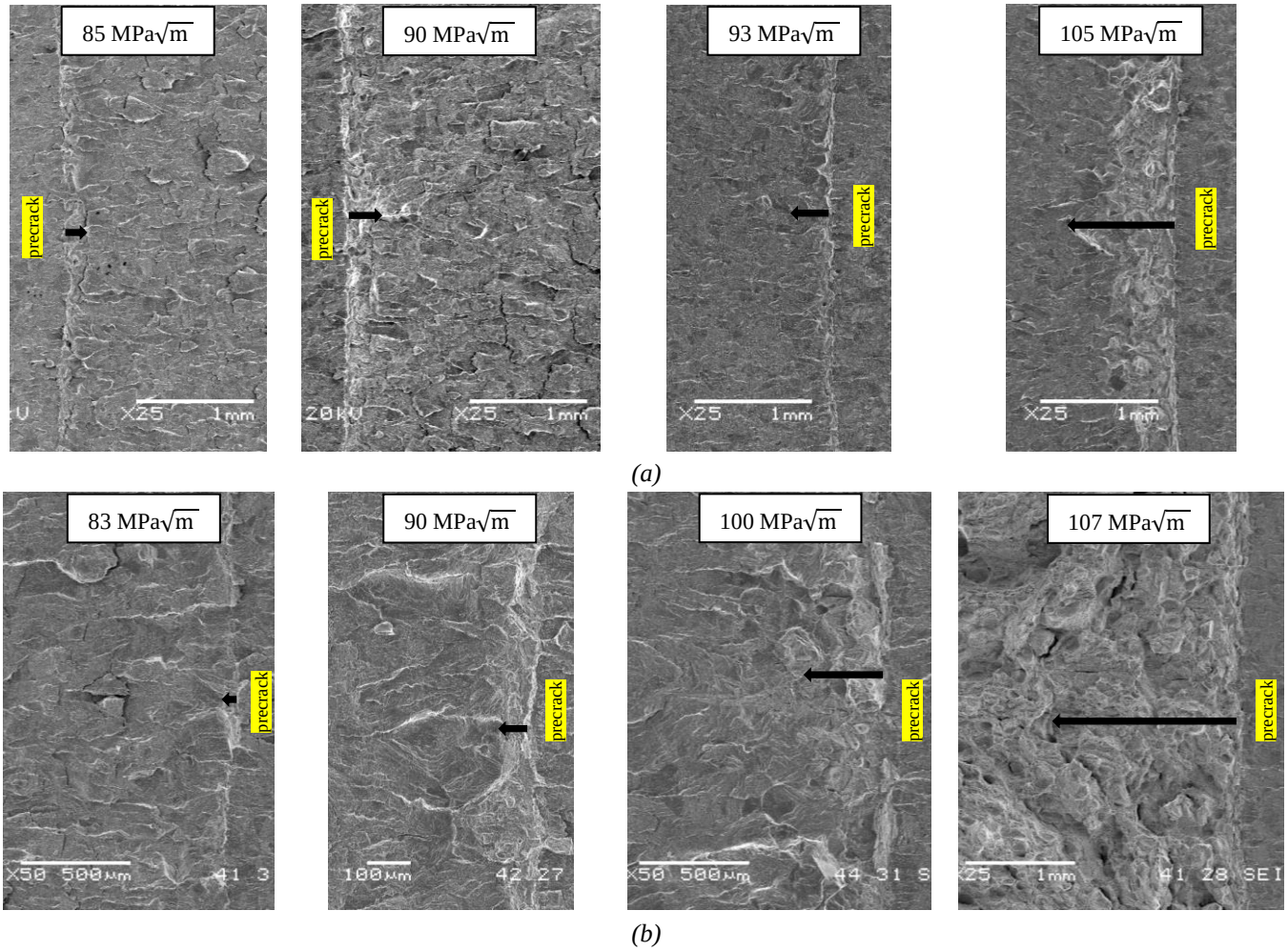

Figure 4.94. Crack growth (SEM) at mid-thickness under different stress intensity factors, K_{app}, applied during 24h, (a) 42CrMo4-700-CG and (b) 42CrMo4-725-CG steels. Maximum crack growth is indicated by a black arrow.

Crack growth takes place in the 42CrMo4-700-CG grade under the minimum applied stress intensity factor (K_{app}=85 MPa$\sqrt{m}$) due to the MLD micromechanism, but, for greater K_{app} applied values, intergranular failure was also detected. Figure 4.95 shows the action of only MLD or both

micromechanisms in different locations along the thickness of the broken specimen under 90 MPa$\sqrt{m}$. Images of Figure 4.95(a, b) correspond to the centre of the specimen, where hydrogen concentration is maximum, and therefore IG fracture (cracking along grain boundaries) takes place in combination with MLD. On the other hand, at 1 mm from the centre (Figure 4.95 (c, d)), intergranular cracking is no longer noticed, being MLD the only failure micromechanism acting at this location. Hydrogen concentration in not enough at this point to produce intergranular crack growth. For even greater K_{app} levels, K_{app}=105 MPa$\sqrt{m}$, decohesion along grain boundaries becomes more relevant and a more brittle behaviour is noticed, as can be deduced from the lack of plastic deformation in the facets of the split grains (see clean grain facets indicated with black arrows in Figure 4.96). In addition, a larger thickness front was affected by the IG micromechanism. It is thus clear that the applied stress intensity factor along with hydrogen accumulation at internal interfaces ahead of the crack tip, play a decisive role in fostering the embrittling mechanism associated to hydrogen in these particular tests.

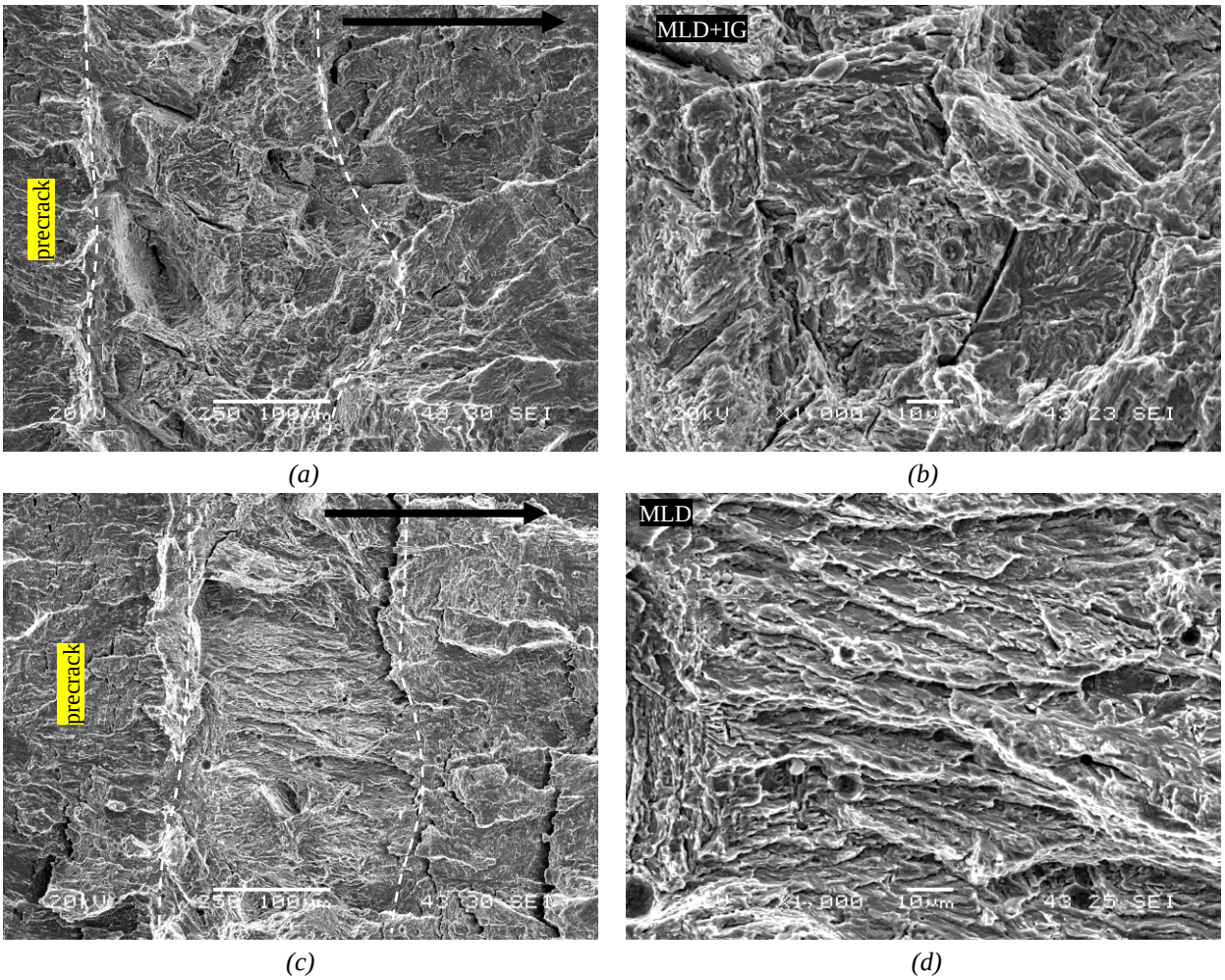

(a) *(b)* *(c)* *(d)*

Figure 4.95. Fracture surface (SEM) of hydrogen pre-charged CT specimen of coarse grain 42CrMo4-700-CG steel submitted to K_{app} = 90 MPa$\sqrt{m}$ for 24 h. (a, c) General views (mid-thickness) and (b, d) details of the corresponding crack growth regions.

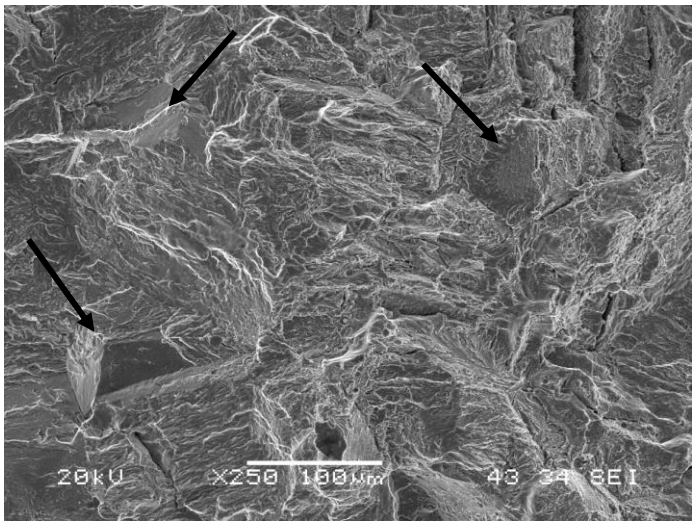

Figure 4.96. Fracture surface (SEM) of hydrogen pre-charged CT specimen of coarse grain 42CrMo4-700-CG steel submitted to K_{app} = 105 MPa$\sqrt{m}$ for 24 h.

Regarding now the 42CrMo4-725-CG steel, with a lower yield strength, no traces of IG fracture were observed at any level of K_{app}. Indeed, the operative fracture mechanism detected under all the applied K_{app} values was always a combination of MVC and MLD, being the latter highly localized in the central region of the specimens (mid-thickness), as can be seen in Figure 4.97. At this respect, this grade behaves better than the other coarse grain steel (42CrMo4-700-CG).

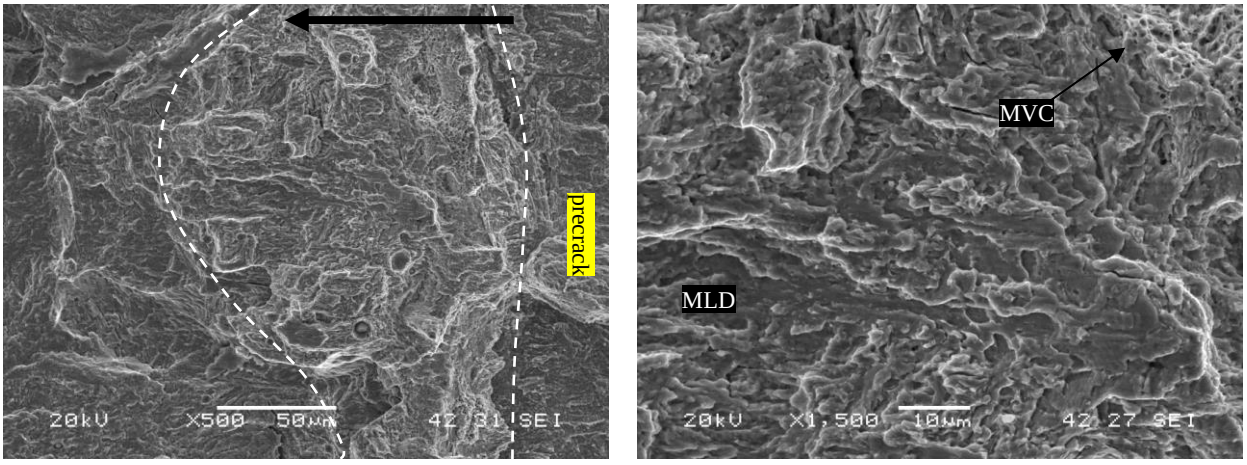

(a) *(b)*

Figure 4.97. Fracture surface (SEM) of hydrogen pre-charged CT specimen of coarse grain 42CrMo4-725-CG grade submitted to K_{app} = 90 MPa$\sqrt{m}$ for 24 h. (a) General view (mid-thickness) and (b) detail of crack growth region.

Another remarkable point observed in the coarse grain steel tempered at 725ºC was the considerable crack growth that took place when the applied K_{app} was 107 MPa$\sqrt{m}$. This specimen failed prematurely (the specimen broke in only 7 hours and the applied K at failure was estimated to be 116 MPa$\sqrt{m}$). Anyway, as can be seen in Figure 4.98, the operative fracture micromechanism at mid-thickness was a mixture of MLD and MVC.

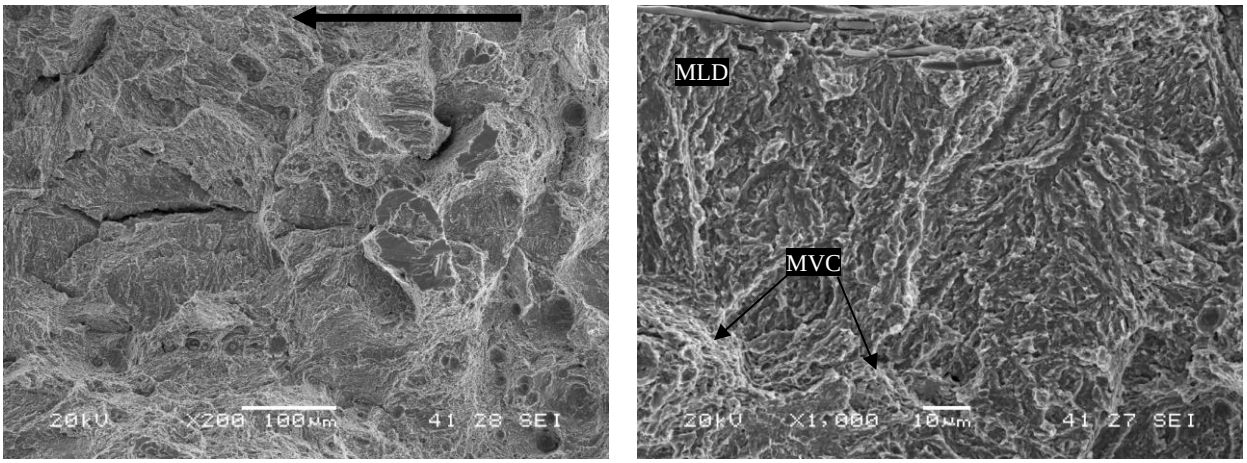

(a) *(b)*

Figure 4.98. Fracture surface (SEM) of hydrogen pre-charged CT specimen of coarse grain 42CrMo4-725-CG grade submitted to K_{app} = 107 MPa$\sqrt{m}$ for 24 h. (a) General view at mid-thickness and (b) detail of the crack growth region.

4.6.3.3. Discussion related to tests performed under constant K

In order to have a better unified vision of all the results obtained in the tests performed under constant K values, the applied intensity factor, K_{app}, versus the measured crack growth, Δa, was represented in Figure 4.99 for the four studied steels. The experimental points fit pretty well to potential laws of the form $K_{app}=C_1\Delta a^{C2}$, in a similar way as it was observed in the fracture toughness results when J was plotted against Δa (sub-section 4.6.2) [180]. Moreover, these K_{app} vs. Δa plots can be used to estimate the threshold stress intensity factor, $K_{th/0.2}$, for the onset of crack growth under internal hydrogen. Similarly to the $J_{0.2/BL}$ parameter used in the fracture toughness tests, a crack propagation of 0.2 mm was established as crack growth criterion in these constant load tests. The values of $K_{th/0.2}$ along with the constants of the potential law, C_1 and C_2, yield strength and prior austenitic grain size, are presented in Table 4.33.

From the results shown in Figure 4.99 and Table 4.33, it is seen that the value of $K_{th/0.2}$ decreases when the yield strength of the steel increases, when the steels having the same prior austenitic grain size are compared. This is in line with the results reported by Pyun and Lee [259] for a quenched and tempered AISI4340 steel, which demonstrated that specimens with lower yield strength required a higher K level for the occurrence of hydrogen assisted-cracking under a given hydrogen pressure. As already explained in this thesis, this behaviour is attributed to the fact that under a given applied K, the normal σ_{yy} stress acting in the process zone ahead of a crack tip in an elastic-plastic material increases as the yield strength does. The condition $K_{app}=K_{th}$ is reached when the hydrogen concentration in this highly stressed area is high enough to attain the critical hydrogen concentration ($C_H=C_{cr}$). At this point, hydrogen segregated in lath and grain boundaries provides the reduction of the cohesive strength to trigger the HEDE mechanism, and martensitic lath, MLD, and/or intergranular, IG, decohesion take place. This explanation is graphically shown in Figure 4.100.

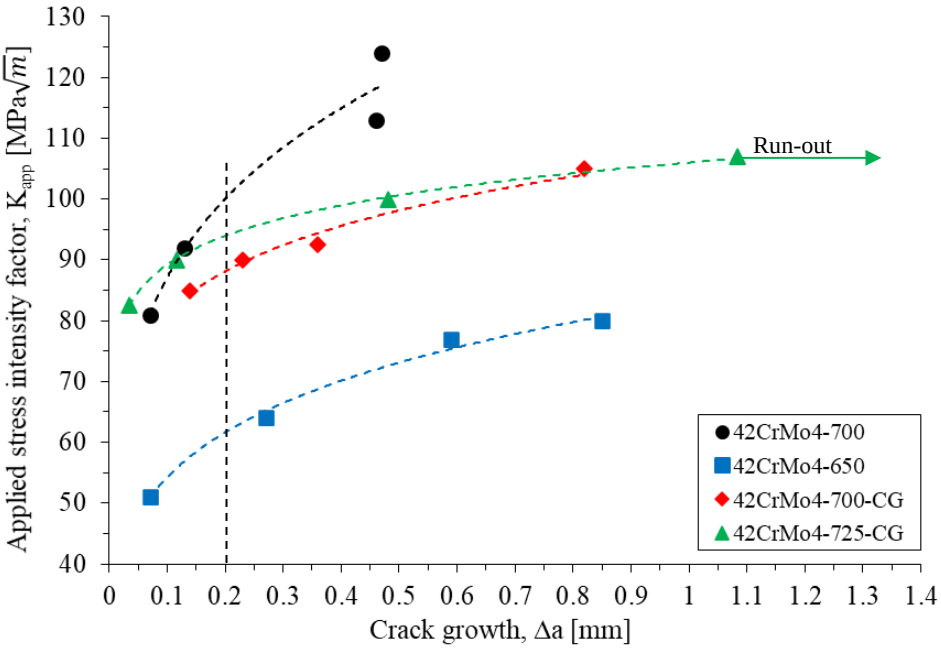

Figure 4.99. Evolution of crack growth, Δa, versus the applied stress intensity factor, K_{app}, with their corresponding potential fits.

Steel grade	PAGS [μm]	σ_{ys} [MPa]	$K_{th/0.2}$ [MPa$\sqrt{m}$]	$J=C_1\Delta a^{C2}$	
				C_1	C_2
42CrMo4-700	20	622	100	138	0.20
42CrMo4-650	20	820	62	83	0.18
42CrMo4-700-CG	150	602	88	107	0.12
42CrMo4-725-CG	150	498	94	106	0.08

Table 4.33. $K_{th/0.2}$ values and potential laws determined on hydrogen pre-charged CT specimens submitted to constant K tests.

Another useful way of displaying these results is representing the crack growth rate, Δa/Δt, (average crack growth in 24 h) in terms of the applied intensity factor, K_{app}, as it is shown in Figure 4.101. If the two steels tempered at the same temperature are compared (fine and coarse grain tempered at 700ºC), crack growth rate is significantly greater in the coarse grain grade and such differences increase with the aplied K factor.

On the other hand, when a higher tempering temperature is applied (725ºC), the measured crack growth rate under low K values is lower than the one corresponding to the fine grain steel, due mainly to reduction of the steel yield strength. However, for higher values of K, the crack growth rate measured on this steel increases as to converge with the behaviour of the other coarse grain grade.

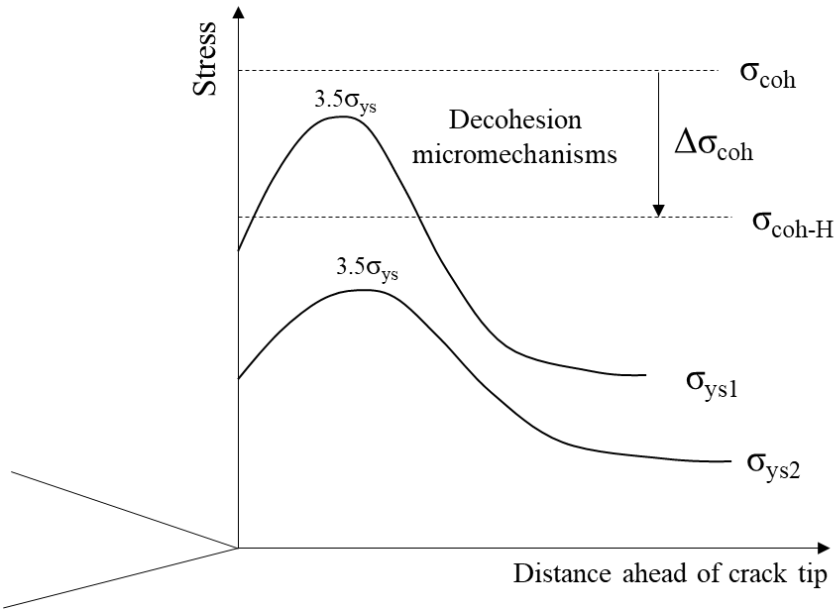

Figure 4.100. Cohesive strength reduction of grain boundaries and lath interfaces due to hydrogen, $\Delta\sigma_{coh}$, being σ_{coh} the cohesive strength of the uncharged steel and σ_{coh-H} the cohesive strength of the steel with internal hydrogen. Influence of the yield strength ($\sigma_{ys1} > \sigma_{ys2}$).

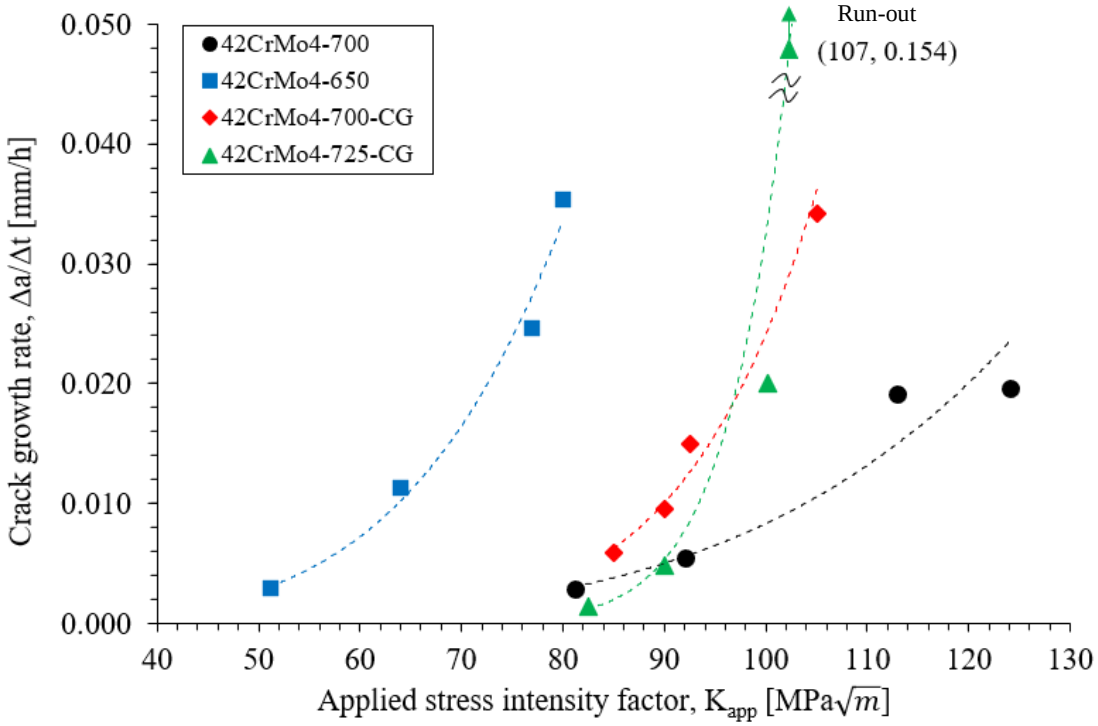

Figure 4.101. Average crack growth rate in 24 h, $\Delta a/\Delta t$, versus the applied stress intensity factor, K_{app}, with their corresponding potential fits.

Finally, an important final fact is also worth noting. The measured $K_{th/0.2}$ values obtained under constant K tests are much lower than the K values derived from the $J_{0.2/BL}$ parameter ($K_{J0.2/BL}$) obtained in fracture toughness tests with hydrogen pre-charged CT specimens tested at the lowest displacement rate (see Table 4.34). This is in agreement with Nibur and Somerday [150], who

noticed that standard fracture toughness tests and static loading tests under constant K applied values, conducted under the same hydrogen pressure, provided different results. This fact suggests that standard J-fracture tests performed under very low displacement rates (0.01 mm/min in this thesis) are not able to faithfully characterize the onset of crack growth under low stress intensity factors occurring when hydrogen is present.

Steel grade	σ_{ys} [MPa]	$K_{th/0.2}$ [MPa$\sqrt{m}$]	$K_{J0.2/BL}$ [MPa$\sqrt{m}$] [1]	$K_{th/0.2}$/ $K_{J0.2/BL}$
42CrMo4-700	622	100	282	0.35
42CrMo4-700-CG	602	88	232	0.38
42CrMo4-725-CG	498	94	247	0.38
42CrMo4-650	820	62	240	0.26

Table 4.34.Comparison between $K_{th/0.2}$ value and fracture toughness $K_{J0.2/BL.}$ [1] $K_{J0.2/BL}=(J_{0.2/BL}\,E/(1-\nu^2))^{1/2}$

4.6.4. Effects of internal hydrogen on the fatigue crack growth rate

The assessment of the hydrogen effects on the fatigue crack growth rate was performed in only four of the seven 42CrMo4 grades studied in this thesis. The selected grades, the same also used in the tests performed under constant K, where those that displayed the best behaviour with internal hydrogen in the fracture toughness tests. Therefore, hydrogen precharged CT specimens of 42CrMo4-700, 42CrMo4-650, 42CrMo4-700-CG and 42CrMo4-725-CG grades, were submitted to cyclic loads under different load ratios and frequencies.

In general lines, and based on the facts observed in the bibliographic review of sub-section 2.5.3, the main objectives of this subsection were:

- Knowing the influence of the yield strength and comparing the behaviour of fine grain and coarse grain microstructures, such as those found in steel welds, and the possible beneficial effects of an appropriate post-welding heat treatment.
- Helping to understand the combined influence of certain tests variables such as load ratio, R, and frequency, f.
- Clarifying the hydrogen embrittlement mechanisms operative under cyclic loads at different ΔK values on all these steels.

4.6.4.1. Influence of tempering temperature

First of all, the results obtained with the 42CrMo4 steel quenched and tempered at 700 and 650ºC for two hours were compared. Therefore, the fatigue crack growth rate, da/dN, was represented in Figure 4.102 versus the applied stress intensity factor range, ΔK, for the uncharged (R=0.1, 10Hz) and the hydrogen-precharged specimens tested at different frequencies under a load ratio of R=0.1.

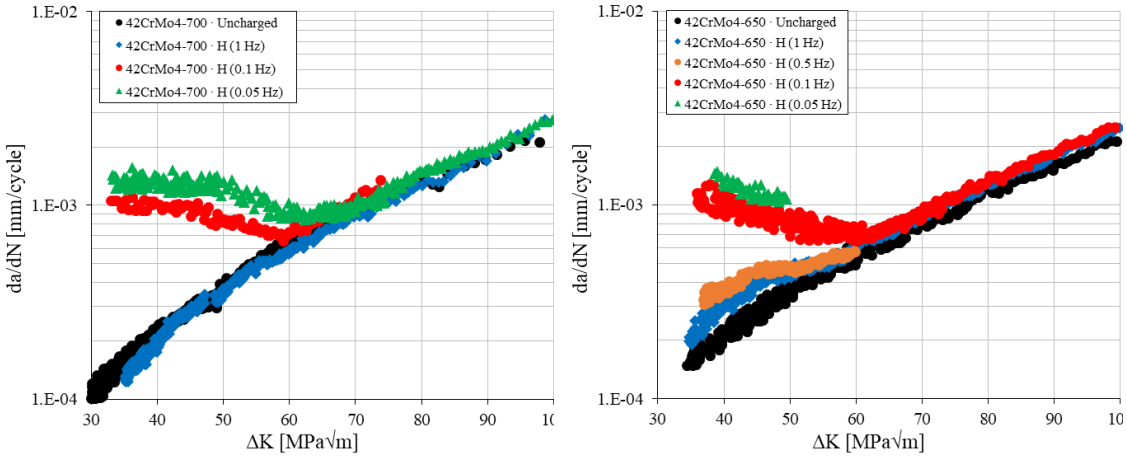

Figure 4.102. da/dN – ΔK curves of uncharged (R=0.1, 10 Hz) and hydrogen precharged CT specimens of (a) 42CrMo4-700 and (b)42CrMo4-650 grades tested at R=0.1. Influence of test frequency.

The remarkable effect of the testing frequency on the acceleration of the fatigue crack growth rate is worth to notice. The maximum hydrogen effects are displayed at the lowest testing frequencies (0.1 and 0.05 Hz) in both grades. It is also worth noting that under these low frequencies, the fatigue crack growth rate, da/dN, remains practically constant (even a slight decrease is apparent) from the beginning of the test, ΔK≈30-35MPa$\sqrt{m}$, up to a value of approximately 60-65MPa$\sqrt{m}$, when the curve overlaps that of uncharged specimens. This behaviour, that resembles the "plateau" region observed by other authors [15], will be discussed later.

When 42CrMo4-700 specimens (σ_{ys}=622 MPa) are tested with internal hydrogen at the highest frequency, 1 Hz, hydrogen does not modify the fatigue crack growth rate (similar to results obtained without hydrogen), however, in the case of the 42CrMo4-650 grade (σ_{ys}= 828 MPa), tested at the same frequency, the presence of internal hydrogen already increases the FCGR, around 1.5-1.6 times for low ΔK applied values in relation to the FCGR measured without hydrogen (see Table 4.35). As explained in previous sections, this difference is explained by the higher yield strength of the steel tempered at 650ºC and, therefore, by its capacity to develop higher stresses in the crack tip process region, where higher hydrogen accumulation will take place in each fatigue cycle.

Testing conditions			ΔK [MPa$\sqrt{m}$]								
Steel grade	R	f [Hz]	35	40	45	50	55	60	65	70	75
42CrMo4-700	0.1	1	0.9	0.9	0.9	0.9	0.9	0.9	0.9	0.9	0.9
		0.1	7.6	5.0	3.4	2.6	1.8	1.3	1.2	1.2	1.2
		0.05	9.4	5.9	4.6	3.8	2.6	1.7	1.4	1.2	1.2
42CrMo4-650	0.1	1	1.5	1.5	1.6	1.2	1.2	1.2	1.1	1.1	1.1
		0.5	2.1	1.8	1.9	1.3	1.3	1.1	-	-	-
		0.1	7.6	4.7	3.7	2.1	1.8	1.4	1.2	1.2	1.2
		0.05	-	5.9	4.5	2.9	-	-	-	-	-

Table 4.35. da/dN multiplication factor related to uncharged specimens, $(da/dN)_H/(da/dN)_{noH}$, at different ΔK values for 42CrMo4-700 and 42CrMo4-650 steels. Influence of test frequency.

On the other hand, at a frequency 10 times lower, 0.1 Hz, where hydrogen effects became remarkable at low ΔK values (the multiplication factor of the FCGR reaches values over 7), the behaviour of both grades is nearly the same. A possible explanation for this behaviour is that under this very low frequency, hydrogen accumulation attains maximum values in both steels and the influence of a higher yield strength becomes less relevant. Furthermore, when the frequency was decreased even more, to 0.05 Hz, the FCGR slightly increases in both cases, around 20-25% with respect to the result at 0.1 Hz.

The fracture surfaces of these fatigued CT specimens were analysed under the scanning electron microscope, and the most relevant features are shown in Figure 4.103, Figure 4.104 and Figure 4.105. Taking into account that the most relevant differences were noted at the lowest test frequencies and low ΔK values, 35-40 MPa$\sqrt{m}$, only the failure surfaces at the appropriate locations of those specimens tested at 0.1 Hz are presented. A ductile topography, characterized by plastic tears and fatigue striations perpendicular to the crack propagation direction (yellow arrows) were observed in the uncharged specimens of both 42CrMo4-700 and 42CrMo4-650 grades (R=0.1 and 10 Hz), as can be observed in Figure 4.103 at different magnifications.

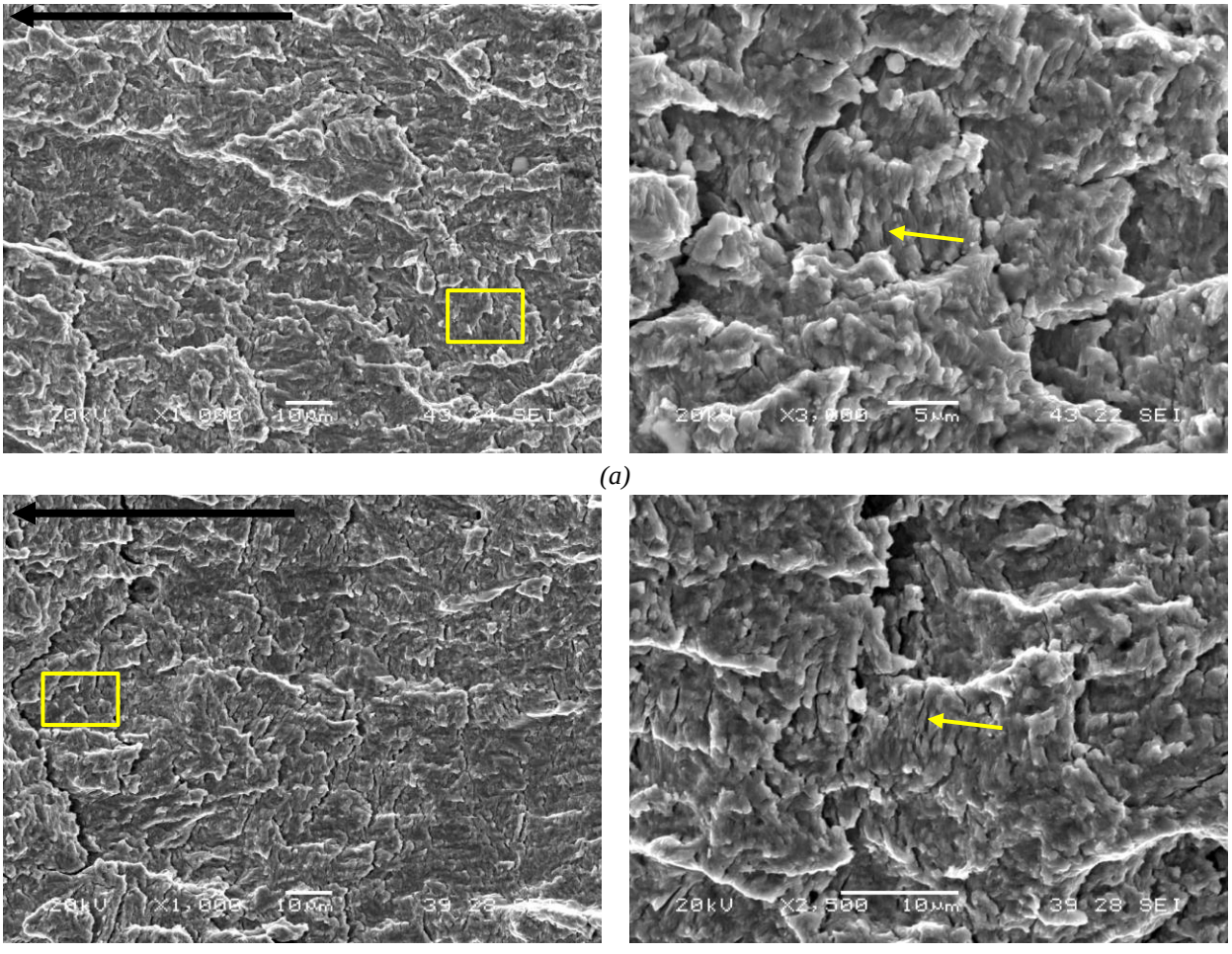

Figure 4.103. SEM fracture surfaces of uncharged specimens (R=0.1, 10 Hz) at ΔK≈35 MPa$\sqrt{m}$. (a) 42CrMo4-700 and (b) 42CrMo4-650. Black arrow shows crack propagation direction.

However, these striation marks were absent on 42CMo4-700 specimens tested with internal hydrogen and the martensitic lath decohesion micromechanism, MLD, becomes the most relevant characteristic feature, as it is exemplified in Figure 4.104. Other authors [38][260] have already pointed out the difficulty of observing fatigue striations in fatigue tests performed in the presence of hydrogen, where, as it had been already justified in the static tests, failure micromechanism is associated to the decrease of the cohesive strength among lath martensite interfaces promoted by hydrogen.

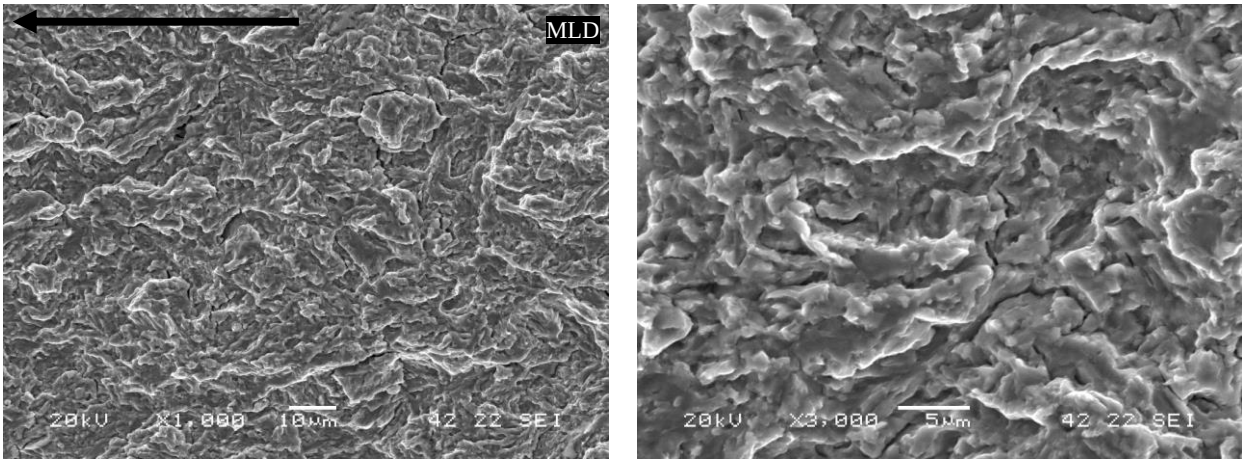

(a) *(b)*

Figure 4.104. SEM fracture surfaces of hydrogen pre-charged specimens (R=0.1, f=0.1) of 42CrMo4-700 steel at ΔK≈35 MPa$\sqrt{m}$. (a) General view and (b) detail of MLD mechanism. Black arrow shows crack propagation direction.

Similar observations can also be made on those samples tested with internal hydrogen in the case of the 42CrMo4-650 steel. Striation marks were not noticed and the MLD micromechanism was generalized, as observed in Figure 4.105(a) and (b). In addition, some small areas of intergranular fracture, IG, are also visible in these specimens. They are marked with yellow arrows in Figure 4.105(c) and (d). However, as seen in these images, IG fracture was not relevant, being MLD the leading micromechanism, which explains the similar FCG behaviour of this grade with respect to the steel tempered at 700ºC.

The influence of the load ratio in the fatigue crack growth rate was also studied in this research work. Hydrogen pre-charged CT specimens of the 42CrMo4-700 steel were submitted to load ratios, R, of 0.1, 0.5 and 0.7, keeping the frequency at 0.1 Hz in all the cases. In addition, a test at R=0.5 was performed on an uncharged specimen (f=10 Hz) for comparison. The obtained results are shown in Figure 4.106.

First of all, under the applied ΔK values, the influence of the R ratio in the hydrogen free steel is observed to be very small. For example, at ΔK=35 MPa$\sqrt{m}$, the increase of R from 0.1 to 0.5 implies a multiplication factor of 1.1-1.2 in FCGR, which even tends to decrease as ΔK increases. The curve corresponding to the uncharged specimen tested at R=0.7 was identical to that of R=0.5 and was not included in this figure.

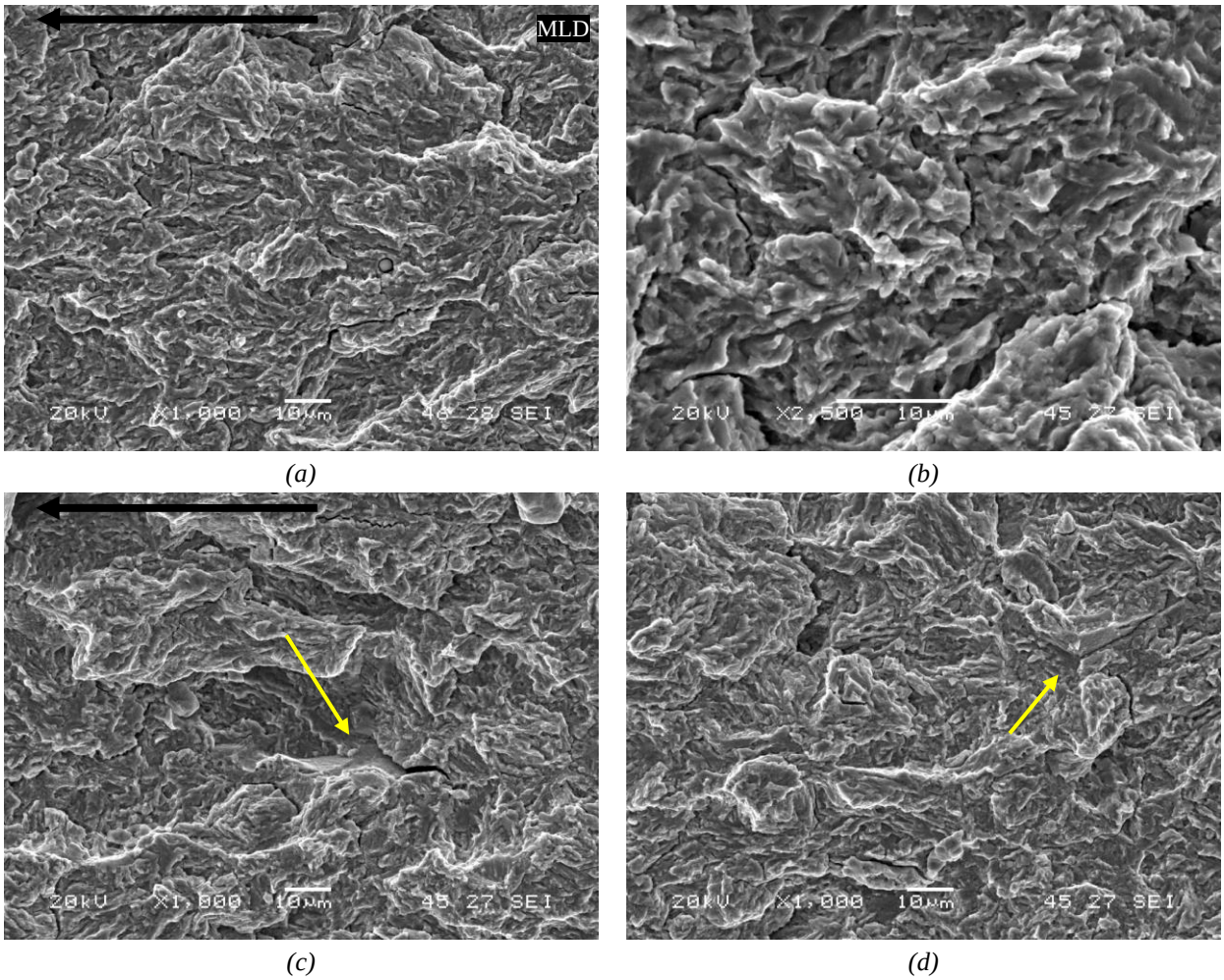

Figure 4.105. SEM fracture surfaces of hydrogen pre-charged specimens (R=0.1 and f=0.1) of 42CrMo4-650 steel at ΔK≈35 MPa$\sqrt{m}$. (a) General view, (b) detail of MLD fracture and (c, d) areas with IG fracture. Black arrow shows crack propagation direction.

Regarding now hydrogen pre-charged specimens, although a considerable FCGR acceleration takes place in all the scenarios, a progressive drop in the FCGR as the R value is increased from 0.1 to 0.5 and 0.7 was detected. In fact, the multiplication factor at 35 MPa$\sqrt{m}$, that was 7.6 for R=0.1, falls to 5.4 and 4.1, respectively at R=0.5 and 0.7. This is a peculiar behaviour, that deserves discussion in the corresponding section.

The operative fracture micromechanisms identified on the surfaces of these uncharged and hydrogen pre-charged specimens were exactly the same as those reported for the specimens tested at a load ratio of 0.1: ductile mechanisms with striation marks in the uncharged specimens and MLD micromechanisms (without any sign of striation marks) in those specimens tested with internal hydrogen at load ratios of 0.5 and 0.7. Figure 4.107 shows an example corresponding to the fracture surface at 35-40 MPa$\sqrt{m}$ of uncharged and hydrogen precharged specimens tested under R=0.5.

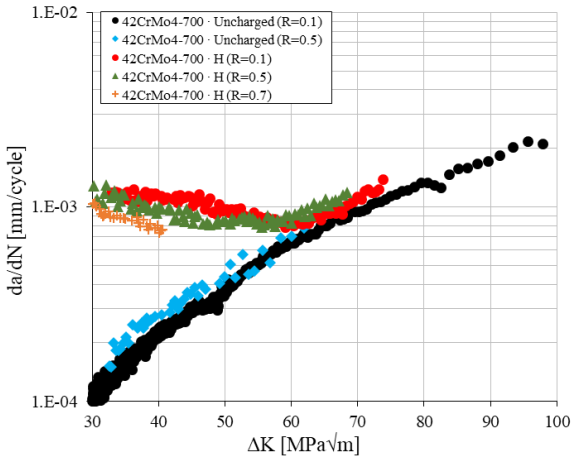

Figure 4.106. da/dN – ΔK curves of uncharged (10Hz) and hydrogen precharged CT specimens of 42CrMo4-700 steel tested at f=0.1 Hz. Influence of the load ratio R.

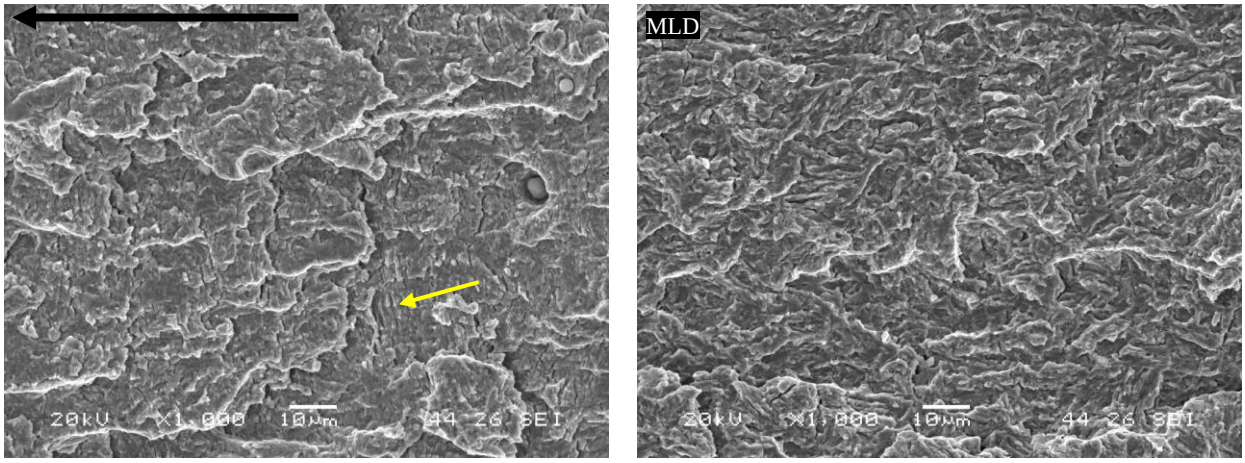

(a) *(b)*

Figure 4.107. SEM fracture surfaces of 42CrMo4-700 steel at ΔK≈35 MPa$\sqrt{m}$ corresponding to (a) uncharged specimen tested at R=0.5 and 10 Hz (notice striation marks) and (b) hydrogen pre-charged specimens tested at R=0.5 and f=0.1 Hz. Black arrow shows crack propagation direction.

4.6.4.2. Influence of the austenitic grain size

The curves representing the fatigue crack growth rate, da/dN, versus the stress intensity factor range, ΔK, for uncharged and hydrogen pre-charged CT specimens corresponding to the coarse grain 42CrMo4-700-CG and 42CrMo4-725-CG steels are respectively shown in Figure 4.108(a) and (b). The presence of internal hydrogen induces an important increase in the FCGR on both coarse grain steels, but these results should be compared with the results relative to the base, fine grain steel, already shown in Figure 4.102.

Figure 4.109 compares the fatigue behaviour of fine grain (42CrMo4-700) and both coarse grain steels tested in air (10 Hz) and with hydrogen (0.1 Hz) under a load ratio of 0.1.

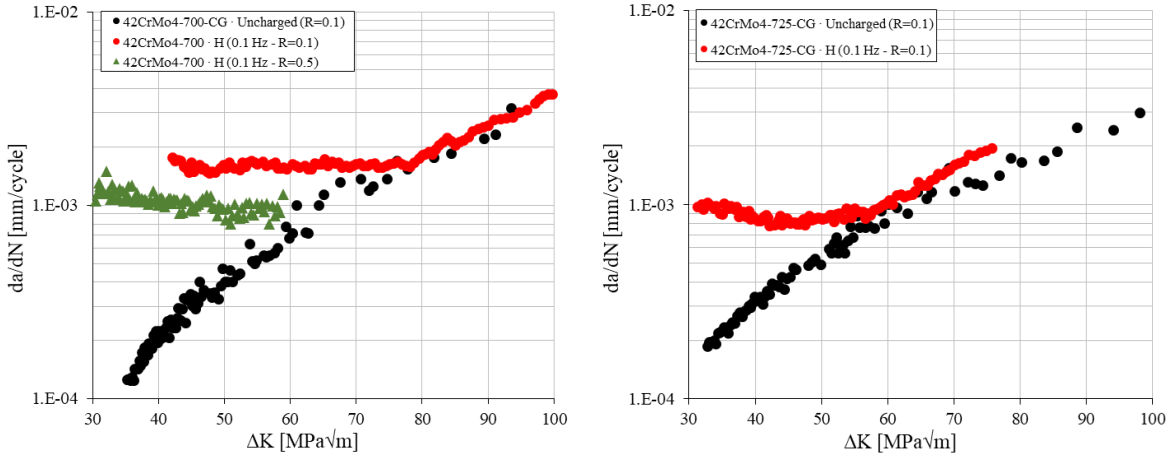

Figure 4.108. da/dN – ΔK curves of uncharged (R=0.1, 10 Hz) and hydrogen precharged CT specimens of (a) 42CrMo4-700-CG and (b) 42CrMo4-725-CG grades.

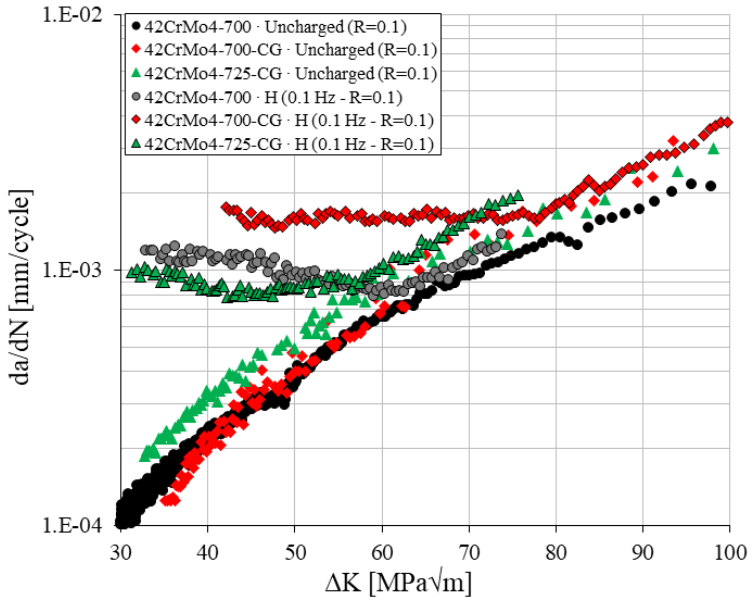

Figure 4.109. Comparison of the fatigue behaviour of uncharged (R=0.1, 10 Hz) and hydrogen precharged (R=0.1, 0.1 Hz) CT specimens of fine grain 42CrMo4-700 and coarse grain grades, 42CrMo4-700-CG, 42CrMo4-725-CG.

Comparing first the behaviour of uncharged specimens, the coarse grain grades show higher FCGRs. The coarse grain grade tempered at 700ºC shows a similar behaviour than the fine grain steel up to 60MPa$\sqrt{m}$, and from this point on, always displays a FCGR about 1.5 times greater, and the corresponding fracture micromechanism changes from ductile (striations as shown in Figure 4.110(a)) to an apparently more brittle one, as observed in Figure 4.110(b). However, at greater magnifications, striation marks were still visible (Figure 4.110(c)). This behaviour was previously observed by Vargas-Arista et al. [203] in the HAZ of a 42CrMo4 steel with yield strengths between 682 and 710 MPa. On the other hand, the fatigue crack growth rate of the coarse grain steel tempered at 725ºC remains above that of the fine grain steel for all ΔK ranges, due to its lower yield strength and fracture toughness. In this case, striation marks are also distinguishable from crack initiation to the last stage of crack growth, as shown in Figure 4.110(d).

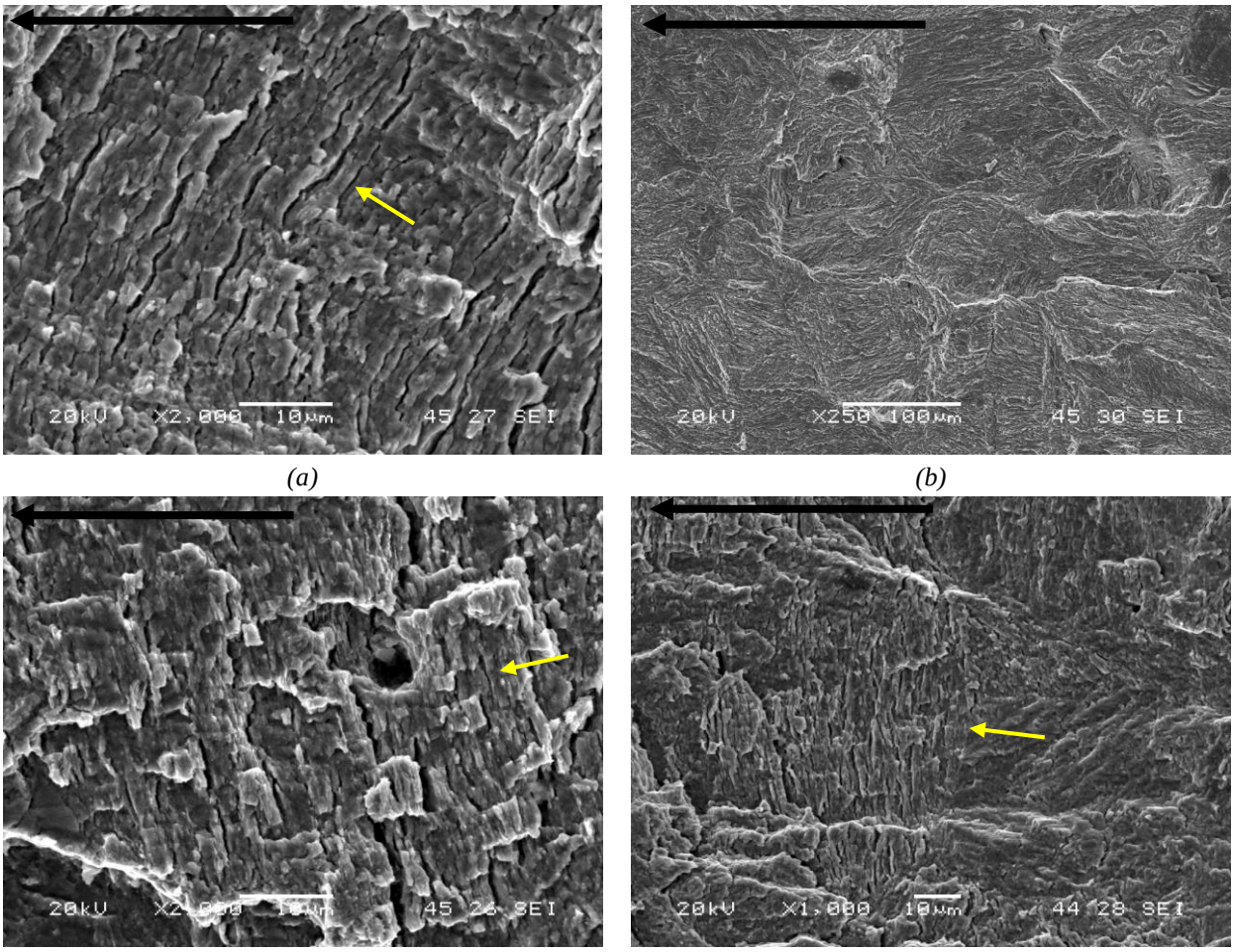

(a) *(b)* *(c)* *(d)*

Figure 4.110. SEM fracture surfaces of uncharged specimens (R=0.1, 10 Hz) of (a) 42CrMo4-700-CG at ΔK≈35 MPa$\sqrt{m}$, (b, c) 42CrMo4-700-CG at ΔK≈80 MPa$\sqrt{m}$ and (c) 42CrMo4-725-CG at ΔK≈35 MPa$\sqrt{m}$. Black arrow shows crack propagation direction.

Regarding now the behaviour of these same steels with internal hydrogen, the prior austenite grain size increase from 20 µm (42CrMo4-700) to ≈150µm (42CrMo4-700-CG) gives rise to a significant increment of the FCGR when the same tempering temperature of 700ºC was used. In fact, as shown in Table 4.36, this coarse grain steel experiences an average FCGR multiplication factor about two times greater than the fine grain steel. This worst fatigue behaviour also manifests in drastic changes in the operative fracture micromechanisms, as can be observed in Figure 4.111. The fatigue fracture surfaces of 42CrMo4-700-CG are now characterized by the combination of IG and MLD. The large size of prior austenitic grains is also worth noting in these images.

Testing conditions			ΔK [MPa$\sqrt{m}$]								
Steel grade	R	f [Hz]	35	40	45	50	55	60	65	70	75
700	0.1	0.1	9.4	5.9	4.6	3.8	2.6	1.7	1.4	1.2	1.2
700-CG			-	14.1	7.0	5.0	3.8	3.0	2.4	1.4	1.2
725-CG			4.4	2.5	1.9	1.7	1.1	1.1	1.2	1.3	1.3

Table 4.36. da/dN multiplication factor related to uncharged specimens, $(da/dN)_H/(da/dN)_{noH}$ (R=0.1, f=10Hz), at different ΔK values for fine grain and coarse grain steels.

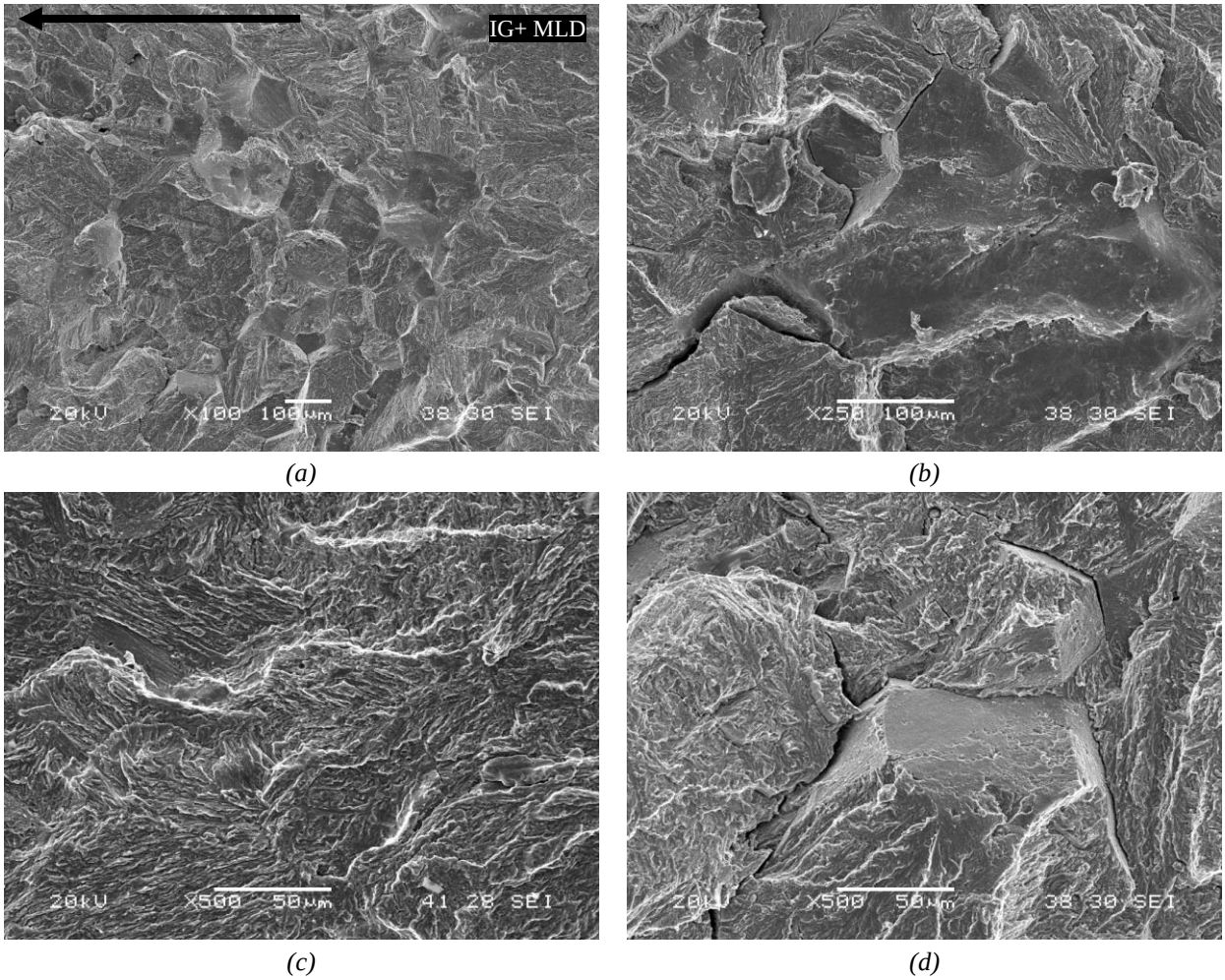

(a) *(b)*

(c) *(d)*

Figure 4.111. SEM fracture surfaces of hydrogen pre-charged specimens (R=0.1 and f=0.1) of 42CrMo4-700-CG steel at ΔK≈45 MPa$\sqrt{m}$. (a, b) General views and (c, d) details of MLD and IG mechanisms. Black arrow shows crack propagation direction.

On the other hand, the 42CrMo4-725-CG steel, despite its large prior austenitic grain size, displays an improve behaviour under cyclic loads, even better than the fine grain steel, as can be observed in Figure 4.109 and Table 4.36. In fact, the average FCGR multiplication factor due to hydrogen is in this coarse grain grade 50% lower than in the case of fine grain steel, up to a ΔK of 60 MPa$\sqrt{m}$. The IG fracture mechanism is not present in the fracture surface of this steel, but a combination of ductile and brittle features instead: striation marks are present in some areas and the MLD micromechanism in others (Figure 4.112).

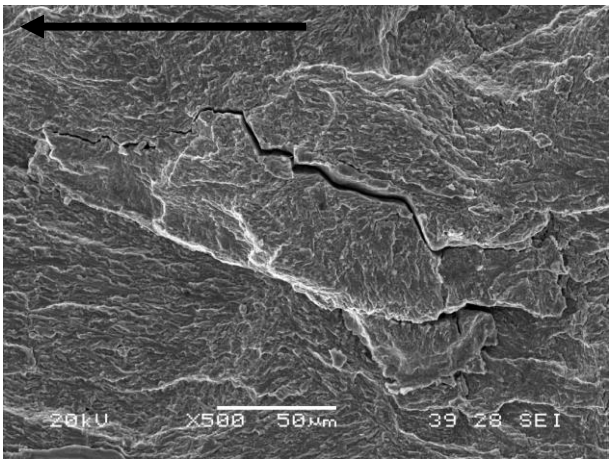

(a)

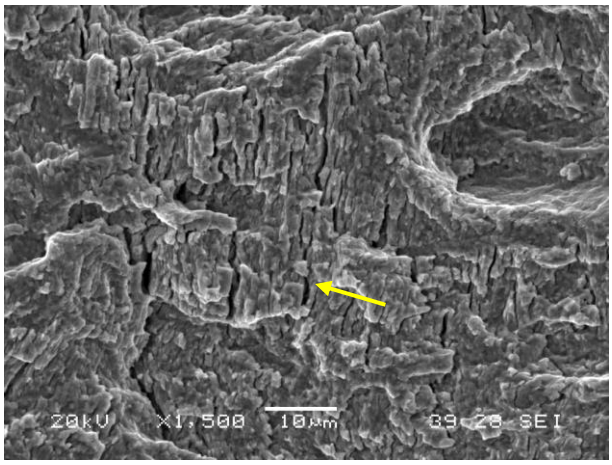

(b)

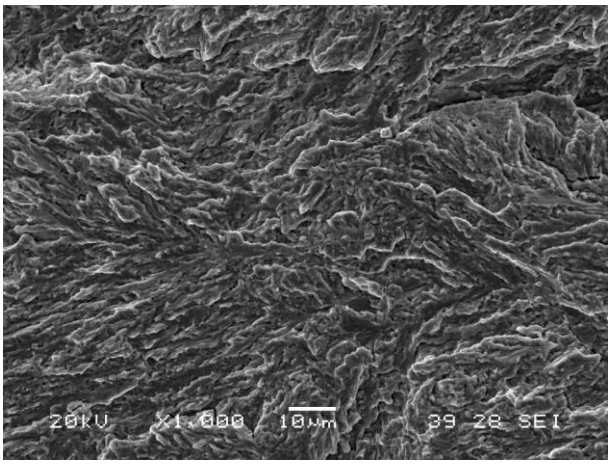

(c)

Figure 4.112. SEM fracture surfaces of hydrogen pre-charged specimens (R=0.1 and f=0.1) of 42CrMo4-725-CG steel at $\Delta K \approx 35$ MPa$\sqrt{m}$. (a) General view, (b) detail of striations and (c) detail of MLD mechanism. Black arrow shows crack propagation direction.

4.6.4.3. Discussion related to fatigue crack growth tests

The negative effect of hydrogen on the fatigue crack growth resistance of quenched and tempered 42CrMo4 steel was evident from the results already presented in this section. Now, the observed effects of some test variables and steel characteristics are discussed and justified.

In first place, the tempering temperature, i.e., yield strength of the steel, seems to play a certain role only under relatively high testing frequencies (1 Hz), being the steel tempered at the lowest temperature, 650ºC, more sensitive to hydrogen under cyclic loads. As discussed extensively in previous sections, when the yield strength of the steel increases, the magnitude of the stresses developed in the crack tip region increase, which in turn facilitates the accumulation of more hydrogen in the process zone during each fatigue cycle. However, it was shown before that under low frequencies, 0.1 and 0.05 Hz, the effect of a higher yield strength becomes already negligible. This behaviour can be explained assuming that, at these very low frequencies, hydrogen accumulation in the process zone already attains maximum values in both grades, which additionally had the same initial hydrogen content of 1.2 ppm, as it was seen in Table 4.13.

On the other hand, test frequency has a very important effect on these fatigue tests. In fact, when the frequency applied in the fatigue test is decreased, the time at which the process zone in the specimen remains under high loads or high stress intensity factors during a single cycle increases Considering for example the case shown in Figure 4.113, a specimen tested at 1 Hz spends 0.5 s in each cycle under stresses higher than the average, K_{ave}, while under 0.1 Hz, this time becomes 5 s. Considering a constant hydrogen diffusion coefficient, D_{app}, the diffusion distance, $x_H = 2\sqrt{D_{app} \cdot t}$, will be around 3 times greater under the lowest frequency, being therefore the crack tip fed with more hydrogen in each cycle. In fact, it has been numerically demonstrated that the concentration of hydrogen in the crack tip region during a fatigue cycle increases as the test frequency is decreased [261].

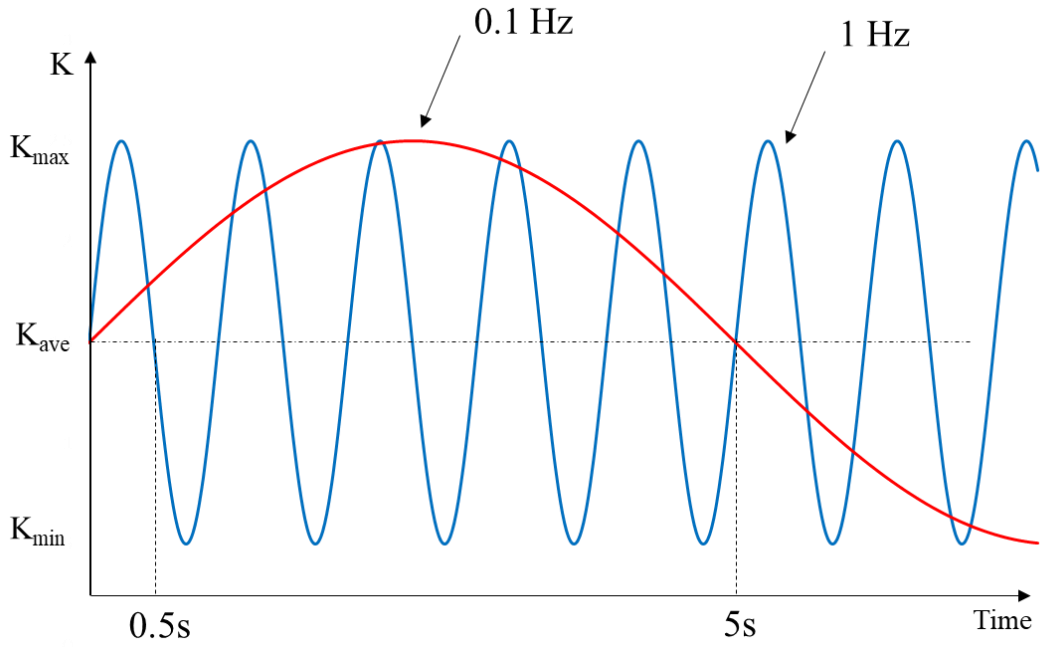

Figure 4.113. Cyclic K evolution at two frequencies, 0.1 and 1 Hz (R=0.1) in fatigue tests.

It was also observed that increasing the load ratio, R, applied in the fatigue tests had not a negative impact in the crack propagation rate measured in any of the tested steels. This is in line with the observations made by other authors [195] at intermediate values of ΔK in tests performed under hydrogen gas. In fact, in this thesis a surprising decrease in the fatigue crack growth rate was noticed when increasing R from 0.1 to 0.5 and 0.7 (see Figure 4.106). In order to explain this behaviour, Figure 4.114 shows the sine wave K evolution in fatigue tests performed under different values of the R ratio. Since $\Delta K = K_{max}(1 - R)$, an increase in R at a fixed ΔK value produces an increase in the maximum stress intensity factor, K_{max}, as well. Therefore, according to *Equation (4.3)*, the plastic zone size will also increase at higher values of R. Some numbers are given in Table 4.37, that shows the approximate value of the plastic zone diameter, d_p, for load ratios of 0.1, 0.5 and 0.7 under ΔK=30 MPa$\sqrt{m}$.

$$d_p = \frac{1}{\pi}\left(\frac{K_{max}}{\sigma_{ys}}\right)^2 \qquad \textit{Equation (4.3)}$$

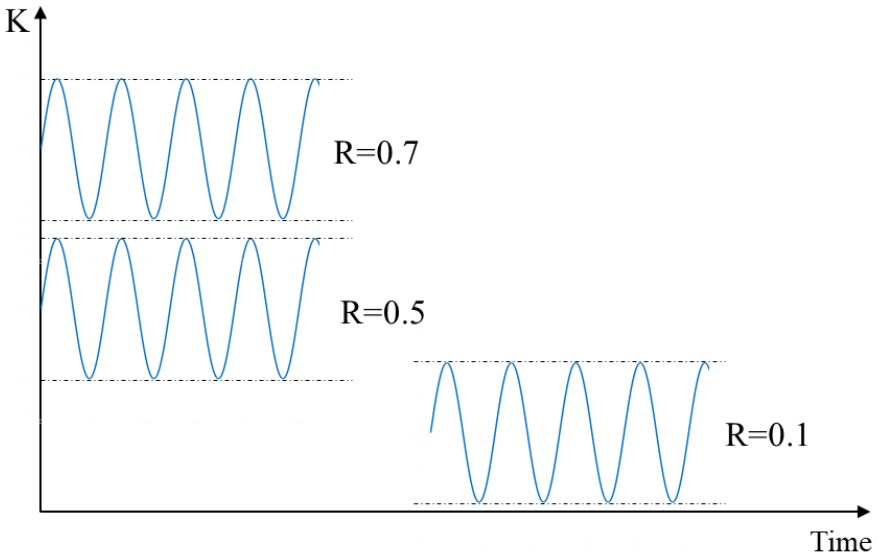

Figure 4.114. Effect of increasing load ratio, R, on the maximum stress intensity factor, K_{max}, reached in each load cycle under a fixed ΔK applied value.

R	K_{min} [MPa]	K_{max} [MPa]	d_p [mm]
0.1	3	33	0.89
0.5	30	60	2.96
0.7	70	100	8.23

Table 4.37. Minimum, K_{min}, and maximum, K_{max}, stress intensity factors and approximate diameter of the plastic zone, d_p, for different values of the load ratio, R, at $\Delta K=30\ MPa\sqrt{m}$.

Although higher K values will also induce higher plastic strains at the crack front and the hydrogen diffusion coefficient will decrease as it was shown in the corresponding chapter of this thesis, as hydrogen would also be transported by dislocations in this specific region (and dislocation density will depend on plastic deformation) the effect of R ratio on the time needed by hydrogen atoms to move into the process zone is uncertain.

Nevertheless, Table 4.3 clearly shows that an increase in the R ratio produces a very important increase of the size of the plastic region developed ahead of the crack tip where hydrogen accumulates. Assuming then a similar hydrogen entrance into the plastic zone from adjacent regions of the sample, hydrogen will distribute in a wider region when a higher R ratio is applied in the fatigue test, local hydrogen content will be then lower and fatigue crack growth rate will decrease as well. This explanation is shown graphically exposed in Figure 4.115.

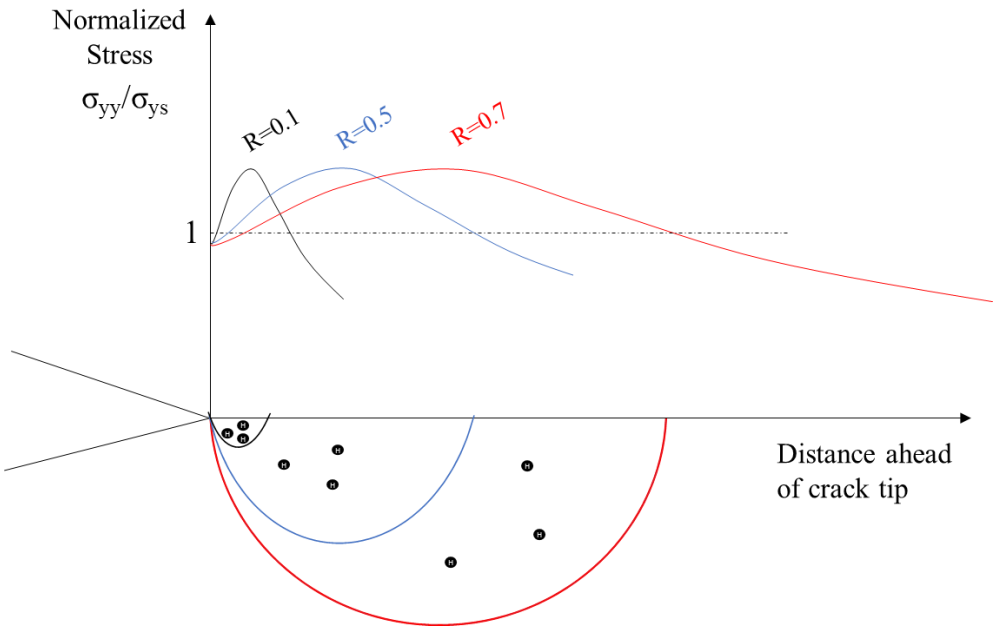

Figure 4.115. Local normal stress, σ_{yy}, and extension of the plastic region ahead of the crack tip under a certain ΔK applied value at different R ratios.

On the other hand, the influence of the austenitization temperature, i.e., prior austenitic grain size, on the fatigue crack growth rate of hydrogen pre-charged specimens is also analysed in this section. As can be observed in Figure 4.116, for a ΔK value of 40 MPa$\sqrt{m}$, an increase of the PAGS from 20 μm to approximately 150 μm (under the same tempering treatment 700ºC/2h) involves an increase of the multiplication factor of the crack growth rate from 6 to 14, and the appearance of intergranular fractureon the failed surface.

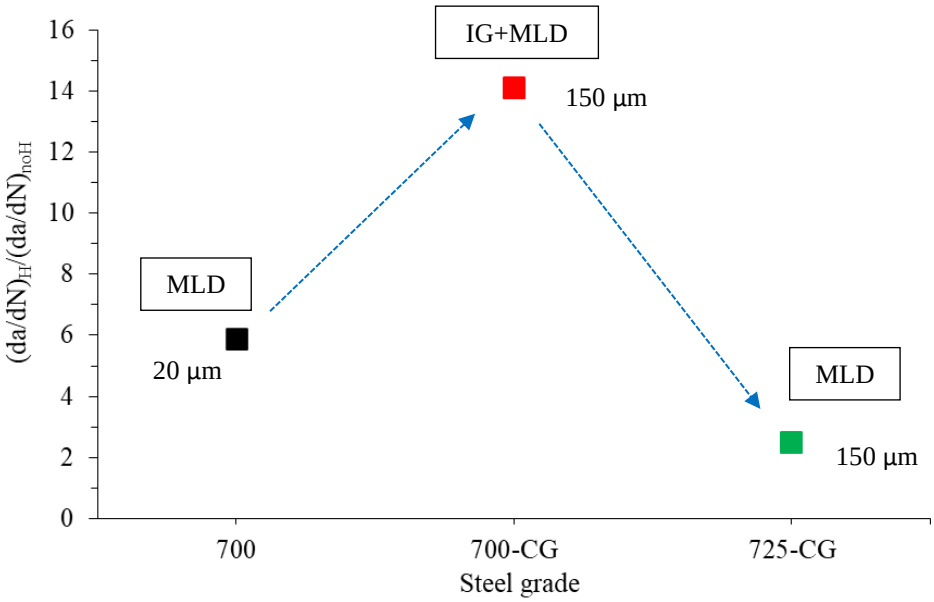

Figure 4.116. da/dN multiplication factor, $(da/dN)_H/(da/dN)_{noH}$, (R=0.1, f=10Hz) at ΔK=40MPa$\sqrt{m}$ for fine grain and coarse grain steels tested at R=0.1 and 0.1 Hz and failure micromechanisms.

Fatigue crack growth rate increases when a higher austenitizing temperature was applied due to the larger austenite grains present in the steel microstructure (as it takes place in the CGHAZ of a weld). This grain growth means a reduction of the total length of prior austenite grain boundaries, and also a reduction of internal lath martensite interfaces (larger martensite laths) resulting in a higher density of dislocations in these interfaces and therefore higher hydrogen concentration capacity. However, the crack growth rate multiplication factor falls from 6 to 2 (Figure 4.116) when a more intense tempering treatment is applied, 725ºC for 4h, and IG fracture is no longer present on the failed surfaces this latter grade. This behaviour is explained by microstructural recovery and dislocation annihilation that takes place during this high temperature tempering treatment. Reduction of microstructural defects at grain boundaries and internal interfaces favours a more homogeneous hydrogen distribution and therefore decreases the likelihood of grain boundary and interface decohesion.

Lastly, the "plateau" phenomenon noticed at intermediate ΔK values in all the steels when tested at low frequencies remains open to discussion. This behaviour, typically observed in stress-corrosion or environmental assisted cracking processes, was also observed by other authors, in fatigue tests performed with hydrogen pre-charged specimens [15,200,262]. It has been frequently explained in terms of a superposition or process competition between sustained-load hydrogen-induced cracking and pure-mechanical fatigue [196,201]. In general terms, it is interpreted as an equilibrium between conventional fatigue crack growth rate and hydrogen delivery rate (hydrogen delivered at the crack tip region through diffusion), giving rise to a "plateau" where crack growth rate keeps constant in a quite wide range of ΔK values.

Coming back again to Figure 4.115, the typical increase of the crack growth rate with ΔK characteristic of the Paris region is counterbalanced by hydrogen redistribution in larger regions submitted to high stresses, where lower local hydrogen contents are attained and, consequently, fatigue crack growth rate tends to decrease as the applied ΔK increases. As a matter of fact, a da/dN "plateau" or even a slight FCGR decrease takes place as ΔK is increased, until the same FCGR as measured in tests performed without hydrogen is reached. On the other hand, hydrogen losses that surely take place in the course of long fatigue tests performed on our hydrogen pre-charged specimens may also be taken into account.

Chapter 5

Conclusions

Study on hydrogen diffusion and embrittlement of quenched and tempered 42CrMo4 steel

PhD Thesis

5. Conclusions

The hydrogen diffusivity, trapping behaviour and embrittlement of a quenched and tempered 42CrMo4 steel was studied in this thesis and, finally, the following conclusions may be drawn. For the shake of clarity, they have been organized in different sections.

- **Microstructure and mechanical properties in the absence of hydrogen**

The microstructure of all the 42CrMo4 grades austenitized at 845ºC for 40 min quenched in water and tempered at different temperatures (700, 650, 600, 550 and 500ºC) for 2h, consisted in tempered martensite (with a PAGS of 20 μm), characterized by martensitic laths and packets with a profuse precipitation of Fe,Cr-rich carbides. As the tempering temperature is increased, the strength and hardness decrease but ductility (both elongation and reduction in area) and fracture toughness increase. A linear correlation was obtained between the tempering temperature, hardness and the XRD FWHM parameter, revealing a linear decrease of the dislocation density with the tempering temperature.

The small CGHAZ generated in the deposition of a weld bead on a 42CrMo4 steel plate was successfully reproduced with a simulative laboratory heat treatment using a high austenitizing temperature (1200ºC) followed by oil quenching, obtaining a grade with an average prior austenitic grain size of 100-150 μm. The higher thermal drop produced when the steel is quenched from 1200ºC (coarse grain microstructure) instead of 845ºC (fine grain base steels produced in conventional quenching treatments) gives rise to a harder and more distorted martensitic structure, with higher internal stresses and, consequently, higher dislocation density. Complete microstructural recovery of the coarse grain microstructure generated after high temperature quenching was attained applying a more intense tempering treatment (725ºC for 4h), which considerably decreased the hardness and strength of the product and hence its dislocation density.

Plastic deformations between 10% and 80% were applied on the fine grain and coarse grain 42CrMo4 grades quenched and tempered at 700ºC, to show an exponential hardness increase with the equivalent plastic deformation. The significant increase in hardness provided by cold rolling can be mostly associated with an increase in dislocation density (work hardening).

- **Hydrogen solubility, diffusion, and microstructural trapping**

Due to trapping phenomena, a single value of the hydrogen diffusion coefficient was not obtained in permeation experiments, but a methodology based in stepped build-up transients has proved to be a reliable way to establish the relationship between trap occupancy and the apparent diffusion coefficient, D_{app}, of the steels. Indeed, three hydrogen diffusion regimes were defined depending on trap occupancy, i.e., hydrogen concentration in the steel microstructure. In the first transient, when hydrogen traps are empty, the lowest apparent diffusion coefficient, D_{app}, is measured, as the interaction of hydrogen atoms with microstructural traps is maximal (Regime I). During the following build-up transients, produced by increasing the cathodic current, hydrogen atoms progressively fill the microstructural traps present in the steel microstructure and D_{app} increases continuously (Regime II), until D_{app} becomes practically constant, when all the hydrogen traps

become saturated and this value corresponds to the lattice hydrogen diffusion coefficient of the steel, D_L (Regime III).

It was found that both, the hydrogen diffusion coefficient calculated for low trap occupancy, D_{app}, and the lattice diffusion coefficient, D_L, decrease, while hydrogen solubility, C_{0app}, (subsurface hydrogen concentration at the entry side when all traps are filled), and the density of hydrogen traps, N_t, increase as the tempering temperature decreases. In fact, good correlations were obtained between these permeation properties and the hardness of the different steel grades, as this basic mechanical property provides an indirect measure of the dislocation density in martensitic microstructures, which is the structural parameter that governs hydrogen diffusion and trapping in martensitic CrMo steels.

Under the same tempering treatment, quenching the steel from a high austenitizing temperature (to reproduce the CGHAZ present in a weld) produces a coarser and more distorted microstructure, with higher dislocation density, decreasing hydrogen diffusivity and increasing the density of trapping sites. Applying a higher tempering temperature for longer times counterbalances this effect, and the steel recovers a permeation behaviour similar to that found in the fine grain product.

Finally, microstructural trapping increases (increase in the dislocation density due to work hardening) and diffusion coefficients decrease when plastic deformations at RT are applied. This effect is even more notorious in the coarse grain microstructure, due to its higher initial hardness.

- **Hydrogen uptake and desorption behaviour in gaseous charged specimens**

The initial hydrogen content, measured after charging with hydrogen gas in a reactor at 19.5 MPa and 450ºC for 21 hours, increased with decreasing the steel tempering temperature, due to the fact that hydrogen microstructural trapping is greater in distorted, high energy martensitic microstructures, with higher density of trapping sites (mainly dislocations). Moreover, the final hydrogen content (residual hydrogen), hydrogen strongly trapped in the steel microstructure, is even more dependent on the steel microstructure, decreasing with increasing tempering temperature, mainly due to stress relaxation and reduction in dislocation density and internal interfaces (martensite laths, blocks and packets).

The hydrogen diffusion coefficient, D_{app}, estimated from fitting the desorption curves by means of finite element simulations (FEM), followed the opposite trend, decreasing as the steel tempering temperature decreases (higher density of trapping sites). In general, these D_{app} values (hydrogen egress) are in accordance with those obtained in permeation experiments (hydrogen entrance), as hydrogen diffusion is taking place in a microstructure partially filled with hydrogen in both situations.

The higher thermal drop produced when the 42CrMo4 steel grade is quenched from 1200ºC (coarse grained microstructure) instead of 845ºC (conventional quenching) gives rise to a more distorted martensitic structure, with higher internal stresses and hence higher dislocation density, thus explaining the larger deeply trapped hydrogen capability of this coarse-grained microstructure, as well as its lower hydrogen diffusion coefficient. A recovered microstructure,

with properties similar to the original, fine grain base steel, was attained when a more intense tempering treatment (725ºC for 4h) is applied.

- **Hydrogen trapping binding energies**

Average hydrogen binding energies of 11.8, 17.0 and 27.4 kJ/mol were determined in fine grain quenched and tempered steel grades. These values were found to be not dependent on the tempering temperature (between 500 and 700ºC). It was also demonstrated that the peak with the highest energy (with an average hydrogen binding energy of 27.4 kJ/mol) is associated with dislocations, the magnitude of this peak being inversely proportional to the tempering temperature (given that the dislocation density decreases with increasing tempering temperature). The less energetic peaks were associated respectively to hydrogen trapped in Fe,Cr-rich carbides-matrix interfaces and martensitic laths, blocks and parquets interfaces.

Considering that the only microstructural difference between fine and coarse grain grades is the prior austenitic grain size, the same peak-trap assignation than that suggested for the fine grain grades can be applied. Due to the greater distortion of the martensitic laths observed in the coarse grain steels, and therefore their greater ability to trap hydrogen, the binding energy associated to the second peak have slightly increased from 17 to 19-20 kJ/mol. The other two binding energies were similar to those determined in the fine grain base steel.

It should be bear in mind that most of the carbides generated during tempering precipitate along internal interfaces, and also dislocations tend to accumulate in these same boundaries, making very difficult, with the employed TDA technique, to isolate the different microstructural traps present in these steels, having close binding energies.

- **Influence of internal hydrogen on the tensile properties**

The tensile properties measured on smooth specimens pre-charged with gaseous hydrogen remained practically unaffected in all the grades tempered at high temperature (above 600ºC), irrespective of the applied displacement rate. However, due to their higher density of hydrogen traps, in the hardest grades (tempered at 500 and 550ºC for 2h), and in the case of the coarse grain steel (higher austenitization temperature) tempered at 700º, a reduction in the ductility parameters was noticed under the lowest displacement rates. On the contrary, when the coarse grain microstructure was tempered at 725ºC for 4h, the smooth tensile properties were practically unaltered by the presence of internal hydrogen at any displacement rate. The type of fracture observed on the failure surfaces of the uncharged and hydrogen pre-charged smooth tensile specimens of all the studied grades was always fully ductile, characterized by microvoids coalescence (MVC).

The embrittlement indexes for strength and reduction in area obtained using hydrogen pre-charged notch tensile specimens (k_t=4.25) were seen to increase with the steel hardness, i.e., density of trapping sites. An increase in the prior austenitic grain size resulted in only a slight decrease in the tensile notched strength, but in a considerable reduction of the reduction in area, especially in tests performed under very low displacement rates. This behaviour is consistent with the change appreciated in the fracture micromechanisms. While microvoids coalescence (MVC)

was found to be the typical ductile failure micromechanism in the absence of hydrogen in all the steels, a combination of ductile and brittle decohesion mechanisms (carbide-matrix interface decohesion, CMD, and martensitic lath interface decohesion, MLD) were observed under internal hydrogen. In addition, when tested under the lowest displacement rates, intergranular fracture (IG) was also found in the case of grades tempered below 600ºC and in the coarse grain steel (with higher density of hydrogen traps).

The use of a more intense tempering treatment (725ºC/4h) after high temperature austenitization (coarse grain) favoured microstructural recovery, the notched tensile behaviour in presence of hydrogen improved considerably and IG micromechanism was no longer present.

The use of lower displacement rates in these tests always gave rise to higher embrittlement indexes (manifested in the appearance of more brittle fracture micromechanisms), as the accumulation of hydrogen atoms in the most stressed area of the notched specimen increases due to the availability of longer diffusion times. The results obtained with the notched tensile tests are justified in base of the magnitude of local hydrostatic and normal stresses developed in the process region ahead of the notch (which increase with the steel yield strength), which are responsible of differences in local hydrogen accumulation within the microstructural features present I the aforementioned region of the steels.

- **Influence of internal hydrogen on the fracture toughness**

The fracture toughness reduction due to the presence of internally pre-charged hydrogen was important in all the studied steel grades, giving rise to a clear decrease of the whole J-resistance curve and particularly on the critical J parameter for the onset of crack growth, $J_{0.2/BL}$ or J_Q. Extreme embrittlement occurred in the grades tempered at the lowest temperatures (higher hardness and yield strength), with higher density of hydrogen trapping sites, when tested under the lowest displacement rates.

These fracture toughness results were justified because hydrogen accumulation in the process zone located ahead of the crack tip in the CT specimen depends on the steel´s dislocation density and on the local hydrostatic stress. As the yield strength of the steel increases, the hydrostatic stress and the hydrogen content accumulated in the process zone also increase, giving rise to a whole change in the failure micromechanism, from a fully ductile one, microvoids coalescence (MCV), to decohesion along martensite lath, block, and packet interphases (MLD) and, in the case of the grades tempered at the lowest temperatures, even decohesion along prior austenite grain boundaries (IG). This fractographic study supports the hydrogen–enhanced-plasticity mediated decohesion model, in which HEDE (martensite lath decohesion, MLD, and prior austenite grain boundary decohesion, IG) is the final failure mechanism. However, HELP always takes place first, providing the accumulation of sufficient hydrogen in the process zone, modifying the local stress state (dislocation pile-ups) and decreasing the cohesion of the aforementioned internal interfaces.

As happened in tensile tests, the use of lower displacement rates always gave rise to higher hydrogen embrittlement indexes, as the accumulation of hydrogen atoms in the most stressed area of the fracture specimen increases due to the availability of longer diffusion times. It was also

demonstrated that only diffusible hydrogen, hydrogen atoms able to move at room temperature, is responsible for hydrogen embrittlement and therefore able to trigger hydrogen-related interface decohesion micromechanisms. In fact, room temperature degassing experiments showed a very good correlation between the measured fracture toughness and the diffusible hydrogen present in the steel. On the contrary, the presence of residual hydrogen strongly trapped in the steel microstructure does not affect its fracture toughness.

On the other hand, hydrogen embrittlement measured in the steel with the coarse grain microstructure was considerably greater than in the base steel tempered at the same temperature. The greater density of hydrogen traps (mainly dislocations) explains the sharper drop in its fracture toughness, also associated to the appearance of intergranular fracture micromechanisms. Applying a more intense tempering treatment was proved to be a successful method to reduce the hydrogen sensitivity of this coarse grain microstructure.

In addition, the toughest steel grades in presence of internal hydrogen (42CrMo4-700, 42CrMo4-650, 42CrMo4-700-CG and 42CrMo4-725-CG) were submitted to constant K tests, which allowed to determine the threshold stress intensity factor for the onset of crack growth under internal hydrogen, $K_{th/0.2}$. HEDE mechanisms were noticed in all the studied grades under this testing condition. Just as happened with the fracture toughness parameter $J_{0.2/BL}$ (and for the same reasons), an increase in $K_{th/0.2}$ value was reported when decreasing the austenitizing temperature and/or increasing the tempering temperature/time, due to the lower density of hydrogen traps. Anyway, the measured $K_{th/0.2}$ values were much lower than the K values derived from the $J_{0.2/BL}$ parameter ($K_{J0.2/BL}$) obtained in standard fracture toughness tests.

- **Influence of internal hydrogen on the fatigue crack growth rate**

Internal hydrogen also modified the fatigue crack growth behaviour of 42CrMo4-700, 42CrMo4-650, 42CrMo4-700-CG and 42CrMo4-725-CG grades. In general, an acceleration of the fatigue crack growth rate was observed under intermediate ΔK values in tests performed under low frequencies. Under these low frequencies, the process zone remains a longer time under high K values and therefore hydrogen accumulation increases, leading to the appearance of MLD and IG micromechanisms. On the other hand, increasing the load ratio, R, does not produce significant effects (in fact, FCGR slightly decreases as R increases), probably due to the greater size of the plastic zone developed ahead of the crack front, which made hydrogen to be distributed in a wider region, where lower local hydrogen concentrations are attained.

No significant differences have been noticed between the fatigue behaviour with internal hydrogen of fine grain steels tempered at different temperatures (700 and 650ºC), specially under low testing frequencies where hydrogen effects are maximum. On the other hand, a considerable acceleration of the fatigue crack growth rate was measured in the microstructure with greater prior austenitic grain size tempered at 700ºC. However, when the coarse grain microstructure was tempered at 725ºC for 4 hours, the best fatigue behaviour in presence of hydrogen was reported.

Finally, the "plateau" region observed in the da/dN vs ΔK curves on all the tested steels is explained taking into account that the typical increase of the crack growth rate with ΔK characteristic of the Paris region is counterbalanced by hydrogen redistribution in larger regions

submitted to high stresses, giving rise to lower local hydrogen contents and, consequently, the fatigue crack growth rate tends to decrease as the applied ΔK increases.

5.1. Outlook and general recommendations

Finally, at the end of this research work, some general recommendations are provided regarding the design and use of quenched and tempered CrMo steels for its safe service for long periods of time in contact with hydrogenated media.

- An appropriate steel grade selection is required for the design of pressure vessels, pipes and other necessary components used under high hydrogen pressure in order to achieve a balance between the steel yield strength and its potential hydrogen embrittlement susceptibility, also taking into account the magnitude of applied loads and the applied hydrogen pressure.
- In welded components, where coarse and hard microstructures may be generated due to the application of high heat inputs, a post welding heat treatment consisting in tempering at higher temperature than the base steel for times between 2 and 10 hours is recommended to guarantee the desired mechanical properties in presence of hydrogen.
- Special attention should be taken in the design of such infrastructures to avoid unnecessary stress concentrators, such as chambers or holes, as they are potential areas for hydrogen accumulation, where cracks could more easily initiate and growth.
- The design of welded infrastructures able to safely manage hydrogen under large pressures may take into account the presence of small cracks, sometimes difficult to be detected by conventional non-destructive inspection. In this case, the threshold stress intensity factor for the onset of crack growth assisted by hydrogen, K_{th}, and the effect of hydrogen on the fatigue crack growth rate on the base steel and on its welds are critical properties that should be considered.
- In relation with the manufacturing process, induced residual stresses and local plastic strains should be closely controlled, as they can provide locations for local hydrogen accumulation where hydrogen embrittlement could be enhanced. The application of stress relief heat treatments at the end of the manufacture process is highly recommended.
- The use of mechanical tests performed on pre-charged specimens is a valid and easy approach to characterize steels in the presence of hydrogen that can be used to compare different steel grades, heat treatments, grain sizes or microstructures, but it cannot replace the final mechanical characterization in which hydrogen may be charged at the same time than mechanical loads are applied ("in situ" charging") to comply with the corresponding standards.
- The addition of controlled quantities of different alloying elements, such as Nb, V or Ti to quenched and tempered CrMo steels, such as the 42CrMo4 grade, may be considered an interesting way for microstructure improvement as to generate very strong, irreversible hydrogen traps, where hydrogen could be retained, avoiding the embrittlement reaction.

5.2. Conclusiones

En esta tesis se han estudiado los fenómenos de difusión, atrapamiento y fragilización por hidrógeno del acero 42CrMo4 templado y revenido. Las principales conclusiones obtenidas, que se resumen a continuación, se han agrupado en diferentes secciones para una mayor claridad.

- **Microestructura y propiedades mecánicas en ausencia de hidrógeno**

La microestructura de todos los grados de acero 42CrMo4, austenizado a 845ºC durante 40 minutos, templado en agua y revenido a diferentes temperaturas (700, 650, 600, 550 y 500ºC) durante 2h, consistió en martensita revenida (con un tamaño de grano austenítico de 20 μm), caracterizada por paquetes y lajas martensíticas con una abundante precipitación de carburos ricos en Fe y Cr. Al aumentar la temperatura de revenido, la resistencia mecánica y la dureza disminuyen, pero la ductilidad (tanto alargamiento como estricción) y la tenacidad a la fractura aumentan. Se ha obtenido una correlación lineal entre la temperatura de revenido, la dureza, y el parámetro FWHM (obtenido mediante difracción de rayos X), lo que indica un descenso lineal de la densidad de dislocaciones con la temperatura de revenido.

Se ha conseguido reproducir la microestructura de la estrecha zona afectada térmicamente de grano grueso generada durante la deposición de un cordón de soldadura en una chapa del acero 42CrMo4 mediante un tratamiento térmico controlado en el laboratorio (austenización a 1200ºC y posterior temple en aceite), obteniéndose un tamaño de grano austenítico de unos 100-150 μm. El mayor choque térmico sufrido al enfriar desde 1200ºC en vez de 854ºC, ha dado lugar a una microestructura más dura y distorsionada, con más tensiones internas y, por lo tanto, mayor densidad de dislocaciones. Mediante un tratamiento térmico de revenido más intenso (725ºC durante 4h), se ha conseguido una regeneración completa de la microestructura de grano grueso generada después de templar desde una temperatura tan elevada, disminuyendo notablemente la dureza y la resistencia mecánica y por lo tanto su densidad de dislocaciones.

Se aplicaron deformaciones plásticas entre el 10% y el 80% en los aceros de grano fino y de grano grueso revenidos a 700ºC durante 2h. Se observó un incremento exponencial de la dureza al aumentar la deformación plástica equivalente. Este aumento significativo de la dureza provocado por la deformación en frío está asociada principalmente a un incremento de la densidad de dislocaciones (endurecimiento por deformación).

- **Solubilidad, difusión y atrapamiento de hidrógeno**

Debido a los fenómenos de atrapamiento, la difusión de hidrógeno en la microestructura del acero 42CrMo4 no se puede caracterizar con un valor único del coeficiente de difusión. Por ello se ha empleado un tipo de ensayo de permeación, basado en realizar sucesivos transitorios crecientes, que ha demostrado ser una metodología apropiada para establecer la relación entre el nivel de ocupación de las trampas y el coeficiente de difusión aparente, D_{app}, en este tipo de aceros. De

hecho, se pueden diferenciar tres regímenes en función del nivel de ocupación de las trampas (concentración de hidrógeno en la microestructura). En el primer transitorio, cuando las trampas están completamente vacías, el coeficiente de difusión aparente adopta el valor más bajo, y la interacción de los átomos de hidrógeno con las trampas microestructurales es máximo (Régimen I). Durante los siguientes transitorios, producidos al incrementar la corriente catódica, los átomos de hidrógeno van llenando progresivamente las trampas y el coeficiente de difusión aumenta en cada transitorio (Régimen II) hasta que todas las trampas están prácticamente saturadas, y D_{app} adopta un valor prácticamente constante, correspondiente al coeficiente de difusión en la red cristalina del acero, D_L (Régimen III).

Se ha demostrado que tanto el coeficiente de difusión de hidrógeno aparente, D_{app}, como el de la red, D_L, disminuyen al disminuir la temperatura de revenido. Por el contrario, tanto la solubilidad, C_{0app} (concentración de hidrógeno subsuperficial en la cara catódica de la probeta cuando las trampas están llenas), como la densidad de trampas, N_t, aumenta al disminuir la temperatura de revenido. De hecho, se han obtenido buenos coeficientes de ajuste entre estas propiedades de permeación y la dureza de los diferentes grados del acero 42CrMo4, al proporcionar esta una medida indirecta de la densidad de dislocaciones, que representa la principal trampa de hidrógeno en estas microestructuras martensíticas.

Bajo el mismo tratamiento de revenido, austenizar a una mayor temperatura (para reproducir la zona afectada térmicamente de grano grueso de una soldadura) produce una microestructura más grosera y distorsionada, con una mayor densidad de dislocaciones, incrementando la densidad de trampas y por tanto disminuyendo la difusividad. La aplicación de una temperatura de revenido más elevada durante más tiempo neutraliza este efecto, recuperando el acero un comportamiento en permeación similar al del acero de grano fino.

Finalmente, la densidad de trampas se multiplica (debido al incremento de la densidad de dislocaciones), y los coeficientes de difusión disminuyen drásticamente, al aplicar diferentes grados de deformación plástica a temperatura ambiente. Este efecto es aún más evidente en la microestructura más grosera, debido a su mayor dureza inicial.

- **Absorción y desorción en probetas cargadas con hidrógeno gaseoso**

La concentración de hidrógeno inicial, medida después de una carga gaseosa en un reactor a presión a 19.5 MPa y 450ºC durante 21h, aumentó al disminuir la temperatura de revenido, debido a que el atrapamiento de hidrógeno aumenta en microestructuras altamente energéticas y distorsionadas, con mayor densidad de defectos (dislocaciones). Además, el contenido de hidrógeno fuertemente retenido (residual) en la microestructura a temperatura ambiente se redujo al aumentar la temperatura de revenido, debido a la relajación microestructural y la reducción tanto de la densidad de dislocaciones como de intercaras internas (de lajas, bloques y paquetes martensíticos).

Sin embargo, por esta misma razón, el coeficiente de difusión de hidrógeno aparente, D_{app}, obtenido mediante el ajuste numérico de las curvas de desorción, disminuyó al disminuir la temperatura de revenido. En general, estos valores de D_{app} (obtenidos para desorción de hidrógeno) concuerdan bastante bien con aquellos obtenidos en los ensayos de permeación

(absorción de hidrógeno), ya que en ambas situaciones la difusión tiene lugar en una microestructura en la que las trampas están parcialmente llenas de hidrógeno.

El mayor gradiente térmico producido al templar el acero desde 1200ºC en vez de 845ºC da lugar a una microestructura mas distorsionada, con mayor densidad de trampas (dislocaciones), lo que explica su mayor concentración de hidrógeno fuertemente atrapado y menor coeficiente de difusión. Una microestructura regenerada, con propiedades similares a la original (de grano fino), se obtuvo mediante la aplicación de un tratamiento térmico más intenso (725ºC/4h).

- **Energía de atrapamiento del hidrógeno en las trampas microestructurales**

Se han determinado energías de atrapamiento promedio de 11.8, 17.0 y 27.4 kJ/mol en los grados templados y revenidos de grano fino. Estos valores no dependen de la temperatura de revenido (entre 500 y 700ºC). También se ha demostrado que el pico correspondiente a la mayor energía de atrape (con un valor medio de 27.4 kJ/mol) está asociado a las dislocaciones, al ser la intensidad del mismo inversamente proporcional a la temperatura de revenido (la densidad de dislocaciones disminuye al aumentar la temperatura de revenido).

Considerando que la única diferencia microestructural entre los grados de grano fino y grueso es el tamaño de grano austenítico, se puede asumir la misma asignación de picos-trampas. Siendo las energías de atrapamiento determinadas en los aceros de grano grueso similares a las de los aceros de grano fino, cabe destacar la mayor energía medida en el pico intermedio, aumentando ligeramente desde 17 a 19-20 kJ mol, al aumentar la temperatura de austenización. Esto se atribuye a la mayor distorsión de las lajas martensíticas en los aceros de grano grueso.

Se debe tener en cuenta que la mayor parte de los carburos generados durante el revenido precipitan a lo largo de las intercaras internas, donde también tienden a acumularse las dislocaciones. Esto dificulta enormemente, con las técnicas de TDA empleadas, aislar las trampas microestructurales que tienen energías de atrapamiento similares.

- **Influencia del hidrógeno interno en las propiedades a tracción**

Las propiedades a tracción medidas utilizando probetas lisas precargadas con hidrógeno gaseoso no se vieron prácticamente nada afectadas en los grados revenidos a mayor temperatura (por encima de 600ºC), independientemente de la velocidad de desplazamiento aplicada. Sin embargo, debido a su mayor densidad de trampas, en los aceros más duros (revenidos a 500 y 550ºC durante 2h) y en el grado con la microestructura más grosera (mayor temperatura de austenización) revenido a 700ºC, se observó una clara disminución de la ductilidad bajo velocidades de desplazamiento bajas. Por el contrario, cuando la microestructura de grano grueso se revino a 725ºC durante 4h, las propiedades a tracción de las probetas precargadas fueron similares a las de aquellas sin hidrógeno interno. En cualquier caso, el tipo de fractura observado en las probetas de tracción lisa de todos los aceros estudiados, con y sin hidrogeno interno, fue siempre dúctil, caracterizado por la coalescencia de microhuecos (CMH).

Los índices de fragilización relativos a la resistencia y a la estricción obtenidos al ensayar probetas de tracción entallada (k_t=4.25) precargadas con hidrógeno, disminuyeron considerablemente al

aumentar la dureza del acero, es decir, su densidad de trampas. Un aumento del tamaño de grano austenítico solamente dió lugar a un ligero descenso de la resistencia mecánica pero a una reducción importante de la estricción, especialmente en los ensayos realizados a menor velocidad de desplazamiento. Este comportamiento concuerda con los cambios observados en los micromecanismso de fractura. Mientras que la coalescencia de microhuecos fue el micromecanismo dúctil típico en ausencia de hidrógeno en todos los aceros, una combinación de CMH y mecanismos frágiles de descohesión (descohesión entre intercaras de carburos y la matriz y de las intercaras de las lajas martensíticas) se observaron en las probetas con hidrógeno interno. Además, bajo la menor velocidad de desplazamiento, también se detectó fractura intergranular (IG) en los grados revenidos por debajo de 600ºC y en el acero con mayor tamaño de grano y de mayor dureza (mayor densidad de trampas).

La aplicación de un tratamiento de revenido más intenso (725ºC/4h) después de una austenización a elevada temperatura (grano grueso) favorece la regeneración microestructural, mejorando considerablemente el comportamiento a tracción en presencia de hidrógeno en probetas entalladas, y haciendo que el micromecanismo de fractura IG no tenga lugar.

El uso de velocidades de deformación bajas en este tipo de ensayos siempre dio lugar a mayores índices de fragilización (manifestados como micromecanismos de fractura frágiles), ya que la acumulación de átomos de hidrógeno en la zona más tensionada cerca de la entalla aumenta al hacerlo los tiempos de difusión. Los resultados obtenidos con las probetas de tracción entallada se justifican en base a la magnitud de las tensiones hidrostáticas y normales generadas alrededor de la zona de proceso cercana a la entalla. Al aumentar su magnitud con el límite elástico del material, son responsables de las diferencias en las concentraciones locales de hidrógeno acumulado en dichas zonas.

- **Influencia del hidrógeno interno en la tenacidad a la fractura**

  La reducción de la tenacidad a la fractura debido a la presencia de hidrógeno interno en probetas precargadas fue considerable en todos los grados de acero estudiados, dando lugar a un claro descenso de la curva J-R y en particular del valor de J crítico para el inicio del crecimiento de grieta, $J_{0.2/BL}$ or J_Q. Una fragilización extrema tuvo lugar en aquellos grados revenidos a las menores temperaturas (mayor dureza y límite elástico), con mayor densidad de trampas, al ensayarse a las velocidades de deformación más bajas.

  Al igual que en los ensayos de tracción realizados en probetas entalladas, los resultados de los ensayos de tenacidad a la fractura se justifican por la elevada acumulación de hidrógeno en la zona de proceso localizada alrededor del frente de grieta en probetas CT, que depende de la densidad de dislocaciones en el acero de las tensiones hidrostáticas locales desarrolladas. Al aumentar el límite elástico del acero, la magnitud de la tensión hidrostática y por lo tanto el hidrógeno acumulado también aumentan, dando lugar a un cambio drástico en los micromecanismos de fallo operativos, de dúctil (CMH) en ausencia de hidrógeno a descohesión a lo largo de las intercaras de lajas, bloques y paquetes martensíticos (MLD) e incluso de los granos austeníticos (IG) en los grados de acero más duros al aplicar bajas velocidades de desplazamiento. Este estudio fractográfico confirma la acción sinérgica y combinada de los modelos de fallo HELP (plasticidad localizada debido al hidrógeno) y

HEDE (descohesión debida al hidrógeno). El mecanismo HELP siempre tiene lugar primero, favoreciendo el movimiento y la acumulación del hidrógeno en la zona de proceso, y modificando las tensiones locales en virtud del apilamiento de dislocaciones al que da lugar. Finalmente, una vez alcanzada la concentración crítica de hidrógeno tiene lugar el mecanismo HEDE, produciéndose la separación entre intercaras internas.

Como sucedía en los ensayos de tracción, el uso de menores velocidades de desplazamiento durante los ensayos siempre da lugar a menores índices de fragilización, debido a una mayor acumulación de átomos de hidrógeno en la zona de proceso (mayores tiempos de difusión). También se ha demostrado que solamente el hidrógeno difusible, es decir los átomos de hidrógeno que se pueden mover libremente a temperatura ambiente, son responsables del fenómeno de fragilización por hidrógeno y, por lo tanto, de desencadenar los mecanismos e fragilización asociados. De hecho, se demostró la existencia de una correlación muy buena entre la tenacidad a fractura medida y el hidrógeno difusible presente en el acero. Por el contrario, el hidrógeno fuertemente retenido en la microestructura a temperatura ambiente no afecta a la tenacidad.

Por otro lado, la fragilización por hidrógeno medida en el acero de grano grueso fue mayor que en el acero base revenido a la misma temperatura. La mayor densidad de trampas de hidrógeno (dislocaciones principalmente) explica la aguda caída de la tenacidad a la fractura, asociada también con la aparición del micromecanismo de fractura intergranular. Aplicar un tratamiento de revenido más intenso ha demostrado ser un método adecuado para reducir la sensibilidad al hidrógeno de esta microestructura más grosera.

Además, los aceros que demostraron una mayor tenacidad en presencia de hidrógeno interno (42CrMo4-700, 42CrMo4-650, 42CrMo4-700-CG y 42CrMo4-725-CG) fueron sometidos a ensayos bajo factor de intensidad de tensión, K, constante. Estos ensayos permitieron determinar el factor de intensidad de tensión umbral, para el inicio del crecimiento de grieta, $K_{th/0.2}$. Micromecanismos de descohesión asociados al HEDE fueron detectados en todos los grados de acero bajo estas condiciones de ensayo. Al igual que sucedía con el parámetro de tenacidad $J_{0.2/BL}$, y por la misma razón, se observa un incremento del valor de $K_{th/0.2}$ al disminuir la temperatura de austenización y/o incrementar la temperatura/tiempo de revenido, debido a la menor densidad de trampas de hidrógeno. De cualquier forma, cabe destacar que el valor de $K_{th/0.2}$ medido fue siempre mucho menor que los valores de $K_{J0.2/BL}$, derivados del parámetro de tenacidad $J_{0.2/BL}$ obtenidos en ensayos estándar de tenacidad a la fractura J.

- **Influencia del hidrógeno interno en la velocidad de crecimiento de grieta por fatiga**

La presencia de hidrógeno interno también modificó el comportamiento a fatiga de los aceros 42CrMo4-700, 42CrMo4-650, 42CrMo4-700-CG y 42CrMo4-725-CG. En general, se observó una aceleración de la velocidad de crecimiento de grieta para valores intermedios de ΔK en ensayos realizados a bajas frecuencias. De hecho, el uso de frecuencias bajas provoca que la zona de proceso permanezca durante más tiempo bajo valores elevados de K y por lo tanto la acumulación de hidrógeno sea mayor, favoreciendo el desarrollo de los micromecanimos MLD e IG. Por otro lado, se ha visto que aumentar el valor de R no produce

efectos destacables, de hecho parece que la velocidad de crecimiento de grietas por fatiga tiende a disminuir ligeramente al aumentar R. Esto se debe probablemente a la mayor zona plástica desarrollada alrededor del frente de grieta, que provoca que el hidrógeno se distribuya en una región más amplia y, por lo tanto, se alcancen menores concentraciones de hidrógeno locales.

No se han apreciado diferencias significativas en el comportamiento a fatiga con hidrógeno interno entre los aceros de grano fino revenido a distintas temperaturas (700 y 650ºC), especialmente a bajas frecuencias, donde el daño por hidrógeno es mayor. Por otro lado, se ha medido un aumento considerable de la velocidad de crecimiento de grieta en la microestructura de grano grueso revenido a 700ºC. Sin embargo, si el revenido tiene lugar a 725ºC durante 4 horas, esta velocidad de crecimiento de grieta por fatiga disminuye considerablemente, situándose incluso por debajo de la de los aceros de grano fino.

Finalmente, la región de velocidad de crecimiento de grieta constante, conocida como "plateau" y observada en las curvas da/dN vs ΔK en todos los aceros ensayados, se puede explicar teniendo en cuenta que el aumento de la velocidad de crecimiento de grieta con ΔK característico de la región de Paris, es contrarrestado por la redistribución de hidrógeno en la zona relativamente grande que está sometida a elevadas tensiones, que se traducen en la disminución de la concentración local de hidrógeno y, por lo tanto, de la caída de la velocidad de crecimiento de grieta al aumentar el ΔK aplicado.

5.3. Perspectivas y recomendaciones generales

Finalmente, para poner fin a este trabajo de investigación, se proporcionan algunas recomendaciones generales relativas al diseño y uso de aceros CrMo templados y revenidos para su uso seguro en servicio durante largos períodos de tiempo en contacto con ambientes ricos en hidrógeno.

- Una adecuada selección del grado de acero es esencial para el diseño de recipientes a presión, tuberías y otros componentes sometidos a elevadas presiones de hidrógeno, con el fin de alcanzar un compromiso entre el límite elástico y su potencial susceptibilidad al fenómeno de fragilización por hidrógeno, teniendo en cuenta, por supuesto, la magnitud de las cargas a las que estará sometido el componente y la presión de trabajo.
- En componentes soldados, dónde se pueden generar microestructuras duras y groseras debido a la aplicación de elevados aportes térmicos, se recomienda aplicar un tratamiento térmico post soldeo consistente en un revenido a temperaturas elevadas (mayor que la realizada generalmente al metal base) entre 2 y 10 h, para garantizar las propiedades mecánicas deseadas en presencia de hidrógeno.
- Se debe prestar especial atención al diseño de todos estos componentes e infraestructuras para evitar concentradores de tensión innecesarios, como chaflanes o agujeros, ya que son zonas potenciales de acumulación de hidrógeno, donde las grietas se pueden iniciar y crecer con mayor facilidad.
- Durante el diseño de estructuras y componentes soldados que vayan a estar sometidos a elevadas presiones de hidrógeno, es necesario tener en cuenta la presencia de pequeños

defectos (grietas) difíciles de detectar mediante técnicas de inspección no destructivas. En este caso, el factor de intensidad de tensión umbral para el inicio del crecimiento de grieta, K_{th}, y el efecto del hidrógeno en la velocidad de crecimiento de grietas por fatiga, son propiedades clave que hay que conocer.

- En relación con el proceso de fabricación, se debe controlar cuidadosamente la posible generación de tensiones residuales y deformaciones plásticas localizadas, ya que pueden proporcional lugares preferentes para la acumulación de hidrógeno. En estos casos se aconseja la aplicación de tratamientos térmicos de alivio de tensiones al finalizar el proceso de fabricación.
- La realización de ensayos mecánicos sobre probetas precargadas con hidrógeno es una metodología válida para caracterizar el comportamiento de los aceros en presencia de hidrógeno, y se puede emplear para comparar diferentes grados, tratamientos térmicos, tamaños de grano y/o microestructuras, pero no puede reemplazar la caracterización mecánica final en la que el hidrógeno se ha de cargar a la vez que se aplica la tensión mecánica (ensayos “in-situ”).
- La adición de cantidades controladas de diferentes elementos de aleación como el Nb, V o Ti en aceros CrMo templados y revenidos, como el 42CrMo4, son una forma interesante y efectiva de generar trampas muy fuertes, de elevada energía e atrape, dónde el hidrógeno queda atrapado irreversiblemente minimizando el fenómeno de fragilización por hidrógeno, ya que este solo depende del hidrógeno diffusible.

References

[1] X. Hao, H. An, H. Qi, X. Gao, Evolution of the exergy flow network embodied in the global fossil energy trade: Based on complex network, Appl. Energy. 162 (2016) 1515–1522. https://doi.org/10.1016/j.apenergy.2015.04.032.

[2] International Renewable Energy Agency (IRENA), Hydrogen: A renewable energy perspective, 2nd Hydrogen Energy Ministerial Meeting, tokyo, Japan, n.d.

[3] Hydrogen Council, Hydrogen scaling up : A sustainable pathway for the global energy transition., 2017.

[4] M. Hirscher, V.A. Yartys, M. Baricco, J. Bellosta von Colbe, D. Blanchard, R.C. Bowman, D.P. Broom, C.E. Buckley, F. Chang, P. Chen, Y.W. Cho, J.C. Crivello, F. Cuevas, W.I.F. David, P.E. de Jongh, R. V. Denys, M. Dornheim, M. Felderhoff, Y. Filinchuk, G.E. Froudakis, D.M. Grant, E.M.A. Gray, B.C. Hauback, T. He, T.D. Humphries, T.R. Jensen, S. Kim, Y. Kojima, M. Latroche, H.W. Li, M. V. Lototskyy, J.W. Makepeace, K.T. Møller, L. Naheed, P. Ngene, D. Noréus, M.M. Nygård, S. ichi Orimo, M. Paskevicius, L. Pasquini, D.B. Ravnsbæk, M. Veronica Sofianos, T.J. Udovic, T. Vegge, G.S. Walker, C.J. Webb, C. Weidenthaler, C. Zlotea, Materials for hydrogen-based energy storage – past, recent progress and future outlook, J. Alloys Compd. 827 (2020). https://doi.org/10.1016/j.jallcom.2019.153548.

[5] L. Briottet, R. Batisse, G. De Dinechin, P. Langlois, L. Thiers, Recommendations on X80 steel for the design of hydrogen gas transmission pipelines, Int. J. Hydrogen Energy. 37 (2012) 9423–9430. https://doi.org/10.1016/j.ijhydene.2012.02.009.

[6] Juan Pablo Zurdo, Hespaña, con H de hidrógeno verde, El País. (2021).

[7] S. Pillot, L. Coudreuse, Hydrogen-induced disbonding and embrittlement of steels used in petrochemical refining, Gaseous Hydrog. Embrittlement Mater. Energy Technol. Probl. Its Characterisation Eff. Part. Alloy Classes. (2012) 51–93. https://doi.org/10.1533/9780857093899.1.51.

[8] M. Tvrdý, S. Havel, L. Hyspecká and K. Mazanec, Hydrogen embrittlement of CrMo and CrMoV pressure vessel steels, Int. J. Pres. Ves. Pip. 9 (1981) 355–365.

[9] J. Koutský, K. Šplíchal, Hydrogen and radiation embrittlement of CrMoV and CrNiMoV ferritic RPV steels, Int. J. Press. Vessel. Pip. 24 (1986) 13–26. https://doi.org/10.1016/0308-0161(86)90027-X.

[10] K. Šplíchal, M. Ruščák, J. Žd'árek, Combination of radiation and hydrogen damage of reactor pressure vessel materials, Int. J. Press. Vessel. Pip. 55 (1993) 361–373. https://doi.org/10.1016/0308-0161(93)90057-Z.

[11] W.H. Johnson, On some remarkable changes produced in iron and steel by the action of hydrogen and acids, Nature. 11 (1875) 393. https://doi.org/10.1038/011393a0.

[12] S. Takagi, Y. Toji, M. Yoshino, K. Hasegawa, Hydrogen embrittlement resistance evaluation of ultra high strength steel sheets for automobiles, ISIJ Int. 52 (2012) 316–322. https://doi.org/10.2355/isijinternational.52.316.

[13] A. Oudriss, A. Fleurentin, G. Courlit, E. Conforto, C. Berziou, C. Rébéré, S. Cohendoz, J.M. Sobrino, J. Creus, X. Feaugas, Consequence of the diffusive hydrogen contents on

tensile properties of martensitic steel during the desorption at room temperature, Mater. Sci. Eng. A. 598 (2014) 420–428. https://doi.org/10.1016/j.msea.2014.01.039.

[14] Y. Murakami, T. Kanezaki, P. Sofronis, Hydrogen embrittlement of high strength steels: Determination of the threshold stress intensity for small cracks nucleating at nonmetallic inclusions, Eng. Fract. Mech. 97 (2012) 227–243. https://doi.org/10.1016/j.engfracmech.2012.10.028.

[15] C. Colombo, G. Fumagalli, F. Bolzoni, G. Gobbi, L. Vergani, Fatigue behavior of hydrogen pre-charged low alloy Cr-Mo steel, Int. J. Fatigue. 83 (2015) 2–9. https://doi.org/10.1016/j.ijfatigue.2015.06.002.

[16] J. Woodtli, R. Kieselbach, Damage due to hydrogen embrittlement and stress corrosion cracking, Eng. Fail. Anal. 7 (2000) 427–450. https://doi.org/10.1016/S1350-6307(99)00033-3.

[17] M. Dadfarnia, P. Sofronis, T. Neeraj, Hydrogen interaction with multiple traps: Can it be used to mitigate embrittlement?, Int. J. Hydrogen Energy. 36 (2011) 10141–10148. https://doi.org/10.1016/j.ijhydene.2011.05.027.

[18] R.A. Oriani, The diffusion and trapping of hydrogen in steel, Acta Metall. 18 (1970) 147–157. https://doi.org/10.1016/0001-6160(70)90078-7.

[19] Y. Wang, X. Wu, Z. Zhou, X. Li, Numerical analysis of hydrogen transport into a steel after shot peening, Results Phys. 11 (2018) 5–16. https://doi.org/10.1016/j.rinp.2018.08.030.

[20] A. McNabb & P.K. Foster, A new analysis of the diffusion of hydrogen in iron and ferritic steels, Trans. Met. Soc. AIME. 227 (1963) 618–27.

[21] J.Y. Lee, J.L. Lee, A trapping theory of hydrogen in pure iron, Philos. Mag. A Phys. Condens. Matter, Struct. Defects Mech. Prop. 56 (1987) 293–309. https://doi.org/10.1080/01418618708214387.

[22] I.M. Robertson, P. Sofronis, A. Nagao, M.L. Martin, S. Wang, D.W. Gross, K.E. Nygren, Hydrogen Embrittlement Understood, Metall. Mater. Trans. B Process Metall. Mater. Process. Sci. 46 (2015) 1085–1103. https://doi.org/10.1007/s11663-015-0325-y.

[23] T. Michler, C. San Marchi, J. Naumann, S. Weber, M. Martin, Hydrogen environment embrittlement of stable austenitic steels, Int. J. Hydrogen Energy. 37 (2012) 16231–16246. https://doi.org/10.1016/j.ijhydene.2012.08.071.

[24] S.P. Lynch, Hydrogen embrittlement (HE) phenomena and mechanisms, Stress Corros. Crack. Theory Pract. (2011) 90–130. https://doi.org/10.1533/9780857093769.1.90.

[25] R. Miresmaeili, L. Liu, H. Kanayama, A possible explanation for the contradictory results of hydrogen effects on macroscopic deformation, Int. J. Press. Vessel. Pip. 99–100 (2012) 34–43. https://doi.org/10.1016/j.ijpvp.2012.08.001.

[26] X. Li, B. Gong, C. Deng, Y. Li, Effect of pre-strain on microstructure and hydrogen embrittlement of K-TIG welded austenitic stainless steel, Corros. Sci. 149 (2019) 1–17. https://doi.org/10.1016/j.corsci.2018.12.018.

[27] C.D. Kim, Hydrogen-damage failures, in: Met. Handbook, Vol.11, Fail. Anal. Prev., American Society for Metals, Metals Park, Ohio, Estados Unidos, 1986.

[28] A.L. Marcelo, R.C. Tokimatsu, I. Ferreira, Hydrogen embrittlement in an AISI 1045 steel component of the sugarcane industry, Eng. Fail. Anal. 16 (2009) 468–474. https://doi.org/10.1016/j.engfailanal.2008.06.014.

[29] G. Straffelini, L. Versari, Brittle intergranular fracture of a thread: The role of a carburizing treatment, Eng. Fail. Anal. 16 (2009) 1448–1453. https://doi.org/10.1016/j.engfailanal.2008.09.020.

[30] M. Yan, Y. Weng, Study on hydrogen absorption of pipeline steel under cathodic charging, Corros. Sci. 48 (2006) 432–444. https://doi.org/10.1016/j.corsci.2005.01.011.

[31] M. Nagumo, Fundamentals of hydrogen embrittlement, 2016. https://doi.org/10.1007/978-981-10-0161-1.

[32] J.C. Lippold, Welding Metallurgy and Weldability, John Wiley and Sons, Ohio State University, 2015.

[33] A. R. Troiano, The role of hydrogen and other interstitials in the mechanical behaviour of metals, Trans. ASM. 52 (1960) 54–80.

[34] G. Pressouyre, I. Bernstein, A quantitative analysis of hydrogen trapping, Metall. Trans. A. 9A (1978) 1571–1580. https://doi.org/10.1007/BF02661939.

[35] R.P. Gangloff, B.P. Somerday, Gaseous Hydrogen Embrittlement of Materials in Energy Technologies: Mechanisms, Modelling and Future Developments, Woodhead Publishing, 2012. https://doi.org/10.1533/9780857095374.

[36] M. Wang, E. Akiyama, K. Tsuzaki, Effect of hydrogen and stress concentration on the notch tensile strength of AISI 4135 steel, Mater. Sci. Eng. A. 398 (2005) 37–46. https://doi.org/10.1016/j.msea.2005.03.008.

[37] J. Yamabe, T. Awane, S. Matsuoka, Investigation of hydrogen transport behavior of various low-alloy steels with high-pressure hydrogen gas, Int. J. Hydrogen Energy. 40 (2015) 11075–11086. https://doi.org/10.1016/j.ijhydene.2015.07.006.

[38] Y. Murakami, S. Matsuoka, Effect of hydrogen on fatigue crack growth of metals, Eng. Fract. Mech. 77 (2010) 1926–1940. https://doi.org/10.1016/j.engfracmech.2010.04.012.

[39] K.A. Nibur, B.P. Somerday, C.S. Marchi, J.W. Foulk, M. Dadfarnia, P. Sofronis, The relationship between crack-tip strain and subcritical cracking thresholds for steels in high-pressure hydrogen gas, Metall. Mater. Trans. A Phys. Metall. Mater. Sci. 44 (2013) 248–269. https://doi.org/10.1007/s11661-012-1400-5.

[40] A. Nagao, M. Dadfarnia, B.P. Somerday, P. Sofronis, R.O. Ritchie, Hydrogen-enhanced-plasticity mediated decohesion for hydrogen-induced intergranular and "quasi-cleavage" fracture of lath martensitic steels, J. Mech. Phys. Solids. 112 (2018) 403–430. https://doi.org/10.1016/j.jmps.2017.12.016.

[41] A. Díaz, J.M. Alegre, I.I. Cuesta, Numerical simulation of hydrogen embrittlement and local triaxiality effects in notched specimens, Theor. Appl. Fract. Mech. 90 (2017) 294–302. https://doi.org/10.1016/j.tafmec.2017.06.017.

[42] C. Colombo, A. Zafra García, J. Belzunce, I. Fernandez Pariente, Sensitivity to hydrogen embrittlement of AISI 4140 steel: A numerical study on fracture toughness, Theor. Appl. Fract. Mech. 110 (2020). https://doi.org/10.1016/j.tafmec.2020.102810.

[43] E. Martínez-Pañeda, A. Golahmar, C.F. Niordson, A phase field formulation for hydrogen assisted cracking, Comput. Methods Appl. Mech. Eng. 342 (2018) 742–761. https://doi.org/10.1016/j.cma.2018.07.021.

[44] G.M. Pressouyre, Trap theory of Hydrogen embrittlement, Acta Metall. 28 (1980) 895–911. https://doi.org/10.1016/0001-6160(80)90106-6.

[45] J. Crank, The Mathematics of Diffusion, 2nd Ed. Oxford Univ. Press. UK. (1975). https://doi.org/10.1016/0306-4549(77)90072-X.

[46] M. Nagumo, Fundamentals of hydrogen embrittlement, Fundam. Hydrog. Embrittlement. (2016) 1–239. https://doi.org/10.1007/978-981-10-0161-1.

[47] Q. Liu, A. Atrens, A critical review of the influence of hydrogen on the mechanical properties of medium-strength steels, Corros. Rev. 31 (2013) 85–103. https://doi.org/10.1515/corrrev-2013-0023.

[48] N. Ishikawa, H. Sueyoshi, A. Nagao, Hydrogen microprint analysis on the effect of dislocations on grain boundary hydrogen distribution in steels, ISIJ Int. 56 (2016) 413–417. https://doi.org/10.2355/isijinternational.ISIJINT-2015-329.

[49] F.G. Wei, K. Tsuzaki, Hydrogen trapping phenomena in martensitic steels, Gaseous Hydrog. Embrittlement Mater. Energy Technol. Probl. Its Characterisation Eff. Part. Alloy Classes. (2012) 493–525. https://doi.org/10.1533/9780857093899.3.493.

[50] K. Kiuchi, R.B. McLellan, The solubility and diffusivity of hydrogen in well-annealed and deformed iron, Acta Metall. 31 (1983) 961–984. https://doi.org/10.1016/0001-6160(83)90192-X.

[51] L. Scoppio, M. Barteri, Methods of hydrogen uptake measurements by electrochemical permeation tests on low alloy steels, in: A. Turnbull (Ed.), Hydrogen transport and cracking in metals. Proceedings of a conference, Teddington UK, 1995: pp. 204–215.

[52] L. Moli-Sanchez, F. Martin, E. Leunis, J. Chene, M. Wery, Hydrogen transport in 34CrMo4 martensitic steel: Influence of microstructural defects on H diffusion, Defect Diffus. Forum. 323–325 (2012) 485–490. https://doi.org/10.4028/www.scientific.net/DDF.323-325.485.

[53] T. Zakroczymski, Electrochemical determination of hydrogen in metals, J. Electroanal. Chem. 475 (1999) 82–88. https://doi.org/10.1016/S0022-0728(99)00355-1.

[54] J.O. Bockris, J. McBreen, L. Nanis, The Hydrogen Evolution Kinetics and Hydrogen Entry into a-Iron, J. Electrochem. Soc. 112 (1965) 1025–1031.

[55] R. Gibala and A.J. Kumnick, Hydrogen Trapping in Iron and Steels, in: R. Gibala and R.F. Hehemann (Ed.), Hydrog. Embrittlement Stress Corros. Crack., American Society for Metals, Metals Park, Ohio, USA, 1984: pp. 61–77.

[56] D. Li, R.P. Gangloff, J.R. Scully, Hydrogen Trap States in Ultrahigh-Strength AERMET 100 Steel, Metall. Mater. Trans. A Phys. Metall. Mater. Sci. 35 A (2004) 849–864. https://doi.org/10.1007/s11661-004-0011-1.

[57] H.K.D.H. Bhadeshia, Prevention of hydrogen embrittlement in steels, ISIJ Int. 56 (2016) 24–36. https://doi.org/10.2355/isijinternational.ISIJINT-2015-430.

[58] G.W. Hong, J.Y. Lee, The interaction of hydrogen and the cementite-ferrite interface in carbon steel, J. Mater. Sci. 18 (1983) 271–277. https://doi.org/10.1007/BF00543835.

[59] A. Nagao, K. Hayashi, K. Oi, S. Mitao, Effect of uniform distribution of fine cementite on hydrogen embrittlement of low carbon martensitic steel plates, ISIJ Int. 52 (2012) 213–221. https://doi.org/10.2355/isijinternational.52.213.

[60] D.G. Enos, J.R. Scully, A critical-strain criterion for hydrogen embrittlement of cold-drawn, ultrafine pearlitic steel, Metall. Mater. Trans. A Phys. Metall. Mater. Sci. 33 (2002) 1151–1166. https://doi.org/10.1007/s11661-002-0217-z.

[61] H.K. Birnbaum, Hydrogen Related Second Phase Embrittlement of Solids, in: R. Gibala and R.F. Hehemann (Ed.), Hydrog. Embrittlement Stress Corros. Crack., American Society for Metals, Metals Park, Ohio, Estados Unidos, 1984: pp. 153–177.

[62] T. Yamaguchi, M. Nagumo, Simulation of hydrogen thermal desorption under reversible trapping by lattice defects, ISIJ Int. 43 (2003) 514–519. https://doi.org/10.2355/isijinternational.43.514.

[63] L. Jemblie, V. Olden, O.M. Akselsen, A coupled diffusion and cohesive zone modelling approach for numerically assessing hydrogen embrittlement of steel structures, Int. J. Hydrogen Energy. 42 (2017) 11980–11995. https://doi.org/10.1016/j.ijhydene.2017.02.211.

[64] I. Maroef, D.L. Olson, M. Eberhart, G.R. Edwards, Hydrogen trapping in ferritic steel weld metal, Int. Mater. Rev. 47 (2002) 191–223. https://doi.org/10.1179/095066002225006548.

[65] A.B. Hadžipašić, J. Malina, Š. Nižník, The influence of microstructure on hydrogen diffusion in dual phase steel, Acta Metall. Slovaca. 17 (2011) 129–137.

[66] W.Y. Choo, J.Y. Lee, Thermal Analysis of Trapped Hydrogen in Pure Iron, 13 (1982) 423–427.

[67] M. Enomoto, D. Hirakami, T. Tarui, Modeling thermal desorption analysis of hydrogen in steel, ISIJ Int. 46 (2006) 1381–1387. https://doi.org/10.2355/isijinternational.46.1381.

[68] H. Hagi, Effect of interface between cementite and ferrite on diffusion of hydrogen in carbon steels, Mater. Trans. JIM. 35 (1994) 168–173. https://doi.org/10.2320/matertrans1989.35.168.

[69] Q. Liu, J. Venezuela, M. Zhang, Q. Zhou, A. Atrens, Hydrogen trapping in some advanced high strength steels, Corros. Sci. 111 (2016) 770–785. https://doi.org/10.1016/j.corsci.2016.05.046.

[70] P. Zhou, W. Li, H. Zhao, X. Jin, Role of microstructure on electrochemical hydrogen permeation properties in advanced high strength steels, Int. J. Hydrogen Energy. 43 (2018) 10905–10914. https://doi.org/10.1016/j.ijhydene.2018.04.241.

[71] A.J. Haq, K. Muzaka, D.P. Dunne, A. Calka, E. V. Pereloma, Effect of microstructure and composition on hydrogen permeation in X70 pipeline steels, Int. J. Hydrogen Energy. 38 (2013) 2544–2556. https://doi.org/10.1016/j.ijhydene.2012.11.127.

[72] C.F. Dong, Z.Y. Liu, X.G. Li, Y.F. Cheng, Effects of hydrogen-charging on the susceptibility of X100 pipeline steel to hydrogen-induced cracking, Int. J. Hydrogen

Energy. 34 (2009) 9879–9884. https://doi.org/10.1016/j.ijhydene.2009.09.090.

[73] Y. Sakamoto, T. Mantani, Effect of quenching and tempering on diffusion of hydrogen in carbon steel, Trans. JIM. 17 (1976).

[74] K. Takasawa, R. Ishigaki, Y. Wada, R. Kayano, Absorption of hydrogen in high-strength low-alloy steel during tensile deformation in gaseous hydrogen, ISIJ Int. 50 (2010) 1496–1502. https://doi.org/10.2355/isijinternational.50.1496.

[75] S. Frappart, A. Oudriss, X. Feaugas, J. Creus, J. Bouhattate, F. Thébault, L. Delattre, H. Marchebois, Hydrogen trapping in martensitic steel investigated using electrochemical permeation and thermal desorption spectroscopy, Scr. Mater. 65 (2011) 859–862. https://doi.org/10.1016/j.scriptamat.2011.07.042.

[76] R. Valentini, A. Salina, Influence of microstructure on hydrogen embrittlement behaviour of 2·25Cr–1 Mo steel, Mater. Sci. Technol. (United Kingdom). 10 (1994) 908–914. https://doi.org/10.1179/mst.1994.10.10.908.

[77] F.G. Wei, K. Tsuzaki, Response of hydrogen trapping capability to microstructural change in tempered Fe-0.2C martensite, Scr. Mater. 52 (2005) 467–472. https://doi.org/10.1016/j.scriptamat.2004.11.008.

[78] I.M. Bernstein, The effect of hydrogen on the deformation of iron, Scr. Metall. 8 (1974) 343–349. https://doi.org/10.1016/0036-9748(74)90136-7.

[79] H. Hagi, Y. Hayashi, Effect of Dislocation Trapping on Hydrogen and Deuterium Diffusion in Iron., Trans. Japan Inst. Met. 28 (1987) 368–374. https://doi.org/10.2320/matertrans1960.28.368.

[80] J.P. Hirth, Effects of hydrogen on the properties of iron and steel, Metall. Trans. A. 11 (1980) 861–890. https://doi.org/10.1007/BF02654700.

[81] G.M. Pressouyre, A classification of hydrogen traps in steel, Metall. Trans. A. 10 (1979) 1571–1573. https://doi.org/10.1007/BF02812023.

[82] A.J. Kumnick, H.H. Johnson, Deep Trapping States for Hydrogen in deformed Iron, Acta Metall. 28 (1980) 33–39.

[83] G.L. Spencer, D.J. Duquette, The Role of Vanadium Carbide Traps in Reducing the Hydrogen Embrittlement Susceptibility of High Strength Alloy Steels, US Army Armament Res. (1998) 1–17.

[84] J.S. Kim, Y.H. Lee, D.L. Lee, K.T. Park, C.S. Lee, Microstructural influences on hydrogen delayed fracture of high strength steels, Mater. Sci. Eng. A. 505 (2009) 105–110. https://doi.org/10.1016/j.msea.2008.11.040.

[85] J.L. Gu, K.D. . Chang, H.S. . Fang, B.Z. . Bai, Delayed Fracture Properties of 1500 MPa Bainite/Martensite Dual-phase High Strength Steel and Its Hydrogen Traps, ISIJ Int. 42 (2002) 1560–1564. https://doi.org/10.2355/isijinternational.42.1560.

[86] T. Depover, K. Verbeken, Thermal desorption spectroscopy study of the hydrogen trapping ability of W based precipitates in a Q&T matrix, Int. J. Hydrogen Energy. 43 (2018) 5760–5769. https://doi.org/10.1016/j.ijhydene.2018.01.184.

[87] Y.F. Jiang, B. Zhang, Y. Zhou, J.Q. Wang, E.H. Han, W. Ke, Atom probe tomographic

observation of hydrogen trapping at carbides/ferrite interfaces for a high strength steel, J. Mater. Sci. Technol. 34 (2018) 1344–1348. https://doi.org/10.1016/j.jmst.2017.11.008.

[88] E. Ohaeri, U. Eduok, J. Szpunar, Hydrogen related degradation in pipeline steel: A review, Int. J. Hydrogen Energy. 43 (2018) 14584–14617. https://doi.org/10.1016/j.ijhydene.2018.06.064.

[89] H. Barthelemy, M. Weber, F. Barbier, Hydrogen storage: Recent improvements and industrial perspectives, Int. J. Hydrogen Energy. 42 (2017) 7254–7262. https://doi.org/10.1016/j.ijhydene.2016.03.178.

[90] T. Zakroczymski, Adaptation of the electrochemical permeation technique for studying entry, transport and trapping of hydrogen in metals, Electrochim. Acta. 51 (2006) 2261–2266. https://doi.org/10.1016/j.electacta.2005.02.151.

[91] S. Frappart, X. Feaugas, J. Creus, F. Thebault, L. Delattre, H. Marchebois, Study of the hydrogen diffusion and segregation into FeCMo martensitic HSLA steel using electrochemical permeation test, J. Phys. Chem. Solids. 71 (2010) 1467–1479. https://doi.org/10.1016/j.jpcs.2010.07.017.

[92] H. Husby, M. Iannuzzi, R. Johnsen, M. Kappes, A. Barnoush, Effect of nickel on hydrogen permeation in ferritic/pearlitic low alloy steels, Int. J. Hydrogen Energy. 43 (2018) 3845–3861. https://doi.org/10.1016/j.ijhydene.2017.12.174.

[93] M.A. V Devanathan, Z. Stachurski, The adsorption and diffusion of electrolytic hydrogen in palladium, Proc. R. Soc. London. Ser. A. Math. Phys. Sci. 270 (1962) 90–102. https://doi.org/10.1098/rspa.1962.0205.

[94] ASTM G148, Standard practice for evaluation of hydrogen uptake, permeation, and transport in metals by an electrochemical technique, ASTM Int. (2011).

[95] A. Díaz, A. Zafra, E. Martínez-Pañeda, J.M. Alegre, J. Belzunce, I.I. Cuesta, Simulation of hydrogen permeation through pure iron for trapping and surface phenomena characterisation, Theor. Appl. Fract. Mech. 110 (2020). https://doi.org/10.1016/j.tafmec.2020.102818.

[96] A. Raina, V.S. Deshpande, N.A. Fleck, Analysis of electro-permeation of hydrogen in metallic alloys, Acta Mater. 144 (2018) 777–785. https://doi.org/10.1016/j.actamat.2017.11.011.

[97] A. Turnbull, Perspectives on hydrogen uptake, diffusion and trapping, Int. J. Hydrogen Energy. 40 (2015) 16961–16970. https://doi.org/10.1016/j.ijhydene.2015.06.147.

[98] E. Fallahmohammadi, F. Bolzoni, G. Fumagalli, G. Re, G. Benassi, L. Lazzari, Hydrogen diffusion into three metallurgical microstructures of a C-Mn X65 and low alloy F22 sour service steel pipelines, Int. J. Hydrogen Energy. 39 (2014) 13300–13313. https://doi.org/10.1016/j.ijhydene.2014.06.122.

[99] E. Fallahmohammadi, F. Bolzoni, L. Lazzari, Measurement of lattice and apparent diffusion coefficient of hydrogen in X65 and F22 pipeline steels, Int. J. Hydrogen Energy. 38 (2013) 2531–2543. https://doi.org/10.1016/j.ijhydene.2012.11.059.

[100] F.D. Fischer, G. Mori, J. Svoboda, Modelling the influence of trapping on hydrogen permeation in metals, Corros. Sci. 76 (2013) 382–389.

https://doi.org/10.1016/j.corsci.2013.07.010.

[101] C. Park, N. Kang, M. Kim, S. Liu, Effect of prestrain on hydrogen diffusion and trapping in structural steel, Mater. Lett. 235 (2019) 193–196. https://doi.org/10.1016/j.matlet.2018.10.049.

[102] D. Rudomilova, T. Prošek, P. Salvetr, A. Knaislová, P. Novák, R. Kodým, G. Schimo-Aichhorn, A. Muhr, H. Duchaczek, G. Luckeneder, The effect of microstructure on hydrogen permeability of high strength steels, Mater. Corros. (2019). https://doi.org/10.1002/maco.201911357.

[103] J.C. Charbonnier, H. Margot-Marette, A.M. Brass, M. Aucouturier, Sulfide stress cracking of high strength modified Cr-Mo steels, Metall. Trans. A. 16 (1985) 935–944. https://doi.org/10.1007/BF02814846.

[104] J.M. Chen, J.K. Wu, Hydrogen diffusion through copper-plated AISI 4140 steels, Corros. Sci. 33 (1992) 657–666. https://doi.org/10.1016/0010-938X(92)90100-H.

[105] M. Garet, A.M. Brass, C. Haut, F. Guttierez-Solana, Hydrogen trapping on non metallic inclusions in Cr-Mo low alloy steels, Corros. Sci. 40 (1998) 1073–1086. https://doi.org/10.1016/S0010-938X(98)00008-0.

[106] N. Parvathavarthini, S. Saroja, R.K. Dayal, H.S. Khatak, Studies on hydrogen permeability of 2.25% Cr-1% Mo ferritic steel: Correlation with microstructure, J. Nucl. Mater. 288 (2001) 187–196. https://doi.org/10.1016/S0022-3115(00)00706-6.

[107] A.M. Brass, F. Guillon, S. Vivet, Quantification of hydrogen diffusion and trapping in 2.25Cr-1Mo and 3Cr-1Mo-V steels with the electrochemical permeation technique and melt extractions, Metall. Mater. Trans. A Phys. Metall. Mater. Sci. 35 A (2004) 1449–1464. https://doi.org/10.1007/s11661-004-0253-y.

[108] T. Si, Y. Liu, Q. Zhang, D. Liu, Y. Li, Effect of microstructure on hydrogen permeation in EA4T and 30CrNiMoV12 railway axle steels, Metals (Basel). 9 (2019). https://doi.org/10.3390/met9020164.

[109] P.A.S. Pereira, C.S.G. Franco, J.L.M. Guerra Filho, D.S. Dos Santos, Hydrogen effects on the microstructure of a 2.25Cr-1Mo-0.25 v steel welded joint, Int. J. Hydrogen Energy. 40 (2015) 17136–17143. https://doi.org/10.1016/j.ijhydene.2015.07.095.

[110] E. De Bruycker, S. Huysmans, F. Vanderlinden, Investigation of the hydrogen embrittlement susceptibility of T24 boiler tubing in the context of stress corrosion cracking of its welds, Procedia Struct. Integr. 13 (2018) 226–231. https://doi.org/10.1016/j.prostr.2018.12.038.

[111] E.I. Galindo-Nava, B.I.Y. Basha, P.E.J. Rivera-Díaz-del-Castillo, Hydrogen transport in metals: Integration of permeation, thermal desorption and degassing, J. Mater. Sci. Technol. 33 (2017) 1433–1447. https://doi.org/10.1016/j.jmst.2017.09.011.

[112] A.J. Kumnick, H.H. Johnson, Hydrogen Transport Through Annealed and Deformed Armco Iron., Met. Trans. 5 (1974) 1199–1206. https://doi.org/10.1007/BF02644334.

[113] P. Castaño-Rivera, N.S. De Vincentis, R.E. Bolmaro, P. Bruzzoni, Relationship between Dislocation Densityand Hydrogen Trappingin a Cold Worked API 5L X60 Steel, Procedia Mater. Sci. 8 (2015) 1031–1038. https://doi.org/10.1016/j.mspro.2015.04.165.

[114] Q. Wang, Y. Sun, S. Gu, Z. He, Q. Wang, F. Zhang, Effect of quenching temperature on sulfide stress cracking behavior of martensitic steel, Mater. Sci. Eng. A. 724 (2018) 131–141. https://doi.org/10.1016/j.msea.2018.03.063.

[115] H.B. Xue, Y.F. Cheng, Hydrogen permeation and electrochemical corrosion behavior of the X80 pipeline steel weld, J. Mater. Eng. Perform. 22 (2013) 170–175. https://doi.org/10.1007/s11665-012-0216-1.

[116] L. Gan, F. Huang, X. Zhao, J. Liu, Y.F. Cheng, Hydrogen trapping and hydrogen induced cracking of welded X100 pipeline steel in H2S environments, Int. J. Hydrogen Energy. 43 (2018) 2293–2306. https://doi.org/10.1016/j.ijhydene.2017.11.155.

[117] Y.D. Han, H.Y. Jing, L.Y. Xu, Welding heat input effect on the hydrogen permeation in the X80 steel welded joints, Mater. Chem. Phys. 132 (2012) 216–222. https://doi.org/10.1016/j.matchemphys.2011.11.036.

[118] S.P. Lynch, Hydrogen embrittlement (HE) phenomena and mechanisms, Stress Corros. Crack. Theory Pract. (2011) 90–130. https://doi.org/10.1533/9780857093769.1.90.

[119] O. Barrera, D. Bombac, Y. Chen, T.D. Daff, E. Galindo-Nava, P. Gong, D. Haley, R. Horton, I. Katzarov, J.R. Kermode, C. Liverani, M. Stopher, F. Sweeney, Understanding and mitigating hydrogen embrittlement of steels: a review of experimental, modelling and design progress from atomistic to continuum, J. Mater. Sci. 53 (2018) 6251–6290. https://doi.org/10.1007/s10853-017-1978-5.

[120] L.B. Pfeil, P.R.S.L. A, The effect of occluded hydrogen on the tensile strength of iron, Proc. R. Soc. London. Ser. A, Contain. Pap. a Math. Phys. Character. 112 (1926) 182–195. https://doi.org/10.1098/rspa.1926.0103.

[121] W.W. Gerberich, R.A. Oriani, M.J. Lji, X. Chen, T. Foecke, The necessity of both plasticity and brittleness in the fracture thresholds of iron, Philos. Mag. A Phys. Condens. Matter, Struct. Defects Mech. Prop. 63 (1991) 363–376. https://doi.org/10.1080/01418619108204854.

[122] R.A. Oriani, A Mechanistic Theory of Hydrogen Embrittlement of Steels, in: Berichte Der Bunsen-Gesellschaft Fur Phys. Chemie, 1972: pp. 848–857.

[123] Y. Takeda, C.J. McMahon, Strain Controlled Vs Stress Controlled Hydrogen Induced Fracture in a Quenched and Tempered Steel., Metall. Trans. A, Phys. Metall. Mater. Sci. 12 A (1981) 1255–1266. https://doi.org/10.1007/BF02642339.

[124] H.K. Birnbaum, Mechanisms Of Hydrogen Related Fracture Of Metals, (1989) 1–18.

[125] H.K. Birnbaum, P. Sofronis, Hydrogen-enhanced localized plasticity-a mechanism for hydrogen-related fracture, Mater. Sci. Eng. A. 176 (1994) 191–202. https://doi.org/10.1016/0921-5093(94)90975-X.

[126] I.M. Robertson, H.K. Birnbaum, P. Sofronis, Chapter 91 Hydrogen Effects on Plasticity, Elsevier, 2009. https://doi.org/10.1016/S1572-4859(09)01504-6.

[127] Z.D. Harris, S.K. Lawrence, D.L. Medlin, G. Guetard, J.T. Burns, B.P. Somerday, Elucidating the contribution of mobile hydrogen-deformation interactions to hydrogen-induced intergranular cracking in polycrystalline nickel, Acta Mater. 158 (2018) 180–192. https://doi.org/10.1016/j.actamat.2018.07.043.

[128] M. Nagumo, Hydrogen related failure of steels - A new aspect, Mater. Sci. Technol. 20 (2004) 940–950. https://doi.org/10.1179/026708304225019687.

[129] R. Srinivasan, T. Neeraj, Hydrogen embrittlement of ferritic steels: Deformation and failure mechanisms and challenges in the oil and gas industry, Jom. 66 (2014) 1377–1382. https://doi.org/10.1007/s11837-014-1054-4.

[130] A. Barnoush, H. Vehoff, Recent developments in the study of hydrogen embrittlement: Hydrogen effect on dislocation nucleation, Acta Mater. 58 (2010) 5274–5285. https://doi.org/10.1016/j.actamat.2010.05.057.

[131] M.B. Djukic, G.M. Bakic, V. Sijacki Zeravcic, A. Sedmak, B. Rajicic, The synergistic action and interplay of hydrogen embrittlement mechanisms in steels and iron: Localized plasticity and decohesion, Eng. Fract. Mech. 216 (2019) 106528. https://doi.org/10.1016/j.engfracmech.2019.106528.

[132] K.A. Nibur, B.P. Somerday, Fracture and fatigue test methods in hydrogen gas, Gaseous Hydrog. Embrittlement Mater. Energy Technol. Probl. Its Characterisation Eff. Part. Alloy Classes. (2012) 195–236. https://doi.org/10.1533/9780857093899.2.195.

[133] S.A. Ahmad, D.A. Ryder, T.J. Davies, On the embrittlement of fracture toughness specimens of two high strength steels, Eng. Fract. Mech. 7 (1975) 357–365.

[134] M. Wang, E. Akiyama, K. Tsuzaki, Effect of hydrogen on the fracture behavior of high strength steel during slow strain rate test, Corros. Sci. 49 (2007) 4081–4097. https://doi.org/10.1016/j.corsci.2007.03.038.

[135] M.L. Martin, M.J. Connolly, F.W. Delrio, A.J. Slifka, Hydrogen embrittlement in ferritic steels, Appl. Phys. Rev. 7 (2020). https://doi.org/10.1063/5.0012851.

[136] X. Zhu, W. Li, H. Zhao, L. Wang, X. Jin, Hydrogen trapping sites and hydrogen-induced cracking in high strength quenching & partitioning (Q&P) treated steel, Int. J. Hydrogen Energy. 39 (2014) 13031–13040. https://doi.org/10.1016/j.ijhydene.2014.06.079.

[137] R.P. Gangloff, B.P. Somerday, Gaseous hydrogen embrittlement of materials in energy technologies: The problem, its characterization and effects on particular alloy clasees, Woodhead Publishing, 2012.

[138] M. Wang, E. Akiyama, K. Tsuzaki, Crosshead speed dependence of the notch tensile strength of a high strength steel in the presence of hydrogen, Scr. Mater. 53 (2005) 713–718. https://doi.org/10.1016/j.scriptamat.2005.05.014.

[139] Y. wei Sun, J. zhi Chen, J. Liu, Investigation into Hydrogen Diffusion and Susceptibility of Hydrogen Embrittlement of High Strength 0Cr16Ni5Mo Steel, J. Iron Steel Res. Int. 22 (2015) 961–968. https://doi.org/10.1016/S1006-706X(15)30097-2.

[140] Y. Momotani, A. Shibata, D. Terada, N. Tsuji, Effect of strain rate on hydrogen embrittlement in low-carbon martensitic steel, Int. J. Hydrogen Energy. 42 (2017) 3371–3379. https://doi.org/10.1016/j.ijhydene.2016.09.188.

[141] G. Álvarez, L.B. Peral, C. Rodríguez, T.E. García, F.J. Belzunce, Hydrogen embrittlement of structural steels: Effect of the displacement rate on the fracture toughness of high-pressure hydrogen pre-charged samples, Int. J. Hydrogen Energy. 44 (2019) 15634–15643. https://doi.org/10.1016/j.ijhydene.2019.03.279.

[142] S. Pillot, C. Chauvy, S. Corre, L. Coudreuse, A. Gingell, D. Héritier, P. Toussaint, Effect of temper and hydrogen embrittlement on mechanical properties of 2,25Cr-1Mo steel grades - Application to Minimum Pressurizing Temperature (MPT) issues. Part I: General considerations & materials' properties, Int. J. Press. Vessel. Pip. 110 (2013) 17–23. https://doi.org/10.1016/j.ijpvp.2013.04.017.

[143] W. Zhao, W. Wang, S. Chen, J. Qu, Effect of simulated welding thermal cycle on microstructure and mechanical properties of X90 pipeline steel, Mater. Sci. Eng. A. 528 (2011) 7417–7422. https://doi.org/10.1016/j.msea.2011.06.046.

[144] L.R.O. Costa, L.F. Lemus, D.S. Dos Santos, Hydrogen embrittlement susceptibility of welded 2 1/4Cr-1Mo steel under elastic stress, Int. J. Hydrogen Energy. 40 (2015) 17128–17135. https://doi.org/10.1016/j.ijhydene.2015.08.027.

[145] K. Takasawa, R. Ikeda, N. Ishikawa, R. Ishigaki, Effects of grain size and dislocation density on the susceptibility to high-pressure hydrogen environment embrittlement of high-strength low-alloy steels, Int. J. Hydrogen Energy. 37 (2012) 2669–2675. https://doi.org/10.1016/j.ijhydene.2011.10.099.

[146] X. Li, B. Gong, C. Deng, Y. Li, Failure mechanism transition of hydrogen embrittlement in AISI 304 K-TIG weld metal under tensile loading, Corros. Sci. 130 (2018) 241–251. https://doi.org/10.1016/j.corsci.2017.10.032.

[147] T. Zhang, W. Zhao, Q. Deng, W. Jiang, Y. Wang, Y. Wang, W. Jiang, Effect of microstructure inhomogeneity on hydrogen embrittlement susceptibility of X80 welding HAZ under pressurized gaseous hydrogen, Int. J. Hydrogen Energy. 42 (2017) 25102–25113. https://doi.org/10.1016/j.ijhydene.2017.08.081.

[148] C. San Marchi, B.P. Somerday, Technical Reference for Hydrogen Compatibility of Materials, Sandia Rep. (2012). https://doi.org/10.1016/j.juro.2008.04.178.

[149] H. Barthélémy, Effects of pressure and purity on the hydrogen embrittlement of steels, Int. J. Hydrogen Energy. 36 (2011) 2750–2758. https://doi.org/10.1016/j.ijhydene.2010.05.029.

[150] K.A. Nibur, B.P. Somerday, Fracture and fatigue test methods in hydrogen gas, in: Gaseous Hydrog. Embrittlement Mater. Energy Technol. Probl. Its Characterisation Eff. Part. Alloy Classes, Woodhead Publishing Limited, 2012: pp. 195–236. https://doi.org/10.1533/9780857093899.2.195.

[151] E.H. Loginow, A.W. and Phelps, Steels for Seamless Hydrogen Pressure Vessels, Corrosion. 31 (1975) 404–412.

[152] Y. Ogawa, H. Matsunaga, J. Yamabe, M. Yoshikawa, S. Matsuoka, Unified evaluation of hydrogen-induced crack growth in fatigue tests and fracture toughness tests of a carbon steel, Int. J. Fatigue. 103 (2017) 223–233. https://doi.org/10.1016/j.ijfatigue.2017.06.006.

[153] H.W. Liu, Stress-corrosion cracking and the interaction between crack-tip stress field and solute atoms, J. Fluids Eng. Trans. ASME. 92 (1970) 633–638. https://doi.org/10.1115/1.3425090.

[154] Y. Kim, Y.J. Chao, M.J. Pechersky, M.J. Morgan, On the effect of hydrogen on the fracture toughness of steel, Int. J. Fract. 134 (2005) 339–347. https://doi.org/10.1007/s10704-005-1974-7.

[155] Y. Wang, J. Gong, W. Jiang, A quantitative description on fracture toughness of steels in hydrogen gas, Int. J. Hydrogen Energy. 38 (2013) 12503–12508. https://doi.org/10.1016/j.ijhydene.2013.07.033.

[156] T. Iijima, H. Itoga, B. An, C.S. Marchi, B.P. Somerday, Fracture properties of a Cr-Mo ferritic steel in high-pressure gaseous hydrogen, Am. Soc. Mech. Eng. Press. Vessel. Pip. Div. PVP. 6B-2015 (2015) 1–7. https://doi.org/10.1115/PVP201545328.

[157] J.H. Liu, L. Wang, Y. Liu, X. Song, J. Luo, D. Yuan, Effects of hydrogen on fracture toughness and fracture behaviour of SA508-III steel, Mater. Res. Innov. 18 (2014) S4255–S4259. https://doi.org/10.1179/1432891714Z.000000000689.

[158] H.E. Townsend, Effects of zinc coatings on the stress corrosion cracking and hydrogen embrittlement of low-alloy steel, Metall. Trans. A. 6 (1975) 877–883. https://doi.org/10.1007/BF02672311.

[159] R. Wang, Effects of hydrogen on the fracture toughness of a X70 pipeline steel, Corros. Sci. 51 (2009) 2803–2810. https://doi.org/10.1016/j.corsci.2009.07.013.

[160] R.L.S. Thomas, J.R. Scully, R.P. Gangloff, Internal hydrogen embrittlement of ultrahigh-strength AERMET 100 steel, Metall. Mater. Trans. A Phys. Metall. Mater. Sci. 34 (2003) 327–344. https://doi.org/10.1007/s11661-003-0334-3.

[161] G. Álvarez, A. Zafra, F.J. Belzunce, C. Rodríguez, Hydrogen embrittlement analysis in a CrMoV steel by means of sent specimens, Theor. Appl. Fract. Mech. 106 (2020) 102450. https://doi.org/10.1016/j.tafmec.2019.102450.

[162] T. An, S. Zhang, M. Feng, B. Luo, S. Zheng, L. Chen, L. Zhang, Synergistic action of hydrogen gas and weld defects on fracture toughness of X80 pipeline steel, Int. J. Fatigue. 120 (2019) 23–32. https://doi.org/10.1016/j.ijfatigue.2018.10.021.

[163] H.S. Lu, Y.H. Yang, G. Chen, X. Chen, X. Wang, Fracture Toughness of Different Locations of Spiral Submerged Arc Welded Joints in API X80 Pipeline Steels, Procedia Eng. 130 (2015) 828–834. https://doi.org/10.1016/j.proeng.2015.12.203.

[164] A. Elrefaey, Y. Javadi, J.A. Francis, M.D. Callaghan, A.J. Leonard, Evolution of microstructure and toughness in 2.25Cr-1Mo steel welds, Int. J. Press. Vessel. Pip. 165 (2018) 20–28. https://doi.org/10.1016/j.ijpvp.2018.05.006.

[165] Y. Shi, Z. Han, Effect of weld thermal cycle on microstructure and fracture toughness of simulated heat-affected zone for a 800 MPa grade high strength low alloy steel, J. Mater. Process. Technol. 207 (2008) 30–39. https://doi.org/10.1016/j.jmatprotec.2007.12.049.

[166] H. Ma, Z. Liu, C. Du, X. Li, Z. Cui, Comparative study of the SCC behavior of E690 steel and simulated HAZ microstructures in a SO2-polluted marine atmosphere, Mater. Sci. Eng. A. 650 (2016) 93–101. https://doi.org/10.1016/j.msea.2015.09.052.

[167] J.B. Ju, W. sik Kim, J. il Jang, Variations in DBTT and CTOD within weld heat-affected zone of API X65 pipeline steel, Mater. Sci. Eng. A. 546 (2012) 258–262. https://doi.org/10.1016/j.msea.2012.03.062.

[168] V. Olden, A. Alvaro, O.M. Akselsen, Hydrogen diffusion and hydrogen influenced critical stress intensity in an API X70 pipeline steel welded joint-Experiments and FE simulations, Int. J. Hydrogen Energy. 37 (2012) 11474–11486.

https://doi.org/10.1016/j.ijhydene.2012.05.005.

[169] J.J.A. Wang, F. Ren, T. Tan, K. Liu, The development of in situ fracture toughness evaluation techniques in hydrogen environment, Int. J. Hydrogen Energy. 40 (2015) 2013–2024. https://doi.org/10.1016/j.ijhydene.2014.11.147.

[170] A. Alvaro, V. Olden, A. Macadre, Hydrogen embrittlement susceptibility of a weld simulated X70 heat affected zone under H2 pressure, Mater. Sci. Eng. A. 597 (2014) 29–36. https://doi.org/10.1016/j.msea.2013.12.042.

[171] L. Duprez, E. Leunis, Ö.E. Güngr, S. Claessens, Hydrogen embrittlement of high strength, low alloy (HSLA) steels and their welds, Gaseous Hydrog. Embrittlement Mater. Energy Technol. Probl. Its Characterisation Eff. Part. Alloy Classes. (2012) 562–591. https://doi.org/10.1533/9780857093899.3.562.

[172] S. Pillot, C. Chauvy, S. Corre, L. Coudreuse, A. Gingell, D. Héritier, P. Toussaint, Effect of temper and hydrogen embrittlement on mechanical properties of 2,25Cr-1Mo steel grades - Application to Minimum Pressurizing Temperature (MPT) issues. Part II: Vintage reactors & MPT determination, Int. J. Press. Vessel. Pip. 110 (2013) 24–31. https://doi.org/10.1016/j.ijpvp.2013.04.018.

[173] EN ISO 15653, Metallic Materials. Method of test for determination of quasistatic fracture toughness of Welds, Eur. Stand. (2010).

[174] L. Lan, X. Kong, Z. Hu, C. Qiu, D. Zhao, L. Du, Hydrogen permeation behavior in relation to microstructural evolution of low carbon bainitic steel weldments, Corros. Sci. 112 (2016) 180–193. https://doi.org/10.1016/j.corsci.2016.07.025.

[175] D.R.G. Mitchell, C.J. Moss, R.R. Griffiths, Optimisation of post-weld heat treatment of a 1.25Cr-0.5Mo pressure vessel for high temperature hydrogen service, Int. J. Press. Vessel. Pip. 76 (1999) 259–266. https://doi.org/10.1016/S0308-0161(98)00131-8.

[176] T. Dai, J.C. Lippold, The effect of postweld heat treatment on hydrogen-assisted cracking of f22/625 overlays, Weld. J. 97 (2018) 75S-90S. https://doi.org/10.29391/2018.97.007.

[177] Y. Song, M. Chai, W. Wu, Y. Liu, M. Qin, G. Cheng, Experimental investigation of the effect of hydrogen on fracture toughness of 2.25Cr-1Mo-0.25V steel and welds after annealing, Materials (Basel). 11 (2018) 1–14. https://doi.org/10.3390/ma11040499.

[178] T. Matsumoto, M. Kubota, S. Matsuoka, P. Ginet, J. Furtado, F. Barbier, Threshold stress intensity factor for hydrogen-assisted cracking of CR-MO steel used as stationary storage buffer of a hydrogen refueling station, Int. J. Hydrogen Energy. 42 (2017) 7422–7428. https://doi.org/10.1016/j.ijhydene.2016.05.124.

[179] Y. Wada, R. Ishigaki, Evaluation of metal materials for hydrogen fuel stations, … Hydrog. Saf. (2005). http://conference.ing.unipi.it/ichs2005/Papers/220113.pdf.

[180] B.P. Somerday, K.A. Nibur, Effect of Applied K Level on the Crack-Arrest Threshold in Hydrogen Environments: Mechanics-Based Interpretation, Corrosion. 75 (2019) 929–937. https://doi.org/10.5006/3106.

[181] W.M. Garrison, N.R. Moody, Hydrogen embrittlement of high strength steels, Gaseous Hydrog. Embrittlement Mater. Energy Technol. Probl. Its Characterisation Eff. Part. Alloy Classes. (2012) 421–492. https://doi.org/10.1533/9780857093899.3.421.

[182] S. Konosu, R. Uemori, M. Yuga, H. Yamamoto, Hydrogen-assisted subcritical crack growth rate in Cr-Mo steels, PVP2014-28720. (2014) 1–12.

[183] S. Konosu, T. Inoue, Y. Murakami, Evaluation of the internal hydrogen-induced threshold stress intensity factor in 2.25Cr1Mo steels determined by the offset potential drop method, Pvp2017-65505. (2017) 1–13.

[184] R.P. Wei, S.R. Novak, Interlaboratory Evaluation of KISCC and da/dt Measurement Procedures for High-Strenght Steels, J. Test. Eval. 15 (1987) 38–75.

[185] T. Das, S.K. Rajagopalan, S. V. Brahimi, X. Wang, S. Yue, A study on the susceptibility of high strength tempered martensite steels to hydrogen embrittlement (HE) based on incremental step load (ISL) testing methodology, Mater. Sci. Eng. A. 716 (2018) 189–207. https://doi.org/10.1016/j.msea.2018.01.032.

[186] Y. Sun, Q. Wang, S. Gu, Z. He, Q. Wang, F. Zhang, Sulfide stress cracking behavior of a martensitic steel controlled by tempering temperature, Materials (Basel). 11 (2018). https://doi.org/10.3390/ma11030412.

[187] A. Macadre, M. Artamonov, S. Matsuoka, J. Furtado, Effects of hydrogen pressure and test frequency on fatigue crack growth properties of Ni–Cr–Mo steel candidate for a storage cylinder of a 70MPa hydrogen filling station, Eng. Fract. Mech. 78 (2011) 3196–3211. https://doi.org/10.1016/j.engfracmech.2011.09.007.

[188] R.L. Amaro, N. Rustagi, K.O. Findley, E.S. Drexler, A.J. Slifka, Modeling the fatigue crack growth of X100 pipeline steel in gaseous hydrogen, Int. J. Fatigue. 59 (2014) 262–271. https://doi.org/10.1016/j.ijfatigue.2013.08.010.

[189] B.P. Somerday, P. Sofronis, K.A. Nibur, C. San Marchi, R. Kirchheim, Elucidating the variables affecting accelerated fatigue crack growth of steels in hydrogen gas with low oxygen concentrations, Acta Mater. 61 (2013) 6153–6170. https://doi.org/10.1016/j.actamat.2013.07.001.

[190] L. Briottet, R. Batisse, G. de Dinechin, P. Langlois, L. Thiers, Recommendations on X80 steel for the design of hydrogen gas transmission pipelines, Int. J. Hydrogen Energy. 37 (2012) 9423–9430. https://doi.org/10.1016/j.ijhydene.2012.02.009.

[191] Z. Hua, X. Zhang, J. Zheng, C. Gu, T. Cui, Y. Zhao, W. Peng, Hydrogen-enhanced fatigue life analysis of Cr–Mo steel high-pressure vessels, Int. J. Hydrogen Energy. 42 (2017) 12005–12014. https://doi.org/10.1016/j.ijhydene.2017.02.103.

[192] M. Dadfarnia, P. Sofronis, J. Brouwer, S. Sosa, Assessment of resistance to fatigue crack growth of natural gas line pipe steels carrying gas mixed with hydrogen, Int. J. Hydrogen Energy. 44 (2019) 10808–10822. https://doi.org/10.1016/j.ijhydene.2019.02.216.

[193] A.J. Slifka, E.S. Drexler, N.E. Nanninga, Y.S. Levy, J.D. McColskey, R.L. Amaro, A.E. Stevenson, Fatigue crack growth of two pipeline steels in a pressurized hydrogen environment, Corros. Sci. 78 (2014) 313–321. https://doi.org/10.1016/j.corsci.2013.10.014.

[194] K.A. Nibur, B.P. Somerday, Pvp2010-25827 Fracture and Fatigue Tolerant Steel Pressure Vessels for, (2010) 1–10.

[195] H.J. Cialone, J.H. Holbrook, Effects of gaseous hydrogen on fatigue crack growth in

pipeline steel, Metall. Trans. A. 16 (1985) 115–122. https://doi.org/10.1007/BF02656719.

[196] S. Suresh, R.O. Ritchie, Mechanistic dissimilarities between environmentally influenced fatigue-crack propagation at near-threshold and higher growth rates in lower strength steels, Met. Sci. 16 (1982) 529–538. https://doi.org/10.1179/msc.1982.16.11.529.

[197] J. Yamabe, H. Matsunaga, Y. Furuya, S. Hamada, H. Itoga, M. Yoshikawa, E. Takeuchi, S. Matsuoka, Qualification of chromium-molybdenum steel based on the safety factor multiplier method in CHMC1-2014, Int. J. Hydrogen Energy. 40 (2015) 719–728. https://doi.org/10.1016/j.ijhydene.2014.10.114.

[198] K. Tazoe, S. Hamada, H. Noguchi, Fatigue crack growth behavior of JIS SCM440 steel near fatigue threshold in 9-MPa hydrogen gas environment, Int. J. Hydrogen Energy. 42 (2017) 13158–13170. https://doi.org/10.1016/j.ijhydene.2017.03.223.

[199] J.H. Chuang, L.W. Tsay, C. Chen, Crack growth behaviour of heat-treated 4140 steel in air and gaseous hydrogen, Int. J. Fatigue. 20 (1998) 531–536. https://doi.org/10.1016/S0142-1123(98)00019-X.

[200] L. Tau, S.L.I. Chan, C.S. Shin, Hydrogen enhanced fatigue crack propagation of bainitic and tempered martensitic steels, Corros. Sci. 38 (1996) 2049–2060. https://doi.org/10.1016/S0010-938X(96)89123-2.

[201] A. Cheng, N.Z. Chen, Fatigue crack growth modelling for pipeline carbon steels under gaseous hydrogen conditions, Int. J. Fatigue. 96 (2017) 152–161. https://doi.org/10.1016/j.ijfatigue.2016.11.029.

[202] J. Yamabe, T. Matsumoto, S. Matsuoka, Y. Murakami, A new mechanism in hydrogen-enhanced fatigue crack growth behavior of a 1900-MPa-class high-strength steel, Int. J. Fract. 177 (2012) 141–162. https://doi.org/10.1007/s10704-012-9760-9.

[203] B. Vargas-Arista, J. Teran-Guillen, J. Solis, G. Garcia-Cerecero, M. Martinez-Madrid, Normalizing effect on fatigue crack propagation at the heat-affected zone of AISI 4140 steel shielded metal arc weldings, Mater. Res. 16 (2013) 772–778. https://doi.org/10.1590/S1516-14392013005000047.

[204] K. Xu, Hydrogen embrittlement of carbon steels and their welds, Gaseous Hydrog. Embrittlement Mater. Energy Technol. Probl. Its Characterisation Eff. Part. Alloy Classes. (2012) 526–561. https://doi.org/10.1533/9780857093899.3.526.

[205] L.W. Tsay, C.C. Liu, Y.H. Chao, Y.H. Shieh, Fatigue crack propagation in 2.25 Cr-1.0Mo steel weldments in air and hydrogen, Mater. Sci. Eng. A. 299 (2001) 16–26. https://doi.org/10.1016/S0921-5093(00)01420-9.

[206] V.R. Nagarajan, S.K. Putatunda, J. Boileau, Fatigue crack growth behavior of austempered AISI 4140 steel with dissolved hydrogen, Metals (Basel). 7 (2017) 1–18. https://doi.org/10.3390/met7110466.

[207] G.K. Williamson, R.E. Smallman, III. Dislocation densities in some annealed and cold-worked metals from measurements on the X-ray Debye-Scherrer spectrum, Philos. Mag. 1 (1956) 34–46. https://doi.org/10.1080/14786435608238074.

[208] M.N. Yoozbashi, S. Yazdani, XRD and TEM study of bainitic ferrite plate thickness in nanostructured, carbide free bainitic steels, Mater. Chem. Phys. 160 (2015) 148–154.

https://doi.org/10.1016/j.matchemphys.2015.03.071.

[209] S. Takebayashl, T. Kunieda, N. Yoshinaga, K. Ushioda, S. Ogata, Comparison of the dislocation density in martensitic steels evaluated by some X-ray diffraction methods, ISIJ Int. 50 (2010) 875–882. https://doi.org/10.2355/isijinternational.50.875.

[210] G.E. Linnert, Welding Metallurgy, vol. 1, American Welding Society, Miami, Florida, USA, 1994.

[211] F. Cverna, ed., Thermal properties of metals, ASM International, Materials Park (OH), 2002.

[212] C.R. Brooks, Principles of the heat treatmnet of plain carbon and low alloyed steels, ASM International, Materials Park (OH), 1996.

[213] A. López-Suárez, Influence of surface roughness on consecutively hydrogen absorption cycles in Ti-6Al-4V alloy, Int. J. Hydrogen Energy. 35 (2010) 10404–10411. https://doi.org/10.1016/j.ijhydene.2010.07.163.

[214] J.A. Carreño, I. Uribe, J.C. Carrillo, Modelling of roughness effect on hydrogen permeation in a low carbon steel, Rev. Metal. (2003) 213–218. https://doi.org/10.3989/revmetalm.2003.v39.iextra.1122.

[215] R. Réquiz, N. Vera, S. Camero, The influence of surface roughness on the hydrogen permeation of type API 5L-X52 steel, Rev. Metal. 40 (2004) 30–38. https://doi.org/10.3989/revmetalm.2004.v40.i1.240.

[216] T. Zakroczymski, Z. Szklarska-Śmiałowska, M. Smialowski, Effect of Arsenic on Permeation of Hydrogen Through Steel Membranes polarized cathodically in aqueous solution, Mater. Corros. 26 (1975) 617–624. https://doi.org/10.1002/maco.19750260804.

[217] S. Ningshen, M. Uhlemann, F. Schneider, H.S. Khatak, Diffusion behaviour of hydrogen in nitrogen containing austenitic alloys, Corros. Sci. 43 (2001) 2255–2264. https://doi.org/10.1016/S0010-938X(01)00017-8.

[218] P. Manolatos, M. Jerome, J. Galland, Necessity of a palladium coating to ensure hydrogen oxidation during electrochemical permeation measurements on iron, Electrochim. Acta. 40 (1995) 867–871. https://doi.org/10.1016/0013-4686(94)00343-Y.

[219] J. Svoboda, G. Mori, A. Prethaler, F.D. Fischer, Determination of trapping parameters and the chemical diffusion coefficient from hydrogen permeation experiments, Corros. Sci. 82 (2014) 93–100. https://doi.org/10.1016/j.corsci.2014.01.002.

[220] A. Zafra, J. Belzunce, C. Rodríguez, Hydrogen diffusion and trapping in 42CrMo4 quenched and tempered steel: influence of quenching temperature and plastic deformation, Mater. Chem. Phys. 255 (2020) 123599.

[221] J. Kittel, X. Feaugas, J. Creus, Impact of charging conditions and membrane thickness on hydrogen permeation through steel: Thick/thin membrane concepts revisited, NACE - Int. Corros. Conf. Ser. 2 (2016) 858–878.

[222] J. Kittel, F. Ropital, J. Pellier, New insights into hydrogen permeation in steels: Measurements through thick membranes, NACE - Int. Corros. Conf. Ser. (2008) 084091–0840922.

[223] A.H.M. Krom, A.D. Bakker, Hydrogen trapping models in steel, Metall. Mater. Trans. B Process Metall. Mater. Process. Sci. 31 (2000) 1475–1482. https://doi.org/10.1007/s11663-000-0032-0.

[224] S.K. Yen, I.B. Huang, Critical hydrogen concentration for hydrogen-induced blistering on AISI 430 stainless steel, Mater. Chem. Phys. 80 (2003) 662–666. https://doi.org/10.1016/S0254-0584(03)00084-1.

[225] H. Izadi, M. Tavakoli, M.H. Moayed, Effect of thermomechanical processing on hydrogen permeation in API X70 pipeline steel, Mater. Chem. Phys. 220 (2018) 360–365. https://doi.org/10.1016/j.matchemphys.2018.09.018.

[226] ASTM G146: Evaluation of disbonding of bimetallic stainless alloy/steel plate for use in high-pressure, high temperature refinery hydrogen service, vol. 03.02, Annual Book of ASTM Standards, 2013.

[227] C.S. Marchi, B.P. Somerday, S.L. Robinson, Permeability, solubility and diffusivity of hydrogen isotopes in stainless steels at high gas pressures, Int. J. Hydrogen Energy. 32 (2007) 100–116. https://doi.org/10.1016/j.ijhydene.2006.05.008.

[228] T. Schaffner, A. Hartmaier, V. Kokotin, M. Pohl, Analysis of hydrogen diffusion and trapping in ultra-high strength steel grades, J. Alloys Compd. 746 (2018) 557–566. https://doi.org/10.1016/j.jallcom.2018.02.264.

[229] A. Turnbull, R.B. Hutchings, D.H. Ferriss, Modelling of thermal desorption of hydrogen from metals, Mater. Sci. Eng. A. 238 (1997) 317–328. https://doi.org/10.1016/S0921-5093(97)00426-7.

[230] UNE-EN ISO 6892-1:2016, Materiales metálicos. Ensayo de tracción. Parte 1: Método de ensayo a temperatura ambiente., (n.d.).

[231] H. Neuber, F.A. Raven, J.S. Brock, Theory of Notch Stresses:principles for exact stress calculation, Julius Springer, Berlin, 1937.

[232] S. Takagi, S. Terasaki, K. Tsuzaki, T. Inoue, F. Minami, Application of Local Approach to Hydrogen Embrittlement Fracture Evaluation of High Strength Steels, Mater. Sci. Forum. 539–543 (2007) 2155–2161. https://doi.org/10.4028/www.scientific.net/msf.539-543.2155.

[233] F.M. Testing, ASME E1820-01Standard Test Method for Measurement of Fracture Toughness, (2001). https://doi.org/10.1520/E1820-09.2.

[234] ASTM E1681: Standard Test Method for Determining a Threshold Stress Intensity Factor for Environment-Assisted Cracking of Metallic Materials, ASTM Int. 03 (2003) 2–7. https://doi.org/10.1520/E1681-03R08E02.2.

[235] G. Krauss, Martensite in steel: Strength and structure, Mater. Sci. Eng. A. 273–275 (1999) 40–57. https://doi.org/10.1016/s0921-5093(99)00288-9.

[236] R.A. Renzetti, H.R.Z. Sandim, R.E. Bolmaro, P.A. Suzuki, A. Möslang, X-ray evaluation of dislocation density in ODS-Eurofer steel, Mater. Sci. Eng. A. 534 (2012) 142–146. https://doi.org/10.1016/j.msea.2011.11.051.

[237] J. Pešička, R. Kužel, A. Dronhofer, G. Eggeler, The evolution of dislocation density during heat treatment and creep of tempered martensite ferritic steels, Acta Mater. 51 (2003)

4847–4862. https://doi.org/10.1016/S1359-6454(03)00324-0.

[238] G. Krauss, STEEL: Heat treatment and processing principles, ASM International, Materials Park (OH), 1990.

[239] George Krauss, Steels: Processing, Structure and Performance, 2005.

[240] H. Huang, W.J.D. Shaw, Hydrogen embrittlement interactions in cold-worked steel, Corrosion. 51 (1995) 30–36. https://doi.org/10.5006/1.3293573.

[241] P. Sofronis, Y. Liang, N. Aravas, Hydrogen induced shear localization of the plastic flow in metals and alloys, Eur. J. Mech. A/Solids. 20 (2001) 857–872. https://doi.org/10.1016/S0997-7538(01)01179-2.

[242] Y.D. Han, R.Z. Wang, H. Wang, L.Y. Xu, Hydrogen embrittlement sensitivity of X100 pipeline steel under different pre-strain, Int. J. Hydrogen Energy. 44 (2019) 22380–22393. https://doi.org/10.1016/j.ijhydene.2019.06.054.

[243] B.C. De Cooman and J.G. Speer, Fundamentals of Steel Product Physical Metallurgy, 3rd ed., Warrendale, USA, 2012.

[244] X. Li, J. Zhang, Y. Wang, M. Ma, S. Shen, X. Song, The dual role of shot peening in hydrogen-assisted cracking of PSB1080 high strength steel, Mater. Des. 110 (2016) 602–615. https://doi.org/10.1016/j.matdes.2016.07.121.

[245] W. Krieger, S. V Merzlikin, A. Bashir, A. Szczepaniak, Spatially resolved detection with Scanning Kelvin Probe Force Microscopy (SKPFM), Acta Mater. (2017). https://doi.org/10.1016/j.actamat.2017.10.066.

[246] W.Y. Choo, J.Y. Lee, Effect of cold working on the hydrogen trapping phenomena in pure iron, Metall. Trans. A. 14 (1983) 1299–1305. https://doi.org/10.1007/BF02664812.

[247] B.J. Berkowitz, F.H. Heubaum, Dislocation Transport of Hydrogen in Steel., NATO Conf. Ser. 6 Mater. Sci. 5 (1983) 823–827.

[248] M. Kurkela, G.S. Frankel, R.M. Latanision, S. Suresh, R.O. Ritchie, Influence of plastic deformation on hydrogen transport in 2 1 4 Cr-1Mo steel, Scr. Metall. 16 (1982) 455–459. https://doi.org/10.1016/0036-9748(82)90172-7.

[249] Y. Takeda, C.J. McMahon Jr., Strain controlled vs. qtress controlled hydrogen induced fracture in a quenched and qempered steel, Metall. Mater. Trans. A. 12A (1981) 1255–1266.

[250] T. Matsuo, N. Homma, S. Matsuoka, Y. Murakami, Effect of hydrogen and prestrain on tensile properties of carbon steel SGP (0.078C-0.012Si-0.35Mn, mass%) for 0.1 MPa hydrogen pipelines, Trans. JSME A. 74 (2008) 1165–73.

[251] A. Nagao, C.D. Smith, M. Dadfarnia, P. Sofronis, I.M. Robertson, Interpretation of Hydrogen-induced Fracture Surface Morphologies for Lath Martensitic Steel, Procedia Mater. Sci. 3 (2014) 1700–1705. https://doi.org/10.1016/j.mspro.2014.06.274.

[252] T. An, S. Zheng, H. Peng, X. Wen, L. Chen, L. Zhang, Synergistic action of hydrogen and stress concentration on the fatigue properties of X80 pipeline steel, Mater. Sci. Eng. A. 700 (2017) 321–330. https://doi.org/10.1016/j.msea.2017.06.029.

[253] P. Novak, R. Yuan, B.P. Somerday, P. Sofronis, R.O. Ritchie, A statistical, physical-based, micro-mechanical model of hydrogen-induced intergranular fracture in steel, J. Mech. Phys. Solids. 58 (2010) 206–226. https://doi.org/10.1016/j.jmps.2009.10.005.

[254] A. Nagao, M.L. Martin, M. Dadfarnia, P. Sofronis, I.M. Robertson, The effect of nanosized (Ti,Mo)C precipitates on hydrogen embrittlement of tempered lath martensitic steel, Acta Mater. 74 (2014) 244–254. https://doi.org/10.1016/j.actamat.2014.04.051.

[255] M.L. Martin, M. Dadfarnia, A. Nagao, S. Wang, P. Sofronis, Enumeration of the hydrogen-enhanced localized plasticity mechanism for hydrogen embrittlement in structural materials, Acta Mater. 165 (2019) 734–750. https://doi.org/10.1016/j.actamat.2018.12.014.

[256] ASME E1820-01Standard Test Method for Measurement of Fracture Toughness, (2015).

[257] R.M. McMeeking, D.M. Parks, On criterioa for J-dominance of crack-tip filds in large-scale yielding, in: ASTM STP 668, American Society for Testing and Materials, Philadelphia, 1979: pp. 175–194.

[258] P. Sofronis, R.M. McMeeking, Numerical analysis of hydrogen transport near a blunting crack tip, J. Mech. Phys. Solids. 37 (1989) 317–350. https://doi.org/10.1016/0022-5096(89)90002-1.

[259] S. Il Pyun, H.K. Lee, Effect of threshold stress intensity on fracture mode transitions for hydrogen-assisted cracking in AISI 4340 steel, Metall. Trans. A. 21 (1990) 2577–2583. https://doi.org/10.1007/BF02647003.

[260] S. Matsuoka, H. Tanaka, N. Homma, Y. Murakami, Influence of hydrogen and frequency on fatigue crack growth behavior of Cr-Mo steel, Int. J. Fract. 168 (2011) 101–112. https://doi.org/10.1007/s10704-010-9560-z.

[261] R. Fernández-Sousa, C. Betegón, E. Martínez-Pañeda, Analysis of the influence of microstructural traps on hydrogen assisted fatigue, Acta Mater. 199 (2020) 253–263. https://doi.org/10.1016/j.actamat.2020.08.030.

[262] P. Fassina, M.F. Brunella, L. Lazzari, G. Re, L. Vergani, A. Sciuccati, Effect of hydrogen and low temperature on fatigue crack growth of pipeline steels, Eng. Fract. Mech. 103 (2013) 10–25. https://doi.org/10.1016/j.engfracmech.2012.09.023.

The Road goes ever on and on

Down from the door where it began.

Now far ahead the Road has gone,

And I must follow, if I can,

Pursuing it with eager feet,

Until it joins some larger way,

Where many paths and errands meet

J.R.R. Tolkien